UNIVERSITÄT
BAYREUTH

Dissertation

Photophysics and Electronic Structure of Molecular Catalysts and Chromophores

Sebastian E. Hammon

Photophysics and Electronic Structure of Molecular Catalysts and Chromophores

Von der Universität Bayreuth
zur Erlangung des Grades eines
Doktors der Naturwissenschaften (Dr. rer. nat.)
genehmigte Abhandlung

von

Sebastian Erich Hammon

aus Bayreuth

1. Gutachter: Prof. Dr. Stephan Kümmel
2. Gutachter: Prof. Dr. Stephan Gekle

Tag der Einreichung: 11. Mai 2022
Tag des Kolloquiums: 20. Juli 2022

Abstract

Solar hydrogen production via water splitting promises to sustainably produce clean fuel for various applications by primarily relying on two of the most abundant resources on Earth, sunlight and water. Photocatalysis is one of the technologies that has attracted increasing research interest for water splitting, along with the degradation of organic pollutants and the synthesis of value-added organic products. Experimental approaches rely on suitable light-active compounds that catalyze the respective chemical reactions which mainly occur in a solution of a substrate mixture. In modern catalysis, metal nanoparticles (MNPs) excel as (co)catalysts in various organic reactions due to their synergistic effects on catalytic performance. By the same token, MNPs are being explored in photocatalysis. However, obtaining detailed insights into the photocatalytic mechanism typically requires state-of-the-art experimental techniques, such as angle-resolved photoemission spectroscopy (ARPES). While these techniques provide a wealth of data, their interpretation can be challenging: On the one hand, the underlying photophysical and electronic phenomena are of complicated quantum nature. On the other hand, viable system designs must meet additional requirements, such as preventing the aggregation of MNPs, which adds to the multi-faceted nature of the systems. Therefore, it has proven expedient to use experimental and theoretical methods to characterize photocatalytic systems jointly. Due to its favorable ratio of accuracy to computational cost, ab-initio density-functional theory (DFT) in its standard Kohn-Sham formulation is currently the most popular electron-structure method in photocatalysis and, moreover, in most interdisciplinary fields of physics with chemistry, biology, and materials science.

This thesis's first of two project lines concerns predicting structural, electronic, and photophysical properties of molecular building blocks of (photo)catalytic systems containing MNPs using ground-state DFT and time-dependent DFT (TDDFT). A primary focus lies on understanding performance-related differences between certain cocatalytic MNP species (Ni, Pd, Pt) found in photocatalytic experiments for hydrogen production. Regarding the conceptual basis, I first present a DFT-based procedure to obtain low-energy molecular structures of systems containing MNPs, since these generally exhibit many geometries that are stable and similar in energy. This procedure is first applied to investigate whether MNPs and solvents interact (significantly). Studying small Pd nanoparticles (clusters) in solution with ketones shows that the interaction can affect the electronic and molecular structure of the metal particles. The interaction manifests itself, *inter alia*: (i) In changes in the electronic density of states of the metal-solvent systems near the Fermi level (compared to their components). (ii) In the quenching of the magnetic moment that Pd clusters otherwise exhibit in the gas phase. The results suggest that the electronic interaction is more pronounced with aromatic than non-aromatic solvents. In the course of a collaboration of physics and chemistry in a joint research center (SFB840, ”From Particulate Nanosystems to Mesotechnology”), we explore new design strategies in photocatalytic hydrogen production to replace cocatalytic noble MNPs with earth-abundant Ni: These novel approaches utilize the metal-organic framework MIL-101 to combine MNPs with either an Ir-based molecular photosensitizer or solid-state photocatalysts (CdS, CdS/TiO_2) without surface blocking ligands. The former enables hydrogen production via proton reduction

in water under visible light. Encapsulating the MNPs, and photosensitizer into the nanopores of MIL-101 prevents metal aggregation. CdS/TiO_2 and CdS decorated with MNPs accomplish the visible light-driven acceptorless dehydrogenation of alcohols and benzylamine under liberation of hydrogen, respectively. The MNPs reduce charge recombination and stabilize the CdS component against photooxidation. In most cases, the combination with MNPs promotes hydrogen production compared to the pure photosensitizer and photocatalyst, respectively. Encouragingly, Ni promotes hydrogen evolution in all cases, consistently outperforming the paradigmatic noble metals Pd and Pt. My studies contribute to a first understanding of the general role of MNPs and the synergistic effects of Ni in these systems: (i) DFT calculations reveal that the Ir photosensitizer and the substrates (benzyl alcohol, benzylamine) bind stronger to Ni than to the noble metal clusters. (ii) TDDFT calculations with optimally tuned range-separated hybrid functionals show that all three metals directly impact the photophysical properties of the photosensitizer via electronic interaction. The respective optical excitations feature a pronounced charge transfer from the metal cluster to the photosensitizer.

The second project line focuses on pump-probe ARPES. This technique is a powerful tool for characterizing the photoactivated state of materials, as it allows direct insights into the excited electronic structure. Here, I develop a method for predicting pump-probe ARPES from molecular systems using TDDFT in real space and real time. To this end, I present a method that unites the key elements of this technique – excitation, ionization, and detection – in a single TDDFT simulation. I first provide a proof of concept. Finally, studying the organic semiconductor molecule perylene-3,4,9,10-tetracarboxylic dianhydride shows that this approach accomplishes the challenging task of capturing many-body signatures of excitations. In other words, this method goes beyond the popular DFT-based single-particle interpretation of ARPES (experiments), and this study provides an example of when many-particle effects are so prominent that they cannot be disregarded. Overall, this method constitutes a viable extension to existing methods that can now be utilized to interpret many-particle effects in pump-probe experiments.

Kurzdarstellung

Die solare Wasserstofferzeugung durch Wasserspaltung verspricht, auf nachhaltige Weise sauberen Kraftstoff für verschiedene Anwendungen zu produzieren, indem sie sich in erster Linie auf zwei der am häufigsten vorkommenden Ressourcen der Erde stützt: Sonnenlicht und Wasser. Die Photokatalyse ist eine der Technologien, die für die Wasserspaltung sowie für den Abbau organischer Schadstoffe und die Synthese von organischen Produkten mit hohem Mehrwert auf zunehmendes Forschungsinteresse stößt. Experimentelle Ansätze beruhen auf geeigneten lichtaktive Materialien, welche die jeweiligen chemischen Reaktionen katalysieren, die überwiegend in Lösung eines Substratgemisches ablaufen. In der modernen Katalyse werden Metallnanopartikel (MNP) in einer Vielzahl von organischen Reaktionen aufgrund ihre synergistische Wirkung auf die katalytische Leistung eingesetzt. Aus diesem Grund werden sie auch in der Photokatalyse erforscht. Um jedoch detaillierte Einblicke in den photokatalytischen Mechanismus zu erhalten, sind in der Regel modernste experimentelle Techniken wie die winkelaufgelöste Photoemissionsspektroskopie (ARPES) erforderlich. Während diese Techniken eine Fülle von Daten liefern, kann deren Interpretation anspruchsvoll sein: Einerseits sind die zugrundeliegenden photophysikalischen und elektronischen Phänomene von komplizierter Quantennatur. Andererseits müssen tragfähige Systemdesigns zusätzliche Anforderungen erfüllen, wie beispielsweise die Unterbindung der Aggregation von MNP, was wiederum zum Facettenreichtum dieser Systeme beiträgt. Aus diesen Gründen hat es sich als zielführend erwiesen, experimentelle und theoretische Methoden gemeinsam zur Charakterisierung photokatalytischer Systeme einzusetzen. Dichtefunktionaltheorie (DFT) in ihrer Standardformulierung nach Kohn-Sham bietet ein vorteilhaftes Verhältnis von Genauigkeit zu Rechenaufwand zur Bestimmung der elektronischen Struktur. Aus diesem Grund ist DFT derzeit die beliebteste ab-initio-Methode in der Photokatalyse und darüber hinaus in den meisten interdisziplinären Bereiche der Physik mit Chemie, Biologie und Materialwissenschaften.

Die erste Projektlinie dieser Arbeit befasst sich mit der Vorhersage der strukturellen, elektronischen und photophysikalischen Eigenschaften von molekularen Bausteinen mit MNP von (photo)katalytischen Systemen mittels Grundzustands-DFT und zeitabhängiger DFT (TDDFT). Ein Hauptaugenmerk liegt auf der Ergründung leistungsbezogener Unterschiede zwischen bestimmten kokatalytischen MNP-Spezies (Ni, Pd, Pt), die in (verschiedenen) photokatalytischen Experimenten zur Wasserstoffproduktion gefunden wurden. Hinsichtlich der konzeptionellen Grundlage stelle ich zunächst ein DFT-basiertes Verfahren vor, um niederenergetische Molekularstrukturen von Systemen zu bestimmen, die MNP enthalten, da diese typischerweise viele Geometrien aufweisen, die stabil und energetisch ähnlich sind. Dieses Verfahren wird zunächst angewandt, um zu untersuchen, ob MNP mit Lösungsmitteln interagieren. Die Untersuchung von kleinen Pd-Nanopartikeln (Cluster) in Lösung mit Ketonen zeigt, dass signifikante Veränderungen in der elektronischen und molekularen Struktur der Metallpartikel durch elektronische Wechselwirkungen auftreten können. Die Wechselwirkung manifestiert sich unter anderem: (i) In Veränderungen der elektronischen Zustandsdichte der Metall-Lösungsmittelsysteme in der Nähe des Fermi-Niveaus (im Vergleich zu ihren Komponenten). (ii) In der Verringerung des magnetischen Moments, das Pd-Cluster ansonsten in der Gasphase zeigen. Die Ergebnisse

deuten darauf hin, dass die Wechselwirkung mit aromatischen Lösungsmitteln stärker ausgeprägt ist als mit nicht-aromatischen. Im Rahmen einer Zusammenarbeit von Physik und Chemie in einem gemeinsamen Sonderforschungsbereich (SFB840, ”Von partikulären Nanosystemen zur Mesotechnologie”), erforschen wir neue Designstrategien in der photokatalytischen Wasserstoffproduktion, um co-katalytische Edelmetall-Nanopartikel, wie Pd und Pt, durch häufiger vorkommendes Ni zu ersetzen: In diesen neuen Ansätzen wird das metallorganische Gerüst MIL-101 verwendet, um MNP entweder mit einem molekularen Photosensibilisator auf Ir-Basis oder mit Festkörperphotokatalysatoren (CdS, CdS/TiO_2) ohne oberflächenblockierende Liganden zu kombinieren. Erstere ermöglichen die Wasserstoffproduktion bei sichtbarem Licht durch Protonenreduktion in Wasser und unterbindet die Metallaggregation, indem MNP und Photosensibilisator in den Nanoporen von MIL-101 eingekapselt werden. CdS/TiO_2 und CdS, deren Oberflächen mit MNP versehen sind, ermöglichen eine durch sichtbares Licht angetriebene akzeptorlose Dehydrierung von Alkoholen bzw. Benzylamin unter Freisetzung von Wasserstoff. Die MNP verringern die Ladungsrekombination und stabilisieren die CdS-Komponente gegen Photooxidation. In den meisten Fällen steigert die Kombination mit MNP die Wasserstoffproduktion im Vergleich zum reinen Photosensibilisator bzw. Photokatalysator. Erfreulicherweise steigert Ni die Wasserstoffentwicklung in allen Fällen und übertrifft dabei durchweg die paradigmatischen Edelmetalle Pd und Pt. Meine Studien zu diesen Systemen tragen zu einem ersten Verständnis der Rolle von MNP und der synergistischen Effekte von Ni bei: (i) DFT-Berechnungen zeigen, dass der Ir-Photosensibilisator und die Substrate (Benzylalkohol, Benzylamin) stärker an Ni- als an die Edelmetall-Cluster binden. (ii) TDDFT-Berechnungen mit optimal abgestimmten reichweitenseparierten Hybridfunktionalen zeigen, dass alle drei Metalle die photophysikalischen Eigenschaften des Photosensibilisators über elektronische Wechselwirkungen beeinflussen. Die jeweiligen optischen Anregungen weisen einen ausgeprägten Ladungstransfer vom Metall-Cluster zum Photosensibilisator auf.

Die zweite Projektlinie dieser Dissertation befasst sich mit der winkelaufgelösten Photoemissionsspektroskopie (ARPES) im Pump-Probe-Schema. Diese Technik ist ein leistungsfähiges Werkzeug zur Charakterisierung des photoaktivierten Zustands von Systemen, da sie direkte Einblicke in die angeregte elektronische Struktur bietet. Hier befasse ich mit der Vorhersage der Pump-Probe-ARPES von molekularen Systemen mittels TDDFT in Echtzeit auf einem Realraum-Gitter. Zu diesem Zweck stelle ich eine Methode vor, mit der die Schlüsselelemente dieser Technik – Anregung, Ionisation und Detektion – in einer einzigen TDDFT-Simulation vereint werden. Ich erbringe zunächst einen Konzeptnachweis. Schließlich zeigen die Untersuchung des organischen Halbleitermoleküls Perylen-3,4,9,10-Tetracarbonsäuredianhydrid, dass dieser Ansatz die schwierige Aufgabe der Erfassung von Viel-Teilchen-Signaturen von Anregungen bewältigt. Somit geht diese Methode über die populäre DFT-basierte Ein-Teilchen-Interpretation von ARPES(-Experimenten) hinaus, und diese Studie liefert ein Beispiel für den Fall, dass Viel-Teilchen-Effekte so ausgeprägt sind, dass sich nicht mehr vernachlässigt werden können. Insgesamt stellt diese Methode eine nützliche Erweiterung zu bestehenden Methoden dar, die nun für die Interpretation von Viel-Teilchen-Effekten in Pump-Probe-Experimenten eingesetzt werden kann.

Contents

Publication 2

Publication 3

Publication 4

Publication 5

Part I

Theory and Outline of Results

Chapter 1

Introduction

Among alternative energy sources, solar energy conversion is one of the cornerstones for achieving global climate stability [dBD11, COD+16, GBS+19]: Solar radiation carries a power of about 120 PW to our Earth's surface, which is immense compared to humanity's projected global demand of about 50 TW by the end of this century [LN06, BTB+11]. Hence, in principle, humankind could sustainably meet its entire energy needs by efficiently harvesting only a small fraction of the energy in the sunlight. The two main strategies for this purpose are the direct conversion of solar energy into electricity through photovoltaics and the storage of solar energy in chemical compounds [BTB+11, TWT+17]. ”Green” hydrogen is in many ways a prime example of how such strategies can be implemented: (i) Solar water splitting ($2H_2O \longrightarrow 2\,H_2 + O_2$) allows to store renewable primary energy into chemical energy, e.g., via photovoltaic-powered electrolytic cells, photoelectrolytic cells, and photocatalysis [TWT+17]. (ii) Hydrogen is considered one of the most promising secondary energy carriers because of its various applications in electricity generation, synthetic fuel production, heating, and seasonal storage [PMB+19, OBY21]. Hydrogen fuel cells, for example, convert chemical energy directly into electrical energy by cold combustion of H_2 and O_2 [MSS12]. (iii) Water is recovered as the only byproduct, and the epitome of a sustainable cycle is closed, in which H_2O acts as the superordinate catalyst. The ecological potential of green hydrogen has long been recognized, and the prognoses are that the global hydrogen demand could increase twenty-five-fold in the long term [OBY21]. However, hydrogen is still predominantly produced in ”gray” form, i.e., by processes such as steam-methane reforming, which relies heavily on conventionally fired chemical reactors [SL07, AHNH17, WEV+19]. Replacing gray with green hydrogen could save about 17% of the global industrial sector's annual carbon dioxide emissions [OBY21]. The bottleneck as to why green hydrogen has not caught up yet is ultimately cost-efficiency and correlated factors (performance, durability, upscaling) [JSB+16, OBY21]. Regarding solar water splitting, achieving high solar-to-hydrogen efficiencies is a crucial factor for economic viability, which is also a driving force for ongoing research in this direction [JSB+16].

Among the methods for water splitting, photocatalysis follows the most ”simplistic” setup [STM16, VGMLP21]: Suitable photoactive compounds suspended in water catalyze the half-reactions of water splitting. Typical photocatalysts are semi-conductor (heterojunction) materials in powders or colloidal forms [SW80, BKP+81, KK00, KKT04, MD10, WWM+10, FHS+15]. For example, compounds based on low-cost TiO_2 are used in many areas of photocatalysis [NKZI21, VGMLP21]. However, reaching a detailed understanding of the respective photocatalytic mechanism is challenging due to the complexity of the quantum-mechanical processes involved. Typically, an important part of the mechanism is the generation of electron-hole pairs upon optical excitation (according to the band gap of the system) that can trigger redox reactions in the respective conduction and valence band of the solid-state photocatalyst [NKZI21]. More elaborate system designs incorporate metal nanoparticles (MNPs) as cocatalyst, since these can significantly improve photocatalytic efficiencies in many cases [TKN09, WHDW12, AACC+15, WBSB18, VGMLP21]. In particular, noble metals such as Pt, Pd, and Ag are widely used due to their resistance to extreme corrosion and oxidation conditions [JCH21, HVR21]. Dispersing MNPs on the surface of solid-state photocatalysts is an efficient way to reduce the overall charge recombination, since the charge separation of the photoinduced electron-hole pairs is enhanced by a rapid electron transfer to the metal [Kam12, MSM+12, HZG+18]. Another advantage of this concept is that it prevents the aggregation of MNPs. Many photoactive materials suitable for hydrogen production operate in the ultraviolet region (UV) [NKZI21]. However, the latter accounts for only about 4% of the incoming solar irradiation, while the visible region (Vis) amounts to some 43% [ZYSA01]. Therefore, developing visible light-active (and economically viable) materials is one of the key challenges to achieving higher yields (for a review, see Ref. [AACC+15]).[1]

Popular alternatives to solid-state photocatalysts are molecular photosensitizers based on photoactive transition-metal complexes [KKG78, KLS79, KW87, WKW91, PRM13, ZAC+14, Wen18, MPBM19, DMC+21]. For example, heteroleptic Ir(III) complexes enable the visible light-driven production of hydrogen via proton reduction in water [GHL+05, TMC+07, CTB+09, WLL+10, GDL+12]. The mechanism of photosensitizers is typically based on photoexcitation leading to charge-separated and long-lived excited states [CHG93, LDM+01, ZWSG13]. Ir-based complexes, for example, facilitate this photo-mechanism by intersystem crossing [DMC+21]. The above excited-state properties can promote redox reactions that ultimately lead to hydrogen evolution [GHL+05, CTB+09, GDL+12]. Efficiencies are typically optimized in combination with an additional cocatalyst for water reduction, which is often a transition-metal complex [CAB08, GSS+09, FBB+16] or a noble metal in colloidal form [TMC+07, ZGX+12]. There are also approaches to combining MNPs with photosensitizers. For this purpose, however, a different strategy than in the above case is required to prevent metal aggregation: For example, polymer ligands [TMC+07, MB10] or metal-organic frameworks [WHDW12, ZL14] stabilize MNPs. Overall, the combination of MNPs with photosensitizers is still less explored than that with solid-state photocatalysts. For example, it is unclear whether MNPs are directly involved in the photophysical mechanism. If so, the underlying processes may be very complex [BBK15].

Detailed experimental insights into the photocatalytic mechanism usually require state-of-the-art time-resolved spectroscopy techniques with nanosecond resolution [NGF+14, ARM16, SSD+17]. These include luminescence, transient-absorption, and photoemission spectroscopy (PES) (for a review, see Ref. [PFL20]). In pump-probe PES, for example, a system is excited by a first laser pulse, and a second triggers photoemission. Therefore, this method is particularly

---

[1] To give an example [AACC+15]: With a band gap of $E_g \approx 2.4$ eV, CdS is in principle better suited for Vis water splitting than TiO_2 ($E_g \approx 3.2$ eV). However, CdS is less corrosion resistant than TiO_2.

suitable for studying the photoactivated state of systems by directly probing the excited electronic structure. While such methods provide a wealth of experimental data, their interpretation can be a demanding task due to the inherent complexity of the underlying processes. Moreover, various aspects of the system design, such as the approach to preventing metal aggregation, may have an impact on these processes. For such reasons, it has proven expedient to use experimental and theoretical methods in tandem to characterize photocatalytic systems; for some successful examples, see Refs. [NGF$^+$14, BHP$^+$14, FBB$^+$16, BMN$^+$17, WXZS17, GHSS21, EBV$^+$21]. Regarding the theoretical description of typical photocatalytic systems, highly accurate wave function-based methods are currently not an option due to the exponential scaling of the computational cost with the system size. Ab initio density-functional theory (DFT) is a viable choice: Firstly, it offers a favorable balance between accuracy and cost, allowing the study of systems with several hundred to a few thousand electrons [Koh99]. Secondly, it can also cope with challenging quantum phenomena, such as charge-transfer excitations in practice [UY14, Mai17, Kü17, SFG$^+$19, VT20]. While ground-state DFT [HK64, KS65] allows for characterizing electronic and structural properties of molecular and solid-state materials, time-dependent DFT (TDDFT) [RG84] in the linear regime provides access to their photophysical properties. Moreover, recent progress has been made in particular in predicting PES and transient-absorption spectroscopy based on simulations of the electron dynamics using TDDFT in real time [WFD$^+$10, DGVM$^+$12, DGBC$^+$13, WDGCR16, DK16, DGS$^+$16, DGHR17]. Efforts are ongoing to extend these methods to increasingly complex scenarios [SHDGR18, BAH$^+$20, SDPR$^+$21].

This thesis's first of two project lines is concerned with predicting structural, electronic, and photophysical properties of (photo)catalytic systems incorporating MNPs. To this end, I analyzed molecular building blocks containing MNPs by means of ground-state DFT and linear-response TDDFT. A primary focus is on understanding performance-related differences between cocatalytic MNP species found in photocatalytic experiments for hydrogen production (see below). At first, Pub. 1 laid some conceptual groundwork and probed whether the interaction between small Pd nanoparticles and solvents of the ketone family significantly affects certain structural and electronic properties of the metal-solvent systems. This study was motivated by the fact that many of the reactions in MNP catalysis occur in solution. Publications 2–4 involved a collaboration of physics and chemistry: In the spirit of green chemistry, we explored ways to replace commonly used noble metals with earth-abundant Ni in different photocatalytic systems designed for the visible light-driven H_2-production: Encouragingly, Ni promotes H_2-production, outperforming the paradigmatic noble metals Pd and Pt across all studies. Publications 2–3 concern the acceptorless dehydrogenation of alcohols and benzylamine under liberation of H_2. In other words, H_2-evolution is the highly attractive byproduct of upgrading organic substrates into value-added products. To this end, a photocatalyst based on CdS/TiO_2 and CdS decorated with MNPs was developed, respectively. Moreover, these photocatalysts were supported on colloidal metal-organic framework crystallites. In these systems, I investigated whether there are differences in the binding affinity to the respective substrate between Ni and the noble metals. Publication 4 combined an Ir-based photosensitizer with MNPs for H_2-production by encapsulation into the pores of a colloidal metal-organic framework to prevent the aggregation of metals. Here, I probed the interaction between the photosensitizer and the metals and what effect this may have on the photophysics of the photosensitizer.

The second project line concerns the prediction of pump-probe angle-resolved PES (ARPES) from molecular systems using TDDFT in real time, where the angle-resolved technique provides access to the electronic structure of materials with energy and momentum resolution [Hü03]. To this end, I conceptually advanced the method of Dauth *et al.* [DK16, DGS$^+$16] for predicting direct ARPES of molecular systems to the pump-probe scenario. Note that direct ARPES refers to studying photoemission from the electronic ground state. In Pub. 5, I applied the advanced pump-probe method to the frequently studied organic semiconductor molecule perylene-3,4,9,10-tetracarboxylic dianhydride (PTCDA), which is a paradigm test system for photoemission.

This thesis is organized as follows. Chapter 2 first outlines the foundations of the standard Kohn-Sham formalism [KS65] to ground-state DFT (Sec. 2.1) and TDDFT (Sec. 2.2). As for the implementation, Sec. 2.3 focuses on several computational methods used throughout this thesis. In practice, DFT relies on approximations to the exchange-correlation energy functional, and in Chapter 3, I discuss those most relevant to this work. Chapter 4 summarizes the main results of the first project line (Pubs. 1–4) in Sec. 4.1 and the second project line (Pub. 5) in Sec. 4.2. Further introduction to MNP catalysis, the various (photo)catalytic systems related to my studies, and ARPES is provided in the respective section. Part II of this thesis contains all publications, including the author's contributions.

CHAPTER 2

Density-Functional Theory and its Applications to Molecular Systems

With an annual publication volume of more than 10,000 papers, ab-initio DFT in its standard Kohn-Sham formulation is currently the most popular method for predicting electronic properties of molecular and solid-state systems [HBM16]. The focus of this thesis is on molecular systems. The foundations of the ground-state and time-dependent version of DFT are outlined in Sec. 2.1 and Sec. 2.2, respectively. For a comprehensive introduction to DFT, the reader is referred to, e.g., Refs. [PK03, ED11, Ull12, MMN$^+$12, SLR$^+$12]. The following Sec. 2.3 addresses the application of DFT in terms of some of the key methods and concepts relevant to this thesis. This concerns: (i) The description of structural and electronic ground-state properties based on ground-state DFT (Sec. 2.3.1). (ii) The simulation of electron dynamics using TDDFT in real time (Sec. 2.3.2). (iii) Obtaining excited-state properties using the Casida approach to linear-response TDDFT (Sec. 2.3.3).

DFT is in principle an exact alternative formulation to quantum mechanics: By virtue of the theorems of Hohenberg-Kohn and Runge-Gross for ground-state DFT and TDDFT, it is guaranteed that all information about a quantum system is contained in its electronic ground-state density $n(\boldsymbol{r})$ and time-dependent density $n(\boldsymbol{r},t)$, respectively. This has the great advantage that the high dimensionality of the many-particle wave function and its associated challenges, such as the exponentially increasing computational costs (”exponential wall”), can be circumvented by primarily considering the electronic density as a function of only three spatial (and one temporal) coordinate [Koh99].

2.1 Fundamentals of Ground-State Density-Functional Theory

In the following, I consider the standard stationary many-body system of N interacting electrons to define the terminology first. From here on, the system is regarded within the Born-Oppenheimer approximation [BO27]. Further, the nuclei are considered as classical point particles. The non-relativistic electronic Hamiltonian in the Born-Oppenheimer approximation is $\hat{H} = \hat{T} + \hat{U} + \hat{V}$. The latter comprises the kinetic energy $\hat{T} = -\hbar^2/(2m)\sum_{i=1}^{N}\nabla_i^2$, the repulsive electron-electron interaction $\hat{U} = e^2/(4\pi\varepsilon_0)\sum_{i<j}^{N}|\boldsymbol{r}_i - \boldsymbol{r}_j|^{-1}$, and the potential energy of the electron-nucleus interaction $\hat{V} = \int v_{\text{ext}}(\boldsymbol{r})\hat{n}(\boldsymbol{r})\,\mathrm{d}\boldsymbol{r} = \sum_{i=1}^{N} v_{\text{ext}}(\boldsymbol{r}_i)$ (or some other external potential). $\hat{n}(\boldsymbol{r}) = \sum_{i=1}^{N}\delta(\boldsymbol{r} - \boldsymbol{r}_i)$ denotes the electron density operator, ∇^2 is the Laplace operator, e

is the elementary charge, m denotes the electron mass, $\hbar$ is the reduced Planck constant, and ε_0 is the vacuum permittivity. The Schrödinger equation of this system reads $\hat{H}\,|\Psi\rangle = E\,|\Psi\rangle$, where $|\Psi\rangle$ is the normalized antisymmetric N-electron wave function, and E is the corresponding energy eigenvalue. From here on, $|\Psi_0\rangle$ refers to the ground state with energy E_0. The ground-state density is $n_0(\boldsymbol{r}) = \langle\Psi_0|\hat{n}|\Psi_0\rangle$ and integrates to N. For simplicity, the following outline of DFT is limited to the case of non-degenerate ground states, but an extension to the degenerate case can be made [Lev82, Lie83].

The Hohenberg-Kohn theorem [HK64] forms the foundation of ground-state DFT by stating that all the information of the stationary many-body system is contained in its electronic ground-state density. This means, *inter alia*, that the ground-state wave function is an (implicit) functional of the ground-state density, denoted as $|\Psi_0\rangle = |\Psi[n_0]\rangle$. Consequently, every ground-state observable is a density functional, such as the ground-state energy $E_0 = E[n_0] = \langle\Psi[n_0]|\hat{H}|\Psi[n_0]\rangle$. The theorem further guarantees that a minimum principle exists for $E[n]$ according to which the true ground state density (n_0) minimizes the energy functional. Therefore, it follows $E[n_0] < E[n]$ for any $n(\boldsymbol{r}) \neq n_0(\boldsymbol{r})$. Moreover, the minimum principle can be cast into a variational equation [Lev79, Lie83]

$$\frac{\delta}{\delta n(\boldsymbol{r})}\left\{E[n] - \mu\left(\int n(\boldsymbol{r}')\,\mathrm{d}\boldsymbol{r}' - N\right)\right\}\Bigg|_{n_0(\boldsymbol{r})} = 0, \tag{2.1}$$

$$E[n] = T[n] + U[n] + V[n]. \tag{2.2}$$

The subsidiary condition ensures the correct normalization of the density by the Lagrange multiplier μ. Equation (2.1) implies that the ground-state density $n_0(\boldsymbol{r})$ can be determined by minimizing the sum (E) of the kinetic (T), the Coulomb interaction (U), and the external potential energy (V) with respect to the density. However, the Hohenberg-Kohn theorem does not provide an explicit scheme to obtain $n_0(\boldsymbol{r})$. To this end, the follow-up work of Kohn and Sham (KS) [KS65] provided a concrete formalism. From the perspective of the KS formalism, the interacting many-body system (of N electrons) is projected onto a non-interacting auxiliary system (of N fermionic particles) with a local multiplicative potential $v_\mathrm{s}(\boldsymbol{r})$ that formally reproduces exactly the density of the true interacting system.

The Hamiltonian of the auxiliary KS system is $\hat{H}_\mathrm{s} = \hat{T} + \hat{V}_\mathrm{s}$. The KS potential operator reads $\hat{V}_\mathrm{s} = \sum_\sigma \sum_i^{N_\sigma} v_{\mathrm{s}\sigma}(\boldsymbol{r}_i)$, switching to a spin-dependent notation with spin indices $\sigma = \{\uparrow,\downarrow\}$. The sum over the spin-dependent particle numbers equals $N_\uparrow + N_\downarrow = N$. The spin densities $n_\sigma(\boldsymbol{r})$ add up to the total density, and $\int n_\sigma(\boldsymbol{r})\,\mathrm{d}\boldsymbol{r}$ yields N_σ. The ground state of the KS system is a Slater determinant $|\Phi\rangle$ that is constructed from the $(N_\uparrow + N_\downarrow)$ energetically lowest[1] solutions $\{|\varphi_{j\sigma}\rangle\}$ of the so-called KS equation [vBH72]

$$\left[-\frac{\hbar^2}{2m}\nabla^2 + v_{\mathrm{s}\sigma}[n_\uparrow, n_\downarrow](\boldsymbol{r})\right]\varphi_{j\sigma}(\boldsymbol{r}) = \varepsilon_{j\sigma}\varphi_{j\sigma}(\boldsymbol{r}). \tag{2.3}$$

---

[1] Normally, the energy eigenvalues are assumed to be ordered as $\varepsilon_{1\sigma} \leq \varepsilon_{2\sigma} \leq \ldots \leq \varepsilon_{N_\sigma\sigma} < \varepsilon_{N_\sigma+1\sigma} \leq \ldots$. Thus, $\varepsilon_{N_\sigma\sigma}$ corresponds to the highest occupied molecular orbital $|\varphi_{N_\sigma\sigma}\rangle$.

The latter is an effective single-particle Schrödinger equation. For completeness, the total energy of the KS system is

$$E_s[n_\uparrow, n_\downarrow] = \langle \Phi | \hat{T} + \hat{V}_s | \Phi \rangle \, [n_\uparrow, n_\downarrow] = T_s[n_\uparrow, n_\downarrow] + \sum_{\sigma=\uparrow,\downarrow} \int \upsilon_{s\sigma}(\boldsymbol{r}) n_\sigma(\boldsymbol{r}) \, \mathrm{d}\boldsymbol{r}, \tag{2.4}$$

$$T_s = -\frac{\hbar^2}{2m} \sum_{\sigma=\uparrow,\downarrow} \sum_{j=1}^{N_\sigma} \int \varphi^*_{j\sigma}(\boldsymbol{r}) \nabla^2 \varphi_{j\sigma}(\boldsymbol{r}) \, \mathrm{d}\boldsymbol{r}. \tag{2.5}$$

E_s contains the non-interacting kinetic energy functional T_s, which is constructed from the $N_\uparrow + N_\downarrow$ energetically lowest single-particle KS orbitals $\{\varphi_{j\sigma}[n_\uparrow, n_\downarrow]\}$. Note that the KS orbitals implicitly depend on the density by virtue of the Hohenberg-Kohn theorem. Hence, $T_s[n_\uparrow, n_\downarrow]$ is an implicit density functional as well.

The central quantity, the ground-state density of the KS system $n(\boldsymbol{r})$ can be constructed from the orbital contributions $|\varphi_{j\sigma}(\boldsymbol{r})|^2$ via

$$n(\boldsymbol{r}) = \sum_{\sigma=\uparrow,\downarrow} n_\sigma(\boldsymbol{r}) = \sum_{\sigma=\uparrow,\downarrow} \sum_{j=1}^{N_\sigma} |\varphi_{j\sigma}(\boldsymbol{r})|^2, \qquad n(\boldsymbol{r}) \equiv n_0(\boldsymbol{r}). \tag{2.6}$$

The yet to be determined potential $\upsilon_{s\sigma}(\boldsymbol{r})$ of Eq. (2.3) needs to be chosen such that $n(\boldsymbol{r})$ is exactly equal to the true ground-state density of the interacting system $n_0(\boldsymbol{r})$. To this end, the standard derivation of $\upsilon_{s\sigma}$ uses a particular partitioning of the interacting energy functional (2.2) that reads [KS65]

$$E[n_\uparrow, n_\downarrow] = T_s[n_\uparrow, n_\downarrow] + V[n] + E_H[n] + E_{xc}[n_\uparrow, n_\downarrow]. \tag{2.7}$$

The terms on the right-hand side of the equation are the following: (i) The kinetic energy T_s of the non-interacting system. (ii) The external energy of the interacting system,

$$V[n] = \int \upsilon_{ext}(\boldsymbol{r}) n(\boldsymbol{r}) \, \mathrm{d}\boldsymbol{r}, \tag{2.8}$$

remains untouched in this partitioning. (iii) $E_H[n]$ is the classical Hartree (or Coulomb) interaction energy,

$$E_H[n] = \frac{e^2}{8\pi\varepsilon_0} \iint \frac{n(\boldsymbol{r}) n(\boldsymbol{r}')}{|\boldsymbol{r} - \boldsymbol{r}'|} \, \mathrm{d}\boldsymbol{r}' \, \mathrm{d}\boldsymbol{r}. \tag{2.9}$$

(iv) The remaining term in Eq. (2.7) is the exchange-correlation (xc) energy functional $E_{xc}[n_\uparrow, n_\downarrow]$. The latter can be formally defined as $E_{xc} := (U - E_H) + (T - T_s)$. That means E_{xc} is the difference between the full Coulomb interaction energy and the Hartree term, plus the difference between the full kinetic energy and the non-interacting one. Therefore, E_{xc} must contain all many-particle effects that the other contributions to Eq. (2.7) cannot contain. Consequently, $E_{xc}[n_\uparrow, n_\downarrow]$ is an extremely complex functional in general, as further discussed below.

Finally, the ingenious idea behind the KS formalism is that the minimization of Eq. (2.4) and

Eq. (2.7) according to Eq. (2.1) have the same solution $n(\boldsymbol{r}) \equiv n_0(\boldsymbol{r})$, if $\upsilon_{s\sigma}(\boldsymbol{r})$ is chosen as

$$\upsilon_{s\sigma}[n_\uparrow, n_\downarrow](\boldsymbol{r}) = \frac{e^2}{4\pi\varepsilon_0} \int \frac{n(\boldsymbol{r}')}{|\boldsymbol{r}-\boldsymbol{r}'|} \mathrm{d}\boldsymbol{r}' + \upsilon_{\mathrm{ext}}(\boldsymbol{r}) + \upsilon_{\mathrm{xc}\sigma}[n_\uparrow, n_\downarrow](\boldsymbol{r}), \tag{2.10}$$

$$\upsilon_{\mathrm{xc}\sigma}[n_\uparrow, n_\downarrow](\boldsymbol{r}) := \frac{\delta E_{\mathrm{xc}}[n_\uparrow, n_\downarrow]}{\delta n_\sigma(\boldsymbol{r})}. \tag{2.11}$$

The first term on the right-hand side of Eq. (2.10) is the Hartree potential $\upsilon_{\mathrm{H}}(\boldsymbol{r})$. The last term is the xc potential $\upsilon_{\mathrm{xc}\sigma}(\boldsymbol{r})$ that follows from the functional derivative of E_{xc} as defined in Eq. (2.11). Typically, E_{xc} and $\upsilon_{\mathrm{xc}\sigma}(\boldsymbol{r})$ are split into an exchange and correlation part in terms of $E_{\mathrm{xc}} = E_{\mathrm{x}} + E_{\mathrm{c}}$ and $\upsilon_{\mathrm{xc}\sigma}(\boldsymbol{r}) = \upsilon_{\mathrm{x}\sigma}(\boldsymbol{r}) + \upsilon_{\mathrm{c}\sigma}(\boldsymbol{r})$, respectively.

In principle, the KS scheme to ground-state DFT is an ab-initio formalism. Since no universal expression of the exact xc functional is known for practical implementation, density-functional approximations (DFAs) are usually necessary for E_{xc} and $\upsilon_{\mathrm{xc}\sigma}$, respectively. One might be tempted to argue that xc effects play a minor role, since, e.g., their contribution to the total energy can be relatively small in percentage terms [PK03]. However, it is precisely these subtle xc effects that significantly shape most properties of the electronic structure [Koh99, PK03]. Moreover, in practice, in most cases only a carefully chosen xc DFA provides an accurate description of the system properties [MHG17]. Furthermore, it is an ongoing task to develop efficient xc DFAs that improve on certain shortcomings of their predecessors. An overview of the xc DFAs relevant to this thesis is provided in Chapter. 3.

2.2 Fundamentals of Time-Dependent Density-Functional Theory

In the following, the interacting N-electron system of the previous section is subjected to an explicitly time-dependent external scalar potential $\upsilon_{\mathrm{ext}}(\boldsymbol{r},t)$, where the corresponding potential operator reads $\hat{V}(t) = \sum_{i=1}^{N} \upsilon_{\mathrm{ext}}(\boldsymbol{r}_i,t)$.[2] This scenario can be described in terms of the time-dependent Schrödinger equation $i\hbar\partial/\partial t\,|\Psi(t)\rangle = (\hat{T} + \hat{V}(t) + \hat{W})\,|\Psi(t)\rangle$ and equivalently, by the time-dependent density $n(\boldsymbol{r},t)$, as discussed in this section. From here on, it is assumed that the many-body system is in the initial state $|\Psi_{\mathrm{in}}\rangle := |\Psi(t=t_0)\rangle$ at time t_0. The time-dependent part of the external potential takes effect for $t \geq t_0$.

The Runge-Gross theorem [RG84] is the time-dependent complement of the stationary Hohenberg-Kohn theorem and forms the foundation for TDDFT. It guarantees that the time-dependent density $n(\boldsymbol{r},t)$ contains all the information about the time-dependent many-body system. For any fixed initial state $|\Psi_{\mathrm{in}}\rangle$, the theorem establishes a one-to-one correspondence between the density $n(\boldsymbol{r},t)$, the external potential $\upsilon_{\mathrm{ext}}(\boldsymbol{r},t)$ (apart from a time-dependent constant) and the many-body wave function $|\Psi(t)\rangle$ (apart from a time-dependent phase factor). Therefore, the many-body wave function is a unique functional of the density and the initial state, denoted as $|\Psi(t)\rangle = |\Psi[n,\Psi_{\mathrm{in}}](t)\rangle$. Thus, all observables $O(t)$, for which the phase factor cancels out, have the same functional dependency as the wave function. That is,

---

[2] Note that TDDFT can be generalized to include time-dependent external vector potentials [GD88].

$O[n,\Psi_{\mathrm{in}}](t) = \langle\Psi[n,\Psi_{\mathrm{in}}](t)|\hat{O}(t)|\Psi[n,\Psi_{\mathrm{in}}](t)\rangle$, where $\hat{O}(t)$ is the associated time-dependent operator. A special case is when the ground state of the stationary many-body system ($|\Psi_0\rangle$) is chosen as the initial state. Then, the observable becomes a unique functional of only the density by the virtue of the Hohenberg-Kohn theorem, i.e., $O(t) = O[n](t)$.

The remaining question at this point is whether the stationary KS formalism can be extended to the time domain. To this end, the van Leeuwen theorem [vL99] provides the formal justification. Applied to the interacting many-body system, the theorem states: There exists a non-interacting system with a unique external potential $\upsilon_{\mathrm{s}}[n,\Psi_{\mathrm{in}},\Phi_{\mathrm{in}}](\boldsymbol{r},t)$ that reproduces the time-dependent density of the interacting system, provided that the initial state of the non-interacting system $|\Phi_{\mathrm{in}}\rangle$ meets some (mild) constraints. Note that υ_{s} can become a unique functional of only the density by a particular choice of $|\Psi_{\mathrm{in}}\rangle$ and $|\Phi_{\mathrm{in}}\rangle$: (i) $|\Psi_{\mathrm{in}}\rangle \equiv |\Psi_0\rangle$, i.e, the interacting system is in its ground state $|\Psi_0\rangle$ at t_0. (ii) $|\Phi_{\mathrm{in}}\rangle \equiv |\Phi_0\rangle$, where $|\Phi_0\rangle$ is the ground state of the static KS system that yields the ground state density (n_0) of the interacting system.

With the formalism being on solid ground, the time-dependent KS (TDKS) equation [vL98]

$$\hat{h}_{\mathrm{s},\sigma}(t)\,\varphi_{j\sigma}(\boldsymbol{r},t) = \left[-\frac{\hbar^2}{2m}\nabla^2 + \upsilon_{\mathrm{s}\sigma}(\boldsymbol{r},t)\right]\varphi_{j\sigma}(\boldsymbol{r},t) = \mathrm{i}\hbar\frac{\partial}{\partial t}\varphi_{j\sigma}(\boldsymbol{r},t) \tag{2.12}$$

follows in its spin-dependent form. The exact time-dependent density of the interacting system $n(\boldsymbol{r},t)$ can be reproduced in analogy to Eq. (2.6) by

$$n(\boldsymbol{r},t) = \sum_{\sigma=\uparrow,\downarrow} n_\sigma(\boldsymbol{r},t) = \sum_{\sigma=\uparrow,\downarrow}\sum_{j=1}^{N_\sigma}|\varphi_{j\sigma}(\boldsymbol{r},t)|^2. \tag{2.13}$$

The TDKS potential of Eq. (2.12) is defined as

$$\upsilon_{\mathrm{s}\sigma}[n_\uparrow,n_\downarrow](\boldsymbol{r},t) = \frac{e^2}{4\pi\varepsilon_0}\int\frac{n(\boldsymbol{r}',t)}{|\boldsymbol{r}-\boldsymbol{r}'|}\,\mathrm{d}\boldsymbol{r}' + \upsilon_{\mathrm{ext}\sigma}(\boldsymbol{r},t) + \upsilon_{\mathrm{xc}\sigma}[n_\uparrow,n_\downarrow](\boldsymbol{r},t)\,. \tag{2.14}$$

The potential terms on the right-hand side of the equation are the following: (i) The time-dependent Hartree potential $\upsilon_{\mathrm{H}}(\boldsymbol{r},t)$. (ii) The spin-dependent external potential, which may include, e.g., the interaction with a time-dependent magnetic field in terms of the Zeeman term. In this thesis, however, only the interaction with (classical) electric fields is of relevance (cf. Pub. 5). Therefore, spin-independent external potentials are considered from here on. (iii) The last term, $\upsilon_{\mathrm{xc}\sigma}(\boldsymbol{r},t)$, contains all the time-dependent xc phenomena. The time-dependent xc potential is generally even more complex than its static counterpart because it is non-local in time. Or in other words, $\upsilon_{\mathrm{xc}\sigma}(\boldsymbol{r},t)$ contains memory effects. Without going into further details, $\upsilon_{\mathrm{xc}\sigma}(\boldsymbol{r},t)$ can be formally derived from the functional derivative of the xc action density functional and some boundary terms relevant to causality [Vig95, Vig08]. Alternatively, the xc potential follows from the functional derivative of an action density functional that is defined in the Keldysh pseudo-time formalism [vL98, vL99]. In practice, however, DFAs are again necessary for $\upsilon_{\mathrm{xc}\sigma}(\boldsymbol{r},t)$, because an exact and practicable form is typically unknown. Most applications rely on the adiabatic approximation $\upsilon^{\mathrm{A}}_{\mathrm{xc}\sigma}(\boldsymbol{r},t)$ to the time-dependent xc potential, which I also used throughout this thesis: $\upsilon^{\mathrm{A}}_{\mathrm{xc}\sigma}(\boldsymbol{r},t)$ is defined as the static xc potential $\upsilon^{(0)}_{\mathrm{xc}\sigma}(\boldsymbol{r})$ of Eq. (2.11) that is evaluated for the instantaneous density at time t,

$$\upsilon_{\mathrm{xc}\sigma}[n_\uparrow,n_\downarrow](\boldsymbol{r},t) \approx \upsilon^{\mathrm{A}}_{\mathrm{xc}\sigma}[n_\uparrow,n_\downarrow](\boldsymbol{r},t) = \upsilon^{(0)}_{\mathrm{xc}\sigma}[n_\uparrow,n_\downarrow](\boldsymbol{r})\bigg|_{n_\sigma=n_\sigma(\boldsymbol{r},t)} . \tag{2.15}$$

Therefore, $\upsilon^{\mathrm{A}}_{\mathrm{xc}\sigma}(\boldsymbol{r},t)$ is local in time and neglects all memory effects. For the application, the adiabatic approximation also implies that one resorts to the static DFAs of ground-state DFT for $\upsilon^{(0)}_{\mathrm{xc}\sigma}(\boldsymbol{r})$ (cf. Chapter 3). Unsurprisingly, the adiabatic functionals inherit the shortcomings of the static xc DFAs that they are based on.

Finally, there is the question how to solve the TDKS equations. Typically, this can be achieved by means of propagator schemes, as further addressed in Sec. 2.3.2. However, a complete solution of Eq. (2.12) is not always necessary. For example, linear-response TDDFT based on perturbation theory already provides access to excited-state properties, such as the photoabsorption spectrum (cf. Sec. 2.3.3).

2.3 Electronic Structure and Electron Dynamics of Molecular Systems

This section serves to provide some background information on the main ground-state DFT and TDDFT methods used throughout this thesis. Furthermore, some of the key implementation decisions and differences between the program codes that I primarily used to carry out my theoretical studies are discussed. These were BTDFT [Sch16, SK18], which is a non-commercial code developed by the Kümmel group, and the two license programs QCHEM [S$^+$15] and TURBOMOLE [TUR19]. Note that performance aspects of the xc DFAs that I used in combination with these methods are discussed in Chapter 3.

2.3.1 Ground-State Calculations and Geometry Optimizations

Performing a ground-state DFT calculation is the first step for almost any DFT application, be it stationary or time-dependent (cf. Secs. 2.3.2–2.3.3). In other words, the static KS Eq. (2.3) needs to be solved for the N-particle system of interest. This implies that the system has been defined by specifying its external potential $\upsilon_{\mathrm{ext}}(\boldsymbol{r})$ (see below). The KS equation is non-linear, since the KS potential $\upsilon_{\mathrm{s}\sigma}(\boldsymbol{r})$ (2.10) is a density functional itself. Therefore, the former is usually solved in a self-consistent iteration procedure.

DFT-based computer codes mainly use two concepts to represent the KS orbitals, which are discussed in this paragraph: (i) One approach is to express orbitals by a set of basis functions [VBG$^+$10, E$^+$10, S$^+$15, TUR19, NWBR20]. There are various types of basis sets (for an overview, see Ref. [JSFL$^+$17]). For finite systems, Gaussian-type basis sets are particularly popular because they facilitate the efficient evaluation of integrals. [SDE$^+$07, Hil13]. For example, TURBOMOLE makes use of ”in-house” developed Gaussian basis sets (named def2)

[WA05, Wei06]. For basis sets, the KS equation is typically cast into a matrix-eigenvalue problem to determine the expansion coefficients of the basis functions (for the respective KS orbital). The basis-set size, i.e., the number of basis functions, usually impacts the accuracy of the calculation [JSFL$^+$17, MP20]. Likewise, the computational cost scales with the basis-set size. Computations with large basis sets can quickly become expensive, even for small to medium-sized molecular systems. Therefore, one usually strives to find the best compromise between accuracy and performance. (ii) Alternatively, KS orbitals are discretized on a real-space grid [KMT$^+$06, A$^+$15, SK18]. An example of such an approach is the BTDFT code, which relies on the following implementation: The grid is an ellipsoid with equidistant grid spacing. The Laplace operator is represented by finite differences of 6'th order. In the course of the spatial discretization, the KS equations correspond to a sparse matrix eigenvalue problem. There exist special algorithms tailored to solve this type of linear equations [AHLT05], and BTDFT falls back on the parallel version of ARPACK [RLY]. The Hartree potential is obtained by solving Poisson's equation. Naturally, the accuracy of this approach depends on the grid spacing and the grid size. As computations become increasingly expensive for fine and/or large grids, an optimal ratio of accuracy to cost is usually sought. Overall, however, the computational cost of grid-based approach tends to scale better with the number of electrons than the basis set-based approach [Sch16, SK18].

So far, little has been said about the nuclei, except that they are considered as specified in Sec. 2.1. In the following, the molecular structure refers to the set of the M nuclear coordinates $\{\boldsymbol{R}_k\}$ of the system. The molecular structure enters parametrically into the part of the external potential that describes the electron-nucleus interaction in terms of

$$v_0(\boldsymbol{r}) = \frac{-e^2}{4\pi\varepsilon_0} \sum_{k=1}^{M} \frac{Z_k}{|\boldsymbol{r}-\boldsymbol{R}_k|}, \qquad v_0(\boldsymbol{r}) \equiv v_{\text{ext}}(\boldsymbol{r}). \tag{2.16}$$

Z_k is the charge of the k'th nucleus. Note that further contributions to the external potential $v_{\text{ext}}(\boldsymbol{r})$ of Eq. (2.10), such as a static external electric field, are not of relevance throughout this thesis. Thus, $v_{\text{ext}}(\boldsymbol{r})$ is completely defined by $v_0(\boldsymbol{r})$, as stated in the second part of Eq. (2.16). Note that in ground-state DFT calculations, the molecular structure is kept fixed in Eq. (2.16).

Another distinguishing feature of DFT codes is whether pseudopotentials[3] are used or not: For instance, BTDFT generally uses norm-conserving Troullier-Martins pseudopotentials for all elements [TM91, KMT$^+$06]. In contrast, all-electron codes – to which TURBOMOLE and QCHEM belong – typically only utilize pseudopotentials for the heavier elements. TURBOMOLE, for example, uses pseudopotentials for elements beyond Kr in combination with the def2-basis sets mentioned above.

At this point, the task is to provide a molecular structure ($\{\boldsymbol{R}_k\}$) that enters Eq. (2.16) or the construction of a pseudopotential. One way is to determine the structure experimentally, e.g., by scanning tunneling microscopy or X-ray diffraction. However, these methods are

---

[3] The contributions of the positive nucleus and the core electrons to the potential to which a valence electron is subjected can be combined to what is referred to as a pseudopotential. Thus, only the valence electrons are treated explicitly.

normally restricted to systems that form some sort of an ordered structure like a crystal, a layered structure or a film on a substrate. In general, it should come as no surprise that it is not always possible to determine the molecular structure experimentally for various reasons. To give two concrete examples within the context of this thesis: (i) MNPs played an important role in larger parts of this work, as discussed in detail in Sec. 4.1. When studying structures of MNPs or molecular arrangements of systems containing these, one must keep in mind that metals tend to aggregate. Therefore, MNPs need to be stabilized in order to be analyzed, unless they are not already spatially confined by, e.g., a metal-organic framework (cf. point ii) [MXNY06, INAH08, ZKL$^+$15]. For example, aggregation can be prevented by covering the MNPs with ligands [LGC20] or by dispersing them on solid supports [GFSDK17]. However, such measures usually impact the nanoparticle's structure as well as other properties [ZCW13, FBR12, FR14, BPM$^+$14, ZH18]. As a consequence, the bare structure of many (small) MNPs (referred to as clusters) has been determined theoretically in terms of their vacuum structure [MHBL01, NSA03, FMH05, PPDS10, KCO$^+$11, LK11, KLW$^+$12, YGS$^+$12, FBR12, LKK15, PUT$^+$16, LSFH18]. (ii) In Pub. 4, certain MNPs and photosensitizer molecules were encapsulated in the nanopores of a mesoscopic, crystalline metal-organic framework (cf. Sec. 4.1). Transmission electron microscopy methods can be used to study the distribution of such components in the crystallite. Quantitative insight into the pores would be necessary to determine any concrete arrangements of the molecular components. However, the (standard) method used in Pub. 4 is limited to providing a qualitative image of the mesoscopic system. For this reason, I determined molecular arrangement between the metal clusters and the photosensitizer molecule theoretically, as discussed in the following.

Popular structure-determination methods are geometry optimizations that are based on an ab-initio treatment of the electronic structure (and a classical one of the nuclei). Geometry optimizations are an important tool of most quantum-chemistry codes, and for a detailed overview of these, see Refs. [VMF$^+$03, Sch03, HS05]. In essence, most of these methods are capable of locating (local) extreme points of the system's structure with respect to the molecular energy. Such approaches thus enable the determination of stable configurations, as well as transition states and reaction paths, which are particularly relevant in chemistry [Sch11]. In this thesis, DFT-based geometry optimizations were used to relax molecular structures, where relaxing refers to the optimization of an initial structure to its (local) stable equilibrium geometry (cf. Pubs. 1–4). For this purpose, information is needed on how the molecular energy changes as a function of the structure of the molecule. Or in other words, the potential energy surface of the system needs to be characterized. Some popular approaches, such as the quasi-Newton method [DM77], start from a quadratic approximation to the potential energy surface at an initial structure [Sch11]. Such an approach allows to locate and characterize extreme points based on the first derivative (energy gradient) and second derivative (Hessian matrix) of the molecular energy with respect to the nuclear coordinates, respectively. Note that I carried out all relaxations with TURBOMOLE, which uses an algorithm from the family of quasi-Newton methods [TUR19]. For the classical treatment of the nuclei, the derivatives of the molecular ground-state energy with respect to the nuclear coordinates are direct functionals of the electron density [Fey39].

Therefore, geometry optimizations that are based on derivatives of the molecular ground-state energy can be built well upon DFT ground-state calculations. Consequently, in practice, the quality of the optimized structures depends on the accuracy of the xc DFA (cf. Chapter 3).

The type of geometry optimization described above requires a reasonable initial structure. Assuming that no (similar) structure exists that can be used as a basis, a completely new structure must be generated. At least nowadays, it is often possible to fall back on existing structures for the individual molecular components of a system, be they of experimental or theoretical origin (for an extensive database, see Ref. [SKG$^+$20]). The difficulty lies rather in finding a reasonable arrangement of the components with respect to each other. In practice, the molecular components are often arranged manually in a poor man's approach, e.g., with the aid of a visual molecule-editor program. Although such an approach is not necessarily poor, chances are high to introduce a structural bias, e.g., by choosing a specific arrangement of a functional group or selecting a structural isomer. Relaxing a ”manually prepared” arrangement can still lead to stable configuration. However, geometry optimization typically only leads to a local minimum. Therefore, one has no certainty that this minimum turns out to be the global one as well (or at least one of the lowest-energy configurations). This issue is especially important for systems that have a potential energy surface rich in local minima. The latter situation applies precisely to the theoretically studied metal-organic systems of Pubs. 1–4, which consist of a metal cluster and certain organic molecules: The metal clusters alone already exhibit several stable low-energy isomers (cf. Sec. 4.1). Furthermore, the combined system can be in many different geometries that are locally stable and of similar energy. Therefore, finding the or one of the relevant low-energy equilibrium structures can equate to searching for a needle in a haystack. For this reason, a procedure was presented in Pub. 1 to obtain low-energy equilibrium structures. To this end, I performed DFT-based Born-Oppenheimer molecular dynamics simulations with a constant temperature thermostat [Nos84, Hoo85] to obtain low-energy structures of the canonical ensemble. These latter then served as initial structures for further DFT-based geometry optimizations (cf. Sec. 4.1).

2.3.2 Electron Dynamics Simulated in Real Time

The objective in Pub. 5 was to fully describe the electron dynamics of photoemission processes using TDDFT. This requires a real-time approach, i.e., a full solution of the TDKS Eq. (2.12). The numerical solution of the latter is usually achieved with propagator techniques, and for an detailed overview of these, the reader is referred to Ref. [CMR04]. As a starting point, these techniques typically describe the time evolution of the KS system in an equivalent way to Eq. (2.12) in terms of the time propagator $\hat{\mathscr{U}}(t,t_0)$:

$$\varphi_{j\sigma}(\boldsymbol{r},t) = \hat{\mathscr{U}}(t,t_0)\varphi_{j\sigma}(\boldsymbol{r},t_0) = \hat{\mathscr{T}}\exp\left\{-\frac{i}{\hbar}\int_{t_0}^{t}\hat{h}_{s\sigma}(t')\mathrm{d}t'\right\}\varphi_{j\sigma}(\boldsymbol{r},t_0)\,, \tag{2.17}$$

where the operator $\hat{\mathscr{T}}$ ensures the correct time-ordering. The time-dependent external potential takes effect for $t \geq t_0$. In this scenario, the initial state $\varphi_{j\sigma}(\boldsymbol{r},t_0)$ is identical to the respective

j'th orbital of the associated stationary KS system. For the numerical solution of Eq. (2.17), the time variable is usually discretized by uniform time steps Δt. That is, $t_k = k\Delta t + t_0$ corresponds to the k'th time step. Then, it is suitable (and formally exact) to determine the full time evolution of the wave function by an incremental propagation. Thus, broken down to its essence, the task is to obtain $\varphi_{j\sigma}(t_{k+1})$ from the propagation step $\varphi_{j\sigma}(t_{k+1}) = \hat{\mathscr{U}}(t_{k+1}, t_k)\varphi_{j\sigma}(t_k)$, assuming that $\varphi_{j\sigma}(t_k)$ is known. This mostly boils down to how to deal with the exponential function on the right-hand side of Eq. (2.17). There exists a wide range of algorithms to approximate $\exp(\hat{A})$ that can be employed for this purpose, where $\hat{A}(t)$ is a time-dependent operator. For a review of such algorithms, see Refs. [MVL03, PTVF07] and Refs. [CMR04, Ull12] for an technical overview and a discussion in the context of TDDFT, respectively.

In the following, I outline the main considerations followed in the BTDFT code, which I used for the real-time simulations in Pub. 5: For a sufficiently small time step Δt, it is a reasonable approach to approximate the integral in the exponent in the right-hand side of Eq. (2.17) according to the midpoint rule:

$$\hat{\mathscr{U}}(t_{k+1}, t_k) \approx \exp\left\{-\frac{i}{\hbar}\hat{h}_{s\sigma}(t_{k+1/2})\Delta t\right\}. \tag{2.18}$$

This requires the evaluation of the TDKS Hamiltonian at $t_{k+1/2} = t_k + \Delta t/2$. To this end, BTDFT uses a predictor-corrector scheme to evaluate $\hat{h}_{s\sigma}(t_{k+1/2})$ from the n prior Hamiltonians ($n = 2$ in Pub. 5). The time step should be chosen small enough so that the highest frequency $\omega_{\max}$ considered can be resolved. In other words, the upper limit for Δt is $\propto 1/\omega_{\max}$ [MVL03]. For instance, in case an external electromagnetic field is applied, $\omega_{\max}$ corresponds to its highest frequency. Furthermore, the time-step size determines the highest excitation energy ($\hbar\omega_{\max}$) that can be resolved by, e.g., the real-time methods used in Pub. 5. In BTDFT, the propagation of each time step is conducted with the Crank-Nicolson algorithm [CN96] that approximates the exponential in Eq. (2.18) to

$$\exp\left\{-\frac{i}{\hbar}\hat{h}_{s\sigma}\Delta t\right\} \approx \frac{1 - \frac{i\Delta t}{2\hbar}\hat{h}_{s\sigma}}{1 + \frac{i\Delta t}{2\hbar}\hat{h}_{s\sigma}}. \tag{2.19}$$

Finally, substituting the approximations (2.18) and (2.19) into Eq. (2.17), and multiplying $1 + i\Delta t/(2\hbar)\hat{h}_{s\sigma}$ from the left yields

$$\left(1 + \frac{i\Delta t}{2\hbar}\hat{h}_{s\sigma}(t_{k+1/2})\right)\varphi_{j\sigma}(\boldsymbol{r}, t_{k+1}) = \left(1 - \frac{i\Delta t}{2\hbar}\hat{h}_{s\sigma}(t_{k+1/2})\right)\varphi_{j\sigma}(\boldsymbol{r}, t_k)\,. \tag{2.20}$$

Since BTDFT uses a discretization of space, Eq. (2.20) can be further cast into a matrix equation. The latter can be solved to obtain $\varphi_{j\sigma}(t_{k+1})$ using linear-algebra algorithms, as further detailed in Ref. [Sch16].

At this point, it should be noted that in addition to real-space grid approaches [YB96, KMT$^+$06, MK07, SK18, JSL19, TD$^+$20], the real-time propagation is often performed equivalently with basis sets [VBG$^+$10, E$^+$10, BLL16, WD16, DWC$^+$17, RKP$^+$17, ZH18, MSS20, E$^+$21]. Overall, real-time TDDFT approaches are gaining popularity for reasons such as the following [CRSU00, MCBR03, MK08, LG11, LCL11, A$^+$15, PI16, SK18, LGI$^+$20]: (i) They can be designed to be computationally efficient, allowing the study of large systems. (ii) The propagation is well suited for orbital parallelization and grid parallelization in the case of real-space grids. (iii) The computational effort scales favorably with the particle number N, since unoccupied orbitals are irrelevant for real-time TDDFT. (iv) First principles approaches are attractive in general due to their predictive power (without any, e.g., fitting parameters). Real-time TDDFT is suitable for describing electron dynamics for a variety of scenarios. This includes the study of high-harmonic generation processes of atomic and molecular systems in intense laser fields [URS97, TC98a, TC98b, TC01, HCTC07, Oto12, RJJBB20], transport phenomena such as conduction through atomic and molecular chains [BCG05, CEVV06, KCBC08, EVVV09, SK16a], and time-resolved spectroscopy (cf. Chapter 1). Furthermore, real-time approaches to determine excited-state properties that remain in the linear-response regime are gaining popularity as an alternative to explicitly linearized techniques based on perturbation theory (cf. Sec. 2.3.3) [YB96, YB99, MK07, LG11, BLL16, SK18, SRGGLL$^+$18, SFG$^+$19]. Note that TDDFT also builds a solid framework to include nuclear motion into the dynamics, leading to Ehrenfest Dynamics [MH00, GKZC04], which facilitates further applications [SGQS12, FRB$^+$14].

Not withstanding the success of real-time TDDFT, naturally, there are also challenges, and these relate to two issues in particular [Mai16]: Firstly, shortcomings of the approximation to the time-dependent xc functional can affect the accuracy of the predictions quite severely. Secondly, observables of which no direct time-dependent density functional expression is known are difficult to access. Therefore, while real-time TDDFT approaches are attractive, they do not qualify as black box methods per se, and careful considerations must be made in practice. It is beyond the scope of this section to go into the latter points in full, hence I refer to Refs. [Ull12, UY14, Mai16] for a detailed overview. However, with respect to this thesis, such an approach can best be exemplified by Pub. 5: Firstly, I carefully evaluated the trust range and confirmed the reliability for the observables that were reported. Secondly, I utilized an elaborate real-time detection scheme [PRS00, DMRS10, DGS$^+$16] to obtain angle-resolved photoemission spectra.

2.3.3 Excited-State Properties from Linear-Response Theory

TDDFT is closely related to spectroscopy, largely due to the fact that some of its linear-response methods are a standard tool for obtaining excited-state properties, such as the photoabsorption spectrum (optical excitation spectrum) and the transition density. For this purpose, linear-response techniques mainly take two different routes: (i) The Casida [Cas95, CJCS98] and Sternheimer [ABMR07, HSK18] formalisms, for example, are based on explicitly linearized TDDFT. (ii) As pioneered by Ref. [YB96], the system's linear response to a weak perturbation can alternatively be obtained from real-time TDDFT, i.e., via the full propagation of the TDKS equations. In this section, I focus on the Casida approach, which was used in Pubs. 4–5.

The Casida approach to linear-response TDDFT is an integral part of most TDDFT program packages (such as TURBOMOLE and QCHEM). From the viewpoint of this approach, a many-particle excitation is a superposition of one-electron excitations from occupied to unoccupied (virtual) orbitals of the ground-state KS Hamiltonian (cf. Sec. 2.1). In order to outline the Casida approach in formulae, it is worth taking a brief detour into time-dependent linear-response theory in general [Ull12]: Suppose an interacting system is initially in the ground state associated with the external potential $v_0(\boldsymbol{r})$. Then, the system experiences a small external perturbation $v_1(\boldsymbol{r},t)$ at t_0, i.e., this scenario corresponds to the external potential $v_{\text{ext}}(\boldsymbol{r},t) = v_0(\boldsymbol{r}) + v_1(\boldsymbol{r},t)\theta(t-t_0)$, where the switch-on of the perturbation is described by the Heaviside step function θ. The full density response to the perturbation is defined as the difference between the time-dependent density and the ground-state density $\delta n(\boldsymbol{r},t) = n(\boldsymbol{r},t) - n_0(\boldsymbol{r})$. Time-dependent linear-response methods aim to determine the part of the system's response that is proportional to $v_1(\boldsymbol{r},t)$, such as the first-order density response $n_1(\boldsymbol{r},t)$. The latter is one of the central quantities for linear-response TDDFT and follows from expanding the full density response $\delta n(\boldsymbol{r},t)$ to the first order in powers of the perturbation:

$$\begin{aligned} n_1(\boldsymbol{r},t) &= \int \mathrm{d}t' \int \left.\frac{\delta n(\boldsymbol{r},t)}{\delta v_{\text{ext}}(\boldsymbol{r}',t')}\right|_{v_0[n_0](\boldsymbol{r})} v_1(\boldsymbol{r}',t')\ \mathrm{d}\boldsymbol{r}' \\ &= \int \mathrm{d}t' \int \chi(\boldsymbol{r},\boldsymbol{r}',t-t') v_1(\boldsymbol{r}',t')\ \mathrm{d}\boldsymbol{r}'. \end{aligned} \tag{2.21}$$

χ denotes the density-density response function, and its spectral representation reads

$$\chi(\boldsymbol{r},\boldsymbol{r}',\omega) = \lim_{\beta\to 0^+} \sum_I^{\infty} \left[\frac{\langle\Psi_0|\hat{n}(\boldsymbol{r})|\Psi_I\rangle\,\langle\Psi_I|\hat{n}(\boldsymbol{r}')|\Psi_0\rangle}{\hbar\omega - \Omega_I + i\beta} - \frac{\langle\Psi_0|\hat{n}(\boldsymbol{r})|\Psi_I\rangle\,\langle\Psi_I|\hat{n}(\boldsymbol{r}')|\Psi_0\rangle}{\hbar\omega + \Omega_I + i\beta} \right]. \tag{2.22}$$

The sum runs over all excited states, where $|\Psi_I\rangle$ and Ω_I refer to the wave function and excitation energy of the I'th state, respectively. Note that $\chi(\boldsymbol{r},\boldsymbol{r}',\omega)$ has poles at all excitation energies of the stationary interacting system, which are of interest for us. The bridge to TDDFT can be built by means of the van Leeuwen's theorem (cf. Sec. 2.2), since it ensures that the time-dependent density response of the TDKS system is identical to that of the interacting one, i.e.,

$$n_1(\boldsymbol{r},t) = \int \mathrm{d}t' \int \chi_{\text{s}}(\boldsymbol{r},\boldsymbol{r}',t-t') v_{\text{s}1}(\boldsymbol{r}',t')\ \mathrm{d}\boldsymbol{r}'. \tag{2.23}$$

$v_{\text{s}1}(\boldsymbol{r},t)$ is the explicitly linearized perturbation in the KS system, and χ_{s} is the density-density response function of the non-interacting KS particles. χ_{s}'s spectral representation features poles at the KS excitation energies, i.e., only at differences between the orbital eigenvalues $\hbar\omega_{jk} = \varepsilon_j - \varepsilon_k$. A connection between the interacting density-density response function and that of the KS system can be established by the comparison of Eqs. (2.21) and (2.23), and making some further transformations yields

$$\chi(\boldsymbol{r},\boldsymbol{r}',\omega) = \chi_{\text{s}}(\boldsymbol{r},\boldsymbol{r}',\omega) + \int \mathrm{d}\boldsymbol{r}'' \int \chi_{\text{s}}(\boldsymbol{r},\boldsymbol{r}'',\omega) f_{\text{Hxc}}(\boldsymbol{r}'',\boldsymbol{r}''',\omega)\chi(\boldsymbol{r}''',\boldsymbol{r}',\omega)\,\mathrm{d}\boldsymbol{r}'''. \tag{2.24}$$

This equation includes the so-called Hartree-xc kernel

$$f_{\mathrm{Hxc}}(\boldsymbol{r},\boldsymbol{r}',t-t') = \left.\frac{\delta\left[v_{\mathrm{H}}(\boldsymbol{r},t)+v_{\mathrm{xc}}[n](\boldsymbol{r},t)\right]}{\delta n(\boldsymbol{r}',t')}\right|_{n_0(\boldsymbol{r})} = \frac{e^2}{4\pi\varepsilon_0}\frac{1}{|\boldsymbol{r}-\boldsymbol{r}'|} + f_{\mathrm{xc}}(\boldsymbol{r},\boldsymbol{r}',t-t'). \quad (2.25)$$

Note that the temporal Fourier transform of Eq. (2.25) with respect to $t-t'$ leads to the frequency-dependent version $f_{\mathrm{Hxc}}(\boldsymbol{r},\boldsymbol{r}',\omega)$ in Eq. (2.24).

In the Casida formalism, Eq. (2.24) is recast into a matrix equation [Cas95, Cas96],

$$\begin{pmatrix} \mathbb{A} & \mathbb{B} \\ \mathbb{B}^* & \mathbb{A}^* \end{pmatrix}\begin{pmatrix} \mathbf{X} \\ \mathbf{Y} \end{pmatrix} = \omega\begin{pmatrix} -\mathbb{1} & 0 \\ 0 & \mathbb{1} \end{pmatrix}\begin{pmatrix} \mathbf{X} \\ \mathbf{Y} \end{pmatrix}, \quad (2.26)$$

which is solved to obtain the many-body excitations energies, and the corresponding oscillator strengths can be deduced from the eigenvectors. To explain the notation: Equation (2.26) is defined in the basis of the KS electron-hole pairs of the stationary system $\{\varphi^*_{j\sigma}\varphi_{k\sigma}\}$, returning to a spin-polarized notation ($\sigma,\sigma' = \{\uparrow,\downarrow\}$). Occupied and unoccupied KS states are labeled (j,j') and (k,k') in the following, respectively. Note that the stationary KS orbitals as well as their eigenvalues ($\varepsilon_{j\sigma}$) are usually obtained by a prior ground-state DFT calculation (cf. Sec. 2.3.1). Each excitation energy, $\hbar\omega = \hbar\Omega_I$, is linked to a pair of $\mathbf{X}(\Omega_I)$ and $\mathbf{Y}(\Omega_I)$. Where $\mathbf{X}$ and $\mathbf{Y}$ are referred to as the excitation ($j\to k$) and deexcitation ($k\to j$) amplitudes, respectively. Put simply, these contain the information about the proportional contribution of each particle-hole pair to a many-body excitation. The matrix elements of Eq. (2.26) read as

$$A_{jk\sigma,j'k'\sigma'}(\omega) = \delta_{jj'}\delta_{kk'}\delta_{\sigma\sigma'}(\varepsilon_{k\sigma}-\varepsilon_{j\sigma'}) + K_{jk\sigma,j'k'\sigma'}(\omega), \quad (2.27)$$

$$B_{jk\sigma,j'k'\sigma'}(\omega) = K_{jk\sigma,k'j'\sigma'}(\omega). \quad (2.28)$$

The coupling-matrix elements are defined as

$$K_{jk\sigma,j'k'\sigma'} = \int \mathrm{d}\boldsymbol{r}\int \varphi^*_{j\sigma}(\boldsymbol{r})\varphi_{k\sigma}(\boldsymbol{r})f_{\mathrm{Hxc},\sigma\sigma'}(\boldsymbol{r},\boldsymbol{r}',\omega)\varphi^*_{k'\sigma'}(\boldsymbol{r}')\varphi_{j'\sigma'}(\boldsymbol{r}')\,\mathrm{d}\boldsymbol{r}'. \quad (2.29)$$

If the coupling-matrix elements were neglected, Eq. (2.26) would simply return the KS excitation energies. This in turn implies that it is one of the crucial roles of f_{Hxc} to shift the poles from the single-particle excitations to those of the true many-body system (Ω_I) [TK14]. In the Tamm-Dancoff approximation [HHG99], the matrix $\mathbb{B}$ in Eq. (2.26) is set to zero. Thus, the Casida equation takes the simpler form $\mathbb{A}\mathbf{X} = \omega\mathbf{X}$, which means that the deexcitations of the system are neglected.

In principle, the Casida formalism gives access to the exact many-body excitations. In practice, of course, these can only be determined approximately: On the one hand, the exact xc kernel f_{xc} is usually unknown, making approximations necessary (see below). On the other hand, only a truncated basis, i.e., a finite number of electron-hole pairs can be considered. In addition to the excitation energies, the Casida approach gives access to a number of other properties, such as the oscillator strength [Cas95, Cas96]. Further examples are the transition density and the excited-state density, which are often used to visualize density changes associated with an excitation (cf. Pubs. 4–5): The transition density at Ω_I follows from

$$n_{1\sigma}(\boldsymbol{r},\Omega_I)=\sum_{j,k}\left[\varphi^*_{k\sigma}(\boldsymbol{r})\varphi_{j\sigma}(\boldsymbol{r})X_{jk\sigma}(\Omega_I)+\varphi^*_{j\sigma}(\boldsymbol{r})\varphi_{k\sigma}(\boldsymbol{r})Y_{jk\sigma}(\Omega_I)\right]. \tag{2.30}$$

The excited-state density of the I'th excitation can also be constructed on the basis of the amplitudes $\mathbf{X}(\Omega_I)$ and $\mathbf{Y}(\Omega_I)$.

When the KS orbitals are assumed to be real, the Casida Eq. (2.26) can be written in the more compact form [Ull12]:

$$\mathbb{C}\mathbf{Z}=\omega^2\mathbf{Z}, \tag{2.31}$$

with

$$\mathbb{C}=(\mathbb{A}-\mathbb{B})^{1/2}(\mathbb{A}+\mathbb{B})(\mathbb{A}-\mathbb{B})^{1/2}, \tag{2.32}$$

$$\mathbf{Z}=(\mathbb{A}-\mathbb{B})^{1/2}(\mathbf{X}-\mathbf{Y}). \tag{2.33}$$

Note that implementations in TDDFT program packages are often based on Eqs. (2.31-2.33) [Ull12]. Moreover, in practice, the Casida equation is mostly solved in the adiabatic approximation (cf. Eq. 2.15). That is, the kernel f_{Hxc} becomes frequency-independent. Then, Eq. (2.31) takes the form of a Hermitian eigenvalue problem. Furthermore, the adiabatic xc kernel $f^{\mathrm{A}}_{\mathrm{xc}}$ can be obtained from the functional derivative according to Eq. (2.25) using Eq. (2.15). In practice, this has the advantage that the xc functional approximations of ground-state DFT can be used to derive the xc kernel. At the same time, however, double excitations are lost in this approximation [MZCB04, TK14].

In conclusion, one of the main advantages of the Casida approach is the direct access to various excited-state properties. This includes that, in principle, all excitations appearing as poles in Eq. (2.22) can be determined, even the dark ones that do not carry any oscillator strength. One downside is that the computational cost scales rather poorly with the system size, since both occupied and unoccupied states are part of this formalism. For example, the other approaches mentioned above perform better in this respect, since they only consider occupied orbitals. Consequently, the computational cost can quickly become a bottleneck for, e.g., systems with a dense excitation spectrum, as an increasingly elaborate diagonalization is required to obtain the roots of the Casida matrix.[4] For example, the transition-metal clusters studied in Pub. 4 exhibit a characteristically dense excitation spectrum (of up to roughly 1000 excitations in the Vis alone), and above a critical system size, the study of systems containing these clusters can become infeasible due to the computational cost.

---

[4] Instead of a full diagonalization of the Casida matrix, codes typically use special algorithms to extract its roots ($\{\Omega_I\}$) in energetic ascending order starting with the lowest one. This also implies that if excitations above a certain threshold are actually only of interest, all those below must still be determined.

CHAPTER 3

Exchange-correlation Density-Functional Approximations

The exact xc energy functional E_{xc} can be formally defined (cf. Sec. 2.1). However, a universal expression for the actual application is unknown. For this reason, DFAs to E_{xc} are the key element for implementing the KS formalism to DFT. The xc energy functional can be written as

$$E_{\mathrm{xc}}[n_\uparrow, n_\downarrow] = \int e_{\mathrm{xc}}[n_\uparrow, n_\downarrow](\boldsymbol{r})\, \mathrm{d}\boldsymbol{r}, \tag{3.1}$$

and the objective is to find accurate approximations to the xc energy density $e_{\mathrm{xc}}[n_\uparrow, n_\downarrow](\boldsymbol{r})$. The latter is in general a non-local density functional, i.e., e_{xc} at a point $\boldsymbol{r}$ depends on the density $n_\sigma(\boldsymbol{r}')$ at all points in space [PK03]. The static xc potential $v_{\mathrm{xc}\sigma}(\boldsymbol{r})$ is derived from the functional derivative of E_{xc} (Sec. 2.1). Moreover, most applications of TDDFT are carried out in the adiabatic approximation [Mai16]. In other words, the DFAs to E_{xc} are used to derive the time-dependent adiabatic xc potential of TDDFT (cf. Sec. 2.2). John Perdew makes the analogy to the development of DFAs to Eq. (3.1) as the ”Jacob's ladder” of DFT [PK03]: The predictive power of each successive DFA generation, while generally becoming more complex and costly, approaches the ”heaven” of chemical accuracy ”rung by rung” (1 kcal/mol $\approx$ 0.04 eV per particle). In the course of this chapter, I go into more detail about the most important xc DFAs that I used throughout this thesis to describe molecular systems in terms of their molecular and electronic structure: (i) Local and semi-local approximations belonging to the lowest ”rungs” (Sec. 3.1), for which $e_{\mathrm{xc}}(\boldsymbol{r})$ at point $\boldsymbol{r}$ is determined by the local density $n(\boldsymbol{r})$ and its gradient $\nabla n_\sigma(\boldsymbol{r})$. (ii) The higher-rung global hybrid and range-separated hybrid functionals that feature a fixed fraction and the full (non-local) exact exchange energy density in the long-range part of the functional (Sec. 3.2), respectively.

3.1 Local and Semi-local Functionals

The ”mother of all DFAs” is the local density approximation (LDA) [HK64]

$$E_{\mathrm{xc}}^{\mathrm{LDA}}[n_\uparrow, n_\downarrow] = \int e_{\mathrm{xc}}^{\mathrm{LDA}}\big(n_\uparrow(\boldsymbol{r}), n_\downarrow(\boldsymbol{r})\big)\, \mathrm{d}\boldsymbol{r}. \tag{3.2}$$

The LDA follows the simple approach of evaluating the xc energy density $e_{\mathrm{xc}}^{\mathrm{h}}(\bar{n})$ of the homogeneous electron gas with density $\bar{n} = \bar{n}_\uparrow + \bar{n}_\downarrow$ for the density $n(\boldsymbol{r}) = n_\uparrow(\boldsymbol{r}) + n_\downarrow(\boldsymbol{r})$ of the inhomogeneous system:

$$e_{\mathrm{xc}}^{\mathrm{LDA}}(n(\boldsymbol{r})) = e_{\mathrm{xc}}^{\mathrm{h}}(\bar{n})\Big|_{\bar{n}\to n(\boldsymbol{r})}, \qquad e_{\mathrm{x}}^{\mathrm{h}}(\bar{n}) = -\frac{3e^2}{16\pi\varepsilon_0}\left(\frac{3}{\pi}\right)^{1/3}\bar{n}^{4/3}. \tag{3.3}$$

For $e_{\mathrm{xc}}^{\mathrm{h}}(\bar{n}) = e_{\mathrm{x}}^{\mathrm{h}}(\bar{n}) + e_{\mathrm{c}}^{\mathrm{h}}(\bar{n})$, the exchange $e_{\mathrm{x}}^{\mathrm{h}}$ is known exactly, as stated in Eq. (3.3). The correlation $e_{\mathrm{c}}^{\mathrm{h}}$ can be determined highly accurately by Monte-Carlo simulations [CA80, UG94] and parameterized, e.g., according to Perdew and Wang [PW92]. The corresponding LDA potential follows from substituting Eq. (3.2) into Eq. (2.11):

$$\upsilon_{\mathrm{xc}\sigma}^{\mathrm{LDA}}(\boldsymbol{r}) = \frac{\mathrm{d}e_{\mathrm{xc}}^{h}(\bar{n}_\uparrow,\bar{n}_\downarrow)}{\mathrm{d}\bar{n}_\sigma}\bigg|_{\bar{n}_\sigma\to n_\sigma(\boldsymbol{r})}. \tag{3.4}$$

In Pub. 5, the adiabatic LDA (ALDA) was the "workhorse" in the TDDFT-based study: The corresponding adiabatic approximation to the time-dependent xc potential is obtained by substituting the static $\upsilon_{\mathrm{xc}\sigma}^{\mathrm{LDA}}(\boldsymbol{r})$ into Eq. (2.15):

$$\upsilon_{\mathrm{xc}\sigma}^{\mathrm{ALDA}}(\boldsymbol{r},t) = \upsilon_{\mathrm{xc}\sigma}^{\mathrm{LDA}}(\boldsymbol{r})\Big|_{n_\sigma(\boldsymbol{r})\to n_\sigma(\boldsymbol{r},t)} = \frac{\mathrm{d}e_{\mathrm{xc}}^{h}(\bar{n}_\uparrow,\bar{n}_\downarrow)}{\mathrm{d}\bar{n}_\sigma}\bigg|_{\bar{n}_\sigma\to n_\sigma(\boldsymbol{r},t)}. \tag{3.5}$$

Generalized gradient approximations (GGAs) conceptually improve on LDA by taking not only the local density $n_\sigma(\boldsymbol{r})$ into account but also the semi-local spatial gradient $\nabla n_\sigma(\boldsymbol{r})$,

$$E_{\mathrm{xc}}^{\mathrm{GGA}} = \int e_{\mathrm{xc}}^{\mathrm{GGA}}\left(n_\uparrow(\boldsymbol{r}), n_\downarrow(\boldsymbol{r}), \nabla n_\uparrow(\boldsymbol{r}), \nabla n_\downarrow(\boldsymbol{r})\right)\,\mathrm{d}\boldsymbol{r}\,. \tag{3.6}$$

Otherwise, there is no universal rule for the development of $e_{\mathrm{xc}}^{\mathrm{GGA}}(\cdot)$, yet GGAs follow two paths in particular: (i) Empirical functionals partly use parameters determined by fits to data sets, such as the B88 [Bec88] and LYP [LYP88] functional. (ii) Non-empirical functionals generally focus on satisfying several of the known constraints of the exact xc functional (e.g., PW86 [PW86], PW91 [PZE91, BPW98]). Due to the different construction strategies, a multitude of GGA functionals exist, some of which are used in combination [vB04, MHG17]. For example, BLYP is a popular empirical functional that combines B88 exchange and LYP correlation. Another important GGA is the famous non-empirical Perdew-Burke-Ernzerhof (PBE) functional, which – in the words of Perdew *et al.* – is the "GGA [PW91] made simple" [PBE96]. Note that PBE was the workhorse for determining the ground-state electronic structure and molecular structures of the metal-organic systems that I studied in Pubs. 1–4. Long-range dispersion interactions can, *inter alia*, crucially impact the molecular structure of systems. However, (semi-)local xc functionals, as well as global hybrids (Sec. 3.2), infamously fail at their description [AT02, ZPK04, Gri04]. Fortunately, this issue has prompted a variety of dispersion-correction schemes (for an overview, see Refs. [Gri11, KM12, CBG17]). In this thesis, dispersion corrections were taken into account for geometry optimizations (cf. Sec. 2.3.1) via the D3 scheme of Grimme *et al.* [GAEK10].

The issue with LDA is obvious: The density of a real system is rarely ever uniform. Therefore, one might expect LDA to be appropriate only for ”free-electron-gas-like” systems, i.e., systems with slowly varying electron densities over space (and time). Nevertheless, LDA often provides reasonable results for a broader range of systems, e.g., within the following scope [SSTP03, Ull12]: Typically, total atomic and molecular energies are off by some 1–5%, and molecular equilibrium distances and geometries are accurate within $\approx 3\%$. LDA's qualitative success can be attributed in part to a systematic error cancellation between its exchange and correlation energy. Another aspect is that LDA satisfies a number of the known exact constraints of the true xc functional and related quantities, such as the sum rule for the xc hole [PK03]. At the same time, LDA does not meet a number of other constraints. For example, instead of showing the correct $-e^2/r$ asymptotic of the exact xc potential for $r \to \infty$, $v_{\mathrm{xc}\sigma}^{\mathrm{LDA}}(\boldsymbol{r})$ falls exponentially to zero [AvB85]. As a consequence, the KS orbitals are typically underbound. This has further implications, *inter alia*, for the so-called ionization-potential theorem of exact KS-DFT [LPS84, AvB85]: The (negative) eigenvalue of the highest occupied KS orbital $-\varepsilon_{\mathrm{HOMO}}$ is identical to the lowest relaxed vertical ionization potential IP of the N-electron system.[1] However, $-\varepsilon_{\mathrm{HOMO}}^{\mathrm{LDA}}$ is off by $\approx$ 30–50%, which translates to an error of about 1 eV for many molecular systems [SSTP03, Ull12]. In Pub. 5, I studied angle-resolved photoemission processes of the PTCDA molecule using real-time TDDFT with ALDA. For this particular molecule, it has been shown that simulating direct ARPES in real-time with ALDA allows for a qualitatively correct interpretation of the corresponding ARPES experiments [DGS$^+$16]. For other molecular systems, the real-time description of photoemission can benefit from a (one-electron) self-interaction correction (of ALDA [PZ81]) [WFD$^+$10, DK16]. The latter refers to the spurious self-interaction energy contained in the Hartree term (2.9), which is generally more pronounced in localized than in delocalized electronic states [SK16b]. Note that GGAs considerably reduce self interaction compared to LDA. However, GGAs still cannot compensate for it as effectively as, e.g., the hybrid functionals of the next section [PKC02, BGT18]. As a consequence, (semi-)local xc DFAs may spuriously prefer the delocalization of electrons to decrease self interaction, as further reviewed in Ref. [KK20].

In general, GGAs lead to improvements over LDA [SSTP03, SSTP04, MHG17]. However, GGAs still share further shortcomings of LDA, such as the lack of a derivative discontinuity of the xc functional [Toz98] or the incorrect asymptotic behavior of the xc potential, leading to implications similar to those discussed above. GGAs perform reasonable well in transition-metal chemistry, e.g., in terms of bond energies, bond lengths, and barrier heights [Har06, SZT05, BRP$^+$08, YZZT10]. Moreover, PBE performs consistently well for predicting structural and electronic properties of transition-metal clusters, such as average bond distances and binding energies per atom [SGNR14, SR15]. GGAs also yield somewhat better results for low-lying excitation energies obtained from linear-response TDDFT (cf. Sec. 2.3.3). Nevertheless, the

---

[1] Unfortunately, only $\varepsilon_{\mathrm{HOMO}}$ carries rigorous physical meaning. That is, the lowest unoccupied KS orbital energy $\varepsilon_{\mathrm{LUMO}}$ does not correspond to the electron affinity EA of the N-electron system, because it is precisely off by the so-called xc derivative discontinuity [PK03]. Consequently, the KS gap, $\varepsilon_{\mathrm{HOMO}} - \varepsilon_{\mathrm{LUMO}}$, neither matches the fundamental gap nor mimics quasi-particle levels.

absolute error is still relatively large, e.g., about 0.5 eV for the lowest vertical excitation of medium-sized organic molecules from the test set of Ref. [JWPA09]. Furthermore, the wrong asymptotic behavior and missing non-locality are two main factors why (semi-)local functionals drastically fail for the class of charge-transfer excitations [KSRAB12, Kü17], which are further discussed in the next section.

Overall, (semi-)local functionals usually do not lead to the desired chemical accuracy. Nonetheless, they can still capture the correct qualitative trend under the right circumstances[2] and provide the best cost/accuracy ratio among the xc DFAs to this end [GD13].

3.2 Global Hybrid and Range-Separated Hybrid Functionals

Hybrid functionals incorporate the exact-exchange energy (EXX) functional,[3]

$$E_{\mathrm{x}}^{\mathrm{exact}} = -\frac{e^2}{8\pi\varepsilon_0}\sum_{\sigma}\sum_{i,j=1}^{N_\sigma}\int\int\frac{\varphi_{i\sigma}^*(\boldsymbol{r})\,\varphi_{i\sigma}(\boldsymbol{r}')\,\varphi_{j\sigma}^*(\boldsymbol{r}')\,\varphi_{j\sigma}(\boldsymbol{r})}{|\boldsymbol{r}-\boldsymbol{r}'|}\,\mathrm{d}\boldsymbol{r}\,\mathrm{d}\boldsymbol{r}', \tag{3.7}$$

which is the analogue of the exact Fock exchange evaluated for the KS orbitals [Eng03]. Note that orbital functionals such as EXX are non-local, since KS orbitals depend implicitly on the density (cf. Sec. 2.1). Dealing with orbital functionals raises the question, how to obtain the corresponding xc potential and xc kernel from the functional derivative, e.g., of Eq. (3.7), with respect to the density. This leads to the elaborate optimized-effective-potential method [SH53, UGG95, KP03, KK08] and approximations to it [KLI92a, KLI92b, DG01, ISS$^+$07]. As a rigorous alternative, one can also take derivatives with respect to the orbitals in a generalized Kohn-Sham (gKS) theory [SGV$^+$96, BLS10, BK18]. The price to pay, however, is that the corresponding gKS potential is no longer a local, multiplicative one – in contrast to the ”regular” KS potential. Note that most quantum-chemistry codes, including those that I used (TURBOMOLE, QCHEM, cf. Sec. 2.3), implement orbital functionals in the gKS scheme.

EXX features some promising properties, such as the elimination of the self-interaction contribution from the Hartree term, and its potential shows the correct asymptotic behavior ($-e^2/r$). However, there are non-trivial compatibility issues with combining full EXX and correlation functionals [KK08]. For this reason, hybrid functionals choose other ways to incorporate EXX [Bec93, PEB96, LSWS97, AB99, YTH04, PSTS08, SKM$^+$14], as discussed for the global and range-separated approaches in the following.

The basic strategy of global hybrid functionals [Bec93],

$$E_{\mathrm{xc}}^{\mathrm{GH}} = aE_{\mathrm{x}}^{\mathrm{exact}} + (1-a)E_{\mathrm{x}}^{\mathrm{SL}} + E_{\mathrm{c}}^{\mathrm{SL}}, \quad 0 \le a \le 1, \tag{3.8}$$

is to mix a fixed fraction a of EXX with complementary exchange $(1-a)$ and full correlation of typically a (semi-)local xc functional (abbreviated SL here). For example, PBE0 is a popular,

---

[2] Note that throughout Pubs. 1–5, I always evaluated the trust range and reliability of the utilized (semi-)local xc functionals.

[3] $E_{\mathrm{x}}^{\mathrm{exact}} = \int e_{\mathrm{x}}^{\mathrm{exact}}(\boldsymbol{r})\,\mathrm{d}\boldsymbol{r}$, where $e_{\mathrm{x}}^{\mathrm{exact}}(\boldsymbol{r})$ is the exact exchange-energy density.

non-empirical global hybrid that incorporates the GGA PBE with a mixing of $a = 0.25$ [AB99, ASB99]:

$$E_{\mathrm{xc}}^{\mathrm{PBE0}} = \frac{1}{4}E_{\mathrm{x}}^{\mathrm{exact}} + \frac{3}{4}E_{\mathrm{x}}^{\mathrm{PBE}} + E_{\mathrm{c}}^{\mathrm{PBE}}. \tag{3.9}$$

The mixing can also be empirically motivated, as in the case of the ”workhorse” of computational chemistry, the B3LYP functional [Bec93, SDCF94]:

$$E_{\mathrm{xc}}^{\mathrm{B3LYP}} = (1-a)E_{\mathrm{x}}^{\mathrm{LDA}} + aE_{\mathrm{x}}^{\mathrm{exact}} + b\Delta E_{\mathrm{x}}^{\mathrm{B88}} + cE_{\mathrm{c}}^{\mathrm{LYP}} + (1-c)E_{\mathrm{c}}^{\mathrm{LDA}}. \tag{3.10}$$

The latter uses 3 parameters ($a = 0.20$, $b = 0.72$, and $c = 0.81$) and thereby combines EXX with LDA, as well as the GGAs B88 and LYP (cf. Sec. 3.2).

Hybrid functionals generally benefit from the positive properties of EXX, which translate, e.g., to an improved asymptotic behavior ($-e^2a/r$) and a partial correction of the Hartree self-interaction contribution. In many cases, global hybrids lead to more accurate prediction of molecular properties compared to (semi-)local DFAs [SSTP04, MPSK08, BRP$^+$08, KSRAB12, MHG17], e.g., in terms of ionization potentials, formation enthalpies, and equilibrium bond lengths (with respect to the test set of Ref. [SSTP03]). B3LYP excels in its performance for organic molecules and main group chemistry in particular [MHG17]. For example, the mean absolute error for the enthalpy of formation amounts to less than 3 kcal/mol with respect to the test set of Ref. [TRJ08]. In Pub. 5, I used B3LYP as a crosscheck to LDA in the study of the organic PTCDA molecule, since it leads to a good description of the molecule's electronic structure [DMK$^+$06]. Not withstanding B3LYP's success, one must keep in mind that it does not fulfill the homogeneous-electron-gas limit, and therefore fails for free-electron-gas-like systems [PMK07]. In this regard, PBE0 performs significantly better, since it describes the homogeneous electron gas exactly. In this work, PBE0 was used, *inter alia*, to cross-check delocalized electronic states predicted by the GGA PBE (cf. Pub. 1), since GGAs are prone to overestimate delocalization due to the self-interaction error (cf. Sec. 3.1). Global hybrids are a suitable candidate for this task, as they partially remove this error.

It should be noted that studying metal-organic systems containing transition-metal clusters, such as those from Pubs. 1–4, by global hybrid xc functionals requires special care [SGNR14, SR15]: (i) Transition-metal clusters often prefer ground states that feature non-zero magnetic moments, i.e., they are spin-polarized, as discussed further in Sec. 4.1. Hybrids functionals may spuriously predict too large magnetic moments due to the energy-lowering contribution of EXX for electrons with parallel spin. (ii) In some cases, a fraction of approximately 20% EXX and larger has been linked to a poor description of some structural and electronic properties of metals and metal clusters, such as weakened metallic bonds and overestimated nearest-neighbor distances. Similar observations were made for some of the systems studied in Pubs. 1–4, and in particular for systems that contain Ni cluster (cf. Pub. 3).

In Pub. 4, the focus was on the study of long-range charge-transfer (CT) excitations using the Casida approach to linear-response TDDFT (cf. Sec. 2.3.3). While global hybrids describe non-CT excitations reasonably well, with mean average errors between 0.2 eV and 0.3 eV [JWPA09], they fail almost as drastically as (semi-)local functionals for CT excitations [DHG04, Mai05, PBHT08, SKB09b, KSRAB12, KNTK13]. This failure of ”standard” xc functionals had been a genuine limitation to the research scope of DFT, since CT excitations play an important role in various energy-conversion processes [VK04, BBK15, XTY$^+$18, CCW$^+$19]. Hence, it was considered a major breakthrough when range-separated hybrid (RSH) functionals allowed the reliable description of this type of excitations [YTH04, PHS$^+$06, RH08, SKB09b, SKB09a, KSBK11, KSRAB12, Kü17]. The version of RSH functionals used in this thesis splits the Coulomb operator ($1/|\boldsymbol{r}-\boldsymbol{r}'|$) into a short-range and long-range term via

$$\frac{1}{|\boldsymbol{r}-\boldsymbol{r}'|} = \underbrace{\frac{1-\operatorname{erf}(\omega|\boldsymbol{r}-\boldsymbol{r}'|)}{|\boldsymbol{r}-\boldsymbol{r}'|}}_{\text{short range}} + \underbrace{\frac{\operatorname{erf}(\omega|\boldsymbol{r}-\boldsymbol{r}'|)}{|\boldsymbol{r}-\boldsymbol{r}'|}}_{\text{long range}}, \tag{3.11}$$

where ω is the range-separation parameter and $\operatorname{erf}(\cdot)$ denotes the error function [GAP96, LSWS97, ITYH01, BN05]. The parameter ω is either determined empirically [ITYH01, RH08, CHG09] or follows from physical considerations (see below) [SKB09b, KSRAB12, KK18, AK19]. Substituting Eq. (3.11) into the EXX energy functional (3.7), one thus obtains two range-separated terms (abbreviated SR and LR), $E_\mathrm{x}^\mathrm{exact} = E_\mathrm{x}^\text{SR-exact} + E_\mathrm{x}^\text{LR-exact}$. The type of RSH functional relevant to this work uses long-range EXX in combination with semi-local exchange in the short range, as well as full semi-local correlation at all ranges (abbreviated SL):

$$E_\mathrm{xc}^\mathrm{RSH} = E_\mathrm{x}^\text{SR-SL} + E_\mathrm{x}^\text{LR-exact} + E_\mathrm{c}^\mathrm{SL}. \tag{3.12}$$

This construction strategy ensures that the corresponding xc potential features the correct asymptotic behavior ($-e^2/r$) via $E_\mathrm{x}^\text{LR-exact}$ (independently of ω) and benefits from a decent short-range description via $E_\mathrm{x}^\text{SR-SL}$. In Pub. 5, I utilized the RSH functional ωPBE that follows from inserting the GGA PBE into Eq. (3.12) [HJS08, RMH09]. For determining the range-separation parameter, I used a non-empirical tuning process: In short, this procedure aims to find an optimal parameter ω_opt such that the ionization-potential theorem (cf. Sec. 3.1) is obeyed as closely as possible for both the neutral (N) and anionic system ($N+1$). That means, ideally $-\varepsilon_\mathrm{HOMO}(M;\omega_\mathrm{opt}) = IP(M;\omega_\mathrm{opt})$ for $M = \{N, N+1\}$. Accordingly, the RSH xc functional that uses ω_opt in its construction (3.12) is referred to as optimally-tuned (for further details, see Pub. 5). Furthermore, it has been shown that this non-empirical tuning procedure has predictive power for CT excitations, as well as other types of excitations [LB07, SKB09b, SKB09a, BLS10, KSBK11, JMP$^+$14, Kü17, BMN$^+$17, ZLT19], which can match that of methods based on many-body perturbation theory [KSRAB12, JDB15].

CHAPTER 4

Overview of the Main Results

This thesis's first of two project lines (Sec. 4.1) stands in close conjunction with experiments and concerns MNP catalysis. A primary focus is on understanding performance-related differences between certain cocatalytic MNP species (Ni, Pd, Pt) found in novel photocatalytic systems for hydrogen production (cf. Chapter. 1). On a fundamental level, I studied photophysical processes as well as structural and electronic properties of catalytic systems containing MNPs at the molecular level, which is particularly challenging due to the complex electronic structure and structural diversity of the metals. For this purpose, I mainly used ab-initio methods based on both stationary DFT and TDDFT, some of which have been further discussed in Chapter 2. At first, Pub. 1 laid the conceptual foundation for investigating physical properties of molecular building blocks of catalytic systems containing small MNPs (clusters) for the subsequent studies. Publication 1 further showed that the electronic interaction of Pd clusters with solvents of the ketone family can directly impact the electronic and molecular structure of the clusters: (i) The electronic density of states of the metal-solvent systems near the Fermi level (and below) significantly differs from that of their constituents. (ii) The solvents stabilize different structural isomers of the metal clusters than those preferred in vacuum. (iii) The intrinsic magnetic moment of the Pd clusters is significantly reduced. Overall, this study suggests that the interaction is more pronounced for aromatic than non-aromatic solvents. Publications 2–4 involved a collaboration of physics and chemistry in a joint research center (SFB840, ”From Particulate Nanosystems to Mesotechnology”): The corresponding experiments combined MNPs with visible light-active photocatalysts (CdS, CdS/TiO_2) and an established Ir-based photosensitizer type for hydrogen production. The experiments found that Ni consistently outperforms the paradigmatic noble metals Pd and Pt. My studies contribute to a first understanding of what role MNPs play in these systems and which aspects underlie the synergistic effects of Ni: (i) Ni shows a stronger binding affinity to essential system components (substrates of Pubs. 2–3 and photosensitizer of Pub. 4) compared to the noble metals. (ii) All studied metals directly impact the photophysical properties of the photosensitizer in close proximity via electronic interaction (Pub. 4). The respective optical excitations feature a pronounced charge transfer from the metal to the photosensitizer.

Second project line (Sec. 4.2): To understand the photo-mechanism of systems such as the previous photocatalysts, insight into the electronically excited system is particularly needed. Pump-probe PES is a vital tool for characterizing the photoactivated state of systems by probing the excited electronic structure (cf. Chapter 1). In this project line, I developed a method for simulating pump-probe ARPES from molecular systems via TDDFT in real time. As a real-time approach describes the full electron dynamics, this method goes beyond, e.g., the popular Casida approach to linear-response TDDFT that I used in Pub. 4 to characterize optical excitations. Publication 5 provided a proof of concept in a transparent one-electron system. By studying a benchmark organic semiconductor molecule (PTCDA), I showed that this approach accomplishes the challenging task of capturing many-body signatures of excitations. In other words, this approach goes explicitly beyond the DFT-based single-particle interpretation of ARPES, and Pub. 5 provides an example when many-particle effects are so prominent that they cannot be ignored.

4.1 Photophysics and Electronic Structure of Molecular Catalysts

In modern catalysis, MNPs often play a key role as efficient (co)catalysts in various organic reactions, as reviewed in Refs. [YXJ17, LC18, TA19, Ast20]. Making use of MNPs is interesting from many points of view. As an aggregate of a few to a few hundred or thousand metal atoms, a MNP represents an intermediate between the atomic and bulk regime. Dispersed MNPs have a higher surface-to-volume ratio than the same amount of bulk material [Bel03]. A large surface area typically means that the particles are sensitive to their chemical environment [NES05]. In other words, the surface atoms can be catalytically active, which in turn can lead to an increased reactivity compared to the bulk material [Bel03, PR08, BGSK16, LFM16]: For example, the adsorption of a substrate on the metal surface is often a crucial mechanistic step, and a large surface area is typically advantageous for this purpose [LC18]. Moreover, MNPs are not a one-to-one miniature of the bulk system in that they can feature different geometries and intrinsic properties depending on their size [PR08, LC18]. For instance, a much-studied property is the magnetism of small transition-metal clusters, which are aggregates of roughly up to 100 atoms with a typical diameter of < 1 nm [MHBL01, NSA03, AF03, WJ07, PPDS10, KCO$^+$11, KLW$^+$12, CRP$^+$14, LKK15, PUT$^+$16, CPD17, Van19]. These studies build on the observation that transition-metal clusters can have magnetic moments per atom that are considerably larger than those of the corresponding bulk material [DBB92, AEDB96, Lee98, Kni02, LHL$^+$14, MTvW$^+$15] – even if the bulk is non-ferromagnetic, such as in the case of Pd [CLAB94].

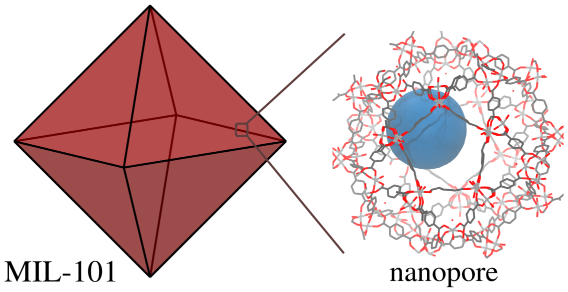

Figure 4.1: Schematic illustration of the MOF MIL-101 crystallite with a typical diameter of a few hundred nanometers. The crystallite is built up of inorganic building units of metal ions or metal and linked by multidentate organic molecules. The pores with a diameter of about 3 nm can be size-selectively loaded with MNPs (or other guest species). Excerpt: Pore loaded with a Pd nanoparticle.

However, since MNPs are prone to aggregate, they usually need to be stabilized in some way, as further discussed in Sec. 2.3.1. Stabilization can even be essential because aggregated colloidal metal particles may lose their catalytic activity [BCV83, EPD$^+$10, SGZ$^+$14]. Metal-organic frameworks (MOFs) are an elegant approach for this purpose, as they stabilize the MNPs without the need of surface blocking ligands [GCKLiX14, WMd+18]. Take the experimental approaches of Pubs. 2–4 as examples: The MNPs were synthesized into the nanopores of a mesoscopic MOF known as MIL-101 [HFM+12]. Fig. 4.1 schematically shows a pore of MIL-101 loaded with a MNP (here Pd). Further, the catalyst can be efficiently recycled from MIL-101 [BCA14]. Due to the high porosity of systems like the MIL-101, they can be visualized as a sort of molecular sponge in which the catalytically active species are readily accessible and substrates and products can diffuse in and out of the nanopores [YXJ17]. The catalytic applications with MIL-101 and congeneric MOFs are versatile (for a review, see Ref. [BCA14]): The MOF-based catalysis of cross-coupling reactions is one of the major research areas [DAG15]. Furthermore, supported Pd nanoparticles in particular efficiently catalyze some of the widely used C–C binding reactions (e.g., Suzuki and Heck) [PL12, TA19, HSS+20]. MOF-supported photocatalysis – for which Pubs. 2–4 are also examples – is among the more recent applications [GZL+22].

In systems such as described above, reactions often take place in solution. This raises the question whether MNPs interact with the solvent. If so, an important aspect is whether this has an impact on the geometric and electronic structure of the MNPs, since changes in one of these latter properties can also affect the catalytic performance [CQYJ+11, CQYJ+11, MS13, DLC+20]. For example, a high electronic density of states (DOS) near the Fermi level can promote the catalytic reactivity [TRMv96, MS13, Lep13]. As mentioned at the outset of this section, (small) transition-metal clusters can exhibit pronounced magnetic moments in vacuum. This leads to the question whether solvated clusters preserve their magnetic moment or whether it is reduced (referred to as quenching). This has particular relevance for potential magnetic applications. For example, detecting solvated metal clusters via their magnetic moment could contribute to answering the ”leaching question” as follows. The latter concerns the fundamental question of the active sites of MNPs in heterogeneous catalysis in solution [KHKP02, ALA05, PVDSJ06, RJ06, PR08, LPOMRMC13, SSH+17]: Does catalysis occur primarily at the surface of larger MNPs, or are small clusters that leached out from the larger MNPs the active species in solution? In the latter scenario (leaching), the larger MNPs serve as a kind of particle reservoir. Although there are strong indications that leached clusters are the active species in some systems [KHKP02, FJTA11, NPZ+12], this issue has not yet been conclusively clarified [BGSK16, LC18]. In this context, a pronounced magnetic moment of possibly leached, i.e., solvated clusters could serve as a basis for their experimental detection. Thus, to put it short, the study of the physical properties of solvated metal clusters is of more general significance.

Publication 1 takes up the latter point by investigating small Pd clusters (aggregates of a few up to about a dozen atoms) in solution with solvents of the ketone family with respect to the three fundamental aspects mentioned above: (i) Is there a (significant) interaction between small Pd clusters and the solvents? (ii) Do the solvated clusters assume a structure different from their vacuum structure? On the one hand, this concerns structural deformations. On the other hand, this also refers to transition between structural isomers, since (small) Pd clusters have many isomers that are stable and similar in energy: Figure 4.2 shows a selection of isomers of the paradigmatic Pd_{13} cluster that was the centerpiece of this study, and Fig. 4.2(b) depicts the bilayer C_s structure that is preferred in vacuum. Further, Pd_{13} is a prime example for a magnetic cluster ($6\,\mu_B$, cf. caption of Fig. 4.2), which leads to the last question addressed in this study: (iii) Is the magnetic moment exhibited by small Pd clusters in vacuum quenched in solution? This part of the study particularly alludes to a detection of possibly leached Pd clusters via their magnetic moment, as discussed above.

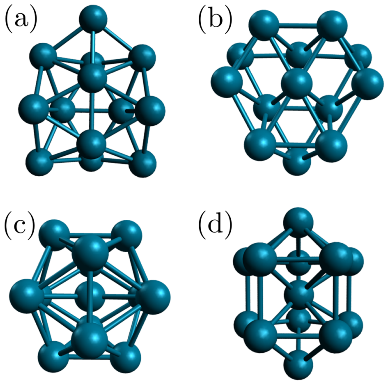

Figure 4.2: (a-c) Three known [KCO⁺11] and (d) a Pd_{13} isomer newly determined in Pub. 1. For the xc functional PBE, (a) a bilayer C_s structure with a magnetic moment of $6\,\mu_B$ is the global minimum, followed by (b) a bilayer $C_{3v}(6\,\mu_B)$, (c) an icosahedron $I_h(8\,\mu_B)$, and (d) a bicapped heptahedron $D_{5h}(8\,\mu_B)$.

Conceptually, I carried out the study of small Pd clusters in solution by explicitly building up a shell of solvent molecules around a central Pd cluster, which is further discussed below. More distant parts of the solvent that go beyond the explicit shell were modeled by a conductor-like screening approach [KS93]. In addition to Pd_{13}, Pd_8 was chosen as another established cluster with a nonzero magnetic moment in vacuum ($4\,\mu_B$) as a crosscheck that our findings are not specific to Pd_{13} [FMH05, GDAJ19, LVCAPA21]. For the solvent, the focus was on acetophenone (C_8H_8O) as a representative organic solvent of which derivatives were used in catalysis studies and particularly in studies on the leaching question addressed above [KHKP02, ALA05, PVDSJ06].

Publication 1 presented a procedure for determining the geometric and electronic structure of molecular systems containing metal clusters: (i) Regarding the molecular structure, these systems can have many geometries that are stable and similar in energy, as discussed further in Sec. 2.3.1. Therefore, one of the difficulties is determining those structures that are relevant. To this end, I used DFT-based Born-Oppenheimer molecular-dynamics simulations to obtain several low-energy structures of the canonical ensemble (at room temperature). Then, these structures were further relaxed using DFT-based geometry optimizations. For example, the right part of Fig. 4.3 shows the most stable structure of Pd_{13} in a solvent shell of five acetophenone molecules determined by this procedure. (ii) Regarding the electronic structure, the description of d-block metals is known to be challenging for many xc-functional approximations [CT09, LKK15, SK16b]. Therefore, I crosschecked the robustness of the mainly used xc functional approximation, which was PBE here (cf. Sec. 3.1), with respect to other types of xc functionals. This procedure also served as general framework for Pubs. 2–4 to study physical properties of catalytic systems via molecular models containing small MNPs.

By means of an in-depth DFT-based analysis of the electronic structure, I revealed a direct electronic interaction between the Pd clusters and the acetophenone solvent shell that is

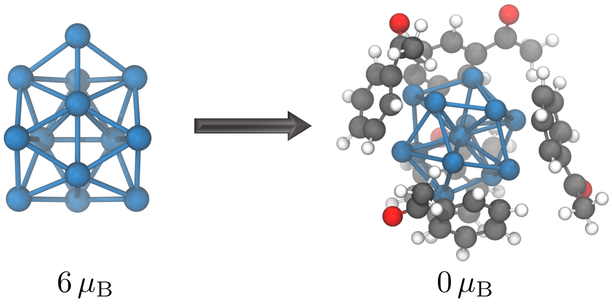

Figure 4.3: The magnetic moment of a Pd_{13} cluster (left) is significantly quenched within a solvent shell of five acetophenones (right). The solvent shell stabilizes $Pd_{13}(I_h)$ instead of the isomer C_s preferred in vacuum (cf. Fig. 4.2). Structures and magnetic moments were obtained from geometry optimizations with PBE. Color code: Pd blue, C grey, H white, O red. See Pub. 1 for details.

manifested in the following findings: (i) The DOS of the metal-solvent systems changes strongly due to the interaction, i.e., it is not simply a superposition of the DOS of its constituents. This is representatively shown for Pd_{13} within a solvent shell of five acetophenones in Fig. 4.4. (ii) The binding between the Pd cluster and the solvent molecules that is accompanied by a noticeable charge transfer from the metal to the solvent. (iii) The solvent shell is capable of stabilizing a Pd-cluster isomer different to that preferred in vacuum (cf. Fig. 4.3). The stabilized cluster isomers indicate a preference for structures that provide a similar surface-area fraction to each solvent molecule. (iv) The interaction causes a significant quenching of the magnetic moment of the Pd clusters, as shown representatively for Pd_{13} in Fig. 4.3.

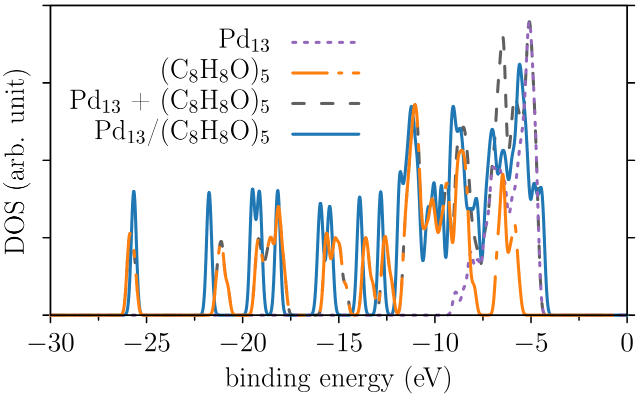

Figure 4.4: DOS of Pd_{13}, $(C_8H_8O)_5$, the combined system $Pd_{13}/(C_8H_8O)_5$, and the sum of the DOSs of Pd_{13} and $(C_8H_8O)_5$, obtained from ground-state DFT calculations with PBE. If there were no interaction between the components of a system, the DOS of the combined system would result from the superposition of the DOS of the individual subsystems. See Pub. 1 for details.

Overall, I found indications that the aromatic character of acetophenone plays an important role in the electronic interaction that leads to the quenching of the magnetic moment. This hypothesis was further corroborated in Pub. 1 by an analogous study with the non-aromatic solvent acetone (C_3H_6O), which, like acetophenone, is a member of the ketone family. This showed that the electronic interaction and magnetic-moment quenching is less pronounced for the non-aromatic solvent. In addition, Pubs. 2–3 provided further evidence in this direction: As a side result of these studies, I found that the presence of one benzyl alcohol and one benzylamine molecule also leads to a reduction of the magnetic moment of Pd_{13}. Taking these results as a whole implies that avoiding aromatic solvents and/or substrates is a crucial aspect to preserve the magnetic moment of Pd clusters. We further expect this conclusion to be relevant for magnetic applications, such as the potential detection of leached/solvated clusters by means of their magnetic moment, as discussed above in the context of leaching.

In Pubs. 2–4, the focus was on utilizing MNPs as cocatalysts in (different) visible light-active photocatalytic systems. All of these systems are supported by a MOF and combine cocatalytic MNPs with the solid-state photocatalysts CdS/TiO_2 (Pub. 2) and CdS (Pub. 3) or an Ir-based molecular photosensitizer (Pub. 4). These studies are linked by the intriguing experimental findings that cocatalytic Ni nanoparticles significantly increase the hydrogen-evolution rate in the associated reactions, while consistently outperforming commonly used noble metals, such as Pd and Pt. In Pub. 4, cocatalytic Pd even led to a decreased hydrogen yield compared to the pure photosensitizer. These findings raise two overarching questions in particular: (i) What is the role of the MNPs in the respective photocatalytic mechanism? (ii) Which aspects lead to the synergistic effects found for Ni? In what follows, I will first discuss each of the publications in more detail, addressing in each case our contributions to answering these questions. At the end of this section, I draw a general conclusion regarding my contributions.

Publications 2–3 performed the visible light-driven acceptorless dehydrogenation of chemical compounds in overall similar systems. The highly attractive byproduct of these reactions is the liberation of one equivalent of H_2. Publication 2 dealt with the dehydrogenation of alcohols as well as the imine synthesis of alcohols and amines by dehydrogenative C-N cross coupling. For this purpose, a novel MOF-supported metal-heterojunction photocatalyst was developed. The latter is based on a composite system of CdS/TiO_2 decorated with transition MNPs that is prepared on the outer surface of a MIL-101 crystallite. Note that the system is denoted as M/CdS/TiO_2@MIL-101 in the following, where M refers to the cocatalysts ($M =$ Ni, Pd, Pt, Au). Figure 4.5 schematically shows Ni/CdS/TiO_2@MIL-101; the photophysical mechanism is discussed further below. Publication 3 followed a similar approach as Pub. 2, with the difference being that the semiconductor CdS is used as the photocatalyst instead of a heterojunction material and benzylamine is considered as substrate instead of alcohols. This approach, M/CdS@MIL-101, successfully catalyzes the dehydrogenation of benzylamine under the release of H_2 ($M =$ Ni, Pd, Pt). Furthermore, this photocatalytic system enables the challenging synthesis of non-symmetric imines by dehydrogenative C-N cross coupling of two different amines.

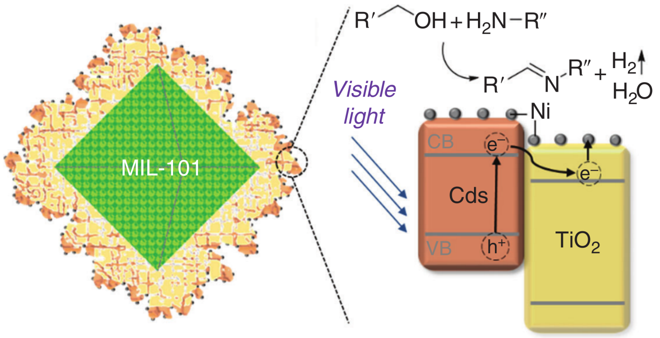

Figure 4.5: (left) Illustrative cross-section of the photocatalyst Ni/CdS/TiO_2 prepared on the outer surface of MIL-101. (right) Excerpt: Light-driven dehydrogenative coupling of alcohols and amines under liberation of H_2. The photophysical mechanism of Ni/CdS/TiO_2 is discussed in the main text. See Pub. 2 for details.

MIL-101 is visible light-inactive, which leaves M/CdS and M/CdS/TiO_2 as the active entity in Pub. 2 and Pub. 3, respectively. In both studies, the experiments confirmed that optical excitation leads to a charge separation between CdS (”hole”) and the MNPs (”electron”), which is a typical finding for such nanohybrid systems [SGQS12, MSM$^+$12, Kam12]. The corresponding photomechanism is exemplarily shown for the heterojunction system Ni/CdS/TiO_2 in the right excerpt of Fig. 4.5: Absorption of visible light causes an excitation from the valence band (VB) to the conduction band (CB) of CdS. Subsequently, electron transfer occurs through TiO_2 to the cocatalytic MNPs (here Ni). Similarly, the electron transfer in the metal-semiconductor system *M*/CdS directly takes place from the excited CdS to the metal. Therefore, the cocatalytic MNPs take on the role of an electron reservoir in both systems. Overall, the spatial charge separation enhances the stability against recombination and further facilitates spatially separated redox half-reactions. In Pub. 3, it was also experimentally found that the charge transfer to Ni is faster compared to the noble metals Pd and Pt. Thus, a concrete aspect for the superior performance of cocatalytic Ni could be elucidated within this system.

My complementary theoretical studies to Pubs. 2–3 can be treated together, as outlined in the following. Reaching a detailed microscopic understanding of the dehydrogenation of the substrates is a very extensive task in general. To gain first insights in this direction, my studies focused on one important step in these reactions, viz., the binding between the cocatalytic MNPs and the substrate. Certain aspects of it, such as the bond strength, can be well analyzed based on DFT. To this end, I probed whether there is a difference in the binding energy between the cocatalytic MNPs and the respective substrate.

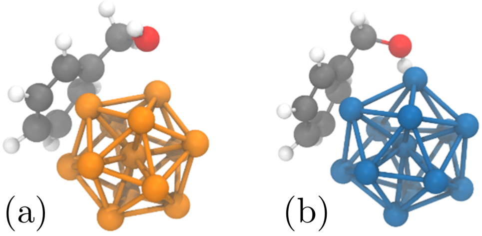

Figure 4.6: Optimzied structures of benzyl alcohol (C_7H_8O) bound to an icosahedral (a) Ni_{13} cluster and (b) Pd_{13} cluster (obtained with PBE). See main text and Pub. 2 for details.

For the substrates, my theoretical studies considered benzyl alcohol and benzylamine, since these were the focus of the experiments of Pub. 2 and Pub. 3, respectively. For the noble metals, Pd was chosen as a representative, which performed considerably worse in direct comparison with Ni in both studies. The binding was studied in a model system consisting of 13-atom metal clusters (Ni_{13}, Pd_{13}) and a substrate molecule, as representatively shown by Ni_{13} combined with benzyl alcohol in Fig. 4.6. Conceptually, the structures were optimized following the procedure of Pub. 1. It should be noted that the 13-atom clusters are clearly smaller than the nanoparticles dispersed on the surface of CdS/TiO_2@MIL-101 and CdS@MIL-101, respectively. However, given that the computational cost rapidly increases for larger MNPs (cf. Sec. 2.3.1), we consider 13-atom clusters minimalistic structures that are suitable for studying the metal-substrate binding for several reasons: (i) The Born-Oppenheimer DFT molecular dynamics simulations at room temperature of Pub. 1 showed that 13-atom metal clusters can adapt their structure to their environment. (ii) The considered transition-metal clusters feature stable isomers with similar geometries, such as the icosahedron [PPDS10, LKK15, PUT$^+$16, CPD17, Van19]. Therefore, the different metals can be compared on a similar structural basis. (iii) Both Ni_{13} and Pd_{13} bind to the substrates (see below).

The results of my theoretical studies in Pubs. 2–3 correlate in that the binding of the substrates benzylamine and benzyl alcohol is stronger to the Ni than to the Pd cluster by several hundred meV. Overall, this indicates that the metal-substrate binding affinity is higher for Ni nanoparticles in both systems, which we expect to be beneficial for an efficient charge transfer between the cocatalyst and the substrate. Further work will be needed to reach a detailed understanding of the influence of the metal-substrate binding on the catalytic mechanism. Overall, however, my results provide first clues for another aspect of why the performance of Ni nanoparticles differ from that of noble metals.

Instead of solid-state photocatalysts, the objective of Pub. 4 was to combine a molecular photosensitizer and cocatalytic MNPs for the visible light-driven production of hydrogen by proton reduction from water. For this purpose, a heteroleptic Ir(III) photosensitizer (denoted as Ir-L1 hereafter) was used that enables the hydrogen production via water reduction without the need of an additional electron relay. Tailored to the synthesis of this study, Ir-L1 ($[\mathrm{Ir(dmOHbpy)(ppy)_2}]^+$) is a slightly modified version of the established $[\mathrm{Ir(bpy)(ppy)_2}]^+$ motif (denoted as Ir-L0 hereafter), where dmOHbpy refers to the ligand 2,2'-bipyridine-4,4'-diyldimethanol, bpy denotes 2,2'-bipyridine, and ppy denotes 2-phenylpyridine. That is, the bipyridyl ligand of Ir-L1 contains additional hydroxyl groups in the backbone compared to the Ir-L0 motif. Triethylamine (TEA) was used as the sacrificial agent in the experiments. Publication 4 presented an experimental "ship-in-a-bottle" approach by which the Ir-L1 photosensitizer and the cocatalytic MNPs (Ni, Pd, Pt) were confined into the pores of MIL-101 by a multistep synthesis. The system is denoted *M*/[Ir-L1]@MIL-101 hereafter. This approach ensures that Ir-L1 and the MNPs are in close proximity without a stabilizing agent blocking their surface, as schematically shown in Fig. 4.7.

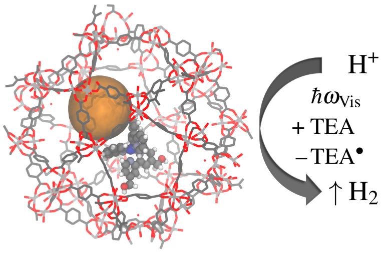

Figure 4.7: Ship-in-a-bottle approach: Both the photosensitizer Ir-L1 and the cocatalytic MNPs (Ni, Pd, Pt) are encapsulated in the pores of MIL-101 (cf. Fig. 4.1). The metal–Ir-L1 systems catalyze the visible light-driven hydrogen production via proton reduction in water. TEA is the sacrificial agent. See main text for details.

Intriguingly, the experiments found that Ni/[Ir-L1]@MIL-101 significantly enhances the hydrogen-evolution rate compared to pure [Ir-L1]@MIL-101 (cf. Fig. 4.8). In contrast, loading [Ir-L1]@MIL-101 with the noble metal Pt resulted in only a small enhancement and Pd led to a near catalytic deactivation. Thus, the MNPs show a clear qualitative effect on the photocatalytic activity. Yet reaching an understanding of such effects is challenging, since it is difficult to obtain insight into the photocatalytic processes within the pores in situ, as further discussed in Pub. 4. However, we considered the proximity mediated by the MOF between the cocatalytic MNPs and the photosensitizer as an important aspect of the system that could promote an inter-molecular interaction. At this point my theoretical investigations take up. The focus was, firstly, to clarify

Figure 4.8: Hydrogen-evolution rate of the photocatalytic water reduction using [Ir-L1]@MIL-101 and *M*/[Ir-L1]@MIL-101 (M = Ni, Pd, Pt). The light source was a blue LED with a wavelength of 470 nm. See main text and Pub. 4 for details.

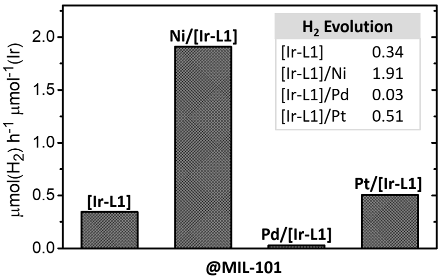

whether Ir-L1 and the MNPs interact significantly. Secondly, I studied the role of the MNPs in the photoabsorption and probed whether they affect the photophysics of the photosensitizer.

At this stage, it is worth outlining the mechanism of Ir-L1 before discussing the photophysical properties of the combined systems (*M*/[Ir-L1]). As we verified both experimentally and theoretically, Ir-L1 functions by a mechanism that is qualitatively identical to that of Ir-L0 [GHL^{+}05, CTB^{+}09, WLL^{+}10, GDL^{+}12, BBK15], i.e., by a mechanism typical of heteroleptic Ir(III) photosensitizers [DMC^{+}21]. The corresponding photomechanism of Ir-L1 is alluded in Fig. 4.9: Ir-L1 features few bright excitations in the upper part of the (theoretical) Vis spectrum, such as the singlet S$_4$ at 3.03 eV (with an oscillator strength of 0.1023). After photoabsorption (of visible light) the pronounced spin-orbit coupling of iridium facilitates rapid inter-system crossing from the singlet into the triplet domain. Subsequently, the lowest triplet state T$_1$ (2.26 eV) is accessed through internal conversion. T$_1$ is a long-lived and charge-separated state. The latter can be seen from the electronic difference density of T$_1$ with the singlet ground state, which is shown in the inset of Fig. 4.9: T$_1$ features a distinct charge transfer from Ir/ppy → bpy, as illustrated by the red and blue wireframes that indicate negative (area of electron lack) and positive (gain) in this and the following difference densities, respectively. Furthermore, it is known that these latter characteristics of T$_1$ facilitate the (TEA-mediated) reduction of protons from water [TMC^{+}07, BHP^{+}14].

Figure 4.9: Theoretical Vis absorption spectrum of Ir-L1 obtained from a TDDFT calculation with the non-empirical optimally tuned ωPBE xc functional. The relative oscillator strength is indicated by the height of the vertical red bars. T$_1$ is marked by the single gray bar. Inset: Difference densities for the brightest singlet S$_4$ (3.03 eV) and the lowest triplet excitation T$_1$ (2.26 eV), with schematic allusion to intersystem crossing and internal conversion. See main text and Pub. 4 for details.

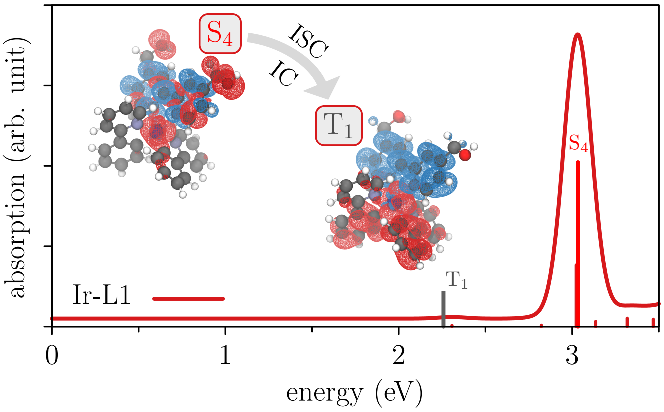

Studying an entire nanopore containing Ir-L1 and a MNP with first-principles methods is computationally unfeasible. Since the main electronic effects were expected to occur in the interaction between the MNPs and Ir-L1, we considered studying a subsystem consisting of these two components a reasonable approach. For the MNPs (Ni, Pd, Pt), the focus was again on 13-atom clusters. We considered these latter as minimalistic structures suitable for the study of the metal–Ir-L1 interaction, based on an analogous reasoning as already discussed for Pubs. 2–3. The molecular structures of the subsystems (M_{13}/Ir-L1) were optimized as described in the context of Pub. 1. Figure 4.10(a) representatively shows the relaxed structure of Ni_{13}/[Ir-L1].

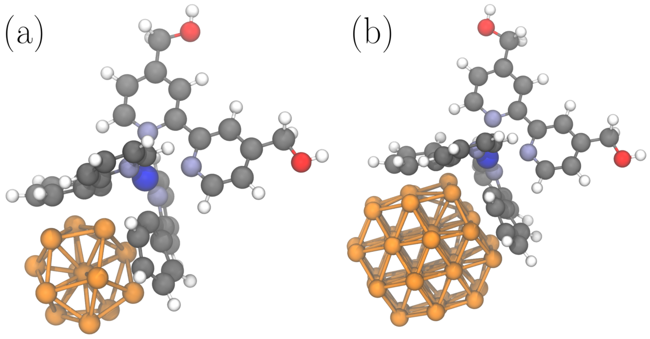

Figure 4.10: Optimized structures of Ir-L1 bound to a (a) Ni_{13} cluster and (b) Ni_{38} cluster. Color code: Ni orange, Ir blue, N purple, C grey, H white, O red. See main text and Pub. 4 for details.

Further DFT-based analysis of these structures showed that all three metal clusters bind to the photosensitizer. With a binding energy of −5.76 eV, Ni_{13}/[Ir-L1] is more strongly bound than Pd_{13}/[Ir-L1] (−4.72 eV) and Pt_{13}/[Ir-L1] (−3.39 eV). Thus, the binding energy is an observable in which Ni differs noticeably from the noble metals Pd and Pt. Furthermore, the pronounced binding is an indication for an electronic interaction between the metals and Ir-L1. The electronic interaction was further corroborated by the analysis of the electronic structure. For example, the electronic DOS of the combined metal–Ir-L1 systems changes strongly compared to that of its constituents (cf. Fig. 4.4, caption). As a crosscheck that the electronic interaction is not specific to 13-atom clusters, I performed an analogous investigation for the considerably larger Ni_{38} (cf. Fig. 4.10b). Reassuringly, the electronic DOS of Ni_{38}/[Ir-L1] showed – qualitatively very similar to Ni_{13} – clear features of a direct interaction. This further corroborates that the M_{13}/Ir-L1 may be interpreted to represent a subsystem in the nanopore.

Finally, I addressed the question of whether the interaction also affects the photophysical properties of the system. Note that I carried out this part of the study with the Casida approach to linear-response TDDFT (cf. Sec. 2.3.3) using the non-empirical optimally tuned ωPBE xc functional (cf. Sec. 3.2). My computations revealed that the presence of all metal clusters (Ni, Pt, Pd) changes the photoabsorption significantly, which is representatively shown for Ni_{13}/[Ir-L1] in Fig. 4.11(a): (i) The combination with each of the metal clusters leads to a very dense excitation spectrum: Instead of the few excitations with large oscillator strength that characterize the bare photosensitizer (cf. Fig. 4.9), M_{13}/[Ir-L1] features hundreds of Vis excitations with smaller oscillator strengths (at the individual excitation). (ii) The Vis photoabsorption of M_{13}/[Ir-L1] increases overall compared to Ir-L1 and clearly differs from that of the individual components (and their superposition, cf. Ni_{13} + Ir-L1). (iii) I further analyzed many of the excitations of M_{13}/[Ir-L1] in detail via difference densities: This showed that for the combined systems, many of the optical excitations involve a charge transfer from the metal to the photosensitizer ligands (cf. Fig. 4.11(b)). Therefore, this suggests that the metals take on the role of an electron donor.

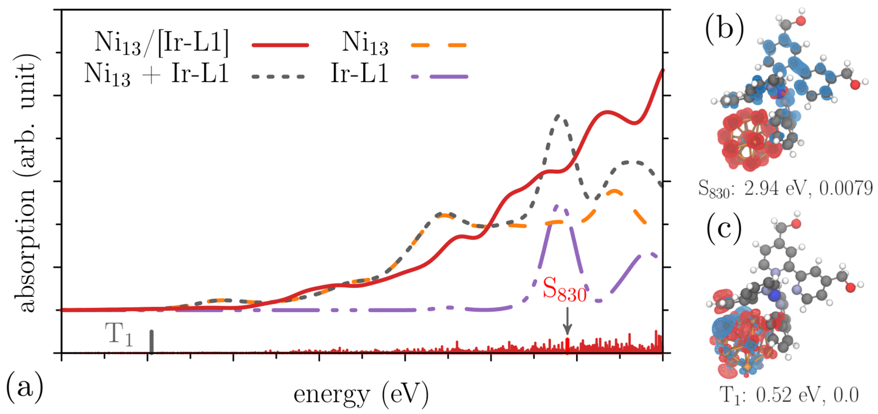

Figure 4.11: (a) Vis absorption spectrum of Ni_{13}/[Ir-L1], Ni_{13}, Ir-L1, and the superposition Ni_{13} + Ir-L1. The spectra were obtained from TDDFT with the non-empirical optimally tuned ωPBE (tuned for Ni_{13}/[Ir-L1]). Vertical red bars and the single gray bar show the relative oscillator strength and lowest spin-flip excitation for Ni_{13}/ [Ir-L1], respectively. (b–c): Difference densities of selected excitations of Ni_{13}/ [Ir-L1] with the given energy and oscillator strength (marked in (a)). (b) The difference density of the optical excitation S_{830} shows a metal particle to ligand charge transfer. (c) Difference density of the spin-flip excitation, denoted by T_1 (in analogy to the pure Ir-L1). See Pub. 4 for details.

In conclusion, the photophysical properties of the metal–Ir-L1 systems significantly change compared to those of the bare Ir-L1 photosensitizer. Thus, it is conceivable that this can play a role in photophysics and photocatalysis. However, each Ni, Pd, and Pt cluster shows a qualitatively very similar impact on the photophysical properties when combined with the photosensitizer. Therefore, the synergistic effect of Ni observed in the experiments cannot be explained by these results alone. One of the aspects that might be worth investigating further in future work is that the charge transfer almost completely ”collapses” in the lowest spin-flip excitation[1] of the metal–Ir-L1 systems. In other words, if the lowest spin-flip state were accessed, this would most likely mean catalytic deactivation. In contrast, accessing the charge-separated lowest triplet state of bare Ir-L1 is vital for catalytic activity. Further, one might speculate that the heavier Pt and Pd metal particles may lead to a stronger spin-orbit coupling than Ni. Consequently, this could result in a higher probability of promoting inter-system crossing to the lowest spin-flipped state. Altogether, further work will be needed to reach a detailed understanding of the photophysical and photocatalytic mechanism. Overall, however, my investigations identified a clear aspect in which Ni differs from the noble metals: The metal–Ir-L1 binding is considerably stronger for Ni. It seems plausible that this difference can affect the spatial arrangement of the molecular constituents within the MIL-101 pore, which in turn may impact the hydrogen-evolution rate.

In summary, Pubs. 1–4 identified several aspects that could be of more general importance to MNP catalysis: My findings revealed that small MNPs interact electronically with other

---

[1] M_{13}/[Ir-L1] are spin-polarized systems, i.e., they have nonzero magnetic moments. Therefore, their lowest spin-flip excitation is the analogue to the lowest triplet excitation T_1 of Ir-L1.

system components (solvent, substrate, photosensitizer), which in turn affects essential system properties. Our results indicated that the MNPs are directly involved in the photophysical processes of the photocatalytic systems and take different roles in these processes depending on the system and synthesis (electron acceptor, electron donor). As for the differences between the cocatalytic metals across the systems of Pubs. 2–4: My calculations consistently indicated that Ni nanoparticles feature a higher binding affinity to other key components (substrate, photosensitizer) than noble metals (Pd, Pt).

4.2 Photophysics of the Excited PTCDA Molecule

Photophysical processes are inherently dynamic and can be based on complex quantum phenomena, such as the electronic mechanisms seen in the photocatalytic systems of Pubs. 2–4. Another process based on phenomena of this category is the emission of photoelectrons due to light-matter interactions in the form of the photoelectric effect [Ein05]. PES makes use of precisely this effect to gain insight into the electronic structure of condensed matter systems (for a review, see Ref. [Hü03]). To this end, PES is a powerful technique since the electronic DOS of the probed system is mapped into the corresponding photoemission observables [Hü03], such as the kinetic-energy spectrum (KES) of the photoelectrons. Many system properties and characteristics can be further derived based on the DOS. In Pub. 4, for example, I revealed an interaction between a photosensitizer and metal clusters by means of a theoretically determined DOS (for further aspects regarding catalysis, see Sec. 4.1). In pump-probe PES, a first laser pulse excites the system (without emission of photoelectrons) before a time-delayed second pulse triggers photoemission [SBJE97, SBN04, WEB05]. Thus, this technique aims to provide insight into the system's excited electronic structure. Furthermore, the angle-resolved detection of the photoelectrons (ARPES) allows for the determination of their kinetic energy and momentum. Among other things, pump-probe ARPES is particularly suited for studying the photoactivated state of photocatalytic systems. For instance, experimental pump-probe approaches have been used to investigate the relaxation mechanism of triplet photosensitizers [MSS+13, MBBU18, MU20, WHL+20] and photoexcited charge carriers (electrons and holes) in semiconductor photocatalysts [MIA+11, BOF+19], respectively. In general, the study of semiconductor materials is one of the main research areas of pump-probe ARPES [CGGL11, SCK+15, MMDJ+17, WRS+21, PNM+22].

Many approaches have been devised for the theoretical description of (AR)PES and for well-known examples, the reader is referred to those given in Pub. 5. Among these latter is a TDDFT-based method previously developed in the Kümmel group [DK16, DGS+16]. This approach simulates the direct photoemission process from the ground state of molecular systems in real time and real space. The corresponding ARPES spectrum, i.e., information about the photoelectrons' kinetic energy and momentum results from the evaluation of the emitted electron density recorded at detection points according to a scheme first presented in Ref. [PRS00]. This method, however, had been limited to direct ARPES, i.e., pump-probe processes had been conceptually excluded and not been investigated. This is where my second project line picked up with the goal of developing an extension for pump-probe processes, which led to Pub. 5. However, taking the step from direct to pump-probe photoemission is not as straightforward as it might seem, because gaining insight into excited system from the perspective of real-time TDDFT has some particular challenges, which can be illustrated particularly well by the following comparison with perturbation theory.

From the perspective of time-dependent perturbation theory in terms of Fermi's Golden Rule, optical processes such as excitation and photoemission can be described on the basis of probability rates for transitions between the eigenstates of the true many-particle system (as reviewed, e.g., in Ref. [DWF$^+$14]). In practice, of course, it is typically unfeasible to determine the many-particle wave function of the initial and final state that enter the matrix element of the perturbation. Therefore, associated quantities such as the Dyson orbital are often approximated by molecular orbitals, i.e., (AR)PES is interpreted by a single-particle picture (see below). Nonetheless, the interpretation of these processes as transitions between states leads to a descriptive notion. In contrast, in a real-time TDDFT description, all information of the pump-probe process is "encoded" in the abstract time-dependent density that is constructed from the occupied TDKS orbitals (cf. Sec. 2.2). Thus, unoccupied orbitals and transition between states are *a priori* not part of this description. Since little had been known about how pump-probe processes can be interpreted within a TDDFT-based real-time description, Pub. 5 aimed at contributing to this understanding. One of the central questions I addressed was how the many-particle character of an electronically excited system is manifested in the photoemission.[2] Or in other words, how is the many-particle character reflected in the ARPES observables? This part of the investigation also alluded to the wide-spread approach [PBF$^+$09] of interpreting ARPES experiments by the single-particle picture (cf. Pub. 5 for a wide range of references). In terms of the the DFT-based single-particle picture, the pump-probe process would correspond to "moving" an electron from an occupied to an unoccupied KS orbital (excitation), from which the electron is then emitted into the continuum of states. That means, the single-particle picture lacks the many-particle relaxation effects that the electronic structure would typically undergo due to excitation and photoemission. One of the key findings of Pub. 5 is that our real-time TDDFT approach can capture the many-particle character of excitations and thus explicitly goes beyond the single-particle picture. This is further discussed below, but first an outline of the real-time method and introduction to some ARPES quantities is in order.

Conceptually, I simulated the photoemission from an electronically excited system as a dynamical process using real-time TDDFT. To this end, the full TDKS equations were solved by numerical propagation (cf. Sec. 2.3.2, Eq. 2.17). The orbitals were represented on a

---

[2] From the standpoint of Casida's approach to linear-response TDDFT (cf. Sec. 2.3.3), the true electronic many-particle excitation can be interpreted as a superposition of (all possible) single-particle transitions that go from occupied to unoccupied eigenstates of the stationary KS Hamiltonian. From here on, an excitation showing many-particle character refers to the situation that more than one transition contributes noticeably to the corresponding superposition. In turn, single-particle character refers to an excitation that is purely or predominantly described by one transition. Approximating the many-particle character by one single-particle transition corresponds to the (DFT-based) single-particle picture.

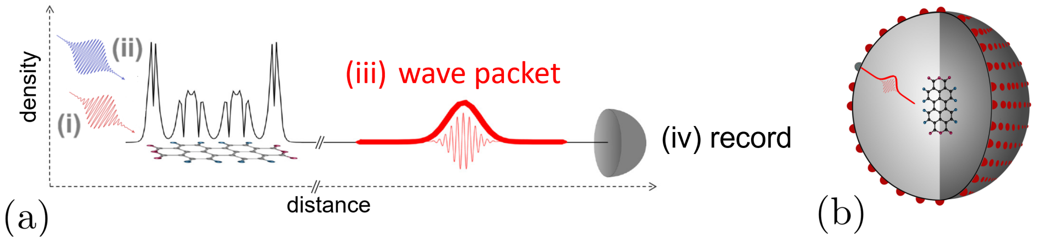

Figure 4.12: The key elements of pump-probe ARPES are captured in a single real-time TDDFT simulation: (a) Pump pulse (i) and probe pulse (ii) lead to the excitation of the system (PTCDA) and the emission of wave packets (iii), respectively. The outgoing wave packet is recorded in time at a detection point (iv). (b) The angle-resolved recording with respect to a ”net” of detection points on a hemisphere is shown for the scenario (a). See main text for details.

numerical real-space grid (cf. Sec. 2.3.1). All key elements of pump-probe ARPES – excitation, photoemission, and detection – are captured in a single calculation, as summarized in the following. At first, the system was in its ground state. Then, the pump-probe dynamics were governed by two classical electric light fields in the dipole approximation (with a temporal delay of few femtoseconds between both). The energy of the pump field ($\hbar\omega_{\mathrm{L},1}$) and its polarization direction was chosen such that it corresponded to a dipole-allowed excitation and its transition-dipole moment. This modeled the pump excitation. The pump field drives the ionization of the system and models the photoemission. To demonstrate that the ARPES signals only emerge from the excited system, the energy of the probe field ($\hbar\omega_{\mathrm{L},2}$) was chosen such that direct photoemission from the ground state was excluded energetically. The laser intensities were chosen moderately low (for guidelines, see Pub. 5). Under the action of an ionizing field, an occupied TDKS orbital $\varphi_j(\boldsymbol{r},t)$ can evolve such that parts of it become an outgoing wave packet. These wave packets are recorded in time at detection points far from the ionized daughter system where the Coulomb interaction is negligibly small. Consequently, this scheme requires a representation on large real-space grids, which raises the computational cost. Yet, the grid-based real-time propagation can be made computationally efficient and scales well with the system size (cf. Sec. 2.3.2). Figure 4.12(a) illustrates the approach until this point. Recording the wave packets at a set of detection points ($\{\boldsymbol{R}_D\}$) that are located on the upper hemisphere with radius R_D around the system center leads to angle-resolved signals (cf. Fig. 4.12b), where $D = 1,\ldots,N_\mathrm{D}$. For high resolution, typically several thousand detection points (N_D) are considered. Note that the scheme for evaluating the recorded wave packets is described in full detail in Pub. 5, so the following outline is kept minimalistic. At a point $\boldsymbol{R}_D$, the outgoing wave packet $\varphi_j(\boldsymbol{R}_D,t)$ is considered as a superposition of plane waves. The magnitude k of the plane-wave vector $\boldsymbol{k}$ is connected to the dispersion relation of free particles $E_\mathrm{kin} = \hbar^2 k^2/(2m)$. The probability of detecting the kinetic energy E_kin in the wave packet can be derived from a temporal Fourier transform of $\varphi_j(\boldsymbol{R}_D,t)$ into the frequency domain. Since the plane waves are purely outgoing ($k > 0$), the direction of the momentum $\boldsymbol{p} = \hbar\boldsymbol{k}$ is fixed by the position at which they are detected, i.e., $\boldsymbol{p}/|\boldsymbol{p}| = \boldsymbol{R}_D/|\boldsymbol{R}_D|$. As the magnitude of the momentum follows from $|\boldsymbol{p}| = \sqrt{2mE_\mathrm{kin}}$, $\boldsymbol{p}$ is uniquely specified through the detection of E_{kin} at $\boldsymbol{R}_D$. At this point at the latest, the outgoing wave packets are interpreted as photoelectrons: The total probability of finding a photoelectron with kinetic energy E_{kin} at $\boldsymbol{R}_D$ is proportional to summing up the probabilities for all outgoing wave packets (that evolved from the occupied TDKS orbitals):

$$I(\boldsymbol{R}_D, E_{\text{kin}}) \propto \sum_{j=1}^{N} |\varphi_j(\boldsymbol{R}_D, E_{\text{kin}}/\hbar)|^2, \tag{4.1}$$

where $\varphi_j(\boldsymbol{R}_D, E_{\text{kin}}/\hbar)$ is the Fourier transform of $\varphi_j(\boldsymbol{R}_D, t)$, and the frequency is written in terms of the kinetic energy. This procedure is repeated for the set of detection points $\{\boldsymbol{R}_D\}$ to obtain the probability of finding a photoelectron with respect to different emission angles. In Pub. 5, the photoemission signals were analyzed based on Eq. (4.1) in two different ways: (i) Taking the sum over all detection points $\{\boldsymbol{R}_D\}$ yields the total KES of the photoemission process. (ii) The angle-resolved probability of finding a photoelectron with momentum $\boldsymbol{p}(E_{\text{kin}})$ is visualized in terms of an intensity momentum map $I(\boldsymbol{p}(E_{\text{kin}}))$. Using spherical coordinates for the description of the photoelectron's emission angles (ϕ, θ), the vector components of the photoelectron's momentum can be written as

$$\hbar k_x = \sqrt{2mE_{\text{kin}}}\cos\phi\,\sin\theta, \quad \hbar k_y = \sqrt{2mE_{\text{kin}}}\sin\phi\,\sin\theta, \quad \hbar k_z = \sqrt{2mE_{\text{kin}}}\cos\theta. \tag{4.2}$$

(ϕ, θ) directly correspond to the angular position of the respective detection point, i.e., $\boldsymbol{R}_D = R_{\text{D}}(\cos\phi\,\sin\theta, \sin\phi\,\sin\theta, \cos\theta)$. Note that ARPES intensity maps are typically plotted in terms of the components of the wave vector $\boldsymbol{k} = \boldsymbol{p}/\hbar$. In line with experiments, k_z is positive due to the detection with respect to the upper hemisphere and therefore fixed by the specification of (k_x, k_y), i.e, $k_z = \sqrt{2mE_{\text{kin}}/\hbar^2 - k_x^2 - k_y^2}$. Thus, plotting $I(k_x, k_y)$ contains the equivalent information as $I(\boldsymbol{k})$.

As an alternative to the real-time TDDFT approach, I also computed $I(k_x, k_y)$ from the so-called plane-wave approach that is based on perturbation theory and Fermi's Golden Rule [PBF+09]. This approach takes the two main assumptions that the photoelectron originates from a molecular orbital and is in a plane-wave final state when it is detected. Thus, this approach interprets photoemission by the single-particle picture. Further, the electromagnetic field is considered in the dipole approximation. On basis of these considerations, one can derive that the ARPES intensity is proportional to [PBF+09, DWF+14]

$$I(k_x, k_y) \propto |\boldsymbol{A} \cdot \boldsymbol{k}|^2 |\tilde{\varphi}_{\text{in}}(\boldsymbol{k})|^2_{k=\text{const.}}. \tag{4.3}$$

The vector potential $\boldsymbol{A}$ describes the electromagnetic field corresponding to the photon energy $\hbar\omega$ and $\boldsymbol{k}$ is the wave vector of the plane-wave final state. $\tilde{\varphi}_{\text{in}}(\boldsymbol{k})$ is the spatial Fourier transform of the initial (stationary) orbital $\varphi_{\text{in}}(\boldsymbol{r})$ from which the electron was emitted. This approach obeys the conservation of energy, i.e., $E_{\text{kin}} = \hbar\omega - |E_{\text{B}}|$, where E_{B} is the electron binding energy. Therefore, the expression on the right-hand side of the Eq. (4.3) is evaluated at the value $|\boldsymbol{k}| = \sqrt{2m(\hbar\omega - |E_{\text{B}}|)}/\hbar$, where E_{B} equals the binding energy (eigenvalue) associated with the initial molecular orbital. Regarding the choice of the latter, a wide-spread approach is to use stationary KS orbitals, as made popular by Ref. [PBF+09].[3]

Publication 5 first provided a proof of concept for the above approach to simulate pump-probe ARPES in real time. To this end, considering a one-electron system represented a reliable test scenario for the following two reasons and their implications: Firstly, the TDKS Eq. (2.12) becomes the time-dependent Schrödinger equation in the one-electron limit. Therefore, the exact dynamics of the system can readily be determined by a TDDFT-based code (the finite numerical accuracy set aside). Consequently, uncertainties that may arise in a many-particle system due to the necessary xc functional approximation are of no concern in this limit. Secondly, the ARPES observables obtained from the real-time simulation can be straightforwardly crosschecked against the anticipated transitions between exactly known states. For a convenient representation on a real-space grid, I considered a model one-electron system. This system is in a s type ground state, and the threefold degenerate lowest unoccupied orbital is of p type. The goal was to simulate the paradigmatic pump-probe process that corresponds to the transitions from $s \rightarrow p$ (excitation) and $p \rightarrow$ continuum (photoemission). For this purpose, the simulation setup was chosen as described above, where the frequency of the pump field matched the eigenvalue difference between the s and p states. To promote excitation and photoemission with respect to one of the degenerate p orbitals, the laser polarization of both the pump and probe lasers corresponded to the orientation of the respective orbital. An in-depth analysis of the KES and ARPES momentum map obtained from the real-time simulation confirmed that the excited p state is correctly reflected in the photoemission process. In particular, the comparison of the ARPES momentum map of the real-time simulation with that obtained using the plane-wave approach (cf. Eq. 4.3) was very instructive: This showed that the real-time description of the pump-probe process for a one-electron system can be interpreted as the mapping of a previously unoccupied orbital, i.e., the respective p orbital in this case.

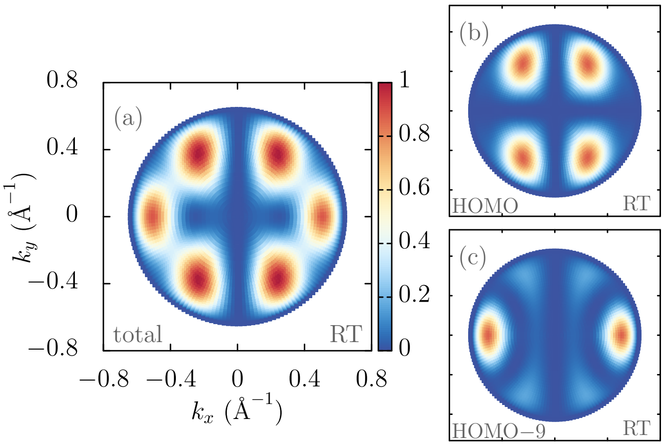

Figure 4.13: ARPES momentum map of the PTCDA molecule obtained from real-time (RT) TDDFT using ALDA. The polarization direction of the pump-probe fields ($\hbar\omega_{\mathrm{L},1} = 2.14$ eV, $\hbar\omega_{\mathrm{L},2} = 6.00$ eV) was set along the long molecular axis. (a) Shows contributions from the time-dependent (b) highest occupied molecular orbital (HOMO) and (c) HOMO-9. The maps were evaluated for an energy interval around the main peak of the corresponding KES. See main text for discussion and Pub. 5 for details.

---

[3] The DFT-based plane-wave approach has very successfully been applied for the interpretation of mostly direct ARPES experiments, i.e., as a single-particle transition from one occupied ground-state orbital directly to a state in the continuum; see the following references for these and other examples [PBF+09, DKK+11, PRU+11, SWR+12, WHS+14, LUR+14, MGG+20, HLH+20, WRS+21].

For a test on a many-particle system, Pub. 5 focused on the semiconductor molecule PTCDA ($C_{24}H_8O_6$). The latter makes a natural choice, as it is an intensely studied system in the PES community [DMK^{+}06, MZS^{+}11, PRU^{+}11, DKK^{+}11, RABK11, SBKN12, KSRAB12, LUR^{+}14, MSH14, DGS^{+}16, PBW^{+}17, WRS^{+}21]. One reason for the interest in PTCDA is that it forms well-defined monolayer films on different surfaces (e.g., of Au, Ag, Cu), which allows very precise measurements [MTSH^{+}01, KKF^{+}11, MSS^{+}13, WHS^{+}14]. As mentioned above, this part of the study was also devised to reach an understanding how the many-particle character of an electronically excited system manifests itself in the photoemission in the real-time TDDFT description. For this purpose, considering a single PTCDA molecule in gas phase was a suitable choice since its first (dipole-allowed) excitation features the desired many-particle character, as a respective linear-response TDDFT calculation showed: From the perspective of linear-response TDDFT (cf. footnote 2), the first excitation of PTCDA corresponds to a superposition of predominantly three single-particle transitions from occupied orbitals to the lowest unoccupied molecular orbital (LUMO), LUMO+1, and LUMO+3. The real-time simulation of the pump-probe process for PTCDA followed the procedure described above, where the frequency of the pump field matched the first excitation energy in order to excite the system from the ground state. In the latter simulation, the many-particle character of the excited system was reflected by the ARPES spectra (KES, momentum map) showing contributions from more than one TDKS orbital. Figure 4.13 shows the ARPES momentum map corresponding to the pump-probe process for PTCDA: (a) The total map resulted from the detection of two wave packets that evolved from the (b) HOMO and (c) HOMO-9. In contrast, in previous real-time simulations of direct ARPES, only a single orbital contributed to individual peaks in the KES and the respective ARPES momentum map (except for degenerate orbitals) [DK16, DGS^{+}16].

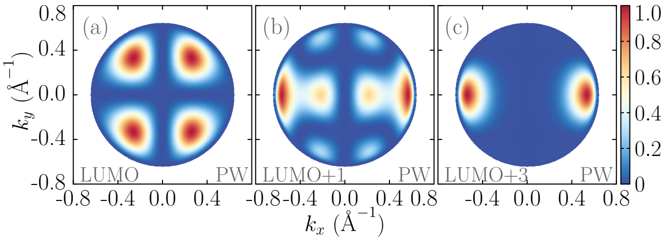

Figure 4.14: ARPES momentum maps obtained from the plane-wave (PW) approach evaluated at 1.54 eV for (a) LUMO, (b) LUMO+1, (c) and LUMO+3 of PTCDA. See main text and Pub. 5 for details.

It was also very insightful to revisit the pump-probe process from perspective of Casida's linear-response formalism to further understand the ARPES features seen in Fig. 4.13. From this viewpoint, the pump pulse leads to the first excitation of PTCDA that can be understood as a superposition of predominantly the LUMO, LUMO+1, and LUMO+3. The probe pulse subsequently causes the emission from that superposition. Following this picture, one would thus expect the total ARPES signal predominantly results from that of the above LUMO+X ($X = \{0, 1, 3\}$). As a straightforward step in this direction, I tested which ARPES signals result from each of the LUMO+X in the single-particle picture by computing the momentum maps from the plane-wave approach (cf. Eq. 4.3) depicted in Fig. 4.14. As a final result of Pub. 5, the comparison between Fig. 4.13(a) and Fig. 4.14 showed that the interpretation "emission from a superposition" is in qualitative agreement with the ARPES patterns that the real-time pump-probe simulation shows. Therefore, we concluded that, firstly, real-time propagation and linear-response theory offer complementary views on the same physical reality. Secondly, the ARPES pattern of one of the LUMO+X is not sufficient to interpret the total signal of the real-time simulation, underlining that the ARPES from the excited PTCDA molecule does not correspond to just one single-particle transition.

In conclusion, the TDDFT-based approach presented in Pub. 5 allows the simulation of pump-probe ARPES for molecular systems in real time and real space. The key elements, excitation, photoemission, and angle-resolved detection, are captured by a single simulation. I provided a proof of concept in the transparent one-electron limit showing that the ARPES signals from an excited one-electron system can be interpreted as the mapping of a previously unoccupied orbital. The pump-probe simulation for the PTCDA molecule in the gas phase revealed the many-body character of its (first) excitation in the corresponding ARPES observables, which showed contributions from two time-dependent orbitals. The photoemission from the excited PTCDA can be interpreted (qualitatively) as the mapping of a superposition of previously unoccupied orbitals. Overall, Pub. 5 contributed to the understanding of the real-time description of pump-probe processes based on TDDFT on a fundamental level. With a view to future applications, it appears worthwhile to analyze the adsorption of PTCDA on surfaces, i.e., the usual experimental ARPES setup (see above), in order to interpret experiments of the type recently put forward by Wallauer *et al.* [WRS+21]. The adsorption geometries necessary for a respective real-time simulation can typically be determined experimentally with reliable accuracy [Tau07, YKL+18, WKH+17].

List of Abbreviations

ωPBE	range-separated hybrid version of the PBE xc functional (cf. Eq. 3.12)	26
Ir-L0	$[\mathrm{Ir(bpy)(ppy)_2}]^+$ photosensitizer	34
Ir-L1	$[\mathrm{Ir(dmOHbpy)(ppy)_2}]^+$ photosensitizer	34
MIL-101	metal-organic framework MIL-101 [HFM$^+$12]	28
bpy	2,2'-bipyridine	34
dmOHbpy	2,2'-bipyridine-4,4'-diyldimethanol	34
ppy	2-phenylpyridine	34
ALDA	adiabatic LDA as defined in Eq. (3.5)	22
ARPES	angle-resolved photoemission spectroscopy	6
B3LYP	global hybrid version of the BLYP xc functional [Bec93, SDCF94], as defined in Eq. (3.10)	25
BLYP	Becke-Lee-Yang-Parr GGA xc functional [Bec88, LYP88]	22
BTDFT	DFT-based real-space pseudopotential code [Sch16, SK18]	12
CT	charge transfer, usually referring to excitations or excited states	25
DFA	density-functional approximation, typically to $E_{\mathrm{xc}}[n_\uparrow, n_\downarrow]$ (Eq. 3.1)	10
DFT	density-functional theory [HK64]	5
DOS	density of states	29
EXX	exact exchange functional, as defined in Eq. (3.7)	24
GGA	class of semilocal xc functionals that is based on a generalized-gradient approximation [PW86]	22
gKS	generalized Kohn-Sham scheme [SGV$^+$96, BK18]	24
HOMO	highest occupied molecular orbital	42

KES	kinetic-energy spectrum	38
KS	Kohn-Sham, usually referring to the KS formalism, orbitals, eigenvalues, potential, or equation [KS65]	8
LDA	local-density approximation xc functional [HK64]	21
LUMO	lowest unoccupied molecular orbital	43
MNP	metal nanoparticle, refers to an aggregate of a few to some hundreds or few thousands of metal atoms	4
MOF	metal-organic framework, often refers to the MIL-101 type	28
PBE	Perdew-Burke-Ernzerhof GGA xc functional [PBE96]	22
PBE0	global hybrid version of the PBE xc functional [AB99, ASB99], as defined in Eq. (3.9)	24
PES	photoemission spectroscopy	4
PTCDA	perylene-3,4,9,10-tetracarboxylic dianhydride or perylenetetracarboxylic dianhydride	6
QChem	quantum-chemistry code employing Gaussian basis sets [E^{+}21]	12
RSH	range-separated hybrid functionals	26
TDDFT	time-dependent DFT [RG84]	5
TDKS	time-dependent KS scheme, usually referring to the time-dependent KS orbitals, potential, or equation [RG84, vL98]	11
TEA	triethylamine	34
TURBOMOLE	quantum-chemistry code employing Gaussian basis sets [TUR19]	12
UV	ultraviolet region of the electromagnetic spectrum	4
Vis	visible region of the electromagnetic spectrum	4
xc	exchange-correlation	9

Bibliography

[A^+15] X. Andrade et al., *Real-space grids and the Octopus code as tools for the development of new simulation approaches for electronic systems*, Phys. Chem. Chem. Phys. **17**, 31371–31396 (2015).

[AACC$^+$15] Z. H. Al-Azri, W.-T. Chen, A. Chan, V. Jovic, T. Ina, H. Idriss and G. I. Waterhouse, *The roles of metal co-catalysts and reaction media in photocatalytic hydrogen production: Performance evaluation of M/TiO$_2$ photocatalysts (M=Pd, Pt, Au) in different alcohol-water mixtures*, J. Catal. **329**, 355–367 (2015).

[AB99] C. Adamo and V. Barone, *Toward reliable density functional methods without adjustable parameters: The PBE0 model*, J. Chem. Phys. **110**, 6158–6170 (1999).

[ABMR07] X. Andrade, S. Botti, M. A. L. Marques and A. Rubio, *Time-dependent density functional theory scheme for efficient calculations of dynamic (hyper)polarizabilities*, J. Chem. Phys. **126**, 184106 (2007).

[AEDB96] S. E. Apsel, J. W. Emmert, J. Deng and L. A. Bloomfield, *Surface-Enhanced Magnetism in Nickel Clusters*, Phys. Rev. Lett. **76**, 1441–1444 (1996).

[AF03] E. Aprà and A. Fortunelli, *Density-functional calculations on platinum nanoclusters: Pt$_{13}$, Pt$_{38}$, and Pt$_{55}$*, J. Phys. Chem. A **107**, 2934–2942 (2003).

[AHLT05] P. Arbenz, U. L. Hetmaniuk, R. B. Lehoucq and R. S. Tuminaro, *A comparison of eigensolvers for large-scale 3D modal analysis using AMG-preconditioned iterative methods*, Int. J. Numer. Methods Eng. **64**, 204–236 (2005).

[AHNH17] Y. A. Alhamdani, M. H. Hassim, R. T. Ng and M. Hurme, *The estimation of fugitive gas emissions from hydrogen production by natural gas steam reforming*, Int. J. Hydrogen Energy **42**, 9342–9351 (2017).

[AK19] T. Aschebrock and S. Kümmel, *Exploring local range separation: The role of spin scaling and one-electron self-interaction*, J. Chem. Phys. **151**, 154108 (2019).

[ALA05] D. Astruc, F. Lu and J. R. Aranzaes, *Nanoparticles as Recyclable Catalysts: The Frontier between Homogeneous and Heterogeneous Catalysis*, Angew. Chem. Int. Ed. **44**, 7852–7872 (2005).

[ARM16] D. M. Arias-Rotondo and J. K. McCusker, *The photophysics of photoredox catalysis: a roadmap for catalyst design*, Chem. Soc. Rev. **45**, 5803–5820 (2016).

[ASB99] C. Adamo, G. E. Scuseria and V. Barone, *Accurate excitation energies from time-dependent density functional theory: Assessing the PBE0 model*, J. Chem. Phys. **111**, 2889–2899 (1999).

[Ast20] D. Astruc, *Introduction: Nanoparticles in Catalysis*, Chem. Rev. **120**, 461–463 (2020).

[AT02] M. J. Allen and D. J. Tozer, *Helium dimer dispersion forces and correlation potentials in density functional theory*, J. Chem. Phys. **117**, 11113–11120 (2002).

[AvB85] C.-O. Almbladh and U. von Barth, *Exact results for the charge and spin densities, exchange-correlation potentials, and density-functional eigenvalues*, Phys. Rev. B **31**, 3231–3244 (1985).

[BAH$^+$20] F. P. Bonafé, B. Aradi, B. Hourahine, C. R. Medrano, F. J. Hernández, T. Frauenheim and C. G. Sánchez, *A Real-Time Time-Dependent Density Functional Tight-Binding Implementation for Semiclassical Excited State Electron-Nuclear Dynamics and Pump-Probe Spectroscopy Simulations*, J. Chem. Theory Comput. **16**, 4454–4469 (2020).

[BBK15] S. I. Bokarev, O. S. Bokareva and O. Kühn, *A theoretical perspective on charge transfer in photocatalysis. The example of Ir-based systems*, Coord. Chem. Rev. **304–305**, 133 – 145 (2015).

[BCA14] S. Bhattacharjee, C. Chen and W.-S. Ahn, *Chromium terephthalate metal–organic framework MIL-101: synthesis, functionalization, and applications for adsorption and catalysis*, RSC Adv. **4**, 52500–52525 (2014).

[BCG05] K. Burke, R. Car and R. Gebauer, *Density Functional Theory of the Electrical Conductivity of Molecular Devices*, Phys. Rev. Lett. **94**, 146803 (2005).

[BCV83] J. Boitiaux, J. Cosyns and S. Vasudevan, *Hydrogenation of highly unsaturated hydrocarbons over highly dispersed palladium catalyst: Part I: behaviour of small metal particles*, Applied Catalysis **6**, 41–51 (1983).

[Bec88] A. D. Becke, *Density-functional exchange-energy approximation with correct asymptotic behavior*, Phys. Rev. A **38**, 3098–3100 (1988).

[Bec93] A. D. Becke, *A new mixing of Hartree-Fock and local density-functional theories*, J. Chem. Phys. **98**, 1372–1377 (1993).

[Bel03] A. T. Bell, *The Impact of Nanoscience on Heterogeneous Catalysis*, Science **299**, 1688–1691 (2003).

[BGSK16] A. Bej, K. Ghosh, A. Sarkar and D. W. Knight, *Palladium nanoparticles in the catalysis of coupling reactions*, RSC Adv. **6**, 11446–11453 (2016).

[BGT18] J. L. Bao, L. Gagliardi and D. G. Truhlar, *Self-Interaction Error in Density Functional Theory: An Appraisal*, J. Phys. Chem. Lett. **9**, 2353–2358 (2018).

[BHP$^+$14] S. I. Bokarev, D. Hollmann, A. Pazidis, A. Neubauer, J. Radnik, O. Kühn, S. Lochbrunner, H. Junge, M. Beller and A. Brückner, *Spin density distribution after electron transfer from triethylamine to an [Ir(ppy)2(bpy)]+ photosensitizer during photocatalytic water reduction*, Phys. Chem. Chem. Phys. **16**, 4789–4796 (2014).

[BK18] R. Baer and L. Kronik, *Time-dependent generalized Kohn–Sham theory*, Eur. Phys. J. B **91**, 170 (2018).

[BKP$^+$81] E. Borgarello, J. Kiwi, E. Pelizzetti, M. Visca and M. Grätzel, *Photochemical cleavage of water by photocatalysis*, Nature **289**, 158–160 (1981).

[BLL16] A. Bruner, D. LaMaster and K. Lopata, *Accelerated Broadband Spectra Using Transition Dipole Decomposition and Padé Approximants*, J. Chem. Theory Comput. **12**, 3741–3750 (2016).

[BLS10] R. Baer, E. Livshits and U. Salzner, *Tuned Range-Separated Hybrids in Density Functional Theory*, Annu. Rev. Phys. Chem. **61**, 85–109 (2010).

[BMN$^+$17] O. S. Bokareva, T. Möhle, A. Neubauer, S. I. Bokarev, S. Lochbrunner and O. Kühn, *Chemical Tuning and Absorption Properties of Iridium Photosensitizers for Photocatalytic Applications*, Inorganics **5**, 23 (2017).

[BN05] R. Baer and D. Neuhauser, *Density Functional Theory with Correct Long-Range Asymptotic Behavior*, Phys. Rev. Lett. **94**, 043002 (2005).

[BO27] M. Born and R. Oppenheimer, *Zur Quantentheorie der Molekeln*, Ann. Phys. **389**, 457–484 (1927).

[BOF$^+$19] M. Borgwardt, S. T. Omelchenko, M. Favaro, P. Plate, C. Höhn, D. Abou-Ras, K. Schwarzburg, R. van de Krol, H. A. Atwater, N. S. Lewis, R. Eichberger and D. Friedrich, *Femtosecond time-resolved two-photon photoemission studies of ultrafast carrier relaxation in Cu_2O photoelectrodes*, Nat. Commun. **10**, 2106 (2019).

[BPM$^+$14] C. Battocchio, F. Porcaro, S. Mukherjee, E. Magnano, S. Nappini, I. Fratoddi, M. Quintiliani, M. V. Russo and G. Polzonetti, *Gold Nanoparticles Stabilized with Aromatic Thiols: Interaction at the Molecule–Metal Interface and Ligand Arrangement in the Molecular Shell Investigated by SR-XPS and NEXAFS*, J. Phys. Chem. C **118**, 8159–8168 (2014).

[BPW98] K. Burke, J. P. Perdew and Y. Wang, *Derivation of a Generalized Gradient Approximation: The PW91 Density Functional*, Electronic Density Functional Theory: Recent Progress and New Directions, Springer Boston , 81–111 (1998).

[BRP$^+$08] M. Bühl, C. Reimann, D. A. Pantazis, T. Bredow and F. Neese, *Geometries of Third-Row Transition-Metal Complexes from Density-Functional Theory*, J. Chem. Theory Comput. **4**, 1449–1459 (2008).

[BTB$^+$11] R. E. Blankenship, D. M. Tiede, J. Barber, G. W. Brudvig, G. Fleming, M. Ghirardi, M. R. Gunner, W. Junge, D. M. Kramer, A. Melis, T. A. Moore, C. C. Moser, D. G. Nocera, A. J. Nozik, D. R.

Ort, W. W. Parson, R. C. Prince and R. T. Sayre, *Comparing Photosynthetic and Photovoltaic Efficiencies and Recognizing the Potential for Improvement*, Science **332**, 805–809 (2011).

[CA80] D. M. Ceperley and B. J. Alder, *Ground State of the Electron Gas by a Stochastic Method*, Phys. Rev. Lett. **45**, 566–569 (1980).

[CAB08] E. D. Cline, S. E. Adamson and S. Bernhard, *Homogeneous Catalytic System for Photoinduced Hydrogen Production Utilizing Iridium and Rhodium Complexes*, Inorg. Chem. **47**, 10378–10388 (2008).

[Cas95] M. E. Casida, *Time-Dependent Density Functional Response Theory for Molecules*, Recent Advances in Density Functional Methods, World Scientific Singapur **1**, 155–192 (1995).

[Cas96] M. E. Casida, *Time-Dependent Density Functional Response Theory of Molecular Systems: Theory, Computational Methods, and Functionals*, Theoretical and Computational Chemistry, Elsevier Amsterdam **4**, 391–439 (1996).

[CBG17] E. Caldeweyher, C. Bannwarth and S. Grimme, *Extension of the D3 dispersion coefficient model*, J. Chem. Phys. **147**, 034112 (2017).

[CCW+19] V. Coropceanu, X.-K. Chen, T. Wang, Z. Zheng and J.-L. Brédas, *Charge-transfer electronic states in organic solar cells*, Nat. Rev. Mater **4**, 689–707 (2019).

[CEVV06] C.-L. Cheng, J. S. Evans and T. Van Voorhis, *Simulating molecular conductance using real-time density functional theory*, Phys. Rev. B **74**, 155112 (2006).

[CGGL11] J. Cabanillas-Gonzalez, G. Grancini and G. Lanzani, *Pump-Probe Spectroscopy in Organic Semiconductors: Monitoring Fundamental Processes of Relevance in Optoelectronics*, Adv. Mater. **23**, 5468–5485 (2011).

[CHG93] M. G. Colombo, A. Hauser and H. U. Guedel, *Evidence for strong mixing between the LC and MLCT excited states in bis(2-phenylpyridinato-C2,N')(2,2'-bipyridine)iridium(III)*, Inorg. Chem. **32**, 3088–3092 (1993).

[CHG09] J.-D. Chai and M. Head-Gordon, *Long-range corrected double-hybrid density functionals*, J. Chem. Phys. **131**, 174105 (2009).

[CJCS98] M. E. Casida, C. Jamorski, K. C. Casida and D. R. Salahub, *Molecular excitation energies to high-lying bound states from time-dependent density-functional response theory: Characterization and correction of the time-dependent local density approximation ionization threshold*, J. Chem. Phys. **108**, 4439–4449 (1998).

[CLAB94] A. J. Cox, J. G. Louderback, S. E. Apsel and L. A. Bloomfield, *Magnetism in 4d-transition metal clusters*, Phys. Rev. B **49**, 12295–12298 (1994).

[CMR04] A. Castro, M. A. L. Marques and A. Rubio, *Propagators for the time-dependent Kohn-Sham equations*, J. Chem. Phys. **121**, 3425–3433 (2004).

[CN96] J. Crank and P. Nicolson, *A practical method for numerical evaluation of solutions of partial differential equations of the heat-conduction type*, Adv. Comput. Math. **6**, 207–226 (1996).

[COD+16] J. Cook, N. Oreskes, P. T. Doran, W. R. L. Anderegg, B. Verheggen, E. W. Maibach, J. S. Carlton, S. Lewandowsky, A. G. Skuce, S. A. Green, D. Nuccitelli, P. Jacobs, M. Richardson, B. Winkler, R. Painting and K. Rice, *Consensus on consensus: a synthesis of consensus estimates on human-caused global warming*, Environ. Res. Lett. **11**, 048002 (2016).

[CPD17] A. S. Chaves, M. J. Piotrowski and J. L. Da Silva, *Evolution of the structural, energetic, and electronic properties of the 3d, 4d, and 5d transition-metal clusters (30 TM_n systems for $n = 2$-15): A density functional theory investigation*, Phys. Chem. Chem. Phys. **19**, 15484–15502 (2017).

[CQYJ+11] M. Crespo-Quesada, A. Yarulin, M. Jin, Y. Xia and L. Kiwi-Minsker, *Structure Sensitivity of Alkynol Hydrogenation on Shape- and Size-Controlled Palladium Nanocrystals: Which Sites Are Most Active and Selective?*, J. Am. Chem. Soc. **133**, 12787–12794 (2011).

[CRP+14] A. S. Chaves, G. G. Rondina, M. J. Piotrowski, P. Tereshchuk and J. L. Da Silva, *The role of charge states in the atomic structure of Cu_n and Pt_n ($n = 2$-14 atoms) clusters: A DFT investigation*, J. Phys. Chem. A **118**, 10813–10821 (2014).

[CRSU00] F. Calvayrac, P.-G. Reinhard, E. Suraud and C. Ullrich, *Nonlinear electron dynamics in metal clusters*, Phys. Rep. **337**, 493–578 (2000).

[CT09] C. J. Cramer and D. G. Truhlar, *Density functional theory for transition metals and transition metal chemistry*, Phys. Chem. Chem. Phys. **11**, 10757–10816 (2009).

[CTB+09] P. N. Curtin, L. L. Tinker, C. M. Burgess, E. D. Cline and S. Bernhard, *Structure-activity correlations among iridium(III) photosensitizers in a robust water-reducing system*, Inorg. Chem. **48**, 10498–10506 (2009).

[DAG15] A. Dhakshinamoorthy, A. M. Asiri and H. Garcia, *Metal–organic frameworks catalyzed C–C and C–heteroatom coupling reactions*, Chem. Soc. Rev. **44**, 1922–1947 (2015).

[DBB92] D. C. Douglass, J. P. Bucher and L. A. Bloomfield, *Magnetic studies of free nonferromagnetic clusters*, Phys. Rev. B **45**, 6341–6344 (1992).

[dBD11] M. da Graça Carvalho, M. Bonifacio and P. Dechamps, *Building a low carbon society*, Energy **36**, 1842–1847 (2011).

[DG01] F. Della Sala and A. Görling, *Efficient localized Hartree-Fock methods as effective exact-exchange Kohn-Sham methods for molecules*, J. Chem. Phys. **115**, 5718–5732 (2001).

[DGBC+13] U. De Giovannini, G. Brunetto, A. Castro, J. Walkenhorst and A. Rubio, *Simulating Pump-Probe Photoelectron and Absorption Spectroscopy on the Attosecond Timescale with Time-Dependent Density Functional Theory*, ChemPhysChem **14**, 1363–1376 (2013).

[DGHR17] U. De Giovannini, H. Hübener and A. Rubio, *A First-Principles Time-Dependent Density Functional Theory Framework for Spin and Time-Resolved Angular-Resolved Photoelectron Spectroscopy in Periodic Systems*, J. Chem. Theory Comput. **13**, 265–273 (2017).

[DGS+16] M. Dauth, M. Graus, I. Schelter, M. Wießner, A. Schöll, F. Reinert and S. Kümmel, *Perpendicular Emission, Dichroism, and Energy Dependence in Angle-Resolved Photoemission: The Importance of The Final State*, Phys. Rev. Lett. **117**, 183001 (2016).

[DGVM+12] U. De Giovannini, D. Varsano, M. A. L. Marques, H. Appel, E. K. U. Gross and A. Rubio, *Ab initio angle- and energy-resolved photoelectron spectroscopy with time-dependent density-functional theory*, Phys. Rev. A **85**, 062515 (2012).

[DHG04] A. Dreuw and M. Head-Gordon, *Failure of Time-Dependent Density Functional Theory for Long-Range Charge-Transfer Excited States: The Zincbacteriochlorin-Bacteriochlorin and Bacteriochlorophyll-Spheroidene Complexes*, J. Am. Chem. Soc. **126**, 4007–4016 (2004).

[DK16] M. Dauth and S. Kümmel, *Predicting photoemission intensities and angular distributions with real-time density-functional theory*, Phys. Rev. A **93**, 022502 (2016).

[DKK+11] M. Dauth, T. Körzdörfer, S. Kümmel, J. Ziroff, M. Wiessner, A. Schöll, F. Reinert, M. Arita and K. Shimada, *Orbital Density Reconstruction for Molecules*, Phys. Rev. Lett. **107**, 193002 (2011).

[DLC+20] C. Dong, Y. Li, D. Cheng, M. Zhang, J. Liu, Y.-G. Wang, D. Xiao and D. Ma, *Supported Metal Clusters: Fabrication and Application in Heterogeneous Catalysis*, ACS Catal. **10**, 11011–11045 (2020).

[DM77] J. E. Dennis, Jr. and J. J. Moré, *Quasi-Newton Methods, Motivation and Theory*, SIAM Rev. **19**, 46–89 (1977).

[DMC+21] S. DiLuzio, V. Mdluli, T. U. Connell, J. Lewis, V. VanBenschoten and S. Bernhard, *High-Throughput Screening and Automated Data-Driven Analysis of the Triplet Photophysical Properties of Structurally Diverse, Heteroleptic Iridium(III) Complexes*, J. Am. Chem. Soc. **143**, 1179–1194 (2021).

[DMK+06] N. Dori, M. Menon, L. Kilian, M. Sokolowski, L. Kronik and E. Umbach, *Valence electronic structure of gas-phase 3,4,9,10-perylene tetracarboxylic acid dianhydride: Experiment and theory*, Phys. Rev. B **73**, 195208 (2006).

[DMRS10] P. M. Dinh, J. Messud, P.-G. Reinhard and E. Suraud, *The self-interaction correction in the time domain*, J. Phys.: Conf. Ser. **248**, 012024 (2010).

[DWC$^+$17] G. Donati, A. Wildman, S. Caprasecca, D. B. Lingerfelt, F. Lipparini, B. Mennucci and X. Li, *Coupling Real-Time Time-Dependent Density Functional Theory with Polarizable Force Field*, J. Phys. Chem. Lett. **8**, 5283–5289 (2017).

[DWF$^+$14] M. Dauth, M. Wiessner, V. Feyer, A. Schöll, P. Puschnig, F. Reinert and S. Kümmel, New. J. Phys. **16**, 103005 (2014).

[E$^+$10] J. Enkovaara et al., *Electronic structure calculations with GPAW: a real-space implementation of the projector augmented-wave method*, J. Phys.: Condens. Matter **22**, 253202 (2010).

[E$^+$21] E. Epifanovsky et al., *Software for the frontiers of quantum chemistry: An overview of developments in the Q-Chem 5 package*, J. Chem. Phys. **155**, 084801 (2021).

[EBV$^+$21] H. Eidsvag, S. Bentouba, P. Vajeeston, S. Yohi and D. Velauthapillai, *TiO_2 as a Photocatalyst for Water Splitting–An Experimental and Theoretical Review*, Molecules **26** (2021).

[ED11] E. Engel and R. M. Dreizler, *Density Functional Theory: An Advanced Course*, Theoretical and Mathematical Physics, Springer Berlin Heidelberg (2011).

[Ein05] A. Einstein, *Über einen die Erzeugung und Verwandlung des Lichtes betreffenden heuristischen Gesichtspunkt*, Ann. Phys. **322**, 132–148 (1905).

[Eng03] E. Engel, *Orbital-Dependent Functionals for the Exchange-Correlation Energy: A Third Generation of Density Functionals*, Lecture Notes in Physics, Springer Berlin Heidelberg **620**, 56–122 (2003).

[EPD$^+$10] C. Evangelisti, N. Panziera, A. D'Alessio, L. Bertinetti, M. Botavina and G. Vitulli, *New monodispersed palladium nanoparticles stabilized by poly-(N-vinyl-2-pyrrolidone): Preparation, structural study and catalytic properties*, J. Catal. **272**, 246–252 (2010).

[EVVV09] J. S. Evans, O. A. Vydrov and T. Van Voorhis, *Exchange and correlation in molecular wire conductance: Nonlocality is the key*, J. Chem. Phys. **131**, 034106 (2009).

[FBB$^+$16] S. Fischer, O. S. Bokareva, E. Barsch, S. I. Bokarev, O. Kühn and R. Ludwig, *Mechanistic Study of Photocatalytic Hydrogen Generation with Simple Iron Carbonyls as Water Reduction Catalysts*, ChemCatChem **8**, 404–411 (2016).

[FBR12] B. Fresch, H.-G. Boyen and F. Remacle, *Magnetostructural effects in ligand stabilized Pd13 clusters: a density functional theory study.*, Nanoscale **4**, 4138–47 (2012).

[Fey39] R. P. Feynman, *Forces in Molecules*, Phys. Rev. **56**, 340–343 (1939).

[FHS$^+$15] D. M. Fabian, S. Hu, N. Singh, F. A. Houle, T. Hisatomi, K. Domen, F. E. Osterloh and S. Ardo, *Particle suspension reactors and materials for solar-driven water splitting*, Energy Environ. Sci. **8**, 2825–2850 (2015).

[FJTA11] P.-P. Fang, A. Jutand, Z.-Q. Tian and C. Amatore, *Au-Pd Core-Shell Nanoparticles Catalyze Suzuki-Miyaura Reactions in Water through Pd Leaching*, Angew. Chem. Int. Ed. **50**, 12184–12188 (2011).

[FMH05] T. Futschek, M. Marsman and J. Hafner, *Structural and magnetic isomers of small Pd and Rh clusters: anab initiodensity functional study*, J. Phys.: Condens. Matter **17**, 5927–5963 (2005).

[FR14] B. Fresch and F. Remacle, *Tuning the Properties of Pd Nanoclusters by Ligand Coatings: Electronic Structure Computations on Phosphine, Thiol, and Mixed Phosphine–Thiol Ligand Shells*, J. Phys. Chem. C **118**, 9790–9800 (2014).

[FRB$^+$14] S. M. Falke, C. A. Rozzi, D. Brida, M. Maiuri, M. Amato, E. Sommer, A. D. Sio, A. Rubio, G. Cerullo, E. Molinari and C. Lienau, *Coherent ultrafast charge transfer in an organic photovoltaic blend*, Science **344**, 1001–1005 (2014).

[GAEK10] S. Grimme, J. Antony, S. Ehrlich and H. Krieg, *A consistent and accurate ab initio parametrization of density functional dispersion correction (DFT-D) for the 94 elements H-Pu*, J. Chem. Phys. **132**, 154104 (2010).

[GAP96] P. M. W. Gill, R. D. Adamson and J. A. Pople, *Coulomb-attenuated exchange energy density functionals*, Mol. Phys. **88**, 1005–1009 (1996).

[GBS$^+$19] D. Gielen, F. Boshell, D. Saygin, M. D. Bazilian, N. Wagner and R. Gorini, *The role of renewable energy in the global energy transformation*, Energy Strategy Reviews **24**, 38–50 (2019).

[GCKLiX14] J. Gascon, A. Corma, F. Kapteijn and F. X. Llabrés i Xamena, *Metal Organic Framework Catalysis: Quo vadis?*, ACS Catal. **4**, 361–378 (2014).

[GD88] S. K. Ghosh and A. K. Dhara, *Density-functional theory of many-electron systems subjected to time-dependent electric and magnetic fields*, Phys. Rev. A **38**, 1149–1158 (1988).

[GD13] F. Gygi and I. Duchemin, *Efficient Computation of Hartree–Fock Exchange Using Recursive Subspace Bisection*, J. Chem. Theory Comput. **9**, 582–587 (2013).

[GDAJ19] A. Granja-DelRío, H. A. Abdulhussein and R. L. Johnston, *DFT-Based Global Optimization of Sub-nanometer Ni–Pd Clusters*, J. Phys. Chem. C **123**, 26583–26596 (2019).

[GDL+12] F. Gärtner, S. Denurra, S. Losse, A. Neubauer, A. Boddien, A. Gopinathan, A. Spannenberg, H. Junge, S. Lochbrunner, M. Blug, S. Hoch, J. Busse, S. Gladiali and M. Beller, *Synthesis and characterization of new iridium photosensitizers for catalytic hydrogen generation from water*, Chem.–Eur. J. **18**, 3220–3225 (2012).

[GFSDK17] B. C. Gates, M. Flytzani-Stephanopoulos, D. A. Dixon and A. Katz, *Atomically dispersed supported metal catalysts: perspectives and suggestions for future research*, Catal. Sci. Technol. **7**, 4259–4275 (2017).

[GHL+05] J. I. Goldsmith, W. R. Hudson, M. S. Lowry, T. H. Anderson and S. Bernhard, *Discovery and high-throughput screening of heteroleptic iridium complexes for photoinduced hydrogen production*, J. Am. Chem. Soc. **127**, 7502–7510 (2005).

[GHSS21] J. M. Garcia, L. F. Heald, R. E. Shaffer and S. G. Sayres, *Oscillation in Excited State Lifetimes with Size of Sub-nanometer Neutral (TiO_2)n Clusters Observed with Ultrafast Pump–Probe Spectroscopy*, J. Phys. Chem. Lett. **12**, 4098–4103 (2021).

[GKZC04] M. Griebel, S. Knapek, G. Zumbusch and A. Caglar, *Von der Schrödingergleichung zur Moleküldynamik*, Numerische Simulation in der Moleküldynamik: Numerik, Algorithmen, Parallelisierung, Anwendungen, Springer Berlin Heidelberg , 17–37 (2004).

[Gri04] S. Grimme, *Accurate description of van der Waals complexes by density functional theory including empirical corrections*, J. Comput. Chem. **25**, 1463–1473 (2004).

[Gri11] S. Grimme, *Density functional theory with London dispersion corrections*, WIREs Comput. Mol. Sci. **1**, 211–228 (2011).

[GSS+09] F. Gärtner, B. Sundararaju, A.-E. Surkus, A. Boddien, B. Loges, H. Junge, P. Dixneuf and M. Beller, *Light-Driven Hydrogen Generation: Efficient Iron-Based Water Reduction Catalysts*, Angew. Chem. Int. Ed. **48**, 9962–9965 (2009).

[GZL+22] M. Guo, M. Zhang, R. Liu, X. Zhang and G. Li, *State-of-the-Art Advancements in Photocatalytic Hydrogenation: Reaction Mechanism and Recent Progress in Metal-Organic Framework (MOF)-Based Catalysts*, Adv. Sci. **9**, 2103361 (2022).

[Har06] J. N. Harvey, *On the accuracy of density functional theory in transition metal chemistry*, Annu. Rep. Prog. Chem., Sect. C: Phys. Chem. **102**, 203–226 (2006).

[HBM16] R. Haunschild, A. Barth and W. Marx, *Evolution of DFT studies in view of a scientometric perspective*, J. Cheminf. **8**, 52 (2016).

[HCTC07] J. Heslar, J. Carrera, D. Telnov and S.-I. Chu, *High-order harmonic generation of heteronuclear diatomic molecules in intense ultrashort laser fields: An all-electron TDDFT study*, Int. J. Quantum Chem. **107**, 3159–3168 (2007).

[HFM+12] J. Hermannsdörfer, M. Friedrich, N. Miyajima, R. Q. Albuquerque, S. Kümmel and R. Kempe, *Ni/Pd@MIL-101: Synergistic Catalysis with Cavity-Conform Ni/Pd Nanoparticles*, Angew. Chem. Int. Ed. **51**, 11473–11477 (2012).

[HHG99] S. Hirata and M. Head-Gordon, *Time-dependent density functional theory within the Tamm-Dancoff approximation*, Chem. Phys. Lett. **314**, 291–299 (1999).

[Hil13] J. G. Hill, *Gaussian basis sets for molecular applications*, Int. J. Quantum Chem. **113**, 21–34 (2013).

[HJS08] T. M. Henderson, B. G. Janesko and G. E. Scuseria, *Generalized gradient approximation model exchange holes for range-separated hybrids*, J. Chem. Phys. **128**, 194105 (2008).

[HK64] P. Hohenberg and W. Kohn, *The Inhomogeneous Electron Gas*, Phys. Rev. **136**, B864–B871 (1964).

[HLH+20] N. Haag, D. Lüftner, F. Haag, J. Seidel, L. L. Kelly, G. Zamborlini, M. Jugovac, V. Feyer, M. Aeschlimann, P. Puschnig, M. Cinchetti and B. Stadtmüller, *Signatures of an atomic crystal in the band structure of a* C_{60} *thin film*, Phys. Rev. B **101**, 165422 (2020).

[Hoo85] W. G. Hoover, *Canonical dynamics: Equilibrium phase-space distributions*, Phys. Rev. A **31**, 1695–1697 (1985).

[HS05] H. P. Hratchian and H. B. Schlegel, *Finding minima, transition states, and following reaction pathways on ab initio potential energy surfaces*, Theory and Applications of Computational Chemistry, Elsevier Amsterdam , 195–249 (2005).

[HSK18] F. Hofmann, I. Schelter and S. Kümmel, *Linear response time-dependent density functional theory without unoccupied states: The Kohn-Sham-Sternheimer scheme revisited*, J. Chem. Phys. **149**, 024105 (2018).

[HSS+20] K. Hong, M. Sajjadi, J. M. Suh, K. Zhang, M. Nasrollahzadeh, H. W. Jang, R. S. Varma and M. Shokouhimehr, *Palladium Nanoparticles on Assorted Nanostructured Supports: Applications for Suzuki, Heck, and Sonogashira Cross-Coupling Reactions*, ACS Appl. Nano Mater. **3**, 2070–2103 (2020).

[HVR21] G. Habibullah, J. Viktorova and T. Ruml, *Current Strategies for Noble Metal Nanoparticle Synthesis*, Nanoscale Res. Lett. **16**, 47 (2021).

[HZG+18] L. Hou, M. Zhang, Z. Guan, Q. Li and J. Yang, *Effect of platinum dispersion on photocatalytic performance of Pt-*TiO_2, J. Nanopart. Res. **20**, 60 (2018).

[Hü03] S. Hüfner, *Photoelectron Spectroscopy: Principles and Applications*, Advanced Texts in Physics, Springer Berlin Heidelberg (2003).

[INAH08] T. Ishida, M. Nagaoka, T. Akita and M. Haruta, *Deposition of Gold Clusters on Porous Coordination Polymers by Solid Grinding and Their Catalytic Activity in Aerobic Oxidation of Alcohols*, Chem.–Eur. J. **14**, 8456–8460 (2008).

[ISS+07] A. F. Izmaylov, V. N. Staroverov, G. E. Scuseria, E. R. Davidson, G. Stoltz and E. Cancès, *The effective local potential method: Implementation for molecules and relation to approximate optimized effective potential techniques*, J. Chem. Phys. **126**, 084107 (2007).

[ITYH01] H. Iikura, T. Tsuneda, T. Yanai and K. Hirao, *A long-range correction scheme for generalized-gradient-approximation exchange functionals*, J. Chem. Phys. **115**, 3540–3544 (2001).

[JCH21] H. Jung, S. Choung and J. W. Han, *Design principles of noble metal-free electrocatalysts for hydrogen production in alkaline media: combining theory and experiment*, Nanoscale Adv. **3**, 6797–6826 (2021).

[JDB15] D. Jacquemin, I. Duchemin and X. Blase, *0–0 Energies Using Hybrid Schemes: Benchmarks of TD-DFT, CIS(D), ADC(2), CC2, and BSE/GW formalisms for 80 Real-Life Compounds*, J. Chem. Theory Comput. **11**, 5340–5359 (2015).

[JMP+14] D. Jacquemin, B. Moore, A. Planchat, C. Adamo and J. Autschbach, *Performance of an Optimally Tuned Range-Separated Hybrid Functional for 0–0 Electronic Excitation Energies*, J. Chem. Theory Comput. **10**, 1677–1685 (2014).

[JSB+16] J. Jia, L. C. Seitz, J. D. Benck, Y. Huo, Y. Chen, J. W. D. Ng, T. Bilir, J. S. Harris and T. F. Jaramillo, *Solar water splitting by photovoltaic-electrolysis with a solar-to-hydrogen efficiency over 30%*, Nat. Commun. **7**, 13237 (2016).

[JSFL+17] S. R. Jensen, S. Saha, J. A. Flores-Livas, W. Huhn, V. Blum, S. Goedecker and L. Frediani, *The Elephant in the Room of Density Functional Theory Calculations*, J. Phys. Chem. Lett. **8**, 1449–1457 (2017).

[JSL19] J. Jornet-Somoza and I. Lebedeva, *Real-Time Propagation TDDFT and Density Analysis for Exciton Coupling Calculations in Large Systems*, J. Chem. Theory Comput. **15**, 3743–3754 (2019).

[JWPA09] D. Jacquemin, V. Wathelet, E. A. Perpète and C. Adamo, *Extensive TD-DFT Benchmark: Singlet-Excited States of Organic Molecules*, J. Chem. Theory Comput. **5**, 2420–2435 (2009).

[Kam12] P. V. Kamat, *Manipulation of Charge Transfer Across Semiconductor Interface. A Criterion That Cannot Be Ignored in Photocatalyst Design*, J. Phys. Chem. Lett. **3**, 663–672 (2012).

[KCBC08] M. Koentopp, C. Chang, K. Burke and R. Car, *Density functional calculations of nanoscale conductance*, J. Phys.: Condens. Matter **20**, 083203 (2008).

[KCO$^+$11] A. M. Köster, P. Calaminici, E. Orgaz, D. R. Roy, J. U. Reveles and S. N. Khanna, *On the ground state of Pd_{13}*, J. Am. Chem. Soc. **133**, 12192–12196 (2011).

[KHKP02] K. Köhler, R. G. Heidenreich, J. G. E. Krauter and J. Pietsch, *Highly Active Palladium/Activated Carbon Catalysts for Heck Reactions: Correlation of Activity, Catalyst Properties, and Pd Leaching*, Chem.–Eur. J. **8**, 622–631 (2002).

[KK00] A. Kudo and H. Kato, *Effect of lanthanide-doping into $NaTaO_3$ photocatalysts for efficient water splitting*, Chem. Phys. Lett. **331**, 373–377 (2000).

[KK08] S. Kümmel and L. Kronik, *Orbital-dependent density functionals: Theory and applications*, Rev. Mod. Phys. **80**, 3–60 (2008).

[KK18] L. Kronik and S. Kümmel, *Dielectric Screening Meets Optimally Tuned Density Functionals*, Adv. Mater. , 1706560 (2018).

[KK20] L. Kronik and S. Kümmel, *Piecewise linearity, freedom from self-interaction, and a Coulomb asymptotic potential: three related yet inequivalent properties of the exact density functional*, Phys. Chem. Chem. Phys. **22**, 16467–16481 (2020).

[KKF$^+$11] H. Karacuban, S. Koch, M. Fendrich, T. Wagner and R. Möller, *PTCDA on Cu(111) partially covered with NaCl*, **22**, 295305 (2011).

[KKG78] K. Kalyanasundaram, J. Kiwi and M. Grätzel, *Hydrogen Evolution from Water by Visible Light, a Homogeneous Three Component Test System for Redox Catalysis*, Helv. Chim. Acta **61**, 2720–2730 (1978).

[KKT04] A. Kudo, H. Kato and I. Tsuji, *Strategies for the Development of Visible-light-driven Photocatalysts for Water Splitting*, Chem. Lett. **33**, 1534–1539 (2004).

[KLI92a] J. B. Krieger, Y. Li and G. J. Iafrate, *Construction and application of an accurate local spin-polarized Kohn-Sham potential with integer discontinuity: Exchange-only theory*, Phys. Rev. A **45**, 101–126 (1992).

[KLI92b] J. B. Krieger, Y. Li and G. J. Iafrate, *Systematic approximations to the optimized effective potential: Application to orbital-density-functional theory*, Phys. Rev. A **46**, 5453–5458 (1992).

[KLS79] M. Kirch, J.-M. Lehn and J.-P. Sauvage, *Hydrogen Generation by Visible Light Irradiation of Aqueous Solutions of Metal Complexes. An approach to the photochemical conversion and storage of solar energy*, Helv. Chim. Acta **62**, 1345–1384 (1979).

[KLW$^+$12] J. Kaiser, L. Leppert, H. Welz, F. Polzer, S. Wunder, N. Wanderka, M. Albrecht, T. Lunkenbein, J. Breu, S. Kümmel, Y. Lu and M. Ballauff, *Catalytic activity of nanoalloys from gold and palladium*, Phys. Chem. Chem. Phys. **14**, 6487–6495 (2012).

[KM12] J. Klimeš and A. Michaelides, *Perspective: Advances and challenges in treating van der Waals dispersion forces in density functional theory*, J. Chem. Phys. **137**, 120901 (2012).

[KMT$^+$06] L. Kronik, A. Makmal, M. L. Tiago, M. M. G. Alemany, M. Jain, X. Huang, Y. Saad and J. R. Chelikowsky, *PARSEC - The pseudopotential algorithm for real-space electronic structure calculations: Recent advances and novel applications to nano-structures*, Phys. Status Solidi Basic Res. **243**, 1063–1079 (2006).

[Kni02] M. B. Knickelbein, *Nickel clusters: The influence of adsorbates on magnetic moments*, J. Chem. Phys. **116**, 9703–9711 (2002).

[KNTK13] A. Karolewski, A. Neubig, M. Thelakkat and S. Kümmel, *Optical absorption in donor-acceptor polymers – alternating vs. random*, Phys. Chem. Chem. Phys. **15**, 20016–20025 (2013).

[Koh99] W. Kohn, *Nobel Lecture: Electronic structure of matter¯wave functions and density functionals*, Rev. Mod. Phys. **71**, 1253–1266 (1999).

[KP03] S. Kümmel and J. P. Perdew, *Simple Iterative Construction of the Optimized Effective Potential for Orbital Functionals, Including Exact Exchange*, Phys. Rev. Lett. **90**, 043004 (2003).

[KS65] W. Kohn and L. J. Sham, *Self-consistent equations including exchange and correlation effects*, Phys. Rev. **140**, A1133–A1138 (1965).

[KS93] A. Klamt and G. Schüürmann, *COSMO: a new approach to dielectric screening in solvents with explicit expressions for the screening energy and its gradient*, J. Chem. Soc., Perkin Trans. 2 , 799–805 (1993).

[KSBK11] A. Karolewski, T. Stein, R. Baer and S. Kümmel, *Communication: Tailoring the optical gap in light-harvesting molecules*, J. Chem. Phys. **134**, 151101 (2011).

[KSRAB12] L. Kronik, T. Stein, S. Refaely-Abramson and R. Baer, *Excitation Gaps of Finite-Sized Systems from Optimally Tuned Range-Separated Hybrid Functionals*, J. Chem. Theory Comput. **8**, 1515–1531 (2012).

[KW87] K. A. King and R. J. Watts, *Dual emission from an ortho-metalated iridium(III) complex*, J. Am. Chem. Soc. **109**, 1589–1590 (1987).

[Kü17] S. Kümmel, *Charge-Transfer Excitations: A Challenge for Time-Dependent Density Functional Theory That Has Been Met*, Adv. Energy Mater. **7**, 1700440 (2017).

[LB07] E. Livshits and R. Baer, *A well-tempered density functional theory of electrons in molecules*, Phys. Chem. Chem. Phys. **9**, 2932–2941 (2007).

[LC18] L. Liu and A. Corma, *Metal Catalysts for Heterogeneous Catalysis: From Single Atoms to Nanoclusters and Nanoparticles*, Chem. Rev. **118**, 4981–5079 (2018).

[LCL11] W. Liang, C. T. Chapman and X. Li, *Efficient first-principles electronic dynamics*, J. Chem. Phys. **134**, 184102 (2011).

[LDM$^+$01] S. Lamansky, P. Djurovich, D. Murphy, F. Abdel-Razzaq, H.-E. Lee, C. Adachi, P. E. Burrows, S. R. Forrest and M. E. Thompson, *Highly Phosphorescent Bis-Cyclometalated Iridium Complexes:FIXMESynthesis, Photophysical Characterization, and Use in Organic Light Emitting Diodes*, J. Am. Chem. Soc. **123**, 4304–4312 (2001).

[Lee98] K. Lee, *Possible magnetism in small palladium clusters*, Phys. Rev. B **58**, 2391–2394 (1998).

[Lep13] L. Leppert, *Structural and electronic properties of transition metal nanoalloys and magnetic compounds*, Doctoral thesis, University of Bayreuth, 2013.

[Lev79] M. Levy, *Universal variational functionals of electron densities, first-order density matrices, and natural spin-orbitals and solution of the v-representability problem*, Proc. Natl. Acad. Sci. **76**, 6062–6065 (1979).

[Lev82] M. Levy, *Electron densities in search of Hamiltonians*, Phys. Rev. A **26**, 1200–1208 (1982).

[LFM16] K. Luo, J. I. Fuks and N. T. Maitra, *Studies of spuriously shifting resonances in time-dependent density functional theory*, J. Chem. Phys. **145**, 044101 (2016).

[LG11] K. Lopata and N. Govind, *Modeling Fast Electron Dynamics with Real-Time Time-Dependent Density Functional Theory: Application to Small Molecules and Chromophores*, J. Chem. Theory Comput. **7**, 1344–1355 (2011).

[LGC20] X. Li, Y. Guo and H. Cao, *Nanostructured surfaces from ligand-protected metal nanoparticles*, Dalton Trans. **49**, 14314–14319 (2020).

[LGI$^+$20] X. Li, N. Govind, C. Isborn, A. E. DePrince and K. Lopata, *Real-Time Time-Dependent Electronic Structure Theory*, Chem. Rev. **120**, 9951–9993 (2020).

[LHL$^+$14] A. Langenberg, K. Hirsch, A. Ławicki, V. Zamudio-Bayer, M. Niemeyer, P. Chmiela, B. Langbehn, A. Terasaki, B. v. Issendorff and J. T. Lau, *Spin and orbital magnetic moments of size-selected iron, cobalt, and nickel clusters*, Phys. Rev. B **90**, 184420 (2014).

[Lie83] E. H. Lieb, *Density functionals for coulomb systems*, Int. J. Quantum Chem. **24**, 243–277 (1983).

[LK11] L. Leppert and S. Kümmel, *The Electronic Structure of Gold–Platinum Nanoparticles: Collecting Clues for Why They Are Special*, J. Phys. Chem. C **115**, 6694–6702 (2011).

[LKK15] L. Leppert, R. Kempe and S. Kümmel, *Hydrogen binding energies and electronic structure of Ni-Pd particles: a clue to their special catalytic properties*, Phys. Chem. Chem. Phys. **17**, 26140–26148 (2015).

[LN06] N. S. Lewis and D. G. Nocera, *Powering the planet: Chemical challenges in solar energy utilization*, Proc. Natl. Acad. Sci. **103**, 15729–15735 (2006).

[LPOMRMC13] A. Leyva-Pérez, J. Oliver-Meseguer, P. Rubio-Marqués and A. Corma, *Water-Stabilized Three- and Four-Atom Palladium Clusters as Highly Active Catalytic Species in Ligand-Free C-C Cross-Coupling Reactions*, Angew. Chem. Int. Ed. **52**, 11554–11559 (2013).

[LPS84] M. Levy, J. P. Perdew and V. Sahni, *Exact differential equation for the density and ionization energy of a many-particle system*, Phys. Rev. A **30**, 2745–2748 (1984).

[LSFH18] J.-X. Liu, Y. Su, I. A. W. Filot and E. J. M. Hensen, *A Linear Scaling Relation for CO Oxidation on CeO_2-Supported Pd*, J. Am. Chem. Soc. **140**, 4580–4587 (2018).

[LSWS97] T. Leininger, H. Stoll, H.-J. Werner and A. Savin, *Combining long-range configuration interaction with short-range density functionals*, Chem. Phys. Lett. **275**, 151 – 160 (1997).

[LUR+14] D. Lüftner, T. Ules, E. M. Reinisch, G. Koller, S. Soubatch, F. S. Tautz, M. G. Ramsey and P. Puschnig, *Imaging the wave functions of adsorbed molecules*, Proc. Natl. Acad. Sci. **111**, 605–610 (2014).

[LVCAPA21] A. Luna-Valenzuela, J. L. Cabellos, J. A. Alonso and A. Posada-Amarillas, *Effects of van der Waals interactions on the structure and stability of $Cu_{8-x}Pd_x$ ($x = 0, 4, 8$) cluster isomers*, Mater. Today Commun. **26**, 102024 (2021).

[LYP88] C. Lee, W. Yang and R. G. Parr, *Development of the Colle-Salvetti correlation-energy formula into a functional of the electron density*, Phys. Rev. B **37**, 785–789 (1988).

[Mai05] N. T. Maitra, *Undoing static correlation: Long-range charge transfer in time-dependent density-functional theory*, J. Chem. Phys. **122**, 234104 (2005).

[Mai16] N. T. Maitra, *Perspective: Fundamental aspects of time-dependent density functional theory*, J. Chem. Phys. **144**, 220901 (2016).

[Mai17] N. T. Maitra, *Charge transfer in time-dependent density functional theory*, Journal of Physics: Condensed Matter **29**, 423001 (2017).

[MB10] S. Metz and S. Bernhard, *Robust photocatalytic water reduction with cyclometalated Ir(iii) 4-vinyl-2,2'-bipyridine complexes*, Chem. Commun. **46**, 7551–7553 (2010).

[MBBU18] A. Mohamadzade, S. Bai, M. Barbatti and S. Ullrich, *Intersystem crossing dynamics in singly substituted thiouracil studied by time-resolved photoelectron spectroscopy: Micro-environmental effects due to sulfur position*, Chem. Phys. **515**, 572–579 (2018).

[MCBR03] M. A. L. Marques, A. Castro, G. F. Bertsch and A. Rubio, *octopus: a first-principles tool for excited electron-ion dynamics*, Comput. Phys. Commun. **151**, 60–78 (2003).

[MD10] K. Maeda and K. Domen, *Photocatalytic Water Splitting: Recent Progress and Future Challenges*, J. Phys. Chem. Lett. **1**, 2655–2661 (2010).

[MGG+20] C. Metzger, M. Graus, M. Grimm, G. Zamborlini, V. Feyer, M. Schwendt, D. Lüftner, P. Puschnig, A. Schöll and F. Reinert, *Plane-wave final state for photoemission from nonplanar molecules at a metal-organic interface*, Phys. Rev. B **101**, 165421 (2020).

[MH00] D. Marx and J. Hutter, *Ab initio molecular dynamics: Theory and Implementation*, Modern methods and algorithms of quantum chemistry, NIC series, John-von-Neumann-Institut for Computing, Jülich **1**, 562–611 (2000).

[MHBL01] M. Moseler, H. Häkkinen, R. N. Barnett and U. Landman, *Structure and Magnetism of Neutral and Anionic Palladium Clusters*, Phys. Rev. Lett. **86**, 2545–2548 (2001).

[MHG17] N. Mardirossian and M. Head-Gordon, *Thirty years of density functional theory in computational chemistry: an overview and extensive assessment of 200 density functionals*, Mol. Phys. **115**, 2315–2372 (2017).

[MIA+11] T. Z. Markus, S. Itzhakov, Y. I. Alkotzer, D. Cahen, G. Hodes, D. Oron and R. Naaman, *Energetics of CdSe Quantum Dots Adsorbed on TiO_2*, J. Phys. Chem. C **115**, 13236–13241 (2011).

[MK07] M. Mundt and S. Kümmel, *Photoelectron spectra of anionic sodium clusters from time-dependent density-functional theory in real time*, Phys. Rev. B **76**, 035413 (2007).

[MK08] S. Meng and E. Kaxiras, *Real-time, local basis-set implementation of time-dependent density functional theory for excited state dynamics simulations*, J. Chem. Phys. **129**, 054110 (2008).

[MMDJ+17] M. K. L. Man, A. Margiolakis, S. Deckoff-Jones, T. Harada, E. L. Wong, M. B. M. Krishna, J. Madéo, A. Winchester, S. Lei, R. Vajtai, P. M. Ajayan and K. M. Dani, *Imaging the motion of electrons across semiconductor heterojunctions*, Nat. Nanotechnol. **12**, 36–40 (2017).

[MMN+12] M. A. L. Marques, N. T. Maitra, F. Nogueira, E. K. U. Gross and A. Rubio, *Fundamentals of Time-Dependent Density Functional Theory*, Lecture Notes in Physics, Springer Berlin Heidelberg **837** (2012).

[MP20] P. Morgante and R. Peverati, *The devil in the details: A tutorial review on some undervalued aspects of density functional theory calculations*, Int. J. Quantum Chem. **120**, e26332 (2020).

[MPBM19] J. A. Milligan, J. P. Phelan, S. O. Badir and G. A. Molander, *Alkyl Carbon-Carbon Bond Formation by Nickel/Photoredox Cross-Coupling*, Angew. Chem. Int. Ed. **58**, 6152–6163 (2019).

[MPSK08] M. Marsman, J. Paier, A. Stroppa and G. Kresse, *Hybrid functionals applied to extended systems*, J. Phys.: Condens. Matter **20**, 064201 (2008).

[MS13] J. H. Mokkath and U. Schwingenschlögl, *Tuning the chemical activity through PtAu nanoalloying: a first principles study*, J. Mater. Chem. A **1**, 9885–9888 (2013).

[MSH14] M. Marks, A. Schöll and U. Höfer, *Formation of metal-organic interface states studied with 2PPE*, J. Electron Spectrosc. Relat. Phenom. **195**, 263–271 (2014).

[MSM+12] D. Mongin, E. Shaviv, P. Maioli, A. Crut, U. Banin, N. Del Fatti and F. Vallée, *Ultrafast Photoinduced Charge Separation in Metal-Semiconductor Nanohybrids*, ACS Nano **6**, 7034–7043 (2012).

[MSS12] S. Mekhilef, R. Saidur and A. Safari, *Comparative study of different fuel cell technologies*, Renew. Sustain. Energy Rev. **16**, 981–989 (2012).

[MSS+13] M. Marks, S. Sachs, C. H. Schwalb, A. Schöll and U. Höfer, *Electronic structure and excited state dynamics in optically excited PTCDA films investigated with two-photon photoemission*, J. Chem. Phys. **139**, 124701 (2013).

[MSS20] C. Müller, M. Sharma and M. Sierka, *Real-time time-dependent density functional theory using density fitting and the continuous fast multipole method*, J. Comput. Chem. **41**, 2573–2582 (2020).

[MTSH+01] S. Mannsfeld, M. Toerker, T. Schmitz-Hübsch, F. Sellam, T. Fritz and K. Leo, *Combined LEED and STM study of PTCDA growth on reconstructed Au(111) and Au(100) single crystals*, Org. Electron. **2**, 121–134 (2001).

[MTvW+15] J. Meyer, M. Tombers, C. van Wúllen, G. Niedner-Schatteburg, S. Peredkov, W. Eberhardt, M. Neeb, S. Palutke, M. Martins and W. Wurth, *The spin and orbital contributions to the total magnetic moments of free Fe, Co, and Ni clusters*, J. Chem. Phys. **143**, 104302 (2015).

[MU20] A. Mohamadzade and S. Ullrich, *Internal conversion and intersystem crossing dynamics of uracil upon double thionation: a time-resolved photoelectron spectroscopy study in the gas phase*, Phys. Chem. Chem. Phys. **22**, 15608–15615 (2020).

[MVL03] C. Moler and C. Van Loan, *Nineteen Dubious Ways to Compute the Exponential of a Matrix, Twenty-Five Years Later*, SIAM Rev. **45**, 3–49 (2003).

[MXNY06] L. D. Menard, F. Xu, R. G. Nuzzo and J. C. Yang, *Preparation of TiO_2-supported Au nanoparticle catalysts from a Au_{13} cluster precursor: Ligand removal using ozone exposure versus a rapid thermal treatment*, J. Catal. **243**, 64–73 (2006).

[MZCB04] N. T. Maitra, F. Zhang, R. J. Cave and K. Burke, *Double excitations within time-dependent density functional theory linear response*, J. Chem. Phys. **120**, 5932–5937 (2004).

[MZS+11] M. Marks, N. L. Zaitsev, B. Schmidt, C. H. Schwalb, A. Schöll, I. A. Nechaev, P. M. Echenique, E. V. Chulkov and U. Höfer, *Energy shift and wave function overlap of metal-organic interface states*, Phys. Rev. B **84**, 081301 (2011).

[NES05] R. Narayanan and M. A. El-Sayed, *Catalysis with Transition Metal Nanoparticles in Colloidal Solution: Nanoparticle Shape Dependence and Stability*, J. Phys. Chem. B **109**, 12663–12676 (2005).

[NGF$^+$14] A. Neubauer, G. Grell, A. Friedrich, S. I. Bokarev, P. Schwarzbach, F. Gärtner, A. E. Surkus, H. Junge, M. Beller, O. Kühn and S. Lochbrunner, *Electron- and energy-transfer processes in a photocatalytic system based on an Ir(III)-photosensitizer and an iron catalyst*, J. Phys. Chem. Lett. **5**, 1355–1360 (2014).

[NKZI21] M. A. Nadeem, M. A. Khan, A. A. Ziani and H. Idriss, *An Overview of the Photocatalytic Water Splitting over Suspended Particles*, Catalysts **11** (2021).

[Nos84] S. Nosé, *A unified formulation of the constant temperature molecular dynamics methods*, J. Chem. Phys. **81**, 511–519 (1984).

[NPZ$^+$12] Z. Niu, Q. Peng, Z. Zhuang, W. He and Y. Li, *Evidence of an Oxidative-Addition-Promoted Pd-Leaching Mechanism in the Suzuki Reaction by Using a Pd-Nanostructure Design*, Chem.–Eur. J. **18**, 9813–9817 (2012).

[NSA03] P. Nava, M. Sierka and R. Ahlrichs, *Density functional study of palladium clusters*, Phys. Chem. Chem. Phys. **5**, 3372–3381 (2003).

[NWBR20] F. Neese, F. Wennmohs, U. Becker and C. Riplinger, *The ORCA quantum chemistry program package*, J. Chem. Phys. **152**, 224108 (2020).

[OBY21] A. M. Oliveira, R. R. Beswick and Y. Yan, *A green hydrogen economy for a renewable energy society*, Curr. Opin. Chem. Eng. **33**, 100701 (2021).

[Oto12] T. Otobe, *First-principle description for the high-harmonic generation in a diamond by intense short laser pulse*, J. Appl. Phys. **111**, 093112 (2012).

[PBE96] J. P. Perdew, K. Burke and M. Ernzerhof, *Generalized Gradient Approximation Made Simple*, Phys. Rev. Lett. **77**, 3865–3868 (1996).

[PBF$^+$09] P. Puschnig, S. Berkebile, A. J. Fleming, G. Koller, K. Emtsev, T. Seyller, J. D. Riley, C. Ambrosch-Draxl, F. P. Netzer and M. G. Ramsey, *Reconstruction of Molecular Orbital Densities from Photoemission Data*, Science **326**, 702–706 (2009).

[PBHT08] M. J. G. Peach, P. Benfield, T. Helgaker and D. J. Tozer, *Excitation energies in density functional theory: An evaluation and a diagnostic test*, J. Chem. Phys. **128**, 044118 (2008).

[PBW$^+$17] P. Puschnig, A. D. Boese, M. Willenbockel, M. Meyer, D. Lüftner, E. M. Reinisch, T. Ules, G. Koller, S. Soubatch, M. G. Ramsey and F. S. Tautz, *Energy Ordering of Molecular Orbitals*, J. Phys. Chem. Lett. **8**, 208–213 (2017).

[PEB96] J. P. Perdew, M. Ernzerhof and K. Burke, *Rationale for mixing exact exchange with density functional approximations*, J. Chem. Phys. **105**, 9982–9985 (1996).

[PFL20] A. Päpcke, A. Friedrich and S. Lochbrunner, *Revealing the initial steps in homogeneous photocatalysis by time-resolved spectroscopy*, J. Phys. Condens. Matter **32**, 153001 (2020).

[PHS$^+$06] M. J. G. Peach, T. Helgaker, P. Sałek, T. W. Keal, O. B. Lutnæs, D. J. Tozer and N. C. Handy, *Assessment of a Coulomb-attenuated exchange-correlation energy functional*, Phys. Chem. Chem. Phys. **8**, 558–562 (2006).

[PI16] M. R. Provorse and C. M. Isborn, *Electron dynamics with real-time time-dependent density functional theory*, Int. J. Quantum Chem. **116**, 739–749 (2016).

[PK03] J. P. Perdew and S. Kurth, *Density Functionals for Non-relativistic Coulomb Systems in the New Century*, Lecture Notes in Physics, Springer Berlin Heidelberg **620**, 1–55 (2003).

[PKC02] V. POLO, E. KRAKA and D. CREMER, *Electron correlation and the self-interaction error of density functional theory*, Mol. Phys. **100**, 1771–1790 (2002).

[PL12] M. Pérez-Lorenzo, *Palladium Nanoparticles as Efficient Catalysts for Suzuki Cross-Coupling Reactions*, J. Phys. Chem. Lett. **3**, 167–174 (2012).

[PMB$^+$19] B. D. Patterson, F. Mo, A. Borgschulte, M. Hillestad, F. Joos, T. Kristiansen, S. Sunde and J. A. van Bokhoven, *Renewable CO_2 recycling and synthetic fuel production in a marine environment*, Proc. Natl. Acad. Sci. **116**, 12212–12219 (2019).

[PMK07] J. Paier, M. Marsman and G. Kresse, *Why does the B3LYP hybrid functional fail for metals?*, J. Chem. Phys. **127**, 024103 (2007).

[PNM$^+$22] M. Puppin, C. W. Nicholson, C. Monney, Y. Deng, R. P. Xian, J. Feldl, S. Dong, A. Dominguez, H. Hübener, A. Rubio, M. Wolf, L. Rettig and R. Ernstorfer, *Excited-state band structure mapping*, Phys. Rev. B **105**, 075417 (2022).

[PPDS10] M. J. Piotrowski, P. Piquini and J. L. F. Da Silva, *Density functional theory investigation of 3d, 4d, and 5d 13-atom metal clusters*, Phys. Rev. B **81**, 155446 (2010).

[PR08] L. D. Pachón and G. Rothenberg, *Transition-metal nanoparticles: synthesis, stability and the leaching issue*, Appl. Organomet. Chem. **22**, 288–299 (2008).

[PRM13] C. K. Prier, D. A. Rankic and D. W. C. MacMillan, *Visible Light Photoredox Catalysis with Transition Metal Complexes: Applications in Organic Synthesis*, Chem. Rev. **113**, 5322–5363 (2013).

[PRS00] A. Pohl, P.-G. Reinhard and E. Suraud, *Towards Single-Particle Spectroscopy of Small Metal Clusters*, Phys. Rev. Lett. **84**, 5090–5093 (2000).

[PRU$^+$11] P. Puschnig, E.-M. Reinisch, T. Ules, G. Koller, S. Soubatch, M. Ostler, L. Romaner, F. S. Tautz, C. Ambrosch-Draxl and M. G. Ramsey, *Orbital tomography: Deconvoluting photoemission spectra of organic molecules*, Phys. Rev. B **84**, 235427 (2011).

[PSTS08] J. P. Perdew, V. N. Staroverov, J. M. Tao and G. E. Scuseria, *Density functional with full exact exchange, balanced nonlocality of correlation, and constraint satisfaction*, Phys. Rev. A **78**, 052513 (2008).

[PTVF07] W. H. Press, S. A. Teukolsky, W. T. Vetterling and B. P. Flannery, *Numerical Recipes: The Art of Scientific Computing*, Cambridge University Press **3** (2007).

[PUT$^+$16] M. J. Piotrowski, C. G. Ungureanu, P. Tereshchuk, K. E. A. Batista, A. S. Chaves, D. Guedes-Sobrinho and J. L. F. Da Silva, *Theoretical Study of the Structural, Energetic, and Electronic Properties of 55-Atom Metal Nanoclusters: A DFT Investigation within van der Waals Corrections, Spin-Orbit Coupling, and PBE+U of 42 Metal Systems*, J. Phys. Chem. C **120**, 28844–28856 (2016).

[PVDSJ06] N. Phan, M. Van Der Sluys and C. Jones, *On the Nature of the Active Species in Palladium Catalyzed Mizoroki-Heck and Suzuki-Miyaura Couplings - Homogeneous or Heterogeneous Catalysis, A Critical Review*, Adv. Synth. Catal. **348**, 609–679 (2006).

[PW86] J. P. Perdew and Y. Wang, *Accurate and simple density functional for the electronic exchange energy: Generalized gradient approximation*, Phys. Rev. B **33**, 8800–8802 (1986).

[PW92] J. P. Perdew and Y. Wang, *Accurate and simple analytic representation of the electron-gas correlation energy*, Phys. Rev. B **45**, 13244–13249 (1992).

[PZ81] J. P. Perdew and A. Zunger, *Self-interaction correction to density-functional approximations for many-electron systems*, Phys. Rev. B **23**, 5048–5079 (1981).

[PZE91] J. P. Perdew, P. Ziesche and H. Eschrig, *Electronic structure of solids 1991*, Akademie Verlag, Berlin (1991).

[RABK11] S. Refaely-Abramson, R. Baer and L. Kronik, *Fundamental and excitation gaps in molecules of relevance for organic photovoltaics from an optimally tuned range-separated hybrid functional*, Phys. Rev. B **84**, 075144 (2011).

[RG84] E. Runge and E. K. U. Gross, *Density-functional theory for time-dependent systems*, Phys. Rev. Lett. **52**, 997–1000 (1984).

[RH08] M. A. Rohrdanz and J. M. Herbert, *Simultaneous benchmarking of ground- and excited-state properties with long-range-corrected density functional theory*, J. Chem. Phys. **129**, 034107 (2008).

[RJ06] J. Richardson and C. Jones, *Poly(4-vinylpyridine) and Quadrapure TU as Selective Poisons for Soluble Catalytic Species in Palladium-Catalyzed Coupling Reactions - Application to Leaching from Polymer-Entrapped Palladium*, Adv. Synth. Catal. **348**, 1207–1216 (2006).

[RJJBB20] R. Reiff, T. Joyce, A. Jaroń-Becker and A. Becker, *Single-active electron calculations of high-order harmonic generation from valence shells in atoms for quantitative comparison with TDDFT calculations*, Journal of Physics Communications **4**, 065011 (2020).

[RKP⁺17] T. P. Rossi, M. Kuisma, M. J. Puska, R. M. Nieminen and P. Erhart, *Kohn–Sham Decomposition in Real-Time Time-Dependent Density-Functional Theory: An Efficient Tool for Analyzing Plasmonic Excitations*, J. Chem. Theory Comput. **13**, 4779–4790 (2017).

[RLY] D. S. R. Lehoucq and C. Yang, Arpack users guide: Solution of large scale eigenvalue problems with implicitly restarted Arnoldi methods, available from `http://www.caam.rice.edu/software/ARPACK/UG/ug.html`, (1997).

[RMH09] M. A. Rohrdanz, K. M. Martins and J. M. Herbert, *A long-range-corrected density functional that performs well for both ground-state properties and time-dependent density functional theory excitation energies, including charge-transfer excited states*, J. Chem. Phys. **130**, 054112 (2009).

[S⁺15] Y. Shao et al., *Advances in molecular quantum chemistry contained in the Q-Chem 4 program package*, Mol. Phys. **113**, 184–215 (2015).

[SBJE97] A. Scholl, L. Baumgarten, R. Jacquemin and W. Eberhardt, *Ultrafast Spin Dynamics of Ferromagnetic Thin Films Observed by fs Spin-Resolved Two-Photon Photoemission*, Phys. Rev. Lett. **79**, 5146–5149 (1997).

[SBKN12] S. Sharifzadeh, A. Biller, L. Kronik and J. B. Neaton, *Quasiparticle and optical spectroscopy of the organic semiconductors pentacene and PTCDA from first principles*, Phys. Rev. B **85**, 125307 (2012).

[SBN04] A. Stolow, A. E. Bragg and D. M. Neumark, *Femtosecond Time-Resolved Photoelectron Spectroscopy*, Chem. Rev. **104**, 1719–1758 (2004).

[Sch03] H. B. Schlegel, *Exploring potential energy surfaces for chemical reactions: An overview of some practical methods*, J. Comput. Chem. **24**, 1514–1527 (2003).

[Sch11] H. B. Schlegel, *Geometry optimization*, WIREs Comput. Mol. Sci. **1**, 790–809 (2011).

[Sch16] I. Schelter, *Excitation dynamics in molecular systems from efficient grid-based real-time density functional theory*, Doctoral thesis, University of Bayreuth, (2016).

[SCK⁺15] M. A. Sentef, M. Claassen, A. F. Kemper, B. Moritz, T. Oka, J. K. Freericks and T. P. Devereaux, *Theory of Floquet band formation and local pseudospin textures in pump-probe photoemission of graphene*, Nat. Commun. **6**, 7047 (2015).

[SDCF94] P. J. Stephens, F. J. Devlin, C. F. Chabalowski and M. J. Frisch, *Ab Initio Calculation of Vibrational Absorption and Circular Dichroism Spectra Using Density Functional Force Fields*, J. Phys. Chem. **98**, 11623–11627 (1994).

[SDE⁺07] K. L. Schuchardt, B. T. Didier, T. Elsethagen, L. Sun, V. Gurumoorthi, J. Chase, J. Li and T. L. Windus, *Basis Set Exchange: A Community Database for Computational Sciences*, J. Chem. Inf. Model. **47**, 1045–1052 (2007).

[SDPR⁺21] T. P. H. Sidiropoulos, N. Di Palo, D. E. Rivas, S. Severino, M. Reduzzi, B. Nandy, B. Bauerhenne, S. Krylow, T. Vasileiadis, T. Danz, P. Elliott, S. Sharma, K. Dewhurst, C. Ropers, Y. Joly, M. E. Garcia, M. Wolf, R. Ernstorfer and J. Biegert, *Probing the Energy Conversion Pathways between Light, Carriers, and Lattice in Real Time with Attosecond Core-Level Spectroscopy*, Phys. Rev. X **11**, 041060 (2021).

[SFG⁺19] I. Schelter, J. M. Foerster, A. T. Gardiner, A. W. Roszak, R. J. Cogdell, G. M. Ullmann, T. B. de Queiroz and S. Kümmel, *Assessing density functional theory in real-time and real-space as a tool for studying bacteriochlorophylls and the light-harvesting complex 2*, J. Chem. Phys. **151**, 134114 (2019).

[SGNR14] T. M. Soini, A. Genest, A. Nikodem and N. Rösch, *Hybrid Density Functionals for Clusters of Late Transition Metals: Assessing Energetic and Structural Properties*, J. Chem. Theory Comput. **10**, 4408–4416 (2014).

[SGQS12] S. Sarkar, E. Guibal, F. Quignard and A. K. SenGupta, *Polymer-supported metals and metal oxide nanoparticles: synthesis, characterization, and applications*, J. Nanopart. Res. **14**, 715 (2012).

[SGV+96] A. Seidl, A. Görling, P. Vogl, J. A. Majewski and M. Levy, *Generalized Kohn-Sham schemes and the band-gap problem*, Phys. Rev. B **53**, 3764–3774 (1996).

[SGZ+14] N. Shang, S. Gao, X. Zhou, C. Feng, Z. Wang and C. Wang, *Palladium nanoparticles encapsulated inside the pores of a metal–organic framework as a highly active catalyst for carbon–carbon cross-coupling*, RSC Adv. **4**, 54487–54493 (2014).

[SH53] R. T. Sharp and G. K. Horton, *A Variational Approach to the Unipotential Many-Electron Problem*, Phys. Rev. **90**, 317 (1953).

[SHDGR18] S. A. Sato, H. Hübener, U. De Giovannini and A. Rubio, *Ab Initio Simulation of Attosecond Transient Absorption Spectroscopy in Two-Dimensional Materials*, Appl. Sci. **8** (2018).

[SK16a] P. Schaffhauser and S. Kümmel, *Using time-dependent density functional theory in real time for calculating electronic transport*, Phys. Rev. B **93**, 035115 (2016).

[SK16b] T. Schmidt and S. Kümmel, *One- and many-electron self-interaction error in local and global hybrid functionals*, Phys. Rev. B **93**, 165120 (2016).

[SK18] I. Schelter and S. Kümmel, *Accurate Evaluation of Real-Time Density Functional Theory Providing Access to Challenging Electron Dynamics*, J. Chem. Theory Comput. **14**, 1910–1927 (2018).

[SKB09a] T. Stein, L. Kronik and R. Baer, *Prediction of charge-transfer excitations in coumarin-based dyes using a range-separated functional tuned from first principles*, J. Chem. Phys. **131**, 244119 (2009).

[SKB09b] T. Stein, L. Kronik and R. Baer, *Reliable Prediction of Charge Transfer Excitations in Molecular Complexes Using Time-Dependent Density Functional Theory*, J. Am. Chem. Soc. **131**, 2818–2820 (2009).

[SKG+20] A. Stuke, C. Kunkel, D. Golze, M. Todorović, J. T. Margraf, K. Reuter, P. Rinke and H. Oberhofer, *Atomic structures and orbital energies of 61,489 crystal-forming organic molecules*, Sci. Data **7**, 58 (2020).

[SKM+14] T. Schmidt, E. Kraisler, A. Makmal, L. Kronik and S. Kümmel, *A self-interaction-free local hybrid functional: Accurate binding energies vis-à-vis accurate ionization potentials from Kohn-Sham eigenvalues*, J. Chem. Phys. **140**, 18A510 (2014).

[SL07] A. P. Simpson and A. E. Lutz, *Exergy analysis of hydrogen production via steam methane reforming*, Int. J. Hydrogen Energy **32**, 4811–4820 (2007).

[SLR+12] D. A. Strubbe, L. Lehtovaara, A. Rubio, M. A. L. Marques and S. G. Louie, *Response Functions in TDDFT: Concepts and Implementation*, Lecture Notes in Physics, Springer Berlin Heidelberg **837**, 139–166 (2012).

[SR15] T. M. Soini and N. Rösch, *Size-dependent properties of transition metal clusters: from molecules to crystals and surfaces – computational studies with the program ParaGauss*, Phys. Chem. Chem. Phys. **17**, 28463–28483 (2015).

[SRGGLL+18] R. Sinha-Roy, P. García-González, X. López Lozano, R. L. Whetten and H.-C. Weissker, *Identifying Electronic Modes by Fourier Transform from δ-Kick Time-Evolution TDDFT Calculations*, J. Chem. Theory Comput. **14**, 6417–6426 (2018).

[SSD+17] R. Schroot, T. Schlotthauer, B. Dietzek, M. Jäger and U. S. Schubert, *Extending Long-lived Charge Separation Between Donor and Acceptor Blocks in Novel Copolymer Architectures Featuring a Sensitizer Core*, Chem.–Eur. J. **23**, 16484–16490 (2017).

[SSH+17] M. Sharma, M. Sharma, A. Hazarika, L. Satyanarayana, G. V. Karunakar and K. K. Bania, *CCl bond activation with Pd(II)-NiO nanoparticles supported on zeolite-Y: The role of charge transfer transition*, Molecular Catalysis **432**, 210–219 (2017).

[SSTP03] V. N. Staroverov, G. E. Scuseria, J. Tao and J. P. Perdew, *Comparative assessment of a new nonempirical density functional: Molecules and hydrogen-bonded complexes*, J. Chem. Phys. **119**, 12129–12137 (2003).

[SSTP04] V. N. Staroverov, G. E. Scuseria, J. Tao and J. P. Perdew, *Tests of a ladder of density functionals for bulk solids and surfaces*, Phys. Rev. B **69**, 075102 (2004).

[STM16] M. H. Shaw, J. Twilton and D. W. C. MacMillan, *Photoredox Catalysis in Organic Chemistry*, The Journal of Organic Chemistry **81**, 6898–6926 (2016).

[SW80] S. Sato and J. White, *Photodecomposition of water over Pt/TiO$_2$ catalysts*, Chem. Phys. Lett. **72**, 83–86 (1980).

[SWR$^+$12] B. Stadtmüller, M. Willenbockel, E. M. Reinisch, T. Ules, F. C. Bocquet, S. Soubatc, P. Puschnig, G. Koller, M. G. Ramsey, F. S. Tautz and C. Kumpf, *Orbital tomography for highly symmetric adsorbate systems*, Europhys. Lett. **100**, 26008 (2012).

[SZT05] N. E. Schultz, Y. Zhao and D. G. Truhlar, *Density Functionals for Inorganometallic and Organometallic Chemistry*, J. Phys. Chem. A **109**, 11127–11143 (2005).

[TA19] A. Trzeciak and A. Augustyniak, *The role of palladium nanoparticles in catalytic C-C cross-coupling reactions*, Coord. Chem. Rev. **384**, 1–20 (2019).

[Tau07] F. Tautz, *Structure and bonding of large aromatic molecules on noble metal surfaces: The example of PTCDA*, Prog. Surf. Sci. **82**, 479–520 (2007).

[TC98a] X.-M. Tong and S.-I. Chu, *Time-dependent density-functional theory for strong-field multiphoton processes: Application to the study of the role of dynamical electron correlation in multiple high-order harmonic generation*, Phys. Rev. A **57**, 452–461 (1998).

[TC98b] X.-M. Tong and S.-I. Chu, *Time-dependent density-functional theory with optimized effective potential and self-interaction correction: Application to the study of coherent control of multiple high-order harmonic generation of He atoms in mixed laser fields*, Int. J. Quantum Chem. **69**, 293–303 (1998).

[TC01] X.-M. Tong and S.-I. Chu, *Multiphoton ionization and high-order harmonic generation of He, Ne, and Ar atoms in intense pulsed laser fields: Self-interaction-free time-dependent density-functional theoretical approach*, Phys. Rev. A **64**, 013417 (2001).

[TD$^+$20] N. Tancogne-Dejean et al., *Octopus, a computational framework for exploring light-driven phenomena and quantum dynamics in extended and finite systems*, J. Chem. Phys. **152**, 124119 (2020).

[TK14] M. Thiele and S. Kümmel, *Frequency Dependence of the Exact Exchange-Correlation Kernel of Time-Dependent Density-Functional Theory*, Phys. Rev. Lett. **112**, 083001 (2014).

[TKN09] H. Tada, T. Kiyonaga and S.-i. Naya, *Rational design and applications of highly efficient reaction systems photocatalyzed by noble metal nanoparticle-loaded titanium(iv) dioxide*, Chem. Soc. Rev. **38**, 1849–1858 (2009).

[TM91] N. Troullier and J. L. Martins, *Efficient pseudopotentials for plane-wave calculations*, Phys. Rev. B **43**, 1993–2006 (1991).

[TMC$^+$07] L. Tinker, N. McDaniel, P. Curtin, C. Smith, M. Ireland and S. Bernhard, *Visible Light Induced Catalytic Water Reduction without an Electron Relay*, Chem.–Eur. J. **13**, 8726–8732 (2007).

[Toz98] D. J. Tozer, *Effective homogeneity of the exchange-correlation energy functional*, Phys. Rev. A **58**, 3524–3527 (1998).

[TRJ08] J. Tirado-Rives and W. L. Jorgensen, *Performance of B3LYP Density Functional Methods for a Large Set of Organic Molecules*, J. Chem. Theory Comput. **4**, 297–306 (2008).

[TRMv96] Y. Tong, A. Renouprez, G. Martin and J. van der Klink, *Electron availability and the surface fermi level local density of states: an alternative way to see catalytic activity of metals*, Stud. Surf. Sci. Catal. **101**, 901–910 (1996).

[TUR19] TURBOMOLE V7.4, a development of University of Karlsruhe and Forschungszentrum Karlsruhe GmbH, 1989-2007, TURBOMOLE GmbH, since 2007, available from `http://www.turbomole.com`, (2019).

[TWT$^+$17] S. Y. Tee, K. Y. Win, W. S. Teo, L.-D. Koh, S. Liu, C. P. Teng and M.-Y. Han, *Recent Progress in Energy-Driven Water Splitting*, Adv. Sci. **4**, 1600337 (2017).

[UG94] C. J. Umrigar and X. Gonze, *Accurate exchange-correlation potentials and total-energy components for the helium isoelectronic series*, Phys. Rev. A **50**, 3827–3837 (1994).

[UGG95] C. A. Ullrich, U. J. Gossmann and E. K. U. Gross, *Time-Dependent Optimized Effective Potential*, Phys. Rev. Lett. **74**, 872–875 (1995).

[Ull12] C. Ullrich, *Time-Dependent Density-Functional Theory: Concepts and Applications*, Oxford Graduate Texts, OUP Oxford (2012).

[URS97] C. A. Ullrich, P.-G. Reinhard and E. Suraud, *Metallic clusters in strong femtosecond laser pulses*, J. Phys. B: At., Mol. Opt. Phys. **30**, 5043–5055 (1997).

[UY14] C. A. Ullrich and Z.-h. Yang, *A Brief Compendium of Time-Dependent Density Functional Theory*, Braz. J. Phys. **44**, 154–188 (2014).

[Van19] M. Van Den Bossche, *DFTB-Assisted Global Structure Optimization of 13- and 55-Atom Late Transition Metal Clusters*, J. Phys. Chem. A **123**, 3038–3045 (2019).

[vB04] U. von Barth, *Basic Density-Functional Theory an Overview*, Phys. Scr. **T109**, 9 (2004).

[VBG$^+$10] M. Valiev, E. Bylaska, N. Govind, K. Kowalski, T. Straatsma, H. Van Dam, D. Wang, J. Nieplocha, E. Apra, T. Windus and W. de Jong, *NWChem: A comprehensive and scalable open-source solution for large scale molecular simulations*, Comput. Phys. Commun. **181**, 1477–1489 (2010).

[vBH72] U. von Barth and L. Hedin, *A local exchange-correlation potential for the spin polarized case. i*, J. Phys. C Solid State Phys. **5**, 1629–1642 (1972).

[VGMLP21] K. Villa, J. R. Galán-Mascarós, N. López and E. Palomares, *Photocatalytic water splitting: advantages and challenges*, Sustain. Energy Fuels **5**, 4560–4569 (2021).

[Vig95] G. Vignale, *Center of Mass and Relative Motion in Time Dependent Density Functional Theory*, Phys. Rev. Lett. **74**, 3233–3236 (1995).

[Vig08] G. Vignale, *Real-time resolution of the causality paradox of time-dependent density-functional theory*, Phys. Rev. A **77**, 062511 (2008).

[VK04] A. Vogler and H. Kunkely, *Charge transfer excitation of organometallic compounds: Spectroscopy and photochemistry*, Coord. Chem. Rev. **248**, 273–278 (2004).

[vL98] R. van Leeuwen, *Causality and Symmetry in Time-Dependent Density-Functional Theory*, Phys. Rev. Lett. **80**, 1280–1283 (1998).

[vL99] R. van Leeuwen, *Mapping from Densities to Potentials in Time-Dependent Density-Functional Theory*, Phys. Rev. Lett. **82**, 3863–3866 (1999).

[VMF$^+$03] T. Vreven, K. Morkuma, O. Farkas, H. B. Schlegel and M. J. Frisch, *Geometry optimization with QM/MM, ONIOM, and other combined methods. I. Microiterations and constraints*, J. Comput. Chem. **24**, 760–769 (2003).

[VT20] P. Verma and D. G. Truhlar, *Status and Challenges of Density Functional Theory*, Trends in Chemistry **2**, 302–318 (2020), Special Issue - Laying Groundwork for the Future.

[WA05] F. Weigend and R. Ahlrichs, *Balanced basis sets of split valence, triple zeta valence and quadruple zeta valence quality for H to Rn: Design and assessment of accuracy*, Phys. Chem. Chem. Phys. **7**, 3297–3305 (2005).

[WBSB18] N. Waiskopf, Y. Ben-Shahar and U. Banin, *Photocatalytic Hybrid Semiconductor–Metal Nanoparticles; from Synergistic Properties to Emerging Applications*, Adv. Mater. **30**, 1706697 (2018).

[WD16] A. Wardlow and D. Dundas, *High-order-harmonic generation in benzene with linearly and circularly polarized laser pulses*, Phys. Rev. A **93**, 023428 (2016).

[WDGCR16] J. Walkenhorst, U. De Giovannini, A. Castro and A. Rubio, *Tailored pump-probe transient spectroscopy with time-dependent density-functional theory: controlling absorption spectra*, Eur. Phys. J. B **89**, 128 (2016).

[WEB05] M. Wollenhaupt, V. Engel and T. Baumert, *Femtosecond laser photoelectron spectroscopy on atoms and small molecules: Prototype Studies in Quantum Control*, Ann. Rev. Phys. Chem. **56**, 25–56 (2005).

[Wei06] F. Weigend, *Accurate Coulomb-fitting basis sets for H to Rn*, Phys. Chem. Chem. Phys. **8**, 1057–1065 (2006).

[Wen18] O. S. Wenger, *Photoactive Complexes with Earth-Abundant Metals*, J. Am. Chem. Soc. **140**, 13522–13533 (2018).

[WEV+19] S. T. Wismann, J. S. Engbæk, S. B. Vendelbo, F. B. Bendixen, W. L. Eriksen, K. Aasberg-Petersen, C. Frandsen, I. Chorkendorff and P. M. Mortensen, *Electrified methane reforming: A compact approach to greener industrial hydrogen production*, Science **364**, 756–759 (2019).

[WFD+10] P. Wopperer, B. Faber, P. M. Dinh, P.-G. Reinhard and E. Suraud, *Angular distributions of photoelectrons from free Na clusters*, Phys. Rev. A **82**, 063416 (2010).

[WHDW12] P. Wang, B. Huang, Y. Dai and M.-H. Whangbo, *Plasmonic photocatalysts: harvesting visible light with noble metal nanoparticles*, Phys. Chem. Chem. Phys. **14**, 9813–9825 (2012).

[WHL+20] E. Woods, O. T. Harris, W. E. Leiter, N. E. Burner, P. Ofosuhene, A. Krez, M. A. Hilton and K. A. Burke, *Lifetime of Triplet Photosensitizers in Aerosol Using Time-Resolved Photoelectric Activity*, ACS Earth and Space Chemistry **4**, 1424–1434 (2020).

[WHS+14] M. Wießner, D. Hauschild, C. Sauer, V. Feyer, A. Schöll and F. Reinert, *Complete determination of molecular orbitals by measurement of phase symmetry and electron density*, Nat. Commun. **5**, 4156 (2014).

[WJ07] L.-L. Wang and D. D. Johnson, *Density functional study of structural trends for late-transition-metal 13-atom clusters*, Phys. Rev. B **75**, 235405 (2007).

[WKH+17] S. Weiß, I. Krieger, T. Heepenstrick, S. Soubatch, M. Sokolowski and F. S. Tautz, *Determination of the adsorption geometry of PTCDA on the Cu(100) surface*, Phys. Rev. B **96**, 075414 (2017).

[WKW91] A. P. Wilde, K. A. King and R. J. Watts, *Resolution and analysis of the components in dual emission of mixed-chelate/ortho-metalate complexes of iridium(III)*, J. Phys. Chem. **95**, 629–634 (1991).

[WLL+10] S. H. Wu, J. W. Ling, S. H. Lai, M. J. Huang, C. H. Cheng and I. C. Chen, *Dynamics of the excited states of $[Ir(ppy)_2bpy]^+$ with triple phosphorescence*, J. Phys. Chem. A **114**, 10339–10344 (2010).

[WMd+18] S. Wang, C. M. McGuirk, A. d'Aquino, J. A. Mason and C. A. Mirkin, *Metal–Organic Framework Nanoparticles*, Adv. Mater. **30**, 1800202 (2018).

[WRS+21] R. Wallauer, M. Raths, K. Stallberg, L. Münster, D. Brandstetter, X. Yang, J. Güdde, P. Puschnig, S. Soubatch, C. Kumpf, F. C. Bocquet, F. S. Tautz and U. Höfer, *Tracing orbital images on ultrafast time scales*, Science **371**, 1056–1059 (2021).

[WWM+10] M. G. Walter, E. L. Warren, J. R. McKone, S. W. Boettcher, Q. Mi, E. A. Santori and N. S. Lewis, *Solar Water Splitting Cells*, Chem. Rev. **110**, 6446–6473 (2010).

[WXZS17] W. Wang, X. Xu, W. Zhou and Z. Shao, *Recent Progress in Metal-Organic Frameworks for Applications in Electrocatalytic and Photocatalytic Water Splitting*, Adv. Sci. **4**, 1600371 (2017).

[XTY+18] J.-Y. Xu, X. Tong, P. Yu, G. E. Wenya, T. McGrath, M. J. Fong, J. Wu and Z. M. Wang, *Ultrafast Dynamics of Charge Transfer and Photochemical Reactions in Solar Energy Conversion*, Adv. Sci. **5**, 1800221 (2018).

[YB96] K. Yabana and G. F. Bertsch, *Time-dependent local-density approximation in real time*, Phys. Rev. B **54**, 4484–4487 (1996).

[YB99] K. Yabana and G. F. Bertsch, *Application of the time-dependent local density approximation to optical activity*, Phys. Rev. A **60**, 1271–1279 (1999).

[YGS+12] I. V. Yudanov, A. Genest, S. Schauermann, H.-J. Freund and N. Rösch, *Size Dependence of the Adsorption Energy of CO on Metal Nanoparticles: A DFT Search for the Minimum Value*, Nano Lett. **12**, 2134–2139 (2012).

[YKL+18] X. Yang, I. Krieger, D. Lüftner, S. Weiß, T. Heepenstrick, M. Hollerer, P. Hurdax, G. Koller, M. Sokolowski, P. Puschnig, M. G. Ramsey, F. S. Tautz and S. Soubatch, *On the decoupling of molecules at metal surfaces*, Chem. Commun. **54**, 9039–9042 (2018).

[YTH04] T. Yanai, D. P. Tew and N. C. Handy, *A new hybrid exchange–correlation functional using the Coulomb-attenuating method (CAM-B3LYP)*, Chem. Phys. Lett. **393**, 51 – 57 (2004).

[YXJ17] Q. Yang, Q. Xu and H.-L. Jiang, *Metal–organic frameworks meet metal nanoparticles: synergistic effect for enhanced catalysis*, Chem. Soc. Rev. **46**, 4774–4808 (2017).

[YZZT10] K. Yang, J. Zheng, Y. Zhao and D. G. Truhlar, *Tests of the RPBE, revPBE, τ-HCTHhyb, ωB97X-D, and MOHLYP density functional approximations and 29 others against representative databases for diverse bond energies and barrier heights in catalysis*, J. Chem. Phys. **132**, 164117 (2010).

[ZAC$^+$14] Z. Zuo, D. T. Ahneman, L. Chu, J. A. Terrett, A. G. Doyle and D. W. MacMillan, *Merging photoredox with nickel catalysis: Coupling of α-carboxyl sp^3-carbons with aryl halides*, Science **345**, 437–440 (2014).

[ZCW13] L. Zhang, J. Chen and J. Wang, *First-principles investigation of transient current in molecular devices by using complex absorbing potentials*, Phys. Rev. B **87**, 205401 (2013).

[ZGX$^+$12] G.-J. Zhang, X. Gan, Q.-Q. Xu, Y. Chen, X.-J. Zhao, B. Qin, X.-J. Lv, S.-W. Lai, W.-F. Fu and C.-M. Che, *Photophysical and electrochemical properties of platinum(ii) complexes bearing a chromophore-acceptor dyad and their photocatalytic hydrogen evolution*, Dalton Trans. **41**, 8421–8429 (2012).

[ZH18] Y. Zhu and J. M. Herbert, *Self-consistent predictor/corrector algorithms for stable and efficient integration of the time-dependent Kohn-Sham equation*, J. Chem. Phys. **148**, 044117 (2018).

[ZKL$^+$15] B. Zhang, S. Kaziz, H. Li, M. G. Hevia, D. Wodka, C. Mazet, T. Bürgi and N. Barrabés, *Modulation of Active Sites in Supported $Au_{38}(SC_2H_4Ph)_{24}$ Cluster Catalysts: Effect of Atmosphere and Support Material*, J. Phys. Chem. C **119**, 11193–11199 (2015).

[ZL14] T. Zhang and W. Lin, *Metal-organic frameworks for artificial photosynthesis and photocatalysis*, Chem. Soc. Rev. **43**, 5982–5993 (2014).

[ZLT19] F. Zapata, E. Luppi and J. Toulouse, *Linear-response range-separated density-functional theory for atomic photoexcitation and photoionization spectra*, J. Chem. Phys. **150**, 234104 (2019).

[ZPK04] U. Zimmerli, M. Parrinello and P. Koumoutsakos, *Dispersion corrections to density functionals for water aromatic interactions*, J. Chem. Phys. **120**, 2693–2699 (2004).

[ZWSG13] J. Zhao, W. Wu, J. Sun and S. Guo, *Triplet photosensitizers: from molecular design to applications*, Chem. Soc. Rev. **42**, 5323–5351 (2013).

[ZYSA01] Z. Zou, J. Ye, K. Sayama and H. Arakawa, *Direct splitting of water under visible light irradiation with an oxide semiconductor photocatalyst*, Nature **414**, 625–627 (2001).

List of Publications

Pub. 1
Magnetic Moment Quenching in Small Pd Clusters in Solution,
Sebastian Hammon, Linn Leppert, and Stephan Kümmel,
The European Physical Journal D **75**, 309 (2021).

Pub. 2
H_2-Generation from Alcohols by the MOF-Based Noble Metal-Free Photocatalyst Ni/CdS/TiO_2@MIL-101,
Dominic Tilgner, Mara Klarner, Sebastian Hammon, Martin Friedrich, Andreas Verch, Niels de Jonge, Stephan Kümmel, and Rhett Kempe,
Australian Journal of Chemistry **72**, 842-847 (2019).

Pub. 3
Visible Light-driven Dehydrogenation of Benzylamine under Liberation of H_2,
Mara Klarner, Sebastian Hammon, Sebastian Feulner, Stephan Kümmel, Lothar Kador, and Rhett Kempe,
ChemCatChem **12**, 4593-4599 (2020).

Pub. 4
Combining Metal Nanoparticles with an Ir(III) Photosensitizer,
Sebastian Hammon, Mara Klarner, Gerald Hörner, Birgit Weber, Martin Friedrich, Jürgen Senker, Rhett Kempe, Thiago Branquinho de Queiroz, and Stephan Kümmel,
The Journal of Physical Chemistry C **125**, 25765-25773 (2021).

Pub. 5
Pump-Probe Photoemission Simulated in Real Time: Revealing Many-Particle Signatures,
Sebastian Hammon and Stephan Kümmel,
Physical Review A **104**, 012815 (2021).

Part II

Publications

Publication 1

Magnetic Moment Quenching in small Pd clusters in solution

Reprinted from
The European Physical Journal D **75**, 309 (2021)
with the permission of EDP Sciences, Società Italiana di Fisica and Springer-Verlag GmbH, part of Springer Nature.

Sebastian Hammon[1], Linn Leppert[2,3], and Stephan Kümmel[1]

[1] Theoretical Physics IV, University of Bayreuth, 95440 Bayreuth, Germany
[2] Electronic Excitations in Light-Converting Systems, University of Bayreuth, 95440 Bayreuth, Germany
[3] MESA+ Institute for Nanotechnology, University of Twente, 7500 AE Enschede, The Netherlands

My contribution

I am the first author of this paper and did all numerical calculations and simulations. This work evolved over an extended period of time. It started as a student project and I obtained important results and the decisive scientific insights during my PhD work. L. Leppert introduced me to many of the technical and practical aspects of computational studies of metal clusters and simulating them using Turbomole. All authors were involved in the scientific discussions. I wrote large parts of the first version of this paper. L. Leppert and S. Kümmel commented on the early versions of the text and myself and S. Kümmel together worked out the final manuscript text. L. Leppert proofread the final manuscript.

Publ. 1

Eur. Phys. J. D (2021)75:309
https://doi.org/10.1140/epjd/s10053-021-00322-1

THE EUROPEAN
PHYSICAL JOURNAL D

Regular Article – Clusters and Nanostructures

Magnetic moment quenching in small Pd clusters in solution

Sebastian Hammon[1], Linn Leppert[2,3], and Stephan Kümmel[1,a]

[1] Theoretical Physics IV, University of Bayreuth, 95440 Bayreuth, Germany
[2] Electronic Excitations in Light-Converting Systems, University of Bayreuth, 95440 Bayreuth, Germany
[3] MESA+ Institute for Nanotechnology, University of Twente, 7500 AE Enschede, The Netherlands

Received 4 October 2021 / Accepted 1 December 2021

Abstract. Small palladium clusters in vacuum show pronounced magnetic moments. With the help of Born–Oppenheimer molecular dynamics simulations based on density functional theory, we investigate for the paradigmatic examples of the Pd_{13} and the Pd_8 cluster whether these magnetic moments prevail when the clusters are solvated. Our results show that the interaction with acetophenone quenches the magnetic moment. The reduction of the magnetic moment is a direct consequence of the electronic interaction between the Pd clusters and the solvent molecules, and not an indirect effect due to a different cluster geometry being stabilized by the solvation shell.

1 Introduction

Metal clusters have fascinated researchers for decades because they mark the transition from the molecular to the bulk regime, are at the heart of many nanomaterials, and can show distinct properties that differ from the corresponding bulk material. Their unique properties have been explored for fundamental reasons [1,2], but also for their reactivity [3] and related applications, e. g., in catalysis [4–11] and photocatalysis [12–19]. Clusters of transition metals are of interest also for their magnetic properties [20–35], because small clusters can show magnetic moments per atom that are substantially larger than the ones in the corresponding bulk materials.

In this paper we study the magnetic moment of solvated palladium clusters. Our motivation for this is twofold and related to two of the above-mentioned possible practical uses of transition metal clusters. On the one hand, isolated small Pd clusters show large magnetic moments [20–23,25,27,28,32–35]. For potential magnetic applications, it is of interest to know whether the magnetic moment prevails when the clusters are not in vacuum, but in interaction with surrounding media. This question is of interest also for a second reason. Pd nanoparticles and multimetallic clusters containing Pd have been demonstrated to be efficient in catalysis [29,30,36] and particularly noteworthy, excel in cross-coupling reactions [4,37–41], as reviewed, e. g., in Refs. [42,43]. In several such experiments, the metal particles are embedded in some support, e. g., a metal organic framework, and the reaction takes place in solution. The question has been raised what really is the active species in such experiments [39,44–50]: Is it the surface of the metal nanoparticle, or are very small clusters, e. g. of Pd, leaching out of the larger particle, i. e., go into solution, and form the catalytically active centers? For a review on this topic, see Ref. [51]. If the leached out particles retain a strong magnetic moment in solution, one might be able to experimentally answer the question whether leached particles contribute importantly to catalysis by detecting the magnetic moments and check for relations between magnetic and catalytic activity.

The phenomenon of leaching has been discussed for different solvents, e.g., water [50,52–54] and organic solvents [44–46]. An accurate description of water with standard exchange-correlation (xc) approximations is a well-known challenge for density functional theory (DFT) [55]. Given the presence of d-electrons in the Pd clusters and the question of the reliability of the magnetic moment prediction of DFT in this context [56], studying the solvation of Pd clusters in water would be a task of considerable complexity. Our focus here is on acetophenone, which is the smallest aromatic ketone and an exemplary organic solvent whose derivatives have been used in studies of leaching and catalysis [44–46]. We investigated small Pd clusters in solution by computationally embedding them in an increasing number of solvent molecules and studying whether and how the magnetic moment changes as a consequence of the interaction. We find that acetophenone has a tendency to reduce the magnetic moment, i. e., a solvated Pd cluster shows a smaller magnetic moment than the same cluster in vacuum. We reach this conclusion based on extensive DFT-based Born–Oppenheimer Molecu-

---

[a] e-mail: stephan.kuemmel@uni-bayreuth.de (corresponding author)

lar Dynamics (MD) simulations, the general setup of which is described in Sect. 2. In Sect. 3 we discuss how cluster structures and magnetic moments change when clusters are surrounded by an increasing number of acetophenone molecules. In Sect. 4 we discuss our results, also comparing to a few select findings for the solvent acetone that are reported in “Appendix B”, and we summarize our results and draw final conclusions.

2 Theoretical and computational methods

The general concept of our study is to start from a Pd cluster with a nonzero spin magnetic moment in its vacuum geometry. We then add solvent molecules, find the low-energy structures that the system consisting of cluster and solvent molecules has, and check which magnetic moment is realized in these structures.

This procedure is straightforward in principle, but complicated in practice. First, we do not know a priori how many solvent molecules we need to take into account for the Pd cluster to be properly solvated. The computational effort escalates rapidly because, on the one hand, the computational costs of the DFT calculations increases with the number of electrons, and on the other hand, the number of low-energy isomers grows rapidly with the number of atoms. Therefore, we build up a solvation shell in a step-by-step manner. This means that we start with one acetophenone (C_8H_8O) molecule and advance to five, and more distant parts of the solvent are approximated via a conductor-like screening model (COSMO) as detailed below.

Second, each system consisting of the cluster and several solvent molecules can be in many different geometries that are locally stable and of similar energy. Therefore, in order to identify low-energy structures, we first perform a Born–Oppenheimer DFT-MD simulation for some time and record the total energy. We then analyze this trajectory, pick out the lowest energy structures, and optimize those further by relaxing them.

Third, since the systems can assume different, stable spin configurations and since the spin configuration does not necessarily change spontaneously during a Born–Oppenheimer simulation, the just described steps have to be taken for each system size for all plausible spin configurations. The details of the procedure will be described in the following.

For our study we focused on the two small clusters Pd_{13} and Pd_8 that show a distinct spin magnetic moment in vacuum [25,28]. They are furthermore good candidates because their vacuum structures have been established [10,22,23,25,27,28,32,57], and their isomers show canonical structural motifs like, e. g., the I_h icosahedron for Pd_{13}.

The energetic ordering of the isomers and spin configurations in clusters can generally depend on the xc functional [28,32,57]. For P_{13}, the C_s bilayer with $6\,\mu_B$ shown in Fig. 1a and the C_{3v} bilayer with $6\,\mu_B$ (b) is preferred by the Perdew–Burke–Ernzerhof [58–60] (PBE) and the PBE0 [61,62] hybrid functional, respectively. For Pd_8, the energetic ordering of the isomers has been discussed in detail in Ref. [63] and we thus limit ourselves to the Pd isomers relevant to our study. The D_{2d} bicapped octahedron shown in Fig. 2a is the previously reported global minimum for PBE [10,25,63,64]. It shows a $4\,\mu_B$ ground state in our calculations. We find a state with $2\,\mu_B$ just 0.02 eV higher in energy, i.e., quasi degenerate. With PBE0 the energetic difference between the two states increases to 0.10 eV. For the other two Pd_8 isomers (Fig. 2b, c) we also find $4\,\mu_B$ as the preferred magnetic moment with both PBE and PBE0. In Tables 3 and 4 in “Appendix A”, we list the energies for each of the Pd_{13} and Pd_8 cluster isomers shown in Figs. 1 and 2, respectively, for both PBE and PBE0, for the low lying stable spin configurations.

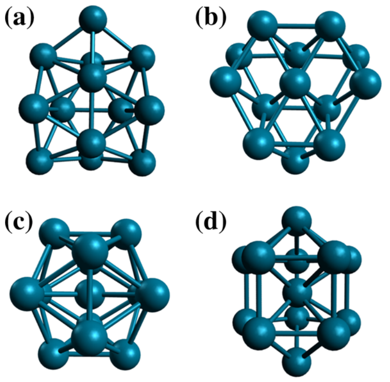

Fig. 1 Three known and one newly determined Pd_{13} isomer and their corresponding ground-state magnetic moment μ obtained with PBE. **a**, **b** Two bilayer structures C_s and C_{3v} with $6\,\mu_B$, **c** an icosahedron I_h and **d** a bicapped heptahedron D_{5h} both with $8\,\mu_B$

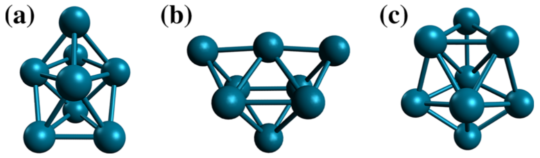

Fig. 2 Relevant Pd_8 isomers and their corresponding ground-state magnetic moment μ obtained with PBE. Pd_8: **a** D_{2d}, **b** C_{2v} and **c** C_1 bicapped octahedron, all with $4\,\mu_B$

For our calculations, we employed the Turbomole [65] program package. The geometry optimizations (relaxations) discussed in Sect. 3 used PBE in combination with the def2-TZVP [66,67] basis set and we used the effective core potential def2-ecp for Pd in combination with all def2 basis sets [66]. For the relaxation of each initial structure, we did several calculations with a fixed number of unpaired electrons to determine the overall lowest energy configurations. In other words, separate calculations were done for a range of spin magnetic moments μ. For, e. g., the ground-state relaxations of $Pd_{13}(C_s)$ and one acetophenone molecule we did calculations with $6\,\mu_B$, i.e., the moment of the bare metal cluster, and 0, 2, and $4\,\mu_B$. As mentioned in Sect. 3.1 we also did some calculation with $8\,\mu_B$ as a crosscheck. In the DFT-MD simulations for the solvated clusters and the subsequent relaxation of selected low-energy structures, the studied magnetic moments could typically be restricted to the range of $[0, 2, 4, 6]\mu_B$ due to the magnetic moment quenching that we discuss in detail below. Nevertheless, we conducted spot checks and also optimized structures with higher magnetic moments. This consistently confirmed that higher moments are energetically less favorable.

For simulating the structural dynamics of the solvated clusters we relied on constant temperature MD simulations with a Nosé-Hoover thermostat [68,69] set to a temperature of 298 K. Again the spin-state was fixed during each of these simulations. The Nosé-Hoover relaxation time $\tau = 560$ a.u. $\approx$ 13 fs was seven times the length of the Born–Oppenheimer dynamics time step $t = 80$ a.u. $\approx$ 1.94 fs. Van-der-Waals' interactions were taken into account via the Grimme correction (DFT-D3) [70]. Solvent effects beyond the solvent molecules that we considered explicitly were modeled with the COSMO approach [71] using a relative permittivity $\epsilon_r = 17.4$ for acetophenone and $\epsilon_r = 20.7$ for acetone [72]. A total simulation time of ca. 6 ps was sufficient for obtaining reliable results about the dominant magnetic moments. For reasons of computational efficiency, we used PBE with def2-SVP [73] in the DFT-MD runs that served to identify low-energy geometries. The thus obtained low-energy structures were then further optimized with higher accuracy as described above.

We computed the binding energy E_B of the composite M/S consisting of a metal cluster M and N solvent molecule(s) S,

$$E_B(M/S) = E_{tot}(M/S) - E_{tot}(M) - NE_{tot}(S), \quad (1)$$

as the difference of the molecular total energies E_{tot} obtained from ground state DFT calculations, where E_{tot} is the total energy for the system in its optimized geometry. Hence, $E_{tot}(M)$ always refers to the structural isomer that provides the lowest energy with the functional employed, e. g., the $Pd_{13}(C_s)$ bilayer with $6\,\mu_B$ for PBE. We indicate the xc functional used to calculate the total energies at the appropriate places throughout the article, unless it is clear that the results refer to the default choice PBE.

As part of our analysis of the interaction between clusters and solvent we checked for charge transfer between the cluster and the solvent molecules. For this we relied on the Bader charge density analysis [74] as implemented in the Bader code [75–79] to assign a charge to each of the atoms in the system. By comparing the charge of each atom in the composite system M/S to that within the separate subsystems M and S, we analyzed whether inter-molecular charge transfer occurs. We also analyzed the interaction based on the (generalized) Kohn-Sham density of states (DOS), obtained from the ground state eigenvalues. As a guide to the eye, we convoluted the eigenvalue spectrum with Gaussians of width 0.08 eV. For better inter-system comparison, we plotted the DOS on the same scale, [0:76] arb. unit, in all figures. In the calculations for the separate systems that are needed for both the Bader charge- and the DOS-analysis, we used the atomic coordinates that the subsystem atoms have in the relaxed, combined system to eliminate differences that would be due only to deviations from the vacuum structure.

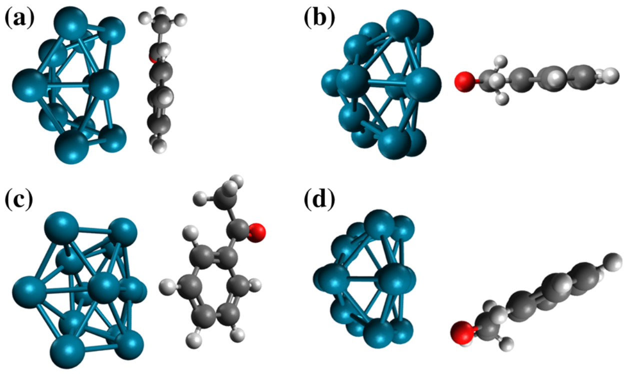

Fig. 3 Different starting geometries for the relaxation of $Pd_{13}(C_s)$ with one C_8H_8O molecule. Color code: Pd blue, C grey, H white, O red. The Pd_{13} geometry is the same in all cases. See main text for details

3 Results: Pd in acetophenone

3.1 Pd_{13} with one acetophenone molecule

We first focus on the Pd_{13} cluster because it is, as discussed above, a stable system with an established geometry. We start by looking at one acetophenone $(0\,\mu_B)$ molecule capping a Pd_{13} cluster. The C_s bilayer structure, cf. Fig. 1a, with a magnetic moment of $6\,\mu_B$ serves as the starting geometry in the following simulations.

Due to its geometry with a benzene ring and the CO and CH_3 groups, it is not a priori clear how the acetophenone molecule will orient itself with respect to the $Pd_{13}(C_s)$ bilayer cluster. Therefore, we performed several geometry optimizations starting from different arrangements of the acetophenone molecule as depicted in Fig. 3, and determined which combination of spatial orientation and magnetic moment is energetically favorable. In one case we aligned the acetophenone parallel to the cluster surface (Fig. 3a). In the other, acetophenone was set perpendicular with CO and CH_3 facing the Pd surface (Fig. 3b). For both cases, we started from several different positions of the acetophenone with respect to the cluster's surface, including inclined arrangements as shown in Fig. 3c and d. For all these arrangements, we ran geometry optimizations for different, fixed spin magnetic moments in the range of $[0, 2, .., 8]\mu_B$. We included the case of 8 μ_B despite the fact that it would imply an increase in magnetic moment compared to the Pd_{13} vacuum structure as a check. However, as expected the $8\,\mu_B$ configuration is energetically clearly less favorable than the others.

The following observations were made in the relaxations: First, a spin configuration with $6\,\mu_B$ is preferred for all orientations and in any case we do not observe

Table 1 Binding energy E_B (second column) for the most stable arrangement of a Pd_{13} cluster (lines 1–5) and a Pd_8 cluster (line 6) surrounded by acetophenone as indicated in the first column

	E_B	$0\,\mu_B$	$2\,\mu_B$	$4\,\mu_B$	$6\,\mu_B$	$8\,\mu_B$
Pd_{13}/C_8H_8O	−1.67	0.14	0.12	0.04	0	0.65
$Pd_{13}/C_8H_8O^a$	−2.07	0.11	0.10	0.03	0	0.57
$Pd_{13}/C_8H_8O^b$	−2.18	0.27	0.50	0.59	0	1.02
$Pd_{13}/(C_8H_8O)_3$	−6.11	0.03	0	0.06	0.34	
$Pd_{13}/(C_8H_8O)_5$	−8.41	0	0.01	0.35		
$Pd_8/(C_8H_8O)_5$	−5.98	0	0.17	0.85		

Columns three to seven list the energies of configurations with other magnetic moments relative to the ground state configuration. Numbers are given in eV and refer to def2-TZVP/PBE, except for *a* and *b*, which list PBE-D3 and PBE0-D3 results as a crosscheck. See main text for details

[a] PBE-D3

[b] PBE0-D3

any significant distortions of the C_s bilayer geometry through a single acetophenone. Second, in the case of an initially parallel orientation, our relaxed structures show that the benzene ring upholds the parallel orientation. In addition, the tilted parallel initial structures (cf. Fig. 3c) transition into a parallel arrangement (cf. Fig. 3a). For the parallel orientation, our binding energies range from −1.43 eV to −1.67 eV for a magnetic moment of $6\,\mu_B$. Third, relaxing the perpendicular initial situation leads to geometries in which CO stays closer to the C_s bilayer surface than the CH_3 group, and the acetophenone remains perpendicular to the surface (similar to Fig. 3b). Inclined perpendicular initial structures (cf. Fig. 3d) generally transition into a clear parallel arrangement (cf. Fig. 3a). However, we also observed in some relaxations that initially perpendicular structures, both with and without inclination, flipped into a parallel geometry. In the perpendicular arrangement, the binding energies range from −0.27 eV to −0.78 eV ($6\,\mu_B$). One can thus conclude that the parallel orientation is clearly the preferred one. An explanation of this finding is provided by analyzing the spatial structure of the valence orbitals. For the parallel arrangement, their probability density delocalizes not only over the cluster, but to some extent also over the molecule, and this results in a lower energy.

The magnetic moment of the combined system is the same as for the bare Pd_{13}, but we occasionally observe stable configurations with lower magnetic moments. The first row of Table 1 summarizes the energetic ordering of the different spin configurations. In each case the table refers to the most stable structure that we found.

We also checked the robustness of the predicted spin configurations with respect to the xc approximation. To this end, we took the parallel initial structures that lead to the most stable configurations with PBE and repeated the optimization using PBE-D3 and PBE0-D3, respectively. The resulting binding energies and energy difference are listed in the second and third rows of Table 1. Reassuringly, both D3 corrected functionals also predict a $6\,\mu_B$ spin magnetic ground state. The energetic ordering of the higher states changes to some extent, but this is not surprising given the small energetic differences between them. Overall, the test confirms the strategy of using PBE for the extensive geometry optimizations.

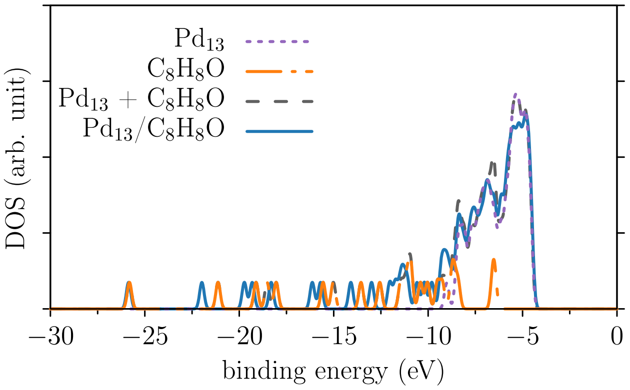

Fig. 4 DOS of Pd_{13}, C_8H_8O, the sum of the DOSs of Pd_{13} and C_8H_8O, and the DOS of the combined system Pd_{13}/C_8H_8O, all obtained from DFT ground state calculations with PBE. The underlying geometry is the one of the parallel arrangement obtained with PBE-D3. See main text for details

Some insight into the electronic interaction between Pd_{13} and C_8H_8O can be obtained from the DOS. The full line in Fig. 4 shows the DOS obtained for the parallel arrangement of Pd_{13}/C_8H_8O. The different dashed lines show the DOS for the separate subsystems Pd_{13} and C_8H_8O, and the sum of the DOSs of the individual subsystems (line labeled $Pd_{13} + C_8H_8O$), as indicated in the inset of Fig. 4. The comparison of the DOSs of the subsystems to the one of the combined system shows that near the Fermi level (HOMO energy, cf. "Appendix A", Table 5) the DOS of the combined system is dominated by Pd_{13} (down to about −8 eV), whereas in the low energy region (below ca. 10 eV) it is dominated by C_8H_8O. The comparison of the DOS of the combined system to the sum of the two independent DOSs however reveals that there is also some electronic interaction, because the two are not identical. Calculating the DOS with PBE0 yields the same qualitative trend (cf. "Appendix A", Fig. 13).

The Bader charge density analysis for the parallel arrangement obtained with PBE-D3 shows a charge transfer of some $0.20\,\mathrm{e}^- \approx 0.2\,\mathrm{e}^-$ from the Pd_{13} cluster to the acetophenone molecule, where e^- is the negative elementary charge. Performing the same analysis with PBE0 for the parallel arrangement obtained with PBE0-D3 yields the same qualitative trend with a charge transfer of some $0.26\,\mathrm{e}^- \approx 0.3\,\mathrm{e}^-$, i.e., the qualitative results are robust with respect to the influence of the xc approximation.

3.2 Pd_{13} with three acetophenone molecules

We worked our way towards a more realistic description of solvation by combining the $\mathrm{Pd}_{13}(C_s)$ cluster with three acetophenone molecules carrying out constant temperature DFT-MD simulations, following the procedure described in Sect. 2. We did separate DFT-MD runs for each of the magnetic moments $\mu \in [0, 2, 4, 6]\mu_\mathrm{B}$. As the start configuration we arranged two acetophenone molecules parallel and one perpendicular to the Pd surface. During the first ca. 1.2 ps the system restructures considerably as it moves from the initial geometry to a lower energy configuration: The one acetophenone that initially had a perpendicular orientation with respect to Pd_{13} angles rapidly into a more stable parallel orientation, which further corroborates the results of the previous section. Then all three solvent molecules keep this type of orientation. This deforms the initial C_s bilayer and for all of the following simulation time stabilizes a new Pd_{13} structure with a higher spatial symmetry D_{5h}. The two basic structural motives are depicted by the insets in Fig. 5a.

In order to see which magnetic moment does now become the energetically preferred one, we record the total energy for each of the runs with different spin configurations. Because of the pronounced, rapid fluctuations in the total energy that are an inherent feature of MD simulations, the decisive trends are easier to see when one averages over some of those fluctuations. Therefore, Fig. 5 depicts the data in two different ways. First, we defined the average energy $\bar{E}(t)$ at a given time $t = t_i$ by

$$\bar{E}(t_i) = \frac{\sum_{j=1}^{i} E_\mathrm{tot}(t_j)}{i}, \tag{2}$$

i. e., as the average over all of the previous discrete time steps i, including the current one. Here, $1 \leq i \leq N_\mathrm{t}$ and the total number of time steps was $N_\mathrm{t} \approx 3100$. Averaging in this way over an increasing number of geometries allows to visualize the trend in the simulations, with fluctuations being totally averaged out. One thus obtains a direct depiction of the total energy trend for each spin configuration. (The more detailed information from a moving average is discussed below.) Figure 5a shows $\bar{E}(t)$ for the simulations of Pd_{13} with three acetophenone molecules. For the sake of convenient energy axis labels, an offset $\bar{E}(t) - E_{ref}$ is used in the plots of Fig. 5, where $E_{ref} = 76617$ eV. After the above mentioned restructuring there is a clear change in the preferred magnetic moment. Figure 5a shows that the DFT-MD run with zero magnetic moment leads to the lowest average energy. The $4\,\mu_\mathrm{B}$ structures are slightly higher in energy, and the $2\,\mu_\mathrm{B}$ and $6\,\mu_\mathrm{B}$ are noticeably higher.

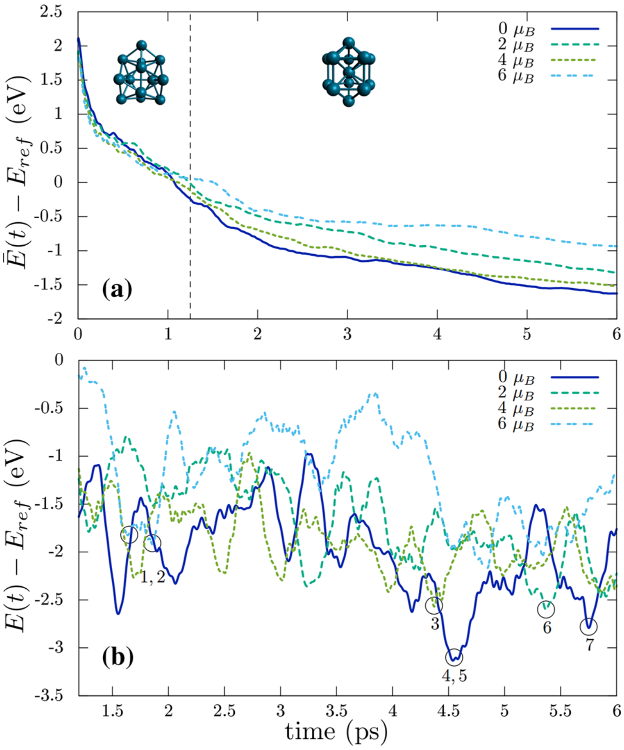

Fig. 5 Total energy analysis of the DFT-MD simulation of Pd_{13} and three acetophenone molecules. The different curves show the simulations for different, fixed magnetic moments. **a** Averaged total energy $\bar{E}(t)$. The vertical line indicates the restructuring period and the insets depict the structure of the central Pd cluster before and after the restructuring. **b** Moving average of the total energy $E(t)$. Inset: At the marked energy minima $min_\mathrm{MD} = 1, \ldots, 7$ structures were extracted for further optimization. See main text for details

For a more detailed insight Fig. 5b depicts the total energy curve of the DFT-MD runs for each magnetic moment. In this plot we used a moving average $E(t)$ of the total energy: At t_i we averaged the total energy over the previous and subsequent Δ time steps:

$$E(t = t_i) = \frac{\sum_{j=i-\Delta}^{i+\Delta} E_\mathrm{tot}(t_j)}{(2\Delta + 1)}, \tag{3}$$

where $\Delta = 50$, $i - \Delta \geq 1$ and $i + \Delta \leq N_t$. Δ was chosen such that some of the smaller energy fluctuations were smoothed out, while preserving the main progression of the (unaveraged) total energy. Comparing $E(t)$ for the different magnetic moments in Fig. 5b confirms that $0\,\mu_\mathrm{B}$ leads to the lowest energy.

In order to confirm yet further which magnetic moment is the energetically preferred one, we selected

Table 2 Binding energies $E_{\rm B}(min_{\rm MD})$ of relaxed structures of Pd_{13} and three acetophenone molecules for different magnetic moments, in eV

μ	$E_{\rm B}(1)$	$E_{\rm B}(2)$	$E_{\rm B}(3)$	$E_{\rm B}(4)$	$E_{\rm B}(5)$	$E_{\rm B}(6)$	$E_{\rm B}(7)$
$0\,\mu_{\rm B}$	−5.96	−5.74	−6.07	−6.00	−5.94	−6.08	−5.95
$2\,\mu_{\rm B}$	−5.90	−5.94	−5.83	−5.99	−5.98	−6.11	−5.98
$4\,\mu_{\rm B}$	−5.90	−5.92	−5.82	−5.74	−5.80	−6.05	−5.80
$6\,\mu_{\rm B}$	−5.61	−5.39	−5.71	−4.90	−4.95	−5.77	−5.07

Low-energy structures obtained from DFT-MD simulations, marked $min_{\rm MD} = 1, \ldots, 7$ in Fig. 5b, served as the unrelaxed initial structures

some of the low energy structures from each run. These are marked by the small circles numbered from 1 to 7 in Fig. 5b, and we refer to these numbers with the notation $min_{\rm MD}$ in the following. We optimized (relaxed) these structures to the energetic minimum in separate calculations. Table 2 lists the binding energy $E_{\rm B}(min_{\rm MD})$ for the relaxed structures.

The relaxed structures show a $0\,\mu_{\rm B}$ or $2\,\mu_{\rm B}$ ground state. In some cases, the binding energies for the $[0, 2, 4]\,\mu_{\rm B}$ structures lie energetically close together, and one has to keep in mind that the employed xc approximations have a finite accuracy. However, the $6\,\mu_{\rm B}$ configurations are quite noticeably less favored. A geometrical analysis of the relaxed structures shows that the distance between the benzene rings of the solvent shell and the Pd surface is on average ca. 1.98 Å.

Solvation thus clearly reduces the magnetic moment, and this raises the question of why that is. It could be a direct effect of the electronic interaction between the acetophenone molecules and the Pd_{13} cluster, or it could be an indirect effect if the new D_{5h} geometry of Pd_{13} that is triggered by the solvation is associated with a lower magnetic moment than the original C_s structure. We checked for this by computing the magnetic moment of the D_{5h} structure in vacuum. First, we took the Pd_{13} coordinates from the $Pd_{13}/(C_8H_8O)_3$ arrangement and calculated the ground state for this bare Pd_{13} structure without the acetophenone molecules. It shows a magnetic moment of $8\,\mu_{\rm B}$. As a further check we also energetically optimized the extracted structure. The relaxed (bare) D_{5h} cluster also has an $8\,\mu_{\rm B}$ magnetic ground state, and it is 0.41 eV higher in energy than the C_s bilayer structure with $6\,\mu_{\rm B}$. Thus, the reduction of the magnetic moment is a direct consequence of the electronic interaction with the acetophenone.

The conclusion that there is a substantial interaction between the cluster and the solvent molecules is also confirmed by analyzing the DOS and the charge transfer. The DOS of $Pd_{13}/(C_8H_8O)_3$ can neither quantitatively nor qualitatively be explained from the superposition of the DOSs of the separate subsystems Pd_{13} and $(C_8H_8O)_3$, as depicted in Fig. 6. The differences are very noticeable, e.g., in the peak structure close to the Fermi level. Compared to the scenario with a single acetophenone molecule, the differences are overall more pronounced. Also the charge transfer from the Pd_{13} cluster to the solvent molecules is more pronounced than in the scenario with one acetophenone, with a value of $\approx 0.7\,e^-$.

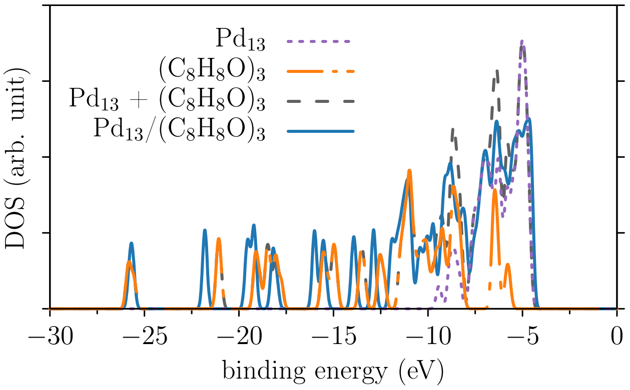

Fig. 6 DOS of Pd_{13}, $(C_8H_8O)_3$, the sum of the DOSs of Pd_{13} and $(C_8H_8O)_3$, and the DOS of the combined system $Pd_{13}/(C_8H_8O)_3$, obtained from DFT ground state calculations with PBE. See main text for details

3.2.1 Pd_{13} with five acetophenone molecules

By combining Pd_{13} with five acetophenone molecules we reach a situation in which the metal cluster is surrounded by the solvent molecules. We used the $Pd_{13}(D_{5h})$ structure from the previous section, i. e., the one stabilized by three acetophenone molecules (cf. Fig. 1d) as the initial geometry for Pd_{13}, and the five acetophenones were initially aligned parallel to the Pd surface. We then again ran separate DFT-MD simulations for each of the magnetic moments $\mu \in [0, 2, 4]\mu_{\rm B}$. Due to the results of the previous section we did not study higher magnetic moments. In the initial phase of the DFT-MD simulations we observed a restructuring of the central Pd_{13}: The solvent shell stabilized an icosahedral I_h cluster (cf. Fig. 7, inset). After this phase, the averaged total energy $\bar{E}(t)$ of the DFT-MD runs plotted in Fig. 7 shows a clear tendency towards a quenching of the spin magnetic moment to either $0\,\mu_{\rm B}$ or $2\,\mu_{\rm B}$, with $4\,\mu_{\rm B}$ being noticeably higher in energy.

We extracted five of the lowest-energy structures from the DFT-MD runs, and their relaxations confirmed the trend: $0\,\mu_{\rm B}$ or $2\,\mu_{\rm B}$ are the preferred low-energy states, while $4\,\mu_{\rm B}$ is clearly higher in energy by some 0.10 eV to 0.45 eV. The most stable structure,

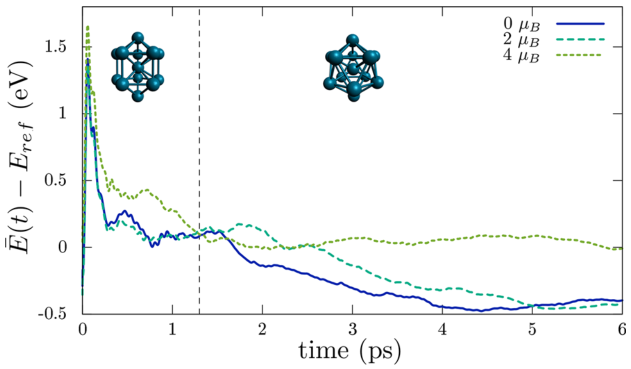

Fig. 7 Averaged total energy $\bar{E}(t)$ of the DFT-MD simulation of Pd_{13} and five acetophenone molecules ($E_{ref} = 97525$ eV). Inset: Initial restructuring phase of ≈ 1.3 ps (vertical line) and the central Pd cluster before and after the restructuring. See main text for details

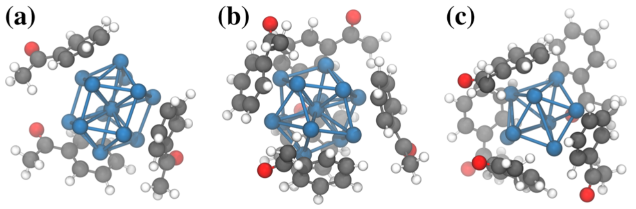

Fig. 8 Optimized structures of Pd_{13} surrounded by a solvent shell of **a** three and **b** five acetophenone molecules. The solvent shells tend to stabilize clusters with a high spatial symmetry. The lowest energy structure of Pd_8 with five acetophenone molecules is depicted in **c**

shown in Fig. 8b, has a binding energy of −8.41 eV with $0\,\mu_B$ (cf. Table 1, line 6). A structure with $2\,\mu_B$ is quasi degenerate, and $4\,\mu_B$ is distinctly less favorable by 0.35 eV.

We also tested again whether the reduction of the magnetic moment is a direct or an indirect effect by calculating the density and the magnetic moment for the bare Pd_{13} in the geometry that it takes in the $Pd_{13}/(C_8H_8O)_5$ arrangement. The bare extracted Pd_{13} cluster recovers the $8\,\mu_B$ that was also found in the optimized I_h structure. This confirms the conclusion of the previous section that the quenching of the magnetic moment is a consequence of an electronic interaction between acetophenone and the metal cluster.

Again, the electronic interaction is also reflected in the charge density and the DOS of $Pd_{13}/(C_8H_8O)_5$: Firstly, the charge transfer from Pd_{13} to the solvent shell continues to increase, to about $1.2\,e^-$. The charge transfer occurs predominantly to the C atoms of the benzene-like ring of all five acetophenone molecules. Secondly, the DOS of the combined system clearly differs from that of the superposition of the stabilized Pd_{13} cluster and the solvent shell (cf. Fig. 9), as seen, e. g., close to the Fermi level. Thus, the stabilized Pd_{13} cluster interacts with the entire shell of five acetophenones.

An analysis of the orbitals of the combined $Pd_{13}/(C_8H_8O)_5$ system with $0\,\mu_B$ corroborates that there is substantial electronic interaction: Many of the valence orbitals are delocalized over all five acetophenone molecules and the central Pd_{13} cluster. This is exemplary shown in Fig. 10a for the highest-occupied molecular orbital (HOMO) of $Pd_{13}/(C_8H_8O)_5$ with $0\,\mu_B$, computed with PBE. Because it is well known that semilocal exchange-correlation functionals tend to overestimate orbital delocalization, we repeated this calculation with the PBE0 functional. Figure 10b shows the HOMO from the PBE0 calculation, and the similarity to panel (a) is apparent. We have furthermore checked the 15 highest occupied orbitals and found that both functionals predict a qualitatively very similar delocalization for these. We can therefore conclude that the observed delocalization is not an artifact of the semilocal xc approximation.

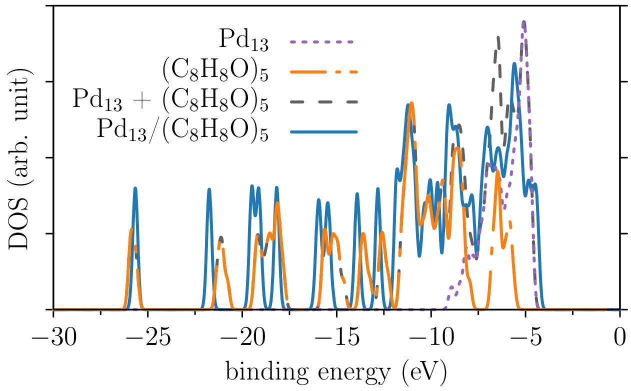

Fig. 9 DOS of Pd_{13}, $(C_8H_8O)_5$, the sum of the DOSs of Pd_{13} and $(C_8H_8O)_5$, and the DOS of the combined system $Pd_{13}/(C_8H_8O)_5$, obtained from DFT ground state calculations with PBE. See main text for details

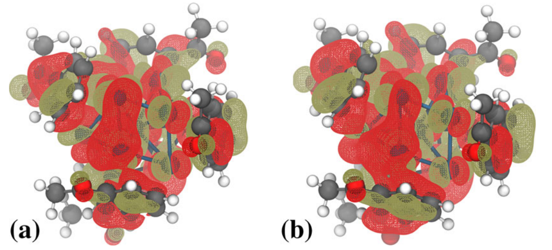

Fig. 10 HOMO of $Pd_{13}/(C_8H_8O)_5$ with $0\,\mu_B$ obtained from a ground state calculation with **a** PBE and **b** PBE0. Tan and red colors correspond to positive and negative values, respectively. The plots used an isovalue of 0.01 bohr^{-3}

3.2.2 Pd_8 with five acetophenone molecules

As the final step of our investigation, we check whether the reduction of the magnetic moment upon solvation is specific to Pd_{13}, or also occurs for another system. To this end, we started from the C_{2v} bicapped octahedron Pd_8 shown in Fig. 2b with a $4\,\mu_B$ ground state and surrounded the cluster by a solvent shell of five ace-

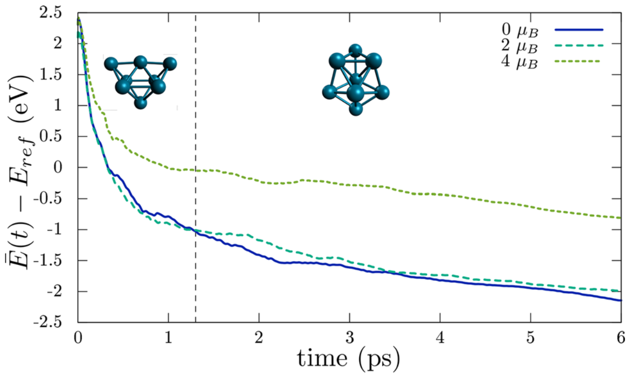

Fig. 11 Averaged total energy $\bar{E}(t)$ of the DFT-MD simulation for Pd_8 and five acetophenone molecules (E_{ref} = 80,115 eV). Inset: Initial restructuring phase of ≈ 1.3 ps (vertical line), and the central Pd_8 cluster before and after. See main text for details

tophenone molecules in parallel alignment towards the Pd surface.

We then ran separate DFT-MD simulations of the composite system for each of the magnetic moments $\mu \in [0, 2, 4]\mu_B$. In the initial phase of the DFT-MD simulations, we observed a restructuring of the central Pd_8 during which the solvent shell stabilized another bicapped octahedron isomer (cf. Fig. 11, inset) with a reduced symmetry C_1. After this phase, the averaged total energy $\bar{E}(t)$ plotted in Fig. 11 shows a clear trend towards a quenching of the magnetic moment: Both $0\,\mu_B$ and $2\,\mu_B$ structures are clearly lower in energy than the $4\,\mu_B$ ones. The relaxation of the two lowest-energy structures from the DFT-MD runs leads to a $0\,\mu_B$ ground state and thus further confirms the reduction of the magnetic moment. The most stable arrangement, see Fig. 8c, has a binding energy of −5.98 eV with $0\,\mu_B$. $2\,\mu_B$ is 0.17 eV higher in energy, and $4\,\mu_B$ is clearly less favorable by 0.85 eV (cf. Table 1, line 5).

We again computed the magnetic moment for the metal cluster in the geometry that it takes in the $Pd_8/(C_8H_8O)_5$ arrangement with $0\,\mu_B$. Without the acetophenone molecules, the magnetic moment goes up to $4\,\mu_B$, with a $2\,\mu_B$ configuration just slightly higher (0.03 eV) in energy. We also again found a delocalization of the valence orbitals over the metal cluster and acetophenone molecules.

We also analyzed the charge density and the Kohn-Sham DOS in the same way as for the Pd_{13} cluster surrounded by acetophenone. This revealed a charge transfer of about $1.0\,e^-$ from the Pd_8 cluster to the solvent shell. The DOS of the combined system $Pd_8/(C_8H_8O)_5$ also differs noticeably from the DOS that results from summing the DOSs of the molecular components (cf. Fig 12). Thus, all the effects observed for Pd_{13} are also found for Pd_8, which is a strong hint that these findings are general.

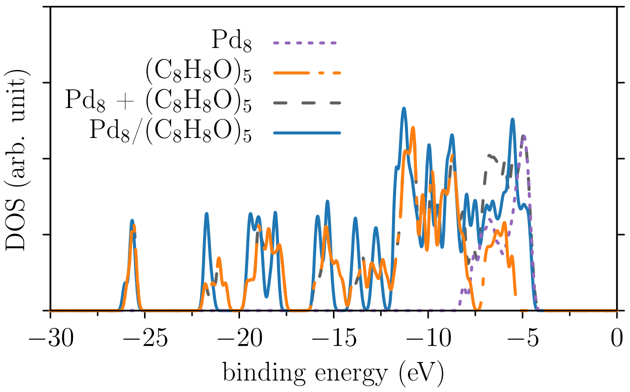

Fig. 12 DOS of $Pd_8/(C_8H_8O)_5$, Pd_8, $(C_8H_8O)_5$, and the sum of the DOS of Pd_8 and $(C_8H_8O)_5$ obtained from DFT ground state calculations with PBE. See main text for details

4 Discussion and conclusion

We used DFT-Born–Oppenheimer MD simulations combined with further geometry optimizations to study how the magnetic moment of Pd clusters changes when those are solvated in the organic solvent acetophenone. Our study focused on Pd_8 and Pd_{13} as the vacuum ground states of these systems are clearly established, have a nonzero magnetic moment, and as these clusters have isomers that show a range of paradigm geometries. Our simulations reveal a clear trend towards a reduction of the magnetic moment. For both clusters the calculations with the largest number of solvent molecules lead to ground states with a zero magnetic moment. Analysis of the molecular orbitals shows that there is a pronounced interaction between the Pd particles and the acetophenone molecules, with the valence orbitals delocalizing over both the metal and the acetophenone. The interaction also manifests in a noticeable charge transfer from the metal cluster to the solvent molecules, and in clear signatures in the DOS. Putting these findings into perspective with earlier studies, we note that the presence of one benzyl alcohol and one benzylamine molecule also lead to a reduction of the magnetic moment of Pd clusters [18,19]. Futschek et al. reported that the quenching of the magnetic moment can also occur in the composite systems of Pd_{13} with the ligands phosphine and thiol [25]. Interestingly, however, the quenching is less pronounced for phospines, as there the system retains a $4\,\mu_B$ state even with high ligand coverage.

Our results show that detecting solvated Pd particles via their magnetic moment, and in this way contributing to answering the “leaching” question that was discussed in the introduction, is going to be difficult when the solvent is acetophenone. The situation may be different, though, for solvents that do not interact as strongly. Our study provides hints that the aromatic character of acetophenone plays an important role in the electronic interaction that leads to the magnetic quenching. In order to check this hypothesis, we computed as an outlook the interaction between Pd_{13} and five acetone molecules. The results are reported in "Appendix B" and show that, indeed, the interaction and magnetic moment quenching are less pronounced for these smaller solvent molecules that do not feature an aromatic ring. Thus, avoiding the strong metal-solvent interaction triggered by the aromatic character is a close lying first step on the search for solvents that preserve the magnetic moment.

Acknowledgements Financial support from the German Research Foundation (DFG SFB 840, B1), from the Bavarian State Ministry of Science, Research, and the Arts for the Collaborative Research Network "Solar Technologies go Hybrid", and from the Bavarian Polymer Institute (KeyLab Theory and Simulation) in terms of computing resources is gratefully acknowledged.

Author contributions

SH ran all calculations that are reported in the paper. SK supervised the work and SH and SK discussed the results regularly. LL introduced SH to technical aspects of using Turbomole. SH and SK wrote the manuscript, with suggestions and comments also from LL. All authors were involved in the scientific discussion of the results and in drawing the conclusions.

Funding Open Access funding enabled and organized by Projekt DEAL.

Data Availability Statement This manuscript has associated data in a data repository. [Authors' comment: The atomic coordinates for the clusters shown in Figures 1 and 2 are provided as xyz-files.]

Appendix A: Electronic structure details

Tables 3 and 4 complement the discussion on the Pd_{13} and Pd_8 cluster isomers of Sect. 2, respectively. Both tables list the total energy of the most stable arrangement (column 3) and the energy differences to configurations with other magnetic moments relative to the former (column 4 and the following) for PBE and PBE0 (column 2). Relaxing $Pd_{13}(D_{5h})$ with PBE0 did not lead to a stable configuration, and $Pd_8(D_{2d})$ with $0\,\mu_B$ was not stable with PBE, therefore no numbers are reported for these cases.

As a further insight into the electronic structure we report how the binding between the Pd cluster and acetophenone affects the energetic position of the frontier orbitals. Table 5 lists the highest occupied molecular orbital (HOMO) eigenvalue and the size of the energy gap to the lowest unoccupied molecular orbital (LUMO) for the most stable arrangement that we found for each composite system M/S, and the same quantities for the different bare cluster isomers and solvent molecules.

For the most stable parallel arrangement of Pd_{13}/C_8H_8O with $6\,\mu_B$ obtained with PBE (line 1), the HOMO is at −4.46 eV and the gap to the LUMO is 0.10 eV. The comparison with the (bare) components $Pd_{13}(C_s)$ (line 6) and C_8H_8O (line 11) shows that both the HOMO and LUMO eigenvalue of the combined system are very similar to the values for the (bare) metal cluster. For the D3-corrected structures of Pd_{13}/C_8H_8O and its components, the HOMO energy and gap deviate by only ±0.01 eV from the values given in Table 5 and are therefore not listed separately.

For the most stable arrangement of $Pd_{13}/(C_8H_8O)_3$, shown in Fig. 8a, the HOMO eigenvalue is −4.43 eV and the gap to the LUMO is 0.11 eV (cf. Table 5,

Table 3 Total energy E_{tot} (third column) for the PBE and PBE0 xc functional (xc, second column) for the lowest energy configuration for each of the Pd_{13} cluster isomers (first column) shown in Fig. 1. Columns four to seven list how much higher in energy other spin configurations (i.e., magnetic moments) are. Numbers are given in eV and refer to def2-TZVP/xc

	xc	E_{tot}	$2\,\mu_B$	$4\,\mu_B$	$6\,\mu_B$	$8\,\mu_B$
$Pd_{13}(C_s)$	PBE	−45,269.83	0.20	0.14	0	0.25
$Pd_{13}(C_s)$	PBE0	−45,253.03	0.15	0.15	0	0.17
$Pd_{13}(C_{3v})$	PBE	−45,269.72	0.06	0.05	0	0.25
$Pd_{13}(C_{3v})$	PBE0	−45,253.35	0.19	0.08	0	0.37
$Pd_{13}(I_h)$	PBE	−45,269.74	0.42	0.31	0.18	0
$Pd_{13}(I_h)$	PBE0	−45,253.30	0.43	0.28	0.16	0
$Pd_{13}(D_{5h})$	PBE	−45,269.42	0.27	0.18	0.08	0

Table 4 Total energy E_{tot} (third column) for the PBE and PBE0 xc functional (xc, second column) for the most stable arrangement of the Pd_8 cluster isomers (first column) shown in Fig. 2. Columns four to six list how much higher in energy other spin configurations (i.e., magnetic moments) are. Numbers are given in eV and refer to def2-TZVP/xc

	xc	E_{tot}	$0\,\mu_{\mathrm{B}}$	$2\,\mu_{\mathrm{B}}$	$4\,\mu_{\mathrm{B}}$
$Pd_8(D_{2d})$	PBE	−27,856.13	–	0.02	0
$Pd_8(D_{2d})$	PBE0	−27,846.32	0.74	0.10	0
$Pd_8(C_{2v})$	PBE	−27,855.74	0.17	0.09	0
$Pd_8(C_{2v})$	PBE0	−27,846.05	0.58	0.12	0
$Pd_8(C_1)$	PBE	−27,856.03	0.11	0.08	0
$Pd_8(C_1)$	PBE0	−27,846.27	0.11	0.08	0

Table 5 HOMO eigenvalue $\varepsilon_{\mathrm{HOMO}}$ (second column) and magnitude of the HOMO-LUMO gap Δ_{s} (third column) for the systems given in the first column

	$\varepsilon_{\mathrm{HOMO}}$	Δ_{s}
$Pd_{13}(C_s)/C_8H_8O$	−4.46	0.10
$Pd_{13}(D_{5h})/(C_8H_8O)_3$	−4.43	0.11
$Pd_{13}(I_h)/(C_8H_8O)_5$	−4.27	0.19
$Pd_8(C_1)/(C_8H_8O)_5$	−4.24	0.37
$Pd_{13}(I_h)/(C_3H_6O)_5$	−3.86	0.07
$Pd_{13}(C_s)$	−4.53	0.15
$Pd_{13}(I_h)$	−4.66	0.09
$Pd_{13}(D_{5h})$	−4.62	0.11
$Pd_8(D_{2d})$	−4.39	0.10
$Pd_8(C_1)$	−4.38	0.17
C_8H_8O	−5.69	3.07
C_3H_6O	−5.62	4.00

The numbers given refer to the most stable arrangement of each composite systems M/S (lines 1–5). For comparison, the same quantities are reported for the stabilized Pd clusters (lines 6–11) and the two solvent molecules (12–13). Numbers are given in eV and refer to def2-TZVP/PBE

line 2). The HOMO of the most stable arrangement of $Pd_{13}/(C_8H_8O)_5$ (cf. Fig. 8b) is at −4.27 eV and the LUMO is 0.19 eV higher in energy (line 3). Thus, compared to the systems with one and three acetophenone molecules, the energy of the HOMO is slightly higher and the gap to the LUMO is slightly larger. The results show that the size of the acetophenone solvent shell has a rather small influence on the HOMO and LUMO.

For completeness, we also included the most stable arrangement of $Pd_8/(C_8H_8O)_5$ (cf. Fig. 8c) in Table 5. The comparison with the separate components shows that also here, the HOMO and LUMO energies are dominated by the Pd cluster (cf. lines 4, 10 and 11).

Finally, we also report results that allow to check the influence of the xc approximation. To this end we looked at the relaxed PBE0-D3 structures of Pd_{13}/C_8H_8O, $Pd_{13}(C_s)$ and C_8H_8O. As expected, the hybrid PBE0 yields a lower HOMO energy and a larger HOMO-LUMO gap for each system: The HOMO of $Pd_{13}(C_s)/C_8H_8O$ (Pd_{13}) is at −5.03 eV (−5.14 eV), and the LUMO is 1.69 eV (1.69 eV) higher. Otherwise, however, the qualitative picture closely corresponds to the one found with PBE. This conclusion is also supported by Fig. 13, which shows the PBE0 DOS computed within the relaxed PBE0-D3 structure for the parallel arrangement of Pd_{13}/C_8H_8O, cf. Sect. 3.1.

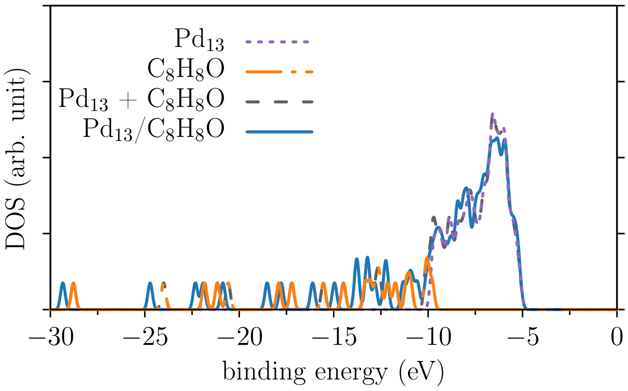

Fig. 13 DOS of Pd_{13}/C_8H_8O, Pd_{13}, C_8H_8O, and the sum of the DOS of Pd_{13} and C_8H_8O obtained from DFT ground state calculations with PBE0

Appendix B: Pd_{13} with five acetone molecules

We here report results for a different solvent to provide an outlook on possible future work. A non-aromatic solvent makes for an interesting comparison, because our findings for acetophenone indicate that the aromatic ring plays an important role in the binding and interaction with the palladium clusters. The results reported here are to be understood as a first, qualitative test.

To keep the differences between the solvents small except for the missing aromatic ring, we remained in the family of ketones and selected acetone (C_3H_6O), which is the simplest of them and of similar polarity as acetophenone. We combined Pd_{13} with five acetone molecules, which compares best with Pd_{13} with three acetophenones in terms of the total system size, and with $Pd_{13}/(C_8H_8O)_5$ in terms of the number of solvent molecules. We chose $Pd_{13}(I_h)$ as the initial geometry for the cluster and calculated optimized structures of $Pd_{13}/(C_3H_6O)_5$ in analogy to the procedures described in the previous sections on acetophenone (cf. also Sect. 2).

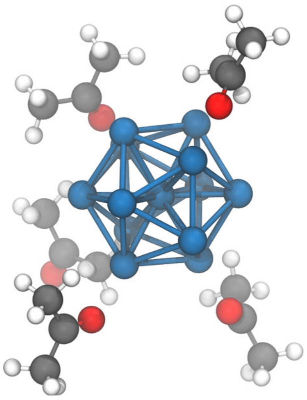

Fig. 14 Optimized structure of Pd_{13} surrounded by five acetophenone molecules. See main text for details

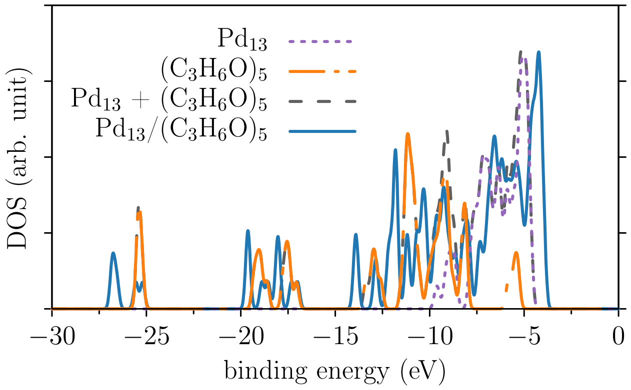

Fig. 15 DOS of $Pd_{13}/(C_8H_8O)_5$, Pd_8, $(C_3H_6O)_5$, and the sum of the DOS of Pd_8 and $(C_3H_6O)_5$ obtained from DFT ground state calculations with PBE. See main text for details

The thus determined most stable arrangement, see Fig. 14, has a binding energy of −3.39 eV and prefers $6\,\mu_B$ with PBE. An arrangement with $4\,\mu_B$ is slightly less favorable by 0.04 eV, followed by $2\,\mu_B$ by 0.08 eV, $0\,\mu_B$ by 0.18 eV, and $8\,\mu_B$ by 0.19 eV. The binding between Pd_{13} and the acetone shell is thus smaller than in the acetophenone systems with similar system size or number of solvent molecules, respectively. For $Pd_{13}/(C_3H_6O)_5$, the quenching to $6\,\mu_B$ - compared to the $8\,\mu_B$ of the $Pd_{13}(I_h)$ cluster in vacuum - is also caused by an electronic interaction, as revealed by the analysis of the stabilized Pd_{13} cluster, which we performed in analogy to the acetophenone systems. However, the quenching is considerably less pronounced than in the comparable acetophenone systems.

We then further characterized the electronic structure in analogy to the previous sections: For the most stable arrangement, the HOMO is at −3.86 eV and the HOMO-LUMO gap is 0.07 eV (cf. "Appendix A", Table 5, line 5). The comparison with the (bare) molecular subsystems $Pd_{13}(I_h)$ (line 7) and C_3H_6O (line 12) shows that both the HOMO and LUMO eigenvalues of the combined system are determined mostly by the (bare) metal cluster.

The binding between Pd_{13} and $(C_3H_6O)_5$ is reflected in the corresponding DOS by qualitative and quantitative changes that one observes when comparing to the superposition of the molecular components, as depicted in Fig. 15. Overall, this suggests a direct electronic interaction between the cluster and the solvent, and in this respect the effects are similar to those found for acetophenone. However, the two solvents differ significantly with respect to the inter-molecular charge transfer: About $0.3\,e^-$ is transferred from Pd_{13} to the acetone shell, which is a factor of about 2 and 4 less than for $Pd_{13}/(C_8H_8O)_3$ and $Pd_{13}/(C_8H_8O)_5$, respectively. The reduced charge transfer, together with the reduced magnetic moment quenching indicate that non-aromatic solvents may better preserve the magnetic moment of solvated clusters.

References

1. M. Brack, Rev. Mod. Phys. **65**, 677–732 (1993)
2. W.A. DeHeer, Rev. Mod. Phys. **65**, 611–676 (1993)
3. Z. Luo, A.W. Castleman, S.N. Khanna, Chem. Rev. **116**, 14456–14492 (2016)
4. D. Srimani, S. Sawoo, A. Sarkar, Org. Lett. **9**, 3639–3642 (2007)
5. G. Johnson, R. Mitric, V. Bonacic-Koutecky, A.J. Castleman, Chem. Phys. Lett. **475**, 1–9 (2009)
6. R. Jana, T.P. Pathak, M.S. Sigman, Chem. Rev. **111**, 1417–1492 (2011)
7. B. Yoon, U. Landman, V. Habibpour, C. Harding, S. Kunz, U. Heiz, M. Moseler, M. Walter, J. Phys. Chem. C **116**, 9594–9607 (2012)
8. A. Dhakshinamoorthy, H. Garcia, Chem. Soc. Rev. **41**, 5262–5284 (2012)
9. J. Souto-Casares, M. Sakurai, J. Chelikowsky, Phys. Rev. B **93**, 174418 (2016)
10. J.-X. Liu, Y. Su, I.A.W. Filot, E.J.M. Hensen, J. Am. Chem. Soc. **140**, 4580–4587 (2018)
11. L. Goncalves, J. Wang, S. Vinati, E. Barborini, X.-K. Wei, M. Heggen, M. Franco, J. Sousa, D.Y. Petrovykh, O.S.G.P. Soares, K. Kovnir, J. Akola, Y.V. Kolen'ko, Int. J. Hydrog. Energy **45**, 1283–1296 (2020)
12. V. Subramanian, E. Wolf, P.V. Kamat, J. Phys. Chem. B **105**, 11439–11446 (2001)
13. P.V. Kamat, J. Phys. Chem. B **106**, 7729–7744 (2002)
14. S. Füldner, R. Mild, H.I. Siegmund, J.A. Schroeder, M. Gruber, B. König, Green Chem. **12**, 400–406 (2010)
15. M.-C. Wu, J. Hiltunen, A. Sápi, A. Avila, W. Larsson, H.-C. Liao, M. Huuhtanen, G. Tóth, A. Shchukarev, N. Laufer, Á. Kukovecz, Z. Kónya, J.-P. Mikkola, R. Keiski, W.-F. Su, Y.-F. Chen, H. Jantunen, P.M. Ajayan, R. Vajtai, K. Kordás, ACS Nano **5**, 5025–5030 (2011)
16. C. Wang, K.E. Dekrafft, W. Lin, J. Am. Chem. Soc. **134**, 7211–7214 (2012)
17. S. Sarina, E. Jaatinen, Q. Xiao, Y.M. Huang, P. Christopher, J.C. Zhao, H.Y. Zhu, J. Phys. Chem. Lett. **8**, 2526–2534 (2017)
18. D. Tilgner, M. Klarner, S. Hammon, M. Friedrich, A. Verch, N. de Jonge, S. Kümmel, R. Kempe, Aust. J. Chem. **72**, 842–847 (2019)

19. M. Klarner, S. Hammon, S. Feulner, S. Kümmel, L. Kador, R. Kempe, ChemCatChem **12**, 4593–4599 (2020)
20. A.J. Cox, J.G. Louderback, S.E. Apsel, L.A. Bloomfield, Phys. Rev. B **49**, 12295–12298 (1994)
21. K. Lee, Phys. Rev. B **58**, 2391–2394 (1998)
22. M. Moseler, H. Häkkinen, R.N. Barnett, U. Landman, Phys. Rev. Lett. **86**, 2545–2548 (2001)
23. P. Nava, M. Sierka, R. Ahlrichs, Phys. Chem. Chem. Phys. **5**, 3372–3381 (2003)
24. E. Aprà, A. Fortunelli, J. Phys. Chem. A **107**, 2934–2942 (2003)
25. T. Futschek, M. Marsman, J. Hafner, J. Phys. Condens. Matter **17**, 5927–5963 (2005)
26. L.-L. Wang, D.D. Johnson, Phys. Rev. B **75**, 235405 (2007)
27. M.J. Piotrowski, P. Piquini, J.L.F. Da Silva, Phys. Rev. B **81**, 155446 (2010)
28. A.M. Köster, P. Calaminici, E. Orgaz, D.R. Roy, J.U. Reveles, S.N. Khanna, J. Am. Chem. Soc. **133**, 12192–12196 (2011)
29. J. Kaiser, L. Leppert, H. Welz, F. Polzer, S. Wunder, N. Wanderka, M. Albrecht, T. Lunkenbein, J. Breu, S. Kümmel, Y. Lu, M. Ballauff, Phys. Chem. Chem. Phys. **14**, 6487–6495 (2012)
30. L. Leppert, R.Q. Albuquerque, A.S. Foster, S. Kümmel, J. Phys. Chem. C **117**, 17268–17273 (2013)
31. A.S. Chaves, G.G. Rondina, M.J. Piotrowski, P. Tereshchuk, J.L. Da Silva, J. Phys. Chem. A **118**, 10813–10821 (2014)
32. L. Leppert, R. Kempe, S. Kümmel, Phys. Chem. Chem. Phys. **17**, 26140–26148 (2015)
33. M.J. Piotrowski, C.G. Ungureanu, P. Tereshchuk, K.E.A. Batista, A.S. Chaves, D. Guedes-Sobrinho, J.L.F. Da Silva, J. Phys. Chem. C **120**, 28844–28856 (2016)
34. A.S. Chaves, M.J. Piotrowski, J.L. Da Silva, Phys. Chem. Chem. Phys. **19**(23), 15484–15502 (2017)
35. M. Van Den Bossche, J. Phys. Chem. A **123**, 3038–3045 (2019)
36. J. Hermannsdörfer, M. Friedrich, N. Miyajima, R.Q. Albuquerque, S. Kümmel, R. Kempe, Angew. Chem. Int. Ed. **51**(46), 11473–11477 (2012)
37. C. Luo, Y. Zhang, Y. Wang, J. Mol. Catal. A Chem. **229**, 7–12 (2005)
38. X. Duan, M. Xiao, S. Liang, Z. Zhang, Y. Zeng, J. Xi, S. Wang, Carbon **119**, 326–331 (2017)
39. M. Sharma, M. Sharma, A. Hazarika, L. Satyanarayana, G.V. Karunakar, K.K. Bania, Mol. Catal. **432**, 210–219 (2017)
40. J.A. Bobb, A.A. Ibrahim, M.S. El-Shall, ACS Appl. Nano Mater. **1**, 4852–4862 (2018)
41. G. Fusini, F. Rizzo, G. Angelici, E. Pitzalis, C. Evangelisti, A. Carpita, Catalysts **10**, 330 (2020)
42. A. Trzeciak, A. Augustyniak, Coord. Chem. Rev. **384**, 1–20 (2019)
43. K. Hong, M. Sajjadi, J.M. Suh, K. Zhang, M. Nasrollahzadeh, H.W. Jang, R.S. Varma, M. Shokouhimehr, ACS Appl. Nano Mater. **3**, 2070–2103 (2020)
44. K. Köhler, R.G. Heidenreich, J.G.E. Krauter, J. Pietsch, Chem. Eur. J. **8**, 622–631 (2002)
45. D. Astruc, F. Lu, J.R. Aranzaes, Angew. Chem. Int. Ed. **44**, 7852–7872 (2005)
46. N. Phan, M. Van Der Sluys, C. Jones, Adv. Synth. Catal. **348**, 609–679 (2006)
47. J. Richardson, C. Jones, Adv. Synth. Catal. **348**, 1207–1216 (2006)
48. P.-P. Fang, A. Jutand, Z.-Q. Tian, C. Amatore, Angew. Chem. Int. Ed. **50**, 12184–12188 (2011)
49. Z. Niu, Q. Peng, Z. Zhuang, W. He, Y. Li, Chem. Eur. J. **18**, 9813–9817 (2012)
50. A. Leyva-Pérez, J. Oliver-Meseguer, P. Rubio-Marqués, A. Corma, Angew. Chem. Int. Ed. **52**, 11554–11559 (2013)
51. A. Bej, K. Ghosh, A. Sarkar, D.W. Knight, RSC Adv. **6**, 11446–11453 (2016)
52. Y. Wang, J. Ren, K. Deng, L. Gui, Y. Tang, Chem. Mater. **12**, 1622–1627 (2000)
53. E.D. Sultanova, V.V. Salnikov, R.K. Mukhitova, Y.F. Zuev, Y.N. Osin, L.Y. Zakharova, A.Y. Ziganshina, A.I. Konovalov, Chem. Commun. **51**, 13317–13320 (2015)
54. T. Yonezawa, K. Kawai, H. Kawakami, T. Narushima, Bull. Chem. Soc. Jpn. **89**, 1230–1232 (2016)
55. M.J. Gillan, D. Alfè, A. Michaelides, J. Chem. Phys. **144**, 130901 (2016)
56. T. Schmidt, S. Kümmel, Computation **4**, 2079–3197 (2016)
57. B. Fresch, H.-G. Boyen, F. Remacle, Nanoscale **4**, 4138–47 (2012)
58. J.P. Perdew, K. Burke, M. Ernzerhof, Phys. Rev. Lett. **77**, 3865–3868 (1996)
59. J.P. Perdew, K. Burke, M. Ernzerhof, Phys. Rev. Lett. **80**, 891 (1998)
60. Y. Zhang, W. Yang, Phys. Rev. Lett. **80**, 890 (1998)
61. C. Adamo, V. Barone, J. Chem. Phys. **110**, 6158–6170 (1999)
62. C. Adamo, G.E. Scuseria, V. Barone, J. Chem. Phys. **111**, 2889–2899 (1999)
63. A. Luna-Valenzuela, J.L. Cabellos, J.A. Alonso, A. Posada-Amarillas, Mater. Today Commun. **26**, 102024 (2021)
64. A. Granja-DelRío, H.A. Abdulhussein, R.L. Johnston, J. Phys. Chem. C **123**, 26583–26596 (2019)
65. TURBOMOLE V7.4 2019, a development of University of Karlsruhe and Forschungszentrum Karlsruhe GmbH, 1989–2007, TURBOMOLE GmbH, since 2007 available from http://www.turbomole.com
66. A. Weigend, Phys. Chem. Chem. Phys. **21**, 3297–3305 (2005)
67. F. Weigend, Phys. Chem. Chem. Phys. **8**, 1057–1065 (2006)
68. S. Nosé, J. Chem. Phys. **81**, 511–519 (1984)
69. W.G. Hoover, Phys. Rev. A **31**, 1695–1697 (1985)
70. S. Grimme, J. Comput. Chem. **25**, 1463–1473 (2004)
71. A. Klamt, G. Schüürmann, J. Chem. Soc. Perkin Trans. **2**, 799–805 (1993)
72. A.A. Maryott, E.R. Smith, *National Bureau of Standards*, 26 (1951)
73. A. Schäfer, H. Horn, R. Ahlrichs, J. Chem. Phys. **97**, 2571–2577 (1992)
74. R.F.W. Bader, Chem. Rev. **91**, 893–928 (1991)
75. Bader V1.04 2020, developed by Wenjie Tang, Andri Arnaldsson, Wenrui Chai, Samuel T. Chill, and Graeme Henkelman available from http://theory.cm.utexas.edu/henkelman/code/bader/

76. G. Henkelman, A. Arnaldsson, H. Jónsson, Comput. Mater. Sci. **36**, 354–360 (2006)
77. E. Sanville, S.D. Kenny, R. Smith, G. Henkelman, J. Comput. Chem. **28**, 899–908 (2007)
78. W. Tang, E. Sanville, G. Henkelman, J. Phys. Condens. Matter **21**, 084204 (2009)
79. M. Yu, D.R. Trinkle, J. Chem. Phys. **134**, 064111 (2011)

Publication 2

H_2-Generation from Alcohols by the MOF-Based Noble Metal-Free Photocatalyst Ni/CdS/TiO_2@MIL-101

reprinted from
Australian Journal of Chemistry **72**, 842-847 (2019) ,
with the permission of CSIRO Publishing.

Tilgner, Dominic[1], Mara Klarner[1], Sebastian Hammon[2], Martin Friedrich[1], Andreas Verch[3,4],
Niels de Jonge[3,5], Stephan Kümmel[2], and Rhett Kempe[1]

[1] Inorganic Chemistry II, Catalyst Design, University of Bayreuth, Bayreuth 95440, Germany
[2] Theoretical Physics IV, University of Bayreuth, Bayreuth 95440, Germany
[3] INM – Leibniz Institute for New Materials, Saarbrücken 66123, Germany
[4] Carl Zeiss AG, Oberkochen 73447, German.
[5] Department of Physics, Saarland University, Saarbrücken 66123, Germany

My contribution

D. Tilgner was the lead contributor to the publication.

S.Kümmel and myself conceived the theoretical study on the binding of benzyl alcohol to different metal co-catalysts in a model. I performed the corresponding computational density functional theory study and associated simulations. S. Kümmel and myself were involved in scientific discussions. S. Kümmel supervised the theoretical study.

D. Tilgner synthesized and characterized all compounds, carried out the catalytic experiments and the related analytics. M. Klarner performed the fluorescence lifetime studies. M. Friedrich, A. Verch, and N. de Jonge performed the HAADFT-STEM measurements and were involved in scientific discussions. R. Kempe supervised the experimental part of this work, was involved in the scientific discussions.

D. Tilgner and R. Kempe conceived the structure of the manuscript. D. Tilgner wrote large parts of the manuscript. M. Klarner wrote the section describing the fluorescence lifetime work. R. Kempe and M. Klarner finalized the experiment-related text of the manuscript together. I wrote the first version of the part of the manuscript that describes the computational study. S. Kümmel and myself finalized this theory-related text of the manuscript together.

RESEARCH FRONT

CSIRO PUBLISHING

Communication

Aust. J. Chem. **2019**, *72*, 842–847
https://doi.org/10.1071/CH19255

H_2-Generation from Alcohols by the MOF-Based Noble Metal-Free Photocatalyst Ni/CdS/TiO_2@MIL-101*

Dominic Tilgner,[A] *Mara Klarner,*[A] *Sebastian Hammon,*[B]
Martin Friedrich,[A] *Andreas Verch,*[C,D] *Niels de Jonge,*[C,E]
Stephan Kümmel,[B] *and Rhett Kempe*[A,F]

[A]Inorganic Chemistry II, Catalyst Design, University of Bayreuth, Bayreuth 95440, Germany.
[B]Theoretical Physics IV, University of Bayreuth, Bayreuth 95440, Germany.
[C]INM – Leibniz Institute for New Materials, Saarbrücken 66123, Germany.
[D]Carl Zeiss AG, Oberkochen 73447, Germany.
[E]Department of Physics, Saarland University, Saarbrücken 66123, Germany.
[F]Corresponding author. Email: kempe@uni-bayreuth.de

The synthesis of important classes of chemical compounds from alcohols helps to conserve Earth's fossil carbon resources, since alcohols can be obtained from indigestible and abundantly available biomass. The utilisation of visible light for the activation of alcohols permits alcohol-based C–N and C–C bond formation under mild conditions inaccessible with thermally operating hydrogen liberation catalysts. Herein, we report on a noble metal-free photocatalyst able to split alcohols into hydrogen and carbonyl compounds under inert gas atmosphere without the requirement of electron donors, additives, or aqueous reaction media. The reusable photocatalyst mediates C–N multiple bond formation using the oxidation of alcohols and subsequent coupling with amines. The photocatalyst consists of a CdS/TiO_2 heterojunction decorated with co-catalytic Ni nanoparticles and is prepared on size-optimised colloidal metal–organic framework (MOF) crystallites.

Manuscript received: 4 June 2019.
Manuscript accepted: 22 July 2019.

The dehydrogenation of alcohols is a fundamental reaction in sustainable chemistry.[1] Alcohols can be obtained via pyrolysis and hydrogenation from lignocellulose,[2] an abundantly available, indigestible, and barely used biomass.[3] Thus, alcohols are a promising renewable carbon feedstock and the development of alcohol refunctionalisation reactions is the key to its use.[4] Alcohols are rather unreactive and dehydrogenation is an elegant way of activating them. The oxidised form, carbonyl compounds, can undergo condensation reactions permitting the formation of C–C or C–N multiple bonds. The synthesis of imines from alcohols and amines introduced by Milstein and coworkers is an example of broad interest for such a C–N bond formation reactions.[5] Our group has developed the synthesis of aromatic N-heterocyclic compounds from alcohols in which C–N and C–C multiple bond formation takes place concertedly.[4,6–9] We expected that a photocatalyst able to mediate C–N bond formation via dehydrogenative coupling under very mild reaction conditions is highly desirable to significantly extend the applicability of existing thermally operating noble metal-free catalysts for such reactions.[5b,6b,8b–c,10]

Here, we report on a photocatalyst that mediates visible light-driven imine synthesis from alcohols and amines. This C–N multiple bond formation takes place via dehydrogenation of alcohols under very mild conditions without sacrificial electron donors (alcohol splitting). Our noble metal-free photocatalyst consists of a CdS/TiO_2 heterojunction prepared on a porous support that is decorated with co-catalytic Ni nanoparticles. The metal–organic framework (MOF) MIL-101 (Cr)[11] was used as the porous support material stabilising the photocatalytic system.[12] We demonstrate the acceptorless dehydrogenation of alcohols by splitting into hydrogen and carbonyl compounds at room temperature with a broad substrate scope to generate aldehydes and dialkyl, diaryl, and aryl-alkyl ketones. Visible light-driven alcohol dehydrogenation without electron donors is rarely found in the literature[13] and often requires aqueous media, including additives.[14] Aqueous media are disadvantageous regarding condensation steps, which are needed in many dehydrogenative coupling/condensation reactions.

We expected that the arrangement of CdS and TiO_2 nanocrystals on a suitable MOF would be an elegant way to create heterojunction systems with efficient charge carrier separation and high photocatalytic activity. The pores of the MOF can be selectively loaded with precursor molecules to control the size and amount of the different nanocrystals without applying

---

*This paper is dedicated to Richard Robson, an outstanding pioneer in the field of porous coordination polymers and metal-organic frameworks.

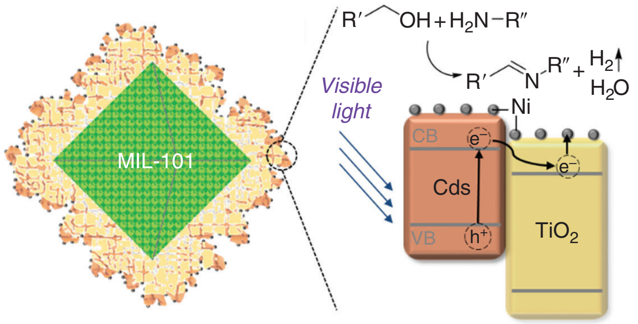

Scheme 1. Illustration of the Ni/CdS/TiO_2@MIL-101 material with a core–shell morphology. The MOF-supported Ni/CdS/TiO_2 heterojunction system is an efficient photocatalyst for the dehydrogenative coupling of alcohols and amines under visible light illumination.

surface blocking ligands. MIL-101 (Cr) was chosen because of its stability during solvothermal modifications and its large pore volume. It was prepared according to a procedure described previously with an average crystallite size of 300 nm (Fig. S1, Supplementary Material).[15] This crystallite size is optimal regarding catalytic performance. The crystallites are large enough to ensure efficient separation for reusability and small enough to have a sufficiently large outer surface for modification with light harvesting materials. We recently reported a synthesis protocol of crystalline TiO_2 (anatase) on the surface of MIL-101 crystallites leading to a core–shell morphology.[12] Titanium(IV) isopropoxide [Ti(O*i*Pr)$_4$)] was infiltrated into the pores of MIL-101 by gas-phase loading. The subsequent hydrolysis of the Ti precursor led to the formation of amorphous TiO_2 inside the cavities of MIL-101. The crystallisation of TiO_2 (anatase) on the surface of MOF crystallites was performed under hydrothermal conditions. The MIL-101 core is crucial since the material collapses by removing the support of the photocatalytic system.[12] In this work, the resulting TiO_2@MIL-101 material was modified with CdS nanocrystals under solvothermal conditions using cadmium acetate dihydrate and dimethyl sulfoxide as precursors to yield CdS/TiO_2@MIL-101.[16] MIL-101 serves as structure-directing centre to form a dense photoactive shell. Thereby, the MOF core offers a platform for the growth of CdS and TiO_2 nanocrystallites covering the outer surface of single MIL-101 crystallites. Finally, we decorated the core–shell material with homogeneously distributed nickel nanoparticles using bis(cyclopentadienyl)nickel(II) [Ni(Cp)$_2$] as the volatile Ni precursor. The Ni/CdS/TiO_2@MIL-101 photocatalyst and the process of charge carrier separation between the semiconducting materials is illustrated in Scheme 1. The TiO_2 and CdS particles form a type II heterojunction at their interface where CdS serves as light absorbing component for the visible spectrum. The directed electron transfer from the conduction band of CdS into that of TiO_2 is a well understood process.[17] We believe that the enhanced photocatalytic efficiency of a MOF-supported CdS/TiO_2 heterojunction is due to a reduced charge recombination rate as described in the literature. Metallic Ni nanoparticles promote the separation of charges, since the electrical potential gradient at the Ni/semiconductor interface enhances the electron transfer.[18] Consequently, the charge carriers initiate spatially separated redox reactions, since they are distributed over three different components. The nanoparticles of the non-noble metal Ni act as electron reservoirs and, thus, as a co-catalyst for H_2 liberation.

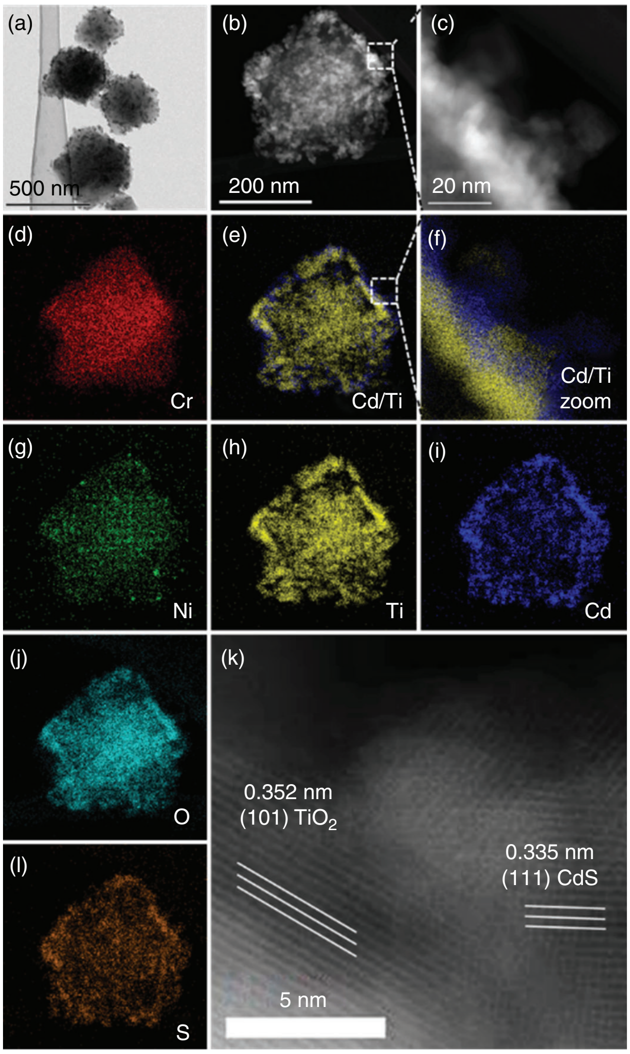

Fig. 1. (a) TEM image of Ni/CdS/TiO_2@MIL-101. (b–l) HAADF-STEM analysis of Ni/CdS/TiO_2@MIL-101 with representative energy-dispersed X-ray element maps. (k) Characteristic lattice planes for crystalline cubic CdS and anatase TiO_2.

The initial specific surface area of MIL-101 decreased perceptibly during the generation of TiO_2 and CdS, as investigated by nitrogen physisorption measurements (Fig. S2, Supplementary Material). Only a minor reduction of the specific surface area was observed after the modification with nickel. Crystalline TiO_2 (anatase) and CdS (cubic) were identified by X-ray powder diffraction (XRD) analysis (Fig. S3, Supplementary Material). The characteristic reflexes between 2° and 20° (2θ) indicate the preserved structure of MIL-101. X-Ray photoelectron spectroscopy (XPS) analysis confirmed the presence of TiO_2 and CdS. Signals of Ni^0 and Ni^{II} were observed in the Ni 2p spectrum. The presence of Ni^{II} can be attributed to the formation of nickel(II) hydroxide when exposed to air during sample handling (Fig. S4, Supplementary Material). We determined the elemental composition of the materials by inductively coupled plasma–optical emission spectrometry (ICP-OES) measurements (Table S1, Supplementary Material). The Ni/CdS/TiO_2@MIL-101 material comprised 3.6 wt-% Ni, 18.8 wt-% CdS, and 26.0 wt-% TiO_2. Diffuse reflectance ultraviolet-visible spectra in the range from 450 to 800 nm show an increased light absorption for TiO_2@MIL-101 and

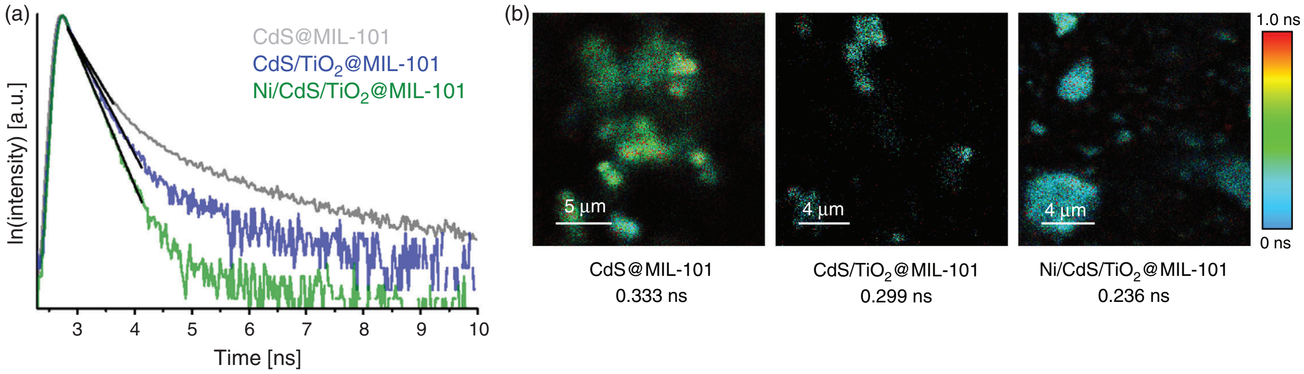

CdS@MIL-101
0.333 ns

CdS/TiO$_2$@MIL-101
0.299 ns

Ni/CdS/TiO$_2$@MIL-101
0.236 ns

Fig. 2. TRPL studies of MIL-101 supported catalysts confirmed the directed electron transfer from excited CdS to TiO$_2$ particles and Ni nanoparticles. (a) TCSPC traces of CdS@MIL-101, CdS/TiO$_2$@MIL-101, and Ni/CdS/TiO$_2$@MIL-101 in semi-log representation with fits to the linear range (black lines; Table S2, Supplementary Material). (b) Microscope images of fluorescing CdS@MIL-101, CdS/TiO$_2$@MIL-101, and Ni/CdS/TiO$_2$@MIL-101 after optical excitation. The colour encodes the photoluminescence lifetime at each spatial point as indicated by the side bar. The photoluminescence lifetime of excited CdS is calculated from the slope of the linear fit function. The values of the photoluminescence lifetime have to be compared relatively, since the instrument response function (IRF) has not been taken into account in the data analysis.

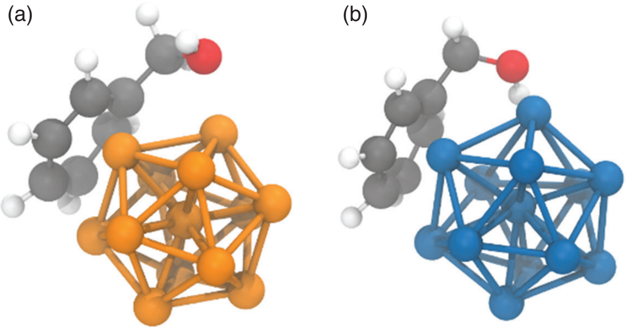

Fig. 3. Lowest energy geometries obtained from Born-Oppenheimer DFT molecular dynamics simulations in which a benzyl alcohol molecule binds to a 13 atom Ni particle (a) and a 13 atom Pd particle (b). See the Supplementary Material for computational details.

CdS/TiO$_2$@MIL-101 in comparison to MIL-101 (Fig. S5, Supplementary Material). The modification with CdS resulted in a distinctive edge for CdS/TiO$_2$@MIL-101, which is comparable to the absorption of cubic CdS. We investigated the size and shape of the Ni/CdS/TiO$_2$@MIL-101 crystallites by transmission electron microscopy (TEM) and high-angle annular dark-field scanning TEM (HAADF-STEM) measurements (Fig. 1). The typical octahedral shape and the homogeneous size distribution of the MIL-101 crystallites was also observed for Ni/CdS/TiO$_2$@MIL-101. Energy dispersed X-ray maps demonstrate the uniform arrangement of TiO$_2$, CdS, and Ni around single MIL-101 crystallites. The interface between the crystalline semiconductors CdS and TiO$_2$ was verified by assigning characteristic lattice planes of adjacent semiconductor particles. Nickel was located on CdS and TiO$_2$ and showed a minimal tendency for agglomeration (Fig. S5, Supplementary Material). We investigated the TiO$_2$@MIL-101 and CdS@MIL-101 materials by TEM measurements to determine the size of the CdS and TiO$_2$ crystallites formed on the surface of MIL-101 (Fig. S7, Supplementary Material). The average particle size was ~35 nm for TiO$_2$ and 20 nm for CdS.

Time-resolved photoluminescence (TRPL) studies on photocatalytic systems allow a deeper understanding of photosynthetic electron dynamics between semiconductor materials and metal nanoparticles.[19] We confirmed the directed electron transfer process from excited CdS across the heterojunction interface to TiO$_2$ and further to Ni nanoparticles by TRPL studies on MIL-101 supported catalysts. The photoluminescence lifetime of bare CdS@MIL-101 corresponds to the recombination rate of electrons and holes after optical excitation. The presence of TiO$_2$ and Ni opens up additional relaxation channels of the excited CdS through the directed electron transfer induced by the potential gradient at the CdS/TiO$_2$ and Ni/semiconductor interface. Thus, the photoluminescence lifetime of CdS, which can be calculated from the linear range of time-correlated single photon counting (TCSPC) traces in semi-log representation, is reduced (Fig. 2; Table S2, Supplementary Material). The charge carrier separation across three different catalyst components leads to the enhanced photocatalytic activity of Ni/CdS/TiO$_2$@MIL-101. To extend the insight into the electron transfer between CdS and metallic species synchrotron-based X-ray absorption spectroscopy and photoelectrochemical characterisation could be combined.[20]

The photocatalytic liberation of hydrogen via the oxidation of alcohols leading to carbonyl compounds was performed under argon atmosphere at room temperature without additives or acceptor molecules. A 50 W blue LED (470 nm) was used as a visible light source (Fig. S9, Supplementary Material). The dehydrogenation of benzyl alcohol was investigated as a model reaction. Acetonitrile was identified as the most suitable solvent and a loading of 4 wt-% Ni showed the highest activity (Tables S3 and S4, Supplementary Material). We investigated the photocatalytic activity of CdS/TiO$_2$@MIL-101 modified with the noble metals Pd, Pt, and Au as co-catalysts to ensure the superior performance of our Ni/CdS/TiO$_2$@MIL-101 catalyst. The Ni-modified catalyst system showed the highest activity in alcohol splitting (Fig. S10a, Supplementary Material). In combination with CdS, the noble metal Pt is especially used as co-catalyst for hydrogen evolution reactions.[21]

A detailed, microscopic understanding of the mechanism of such dehydrogenation reactions is a formidable task that is beyond the scope of this work. However, one straightforward first step towards understanding differences between Ni and noble metals as co-catalysts can be taken computationally. Of the three experimentally tested metals (Pd, Pt, and Au), we chose Pd as the paradigm noble metal catalyst for the comparison with Ni. Choosing Pd is motivated by the observation that similar metal particle geometries are stable for Ni and Pd, so binding properties can be readily compared. With the help of density functional theory (DFT) calculations, we checked whether there is a difference in the binding of benzyl alcohol to the metal particles using a molecular model consisting of a 13-atom metal particle and one benzyl alcohol molecule. We chose the 13-atom clusters, since they form stable structures[22] and can build an icosahedral geometry. The latter is one of the smallest possible faceted structures and, therefore, can be interpreted as a small model system for the binding to a faceted metal nanoparticle. We obtained the geometrical and electronic structure using the *TURBOMOLE*[23] code. Fig. 3 depicts the lowest energy, i.e. strongest bound, conformation in which the alcohol binds to the Ni_{13} and Pd_{13} cluster. Details of the computational procedures are reported in the Supplementary Material (see *Theoretical Procedures*). We paid particular attention to the fact that d-electron metals pose special challenges to many exchange-correlation approximations.[24] Reassuringly, our calculations with different density functionals consistently show that benzyl alcohol binds more strongly to Ni_{13} than to Pd_{13} by several hundred meV (Table S10, Supplementary Material). We therefore consider this trend as reliable. We see this calculation as one first, small step to corroborate the plausibility that Ni shows a different performance as a co-catalyst than Pd. Extensive further computational work, which is beyond the scope of the present manuscript, would be needed to reveal the detailed mechanism.

The beneficial contribution of the heterojunction between the semiconductors was demonstrated by the higher activity of CdS/TiO_2@MIL-101 in comparison to CdS@MIL-101. We also demonstrated the favourable effect resulting from the support of Ni/CdS/TiO_2 on MIL-101 as compared to pure Ni, CdS, TiO_2, and Ni/CdS/TiO_2. All materials without cadmium sulfide as the light-absorbing component showed no activity under visible light illumination (Table S5, Supplementary Material). The reusability of Ni/CdS/TiO_2@MIL-101 was confirmed by performing ten successive runs without a remarkable loss of photocatalytic activity (Fig. S10b, Supplementary Material). The material was analysed by TEM and XRD measurements after the last run to demonstrate the structural integrity (Fig. S11, Supplementary Material). A light on/off experiment was performed to examine whether the dehydrogenation of benzyl alcohol is indeed a visible light-mediated reaction (Fig. S12, Supplementary Material). The amount of H_2 released during the reaction was only increased under illumination. We further checked whether hydrogen is released in equimolar amounts during the photocatalytic reaction for several substrates using methane as an internal standard (Table S7, Supplementary Material). Performing the splitting of alcohols under argon atmosphere is crucial for high yields and the generation of molecular hydrogen (Table S7, Supplementary Material). Our Ni/CdS/TiO_2@MIL-101 photocatalyst can split a broad range of alcohols **1** forming the corresponding aldehydes, aryl-alkyl, diaryl, and dialkyl ketones **2** (Table 1). A variety of functional groups was well tolerated, including halogens, methoxy, hydroxy, trifluoromethyl, and amino groups. In addition, hydrogenation-sensitive functionalities, such as nitrile and nitro groups, and C=C bonds can be tolerated selectively. We converted a total of 38 alcohols into the respective carbonyl compounds in good to excellent yields (Table 1; Table S6, Supplementary Material).

Table 1. Photocatalytic dehydrogenation of aryl, aryl-alky, diaryl, and dialkyl alcohol compounds[A]

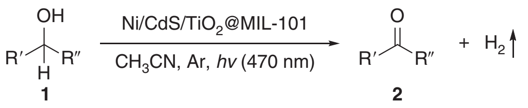

Entry	Product	R	Yield[B] [%]
1	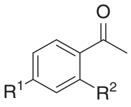	**2a** $R^1 = H$, $R^2 = H$	97
2		**2b** $R^1 = OMe$, $R^2 = H$	96
3		**2c** $R^1 = Me$, $R^2 = H$	92
4		**2d** $R^1 = H$, $R^2 = Me$	81
5[C]		**2e** $R^1 = Me$, $R^2 = Me$	83
6[D]		**2f** $R^1 = F$, $R^2 = H$	71
7		**2g** $R^1 = Cl$, $R^2 = H$	97
8		**2h** $R^1 = Br$, $R^2 = H$	96
9	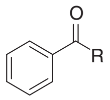	**2i** R = Et	93
10[C]		**2j** R = Bu	83
11[C]		**2k** R = CH_2OH	90
12	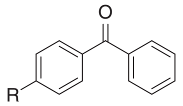	**2l** R = H	88
13		**2m** R = Me	91
14		**2n** R = OMe	82
15[D]	cycloheptanone	**2o**	86
16	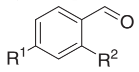	**2p** $R^1 = H$, $R^2 = H$	>99
17[D]		**2q** $R^1 = CN$, $R^2 = H$	93
18[D]		**2r** $R^1 = NO_2$, $R^2 = H$	88
19[D]		**2s** $R^1 = H$, $R^2 = NO_2$	71
20		**2t** $R^1 = H$, $R^2 = NH_2$	96
21		**2u** $R^1 = CF_3$, $R^2 = H$	70
22[D]	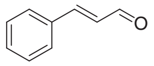	**2v**	70

[A] Reaction conditions: 0.1 mmol alcohol, 0.6 mg Ni/CdS/TiO_2@MIL-101, Ar, 0.3 mL CH_3CN, 27°C, 24 h, 470 nm blue LED 50 W.

[B] Determined by GC using n-dodecane as internal standard.

[C] 1.2 mg Ni/CdS/TiO_2@MIL-101.

[D] 1.2 mg Ni/CdS/TiO_2@MIL-101, 48 h.

Finally, we were interested in photocatalytic C–N multiple bond formation reactions (Table 2). The reaction of benzyl alcohol and aniline was chosen to optimise the reaction conditions (Table S8, Supplementary Material). Imines **5** were obtained in good yields under very mild conditions at room temperature. A notable tolerance for functional group was again observed without the use of additives or sacrificial electron donors. Methyl, methoxy, halide, and hydroxy-substituted benzyl alcohols were well tolerated. In addition, we varied the amine component and found the tolerance for methyl, halogen, and methoxy substituents. We analysed the gas atmosphere to quantify the amount of hydrogen released for selected examples (Table S9, Supplementary Material). Again, no molecular hydrogen and a decreased yield of imine were observed when conducting the C–N bond formation without argon atmosphere. Amines formed via hydrogenation of corresponding imines by the hydrogen liberated were not detected.

Conclusion

In conclusion, we introduced photocatalytic C–N multiple bond formation under visible light illumination by coupling activated carbonyl compounds with amines. The reusable, noble metal-free photocatalyst Ni/CdS/TiO_2@MIL-101 permits quantitative hydrogen generation from alcohols (alcohol splitting) under very mild conditions, inert gas atmosphere, and without the requirement of sacrificial electron donors. The photocatalyst is

Table 2. Photocatalytic synthesis of imines from primary alcohols and amines[A]

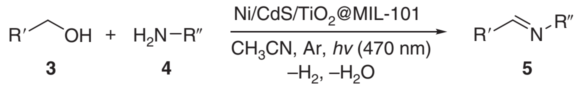

Entry	Product	R	Yield[A] [%]
1	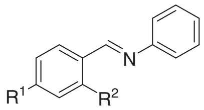	**5a** $R^1 = H, R^2 = H$	92
2		**5b** $R^1 = Me, R^2 = H$	86
3		**5c** $R^1 = H, R^2 = Me$	80
4		**5d** $R^1 = OMe, R^2 = H$	92
5		**5e** $R^1 = F, R^2 = H$	76
6		**5f** $R^1 = Cl, R^2 = H$	88
7		**5g** $R^1 = Br, R^2 = H$	53
8	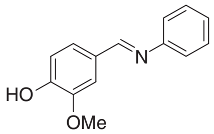	**5h**	72
9	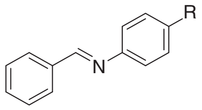	**5i** R = Me	88
10		**5j** R = Cl	77
11		**5k** R = OMe	93
12	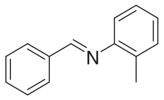	**5l**	62
13	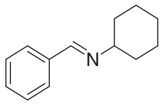	**5m**	87

[A] Reaction conditions: 0.1 mmol amine, 0.13 mmol alcohol, 1.5 mg Ni/CdS/TiO_2@MIL-101, Ar, 0.15 mL CH_3CN, 27°C, 48 h, 470 nm blue LED 50 W.
[B] Determined by GC using n-decane as internal standard.

composed of a CdS/TiO_2 heterojunction with co-catalytic Ni nanoparticles assembled on the MOF MIL-101 as a colloidal porous support. We observed a broad substrate scope with very good tolerance of functional groups and high selectivity. We believe that our reusable photocatalyst represents a valuable platform for a variety of photocatalytic C–N or C–C bond formation reactions which involve the dehydrogenation of alcohols and condensation reaction(s) as key steps.

Supplementary Material

Details of the theoretical procedures, general methods, material synthesis and characterisation, and the general procedure for photocatalytic experiments and screening reactions are available on the Journal's website.

Conflicts of Interest

The authors declare no conflicts of interests.

Acknowledgements

This work was supported by grants from the Deutsche Forschungsgemeinschaft (DFG, SFB 840(B1)). Note that parts of this work were included in the PhD thesis of Dominic Tilgner, Bayreuth 2017. The authors also acknowledge the support of the DAAD, Colloid/Polymer Network, the help of Florian Puchtler (XRD), Dr Jürgen Seidel (XPS), Prof. Dr Lothar Kador (FLIM) and Eduard Arzt for his support through INM. The photoluminescence lifetime measurements were performed in the keylab Electron and Optical Microscopy of the Bayreuth Polymer Institute (BPI).

References

[1] C. Gunanathan, D. Milstein, *Science* **2013**, *341*, 1229712. doi:10.1126/SCIENCE.1229712

[2] T. P. Vispute, H. Zhang, A. Sanna, R. Xiao, G. W. Huber, *Science* **2010**, *330*, 1222. doi:10.1126/SCIENCE.1194218

[3] C. O. Tuck, E. Perez, I. T. Horvath, R. A. Sheldon, M. Poliakoff, *Science* **2012**, *337*, 695. doi:10.1126/SCIENCE.1218930

[4] S. Michlik, R. Kempe, *Nat. Chem.* **2013**, *5*, 140. doi:10.1038/NCHEM.1547

[5] (a) B. Gnanaprakasam, J. Zhang, D. Milstein, *Angew. Chem. Int. Ed.* **2010**, *49*, 1468. [*Angew. Chem.* **2010**, *122*, 1510]. doi:10.1002/ANIE.200907018
(b) A. Mukherjee, A. Nerush, G. Leitus, L. J. W. Shimon, Y. Ben David, N. A. Espinosa Jalapa, D. Milstein, *J. Am. Chem. Soc.* **2016**, *138*, 4298. doi:10.1021/JACS.5B13519

[6] Pyrrole synthesis: (a) D. Forberg, J. Obenauf, M. Friedrich, S. M. Hühne, W. Mader, G. Motz, R. Kempe, *Catal. Sci. Technol.* **2014**, *4*, 4188. doi:10.1039/C4CY01018C
(b) F. Kallmeier, B. Dudziec, T. Irrgang, R. Kempe, *Angew. Chem. Int. Ed.* **2017**, *56*, 7261. [*Angew. Chem.* **2017**, *129*, 7367]. doi:10.1002/ANIE.201702543
For selected work of others see: (c) D. Srimani, Y. Ben-David, D. Milstein, *Angew. Chem. Int. Ed.* **2013**, *52*, 4012. [*Angew. Chem.* **2013**, *125*, 4104]. doi:10.1002/ANIE.201300574
(d) M. Zhang, H. Neumann, M. Beller, *Angew. Chem. Int. Ed.* **2013**, *52*, 597. [*Angew. Chem.* **2013**, *125*, 625]. doi:10.1002/ANIE.201206082
(e) M. Zhang, X. Fang, H. Neumann, M. Beller, *J. Am. Chem. Soc.* **2013**, *135*, 11384. doi:10.1021/JA406666R

[7] Pyridine synthesis: (a) S. Michlik, R. Kempe, *Angew. Chem. Int. Ed.* **2013**, *52*, 6326. [*Angew. Chem.* **2013**, *125*, 6450]. doi:10.1002/ANIE.201301919
(b) T. Hille, T. Irrgang, R. Kempe, *Angew. Chem. Int. Ed.* **2017**, *56*, 371. [*Angew. Chem.* **2017**, *129*, 377]. doi:10.1002/ANIE.201610071
For selected work of others see: (c) D. Srimani, Y. Ben-David, D. Milstein, *Chem. Commun.* **2013**, *49*, 6632. doi:10.1039/C3CC43227K

[8] Pyrimidine synthesis: (a) N. Deibl, K. Ament, R. Kempe, *J. Am. Chem. Soc.* **2015**, *137*, 12804. doi:10.1021/JACS.5B09510
(b) N. Deibl, R. Kempe, *Angew. Chem. Int. Ed.* **2017**, *56*, 1663. [*Angew. Chem.* **2017**, *129*, 1685]. doi:10.1002/ANIE.201611318
For selected work of others see: (c) M. Mastalir, M. Glatz, E. Pittenauer, G. Allmaier, K. Kirchner, *J. Am. Chem. Soc.* **2016**, *138*, 15543. doi:10.1021/JACS.6B10433

[9] (a) D. Forberg, T. Schwob, M. Zaheer, M. Friedrich, N. Miyajima, R. Kempe, *Nat. Commun.* **2016**, *7*, 13201. doi:10.1038/NCOMMS13201
(b) D. Forberg, T. Schwob, R. Kempe, *Nat. Commun.* **2018**, *9*, 1751. doi:10.1038/S41467-018-04143-6

[10] (a) G. Zhang, S. K. Hanson, *Org. Lett.* **2013**, *15*, 650. doi:10.1021/OL303479F
(b) J. Bain, P. Cho, A. Voutchkova-Kostal, *Green Chem.* **2015**, *17*, 2271. doi:10.1039/C5GC00312A
(c) P. Daw, S. Chakraborty, J. A. Garg, Y. Ben-David, D. Milstein, *Angew. Chem. Int. Ed.* **2016**, *55*, 14373. [*Angew. Chem.* **2016**, *128*, 14585]. doi:10.1002/ANIE.201607742
(d) M. Mastalir, M. Glatz, N. Gorgas, B. Stöger, E. Pittenauer, G. Allmaier, L. F. Veiros, K. Kirchner, *Chem. – Eur. J.* **2016**, *22*, 12316. doi:10.1002/CHEM.201603148
(e) S. Parua, S. Das, R. Sikari, S. Sinha, N. D. Paul, *J. Org. Chem.* **2017**, *82*, 7165. doi:10.1021/ACS.JOC.7B00643

[11] G. Férey, C. Mellot-Draznieks, C. Serre, F. Millange, J. Dutour, S. Surblé, I. Margiolaki, *Science* **2005**, *309*, 2040. doi:10.1126/SCIENCE.1116275

[12] For examples of a TiO_2/MIL-101 core-shell material see: (a) D. Tilgner, R. Kempe, *Chem. – Eur. J.* **2017**, *23*, 3184. doi:10.1002/CHEM.201605473
(b) D. Tilgner, M. Friedrich, A. Verch, N. de Jonge, R. Kempe, *ChemPhotoChem* **2018**, *2*, 349. doi:10.1002/CPTC.201700222

[13] (a) Y. Shiraishi, Y. Sugano, S. Tanaka, T. Hirai, *Angew. Chem. Int. Ed.* **2010**, *49*, 1656. doi:10.1002/ANIE.200906573
(b) T. P. A. Ruberu, N. C. Nelson, I. I. Slowing, J. Vela, *J. Phys. Chem. Lett.* **2012**, *3*, 2798. doi:10.1021/JZ301309D
(c) T. Mitkina, C. Stanglmair, W. Setzer, M. Gruber, H. Kisch, B. Konig, *Org. Biomol. Chem.* **2012**, *10*, 3556. doi:10.1039/C2OB07053G
(d) Z. Chai, T.-T. Zeng, Q. Li, L.-Q. Lu, W.-J. Xiao, D. Xu, *J. Am. Chem. Soc.* **2016**, *138*, 10128. doi:10.1021/JACS.6B06860
(e) D. Jiang, X. Chen, Z. Zhang, L. Zhang, Y. Wang, Z. Sun, R. M. Irfan, P. Du, *J. Catal.* **2018**, *357*, 147. doi:10.1016/J.JCAT.2017.10.019

[14] (a) W. Zhai, S. Xue, A. Zhu, Y. Luo, Y. Tian, *ChemCatChem* **2011**, *3*, 127. doi:10.1002/CCTC.201000303
(b) S. Higashimoto, Y. Tanaka, R. Ishikawa, S. Hasegawa, M. Azuma, H. Ohue, Y. Sakata, *Catal. Sci. Technol.* **2013**, *3*, 400. doi:10.1039/C2CY20607B
(c) Z. Liu, J. Caner, A. Kudo, H. Naka, S. Saito, *Chem. – Eur. J.* **2013**, *19*, 9452. doi:10.1002/CHEM.201301347
(d) A. Tanaka, S. Sakaguchi, K. Hashimoto, H. Kominami, *ACS Catal.* **2013**, *3*, 79. doi:10.1021/CS3006499
(e) H. Kasap, C. A. Caputo, B. C. M. Martindale, R. Godin, V. W.-h. Lau, B. V. Lotsch, J. R. Durrant, E. Reisner, *J. Am. Chem. Soc.* **2016**, *138*, 9183. doi:10.1021/JACS.6B04325
(f) L. M. Zhao, Q. Y. Meng, X. B. Fan, C. Ye, X. B. Li, B. Chen, V. Ramamurthy, C. H. Tung, L. Z. Wu, *Angew. Chem. Int. Ed.* **2017**, *56*, 3020. [*Angew. Chem.* **2017**, *129*, 3066]. doi:10.1002/ANIE.201700243
(g) G. Han, Y.-H. Jin, R. A. Burgess, N. E. Dickenson, X.-M. Cao, Y. Sun, *J. Am. Chem. Soc.* **2017**, *139*, 15584. doi:10.1021/JACS.7B08657

[15] J. Hermannsdörfer, M. Friedrich, R. Kempe, *Chem. – Eur. J.* **2013**, *19*, 13652. doi:10.1002/CHEM.201302809

[16] (a) J. He, Z. Yan, J. Wang, J. Xie, L. Jiang, Y. Shi, F. Yuan, F. Yu, Y. Sun, *Chem. Commun.* **2013**, *49*, 6761. doi:10.1039/C3CC43218A
(b) Y. Wang, Y. Zhang, Z. Jiang, G. Jiang, Z. Zhao, Q. Wu, Y. Liu, Q. Xu, A. Duan, C. Xu, *Appl. Catal. B* **2016**, *185*, 307. doi:10.1016/J.APCATB.2015.12.020
(c) Z. Jiang, J. Liu, M. Gao, X. Fan, L. Zhang, J. Zhang, *Adv. Mater.* **2017**, *29*, 1603369. doi:10.1002/ADMA.201603369

[17] (a) H. Gerischer, M. Lübke, *J. Electroanal. Chem.* **1986**, *204*, 225. doi:10.1016/0022-0728(86)80520-4
(b) L. Spanhel, H. Weller, A. Henglein, *J. Am. Chem. Soc.* **1987**, *109*, 6632. doi:10.1021/JA00256A012
(c) K. R. Gopidas, M. Bohorquez, P. V. Kamat, *J. Phys. Chem.* **1990**, *94*, 6435. doi:10.1021/J100379A051
(d) R. Vogel, K. Pohl, H. Weller, *Chem. Phys. Lett.* **1990**, *174*, 241. doi:10.1016/0009-2614(90)85339-E
(e) S. Kohtani, A. Kudo, T. Sakata, *Chem. Phys. Lett.* **1993**, *206*, 166. doi:10.1016/0009-2614(93)85535-V
(f) R. Vogel, P. Hoyer, H. Weller, *J. Phys. Chem.* **1994**, *98*, 3183. doi:10.1021/J100063A022
(g) J. E. Evans, K. W. Springer, J. Z. Zhang, *J. Chem. Phys.* **1994**, *101*, 6222. doi:10.1063/1.468376
(h) D. Baker, P. V. Kamat, *Adv. Funct. Mater.* **2009**, *19*, 805. doi:10.1002/ADFM.200801173

[18] (a) T. Simon, N. Bouchonville, M. J. Berr, A. Vaneski, A. Adrović, D. Volbers, R. Wyrwich, M. Döblinger, A. S. Susha, A. L. Rogach, F. Jäckel, J. K. Stolarczyk, J. Feldmann, *Nat. Mater.* **2014**, *13*, 1013. doi:10.1038/NMAT4049
(b) Y. Xu, R. Xu, *Appl. Surf. Sci.* **2015**, *351*, 779. doi:10.1016/J.APSUSC.2015.05.171

[19] (a) R. Shi, Y. Cao, Y. Bao, Y. Zhao, G. I. N. Waterhouse, Z. Fang, L.-Z. Wu, C.-H. Tung, Y. Yin, T. Zhang, *Adv. Mater.* **2017**, *29*, 1700803. doi:10.1002/ADMA.201700803
(b) H. Zhao, X. Ding, B. Zhang, Y. Li, C. Wang, *Sci. Bull.* **2017**, *62*, 602. doi:10.1016/J.SCIB.2017.03.005

[20] Q. He, Y. Wang, Y. Zhang, H. Jiang, H. Liu, X. Zheng, S. Chen, X. Wu, L. Song, *Sol. RRL* **2018**, 180032

[21] (a) J. He, Z. Yan, J. Wang, J. Xie, L. Jiang, Y. Shi, F. Yuan, F. Yu, Y. Sun, *Chem. Commun.* **2013**, *49*, 6761. doi:10.1039/C3CC43218A
(b) L. Shang, B. Tong, H. Yu, G. I. N. Waterhouse, C. Zhou, Y. Zhao, M. Tahir, L.-Z. Wu, C.-H. Tung, T. Zhang, *Adv. Energy Mater.* **2016**, *6*, 1501241. doi:10.1002/AENM.201501241

[22] (a) A. Langenberg, K. Hirsch, A. Ławicki, V. Zamudio-Bayer, M. Niemeyer, P. Chmiela, B. Langbehn, A. Terasaki, B. v. Issendorff, J. T. Lau, *Phys. Rev. B Condens. Matter Mater. Phys.* **2014**, *90*, 184420. doi:10.1103/PHYSREVB.90.184420
(b) J. Meyer, M. Tomber, T. van Wüllen, G. Niedner-Schattenburg, S. Peredkob, W. Eberhardt, M. Neeb, S. Palutke, M. Martins, W. Wurth, *J. Chem. Phys.* **2015**, *143*, 104302. doi:10.1063/1.4929482
(c) M. B. Knickelbein, *J. Chem. Phys.* **2002**, *116*, 9703. doi:10.1063/1.1477175
(d) S. E. Apsel, J. W. Emmert, J. Deng, L. A. Bloomfield, *Phys. Rev. Lett.* **1996**, *76*, 1441. doi:10.1103/PHYSREVLETT.76.1441
(e) A. J. Cox, J. G. Louderback, S. E. Apsel, L. A. Bloomfield, *Phys. Rev. B Condens. Matter* **1994**, *49*, 12295. doi:10.1103/PHYSREVB.49.12295

[23] *TURBMOLE V7.3* **2018** (University of Karlsruhe and Forschungszentrum Karlsruhe GmbH: Karlsruhe, Germany).

[24] (a) C. J. Cramer, D. G. Truhlar, *Phys. Chem. Chem. Phys.* **2009**, *11*, 10757. doi:10.1039/B907148B
(b) L. Leppert, R. Kempe, S. Kümmel, *Phys. Chem. Chem. Phys.* **2015**, *17*, 26140. doi:10.1039/C5CP04174K
(c) T. Schmidt, S. Kümmel, *Computation* **2016**, *4*, 33. doi:10.3390/COMPUTATION4030033

10.1071/CH19255_AC

Australian Journal of Chemistry 2019, 72(10), 842-847

Supplementary Material

H_2-Generation from Alcohols by the MOF-Based Noble Metal-Free Photocatalyst Ni/CdS/TiO_2@MIL-101

Dominic Tilgner,[A] *Mara Klarner,*[A] *Sebastian Hammon,*[B] *Martin Friedrich,*[A] *Andreas Verch,*[C,D] *Niels de Jonge,*[C,E] *Stephan Kümmel,*[B] *and Rhett Kempe*[A,F]

[A]Inorganic Chemistry II, Catalyst Design, University of Bayreuth, Bayreuth 95440, Germany.

[B]Theoretical Physics IV, University of Bayreuth, Bayreuth 95440, Germany.

[C]INM – Leibniz Institute for New Materials, Saarbrücken 66123, Germany.

[D]Carl Zeiss AG, Oberkochen 73447, Germany.

[E]Department of Physics, Saarland University, Saarbrücken 66123, Germany.

[F]Corresponding author. Email: kempe@uni-bayreuth.de

Table of Contents

Experimental Procedures

General Methods

All chemicals and solvents were purchased commercially from chemical suppliers with purity over 95 % and used without further purification. All manipulations including air or moisture sensitive compounds were carried out under dry and oxygen-free argon atmosphere (Schlenk techniques) or in a nitrogen-filled glovebox (mBraun 120) with a high-capacity recirculator (below 0.1 ppm of oxygen and water).

Elemental analysis was performed by standard protocols employing microwave assisted digestion (7 min at 170 °C (80 % power), 7 min at 180 °C (85 % power), and 20 min at 195 °C (90 % power)) in HCl (32 %, 4.5 mL), HNO3 (65 %, 1.5 mL), and HF (40 %, 1.0 mL). The resulting solution was analysed by inductively coupled plasma optical emission spectrometry (ICP-OES) using a Vista-Pro radial (Varian). Fourier transform infrared (FTIR) spectroscopy measurements were performed with a Cary 630 FTIR spectrometer (Agilent Technologies) over a range from 2000 cm-1 to 550 cm-1. Gas chromatography (GC) analyses were performed using an Agilent Technologies 6850 gas chromatograph equipped with a flame ionization detector (FID) and a MN Optima 17 capillary column (30.0 m x 0.32 mm x 0.25 µm) using n-dodecane or n-decane as internal standard. GC-MS analyses were performed using an Agilent Technologies 6890 gas chromatograph with a MN-MS HP-5 capillary column (30.0 m x 0.32 mm x 0.25 µm) and a coupled mass spectrometer as detector. Gas mixtures were analysed using a 6890N gas chromatograph (Agilent Technologies) equipped with an Agilent special Plot + Molsieve capillary column (30.0 m x 0.32 mm x 0.25 µm). Methane was used as internal standard. Nitrogen physisorption isotherms were determined at -196 °C using a Nova 2000e (Quantachrome) apparatus. Specific surface areas (SSA) were calculated by using p/p0-values from 0.05-0.25 by the BET model. Specific total pore volumes were measured by DFT calculations (N2 at -196 °C on silica (cylindr. pore, NLDFT equilibrium model)). Transmission electron microscopy (TEM) measurements were carried out using a LEO 922O microscope (Zeiss, 200 kV). The samples were suspended in chloroform and sonicated for 5 min. 2 µL of the suspension were placed on a CF200-Cu-grid or a LC200-Cu-grid (Electron Microscopy Sciences) and allowed to dry. TEM micrograph Fig. 1 a was recorded with a 12,500x magnification. High-angle annular dark-field scanning transmission electron microscopy (HAADF-STEM) measurements were performed using an ARM200F (JEOL, 200 kV) equipped with a spherical aberration corrector (CEOS) and an energy-dispersed X-ray analysis (EDX) system (JEOL). HAADF-STEM micrographs (Fig. 1 b, c) were recorded with a magnification of 300,000x and 3,000,000x, respectively. The probe size was 7.0 nm and the probe current was 0.08 nA for all samples. Fig. 1 k is a selected region of Fig. 1 c. Diffuse reflectance ultraviolet-visible spectra were measured using a CARY 300 (Agilent Technologies) with an Ulbricht sphere in the range of 450 to 800 nm. X-ray powder diffraction (XRD) analysis was performed using a

XPERT-PRO diffractometer (Panalytical) (CuKα radiation, 1.54178 Å). The reference card numbers for comparison are 00-021-1272 for TiO2 and 01-080-0019 for CdS. X-ray photoelectron spectroscopy (XPS) measurements were performed using a Specs Phoibos 150 R6 spectrometer equipped with HSA 3500 and MCD-9 detectors, a Specs Focus 500 monochromator, and a XR50M X-ray source (AlKα, 13 kV, 200 W). Time-resolved photoluminescence studies were carried out with a fluorescence lifetime imaging microscope (FLIM) MicroTime200 (Pico Quant). It is equipped with a picosecond diode laser (485 nm) with adjustable output power (set to 0.5 µW) and a bandpass filter 520/35 nm. The optical core is an inverted microscope IX 73 (Olympus) with a confocal unit and a piezo stage for z stacks. The data were recorded with a water immersion objective (60×, NA 1.2.). A single-photon counting APD module (SPAD) is used. Data acquisition is based on time-correlated single photon counting (TCSPC) performed by a TimeHarp 260 Pico board (Pico Quant). Samples are prepared by spin coating thin films of powder material dispersed in a polystyrene (Mw 200k g/mol) matrix on cover slips (18 mm x 18 mm x 200 µm). 2 mg of the sample are suspended in a polystyrene / toluene solution (300 µL, 200 mg/mL). Spin coating is performed at 750 rpm for 15 s, 1500 rpm for 30 s, 3000 rpm for 60 s.

Material Synthesis

Synthesis of MIL-101

MIL-101 was synthesized according to our previous work in order to maintain an average crystallite size of 300 nm.[S1] chromium(III) nitrate nonahydrate (640 mg, 1.60 mmol), terephthalic acid (265 mg, 1.60 mmol), hydrofluoric acid 40 wt.-% (10 µL, 0.228 mmol), and deionized H_2O (8.00 mL) were sealed in a 23 mL Teflon-lined hydrothermal autoclave. The mixture was heated for 1 h at 80 °C (heating rate: 1.7 °C min^{-1}) and for 7.45 h at 220 °C (4.7 °C min^{-1}). The reaction mixture was cooled down fast to 160 °C and slowly to 30 °C (cooling rate: 5.4 °C h^{-1}). Excessively crystallized H_2BDC was removed by filtration over a pore 3 filter. The product was separated from the reaction solution by centrifugation (2000 rpm, 45 min). The MIL-101 was refluxed in ethanol/water (90/10 vol.-%) for 15 h and centrifugalized (1800 rpm, 45 min) to remove the α-CrOOH impurities and to separate the MIL-101 crystals with different size distribution. The green product was dried under vacuum (10^{-4} mbar, 85 °C) (BET: 2820 m^2 g^{-1}).

Synthesis of TiO_2@MIL-101

TiO_2@MIL-101 was synthesized according to our previous work.[S2] Dry MIL-101 powder (400 mg) was placed in a two-chamber-tube with titanium(IV) isopropoxide (0.64 mL) separated by a glass frit. The gas phase infiltration of the TiO_2 precursor occurred at 32 °C in dynamic vacuum (10^{-4} mbar) for 20 h. The resulting bright green powder was processed in hydrolysis by thermal treatment under H_2O

atmosphere at 80 °C. The material was evacuated (10^{-4} mbar) at 85 °C for 20 h, transferred into a 125 mL Teflon-lined hydrothermal autoclave with 50 mL of deionized water, and heated at 150 °C for 10 h (heating rate: 2.0 °C min^{-1}). After cooling down to room temperature, the material was dried under vacuum (10^{-4} mbar, 85 °C). The Ti precursor infiltration, hydrolysis, and hydrothermal treatment described was performed one more time to yield TiO_2@MIL-101.

Synthesis of CdS/TiO_2@MIL-101, CdS@MIL-101, and CdS/TiO_2

200 mg dry TiO_2@MIL-101, MIL-101, or TiO_2 (anatase, acquired commercial) was suspended in 35 mL of dimethyl sulfoxide in a 125 mL Teflon-lined hydrothermal autoclave. 250 mg cadmium(II) acetate dihydrate were added and the reaction mixture was stirred for 2 h. The mixture was heated at 180 °C for 10 h (heating rate: 2.5 °C min^{-1}). After cooling down to room temperature, the resulting CdS/TiO_2@MIL-101 was separated by filtration and washed with ethanol. The material was combined with 40 mL of ethanol and heated at 100 °C for 10 h (heating rate: 1.2 °C min^{-1}) in a 125 mL Teflon-lined hydrothermal autoclave. After cooling down, the material was separated by filtration and dried (10^{-4} mbar, 85 °C).

Synthesis of Ni/CdS/TiO_2@MIL-101, Ni/CdS@MIL-101, Ni/TiO_2@MIL-101, Ni/CdS/TiO_2, Ni/CdS, and Ni/TiO_2

150 mg dry CdS/TiO_2@MIL-101, CdS@MIL-101, TiO_2@MIL-101, CdS/TiO_2, CdS (cubic, acquired commercial), or TiO_2 (anatase, acquired commercial) was placed in a two-chamber-tube with bis(cyclopentadienyl)nickel(II) (20 mg) separated by a glass frit. The gas phase infiltration of the Ni precursor occurred at room temperature (25 °C) in static vacuum (10^{-4} mbar) for 20 h. The reduction of the Ni precursor was performed under hydrogen atmosphere (10 bar H_2) at 90 °C for 20 h in a Parr Instruments steel autoclave. The resulting Ni/CdS/TiO_2@MIL-101 was evacuated (10^{-4} mbar, 85 °C) for 20 h in order to remove former metal ligand recess.

Synthesis of Pd/CdS/TiO_2@MIL-101

The synthesis of Pd/CdS/TiO_2@MIL-101 was performed as described for Ni/CdS/TiO_2@MIL-101 using allyl(cyclopentadienyl)palladium(II) (17 mg). The reduction of the Pd precursor was performed at 10 bar H_2.

Synthesis of Pt/CdS/TiO_2@MIL-101

The synthesis of Pt/CdS/TiO_2@MIL-101 was performed as described for Ni/CdS/TiO_2@MIL-101 using Trimethyl(methylcyclopentadienyl)platinum(IV) (15 mg). The reduction of the Pt precursor was performed at 10 bar H_2.

Synthesis of Au/CdS/TiO_2@MIL-101

150 mg dry CdS/TiO_2@MIL-101 powder was placed in a two-chamber-tube with Chlorocarbonylgold(I) (24 mg) separated by a glass installation. The gas-phase infiltration of the Au precursor occurred at 45 °C in static vacuum (10^{-4} mbar) for 20 h. The reduction of the Au precursor was performed under hydrogen atmosphere (20 bar H_2) at 90 °C for 20 h in a Parr Instruments steel autoclave. The resulting Au/CdS/TiO_2@MIL-101 was evacuated (10^{-4} mbar, 85 °C) for 20 h in order to remove former metal ligand recess.

General Procedure for Photocatalytic Experiments

General procedure for the photocatalytic hydrogen generation by alcohol oxidation

A 10 mL reaction vial was charged with a magnetic stir bar, Ni/CdS/TiO_2@MIL-101 catalyst (0.6 mg), and alcohol (0.1 mmol). The vial was sealed with a rubber septum, evacuated to remove the air atmosphere, and flushed with argon for 2 min. Dry and degassed acetonitrile (0.3 mL) was added and the vial was further purged with argon for 1 min. The vial was illuminated for 24 h by a 50 W blue LED (470 nm, distance 5 cm, ~15000 lx) and cooled by a fan (Figure S9). The reaction temperature was measured to be 27 °C. N-dodecane (10 µL, 44 µmol) was added as internal standard and the catalyst was separated from the reaction solution by centrifugation (9000 rpm, 9 min) before quantitative analysis by GC. The amount of H_2 evolved was determined by injecting 500 µL of methane as internal standard before LED illumination. The gas phase of the reaction was analysed by GC-TDC. Regarding the oxidation of 2-propanol, 7.7 µL (0.1 mmol) of dry and degassed alcohol were added after the evacuation of the vial and dehydrogenated without solvent.

Benzyl alcohol (0.3 mmol, 31.2 µL) and 0.5 mg catalyst were illuminated for 20 h for the comparison of different catalysts (Figure 2a).

Reusability of the Ni/CdS/TiO_2@MIL-101 photocatalyst

A 10 mL reaction vial was charged with a magnetic stir bar, Ni/CdS/TiO_2@MIL-101 catalyst (4 mg), and benzyl alcohol (0.1 mmol). The vial was sealed with a rubber septum, evacuated to remove the air atmosphere, and flushed with argon for 2 min. Dry and degassed acetonitrile (0.5 mL) was added and the vial was further purged with argon for 1 min. The vial was illuminated for 5 h by a 50 W blue LED (470 nm, distance 5 cm, ~15000 lx) and cooled by a fan (Figure S9). N-dodecane (10 µL, 44 µmol) was added as internal standard and the catalyst was separated from the reaction solution by centrifugation (9000 rpm, 9 min) before quantitative analysis by GC. The catalyst was purified with acetonitrile between the runs.

General procedure for the photocatalytic synthesis of imines

A 10 mL reaction vial was charged with a magnetic stir bar, Ni/CdS/TiO_2@MIL-101 catalyst (1.5 mg), amine (0.1 mmol), and alcohol (0.13 mmol). The vial was sealed with a rubber septum, evacuated to remove the air atmosphere, and flushed with argon for 2 min. Dry and degassed acetonitrile (0.15 mL) was added and the vial was further purged with argon for 1 min. The vial was illuminated for 48 h by a 50 W blue LED (470 nm, distance 5 cm, ~15000 lx) and cooled by a fan (Figure S9). The reaction temperature was measured to be 27 °C. N-decane (10 µL, 51 µmol) was added as internal standard and the catalyst was separated from the reaction solution by centrifugation (9000 rpm, 9 min) before quantitative analysis by GC. The amount of H_2 evolved was determined by injecting 500 µL of methane as internal standard before LED illumination. The gas phase of the reaction was analysed by GC-TDC.

Material Characterization

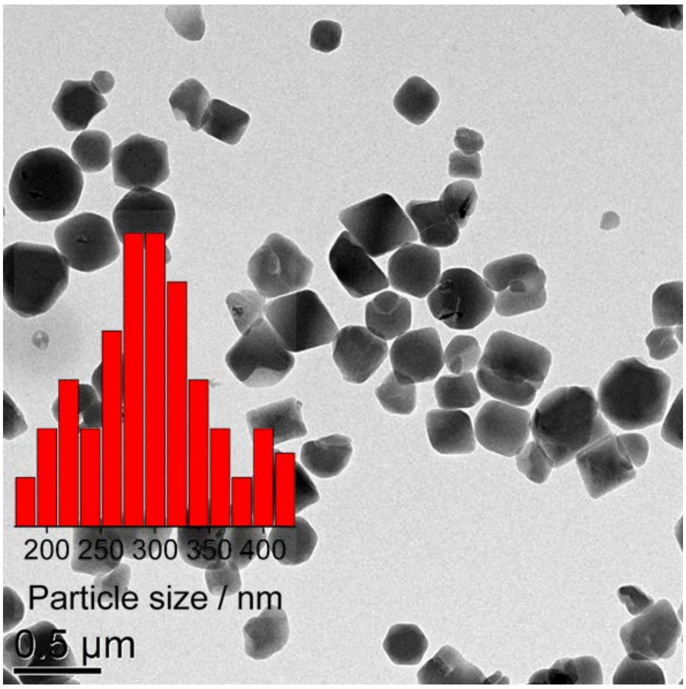

Figure S1. TEM analysis of the as-synthesized MIL-101 crystallites with an average diameter of 300 nm.

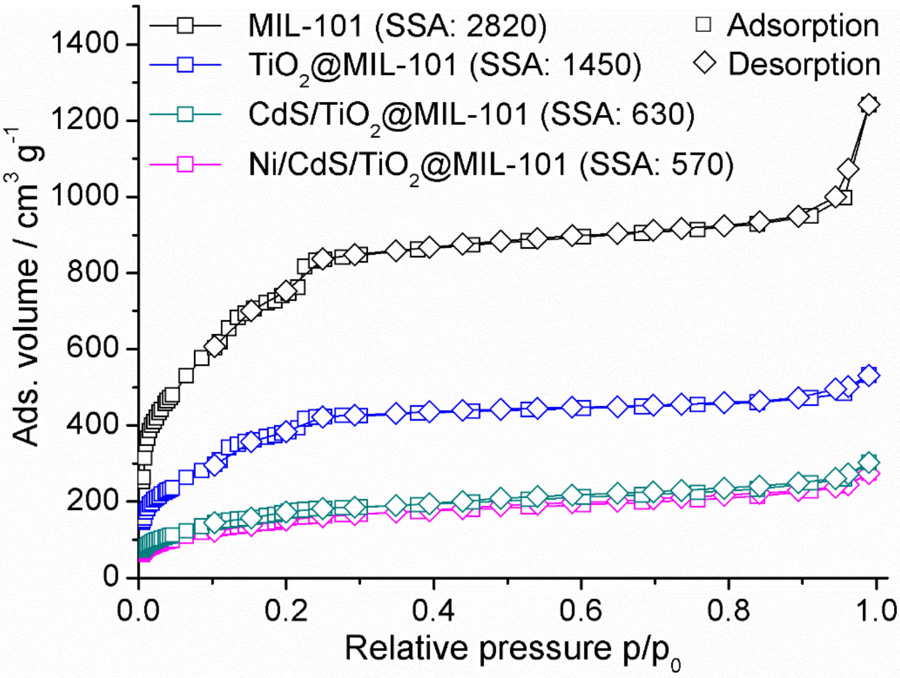

Figure S2. Nitrogen physisorption isotherms of MIL-101, TiO$_2$@MIL-101, CdS/TiO$_2$@MIL-101, and Ni/CdS/TiO$_2$@MIL-101 with the respective specific surface areas (SSA given in m^2 g^{-1}) determined by the BET model.

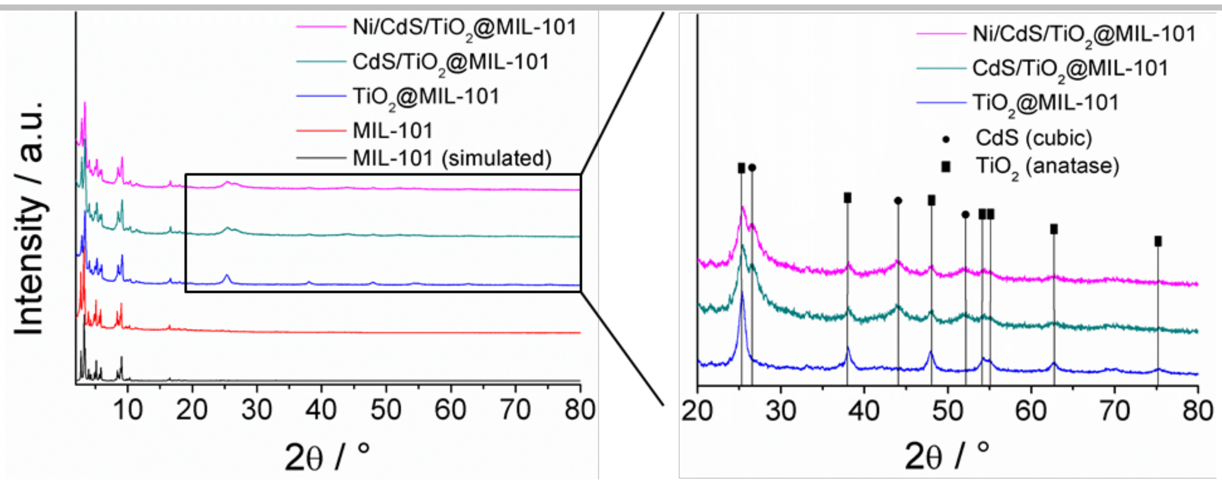

Figure S3. XRD spectra of MIL-101, TiO_2@MIL-101, CdS/TiO_2@MIL-101, and Ni/CdS/TiO_2@MIL-101 with the characteristic reflexes of MIL-101, cubic CdS (Ref. 01-080-0019) and anatase TiO_2 (Ref. 00-021-1272).

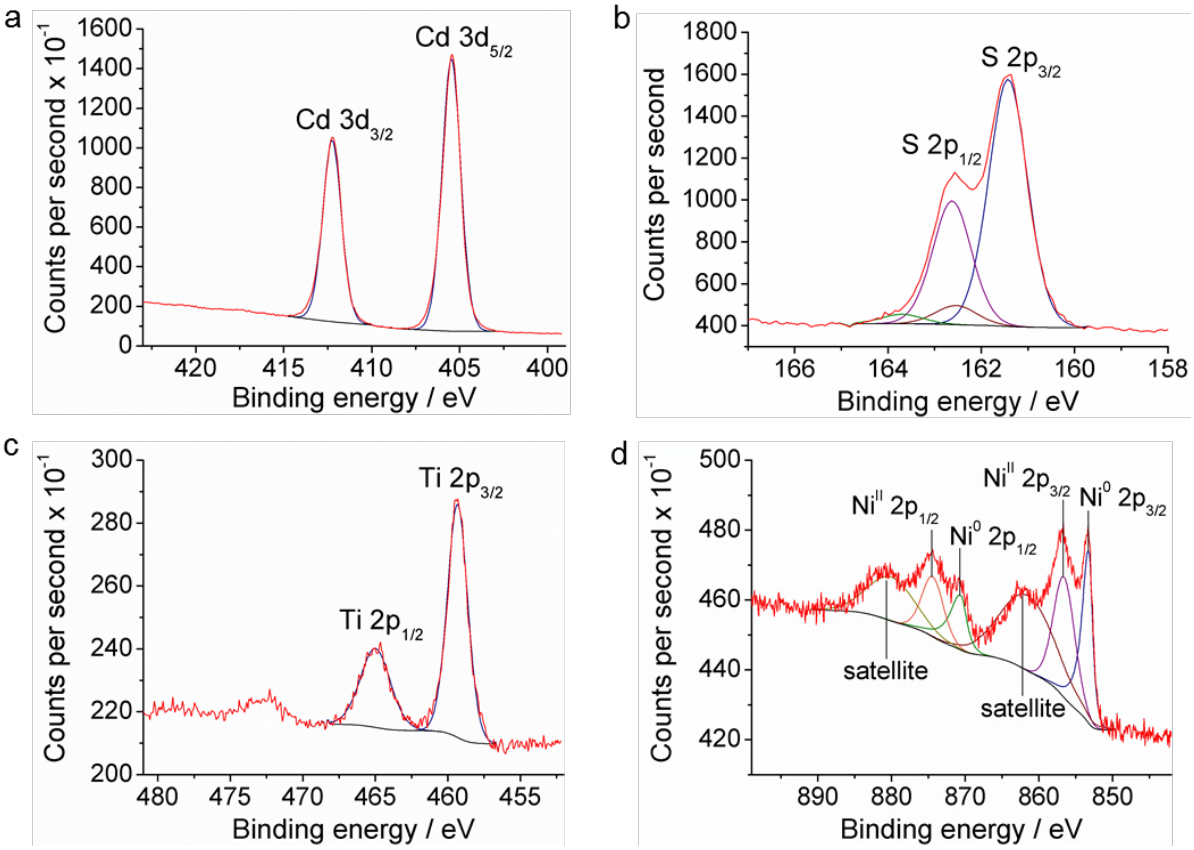

Figure S4. XPS spectra of Ni/CdS/TiO_2@MIL-101 in a) the Cd 3d region, b) the S 2p region, c), the Ti 2p region and, d) the Ni 2p region.

Table S1. ICP-OES analysis of TiO_2@MIL-101, CdS/TiO_2@MIL-101, and M/CdS/TiO_2@MIL-101 (M = Ni, Pd, Pt, Au) with contents given in wt.-%.

Material	Cr	Ti	TiO_2[a]	Cd	CdS[a]	Ni	Pd	Pt	Au
TiO_2@MIL-101	11.2	25.0	41.7	-	-	-	-	-	-
CdS/TiO_2@MIL-101	7.9	17.8	29.7	16.2	20.8	-	-	-	-
Ni/CdS/TiO_2@MIL-101	7.3	15.6	26.0	14.6	18.8	3.6	-	-	-
Pd/CdS/TiO_2@MIL-101	6.8	16.4	27.4	15.6	20.0	-	4.3		-
Pt/CdS/TiO_2@MIL-101	8.2	15.1	25.2	14.3	18.4	-	-	3.1	-
Au/CdS/TiO_2@MIL-101	7.1	14.7	24.5	14.8	19.0	-	-	-	5.6

[a] Calculated on the basis of the Ti and Cd content.

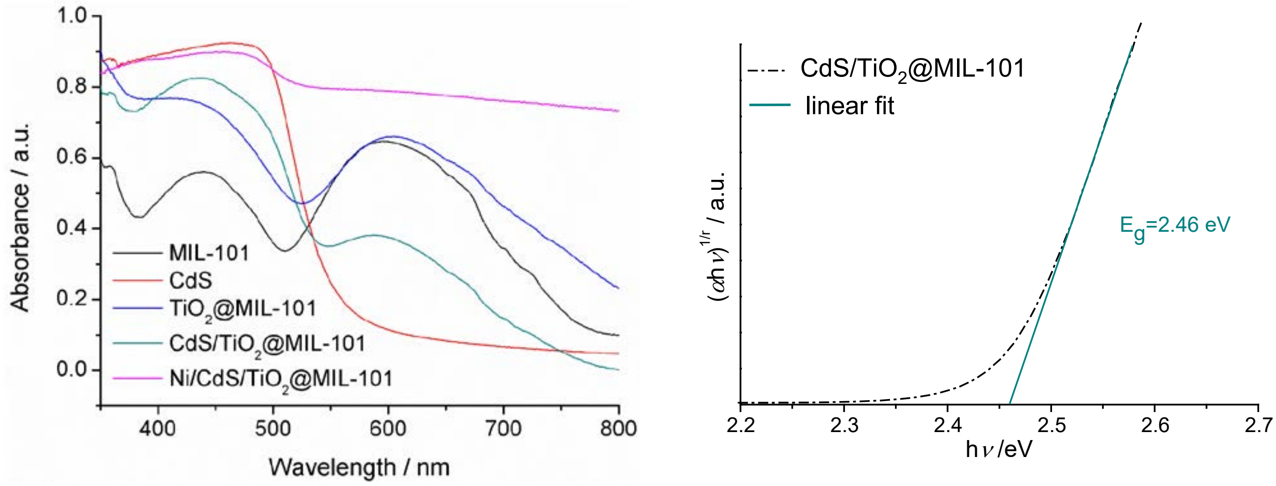

Figure S5. Diffuse reflectance ultraviolet-visible spectra of MIL-101, CdS (cubic), TiO_2@MIL-101, CdS/TiO_2@MIL-101, and Ni/CdS/TiO_2@MIL-101. For CdS/TiO_2@MIL-101, the band gap energy was determined by applying the Munk-Kubelka equation.

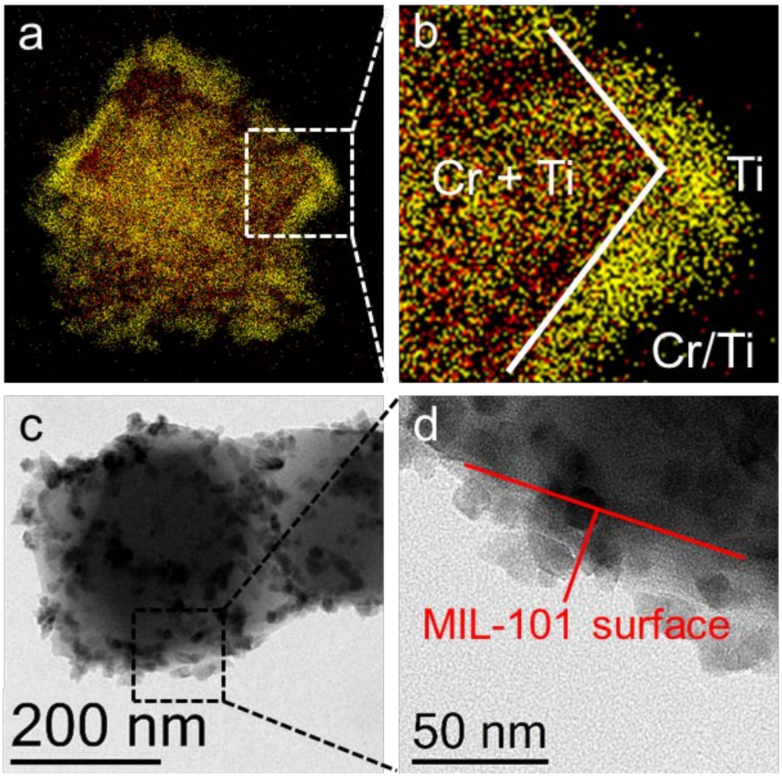

Figure S6. a,b) HAADF-STEM analysis of Ni/CdS/TiO_2@MIL-101 with representative EDX element maps and c,d) TEM analysis of TiO_2@MIL-101 illustrating the core-shell morphology of the materials.

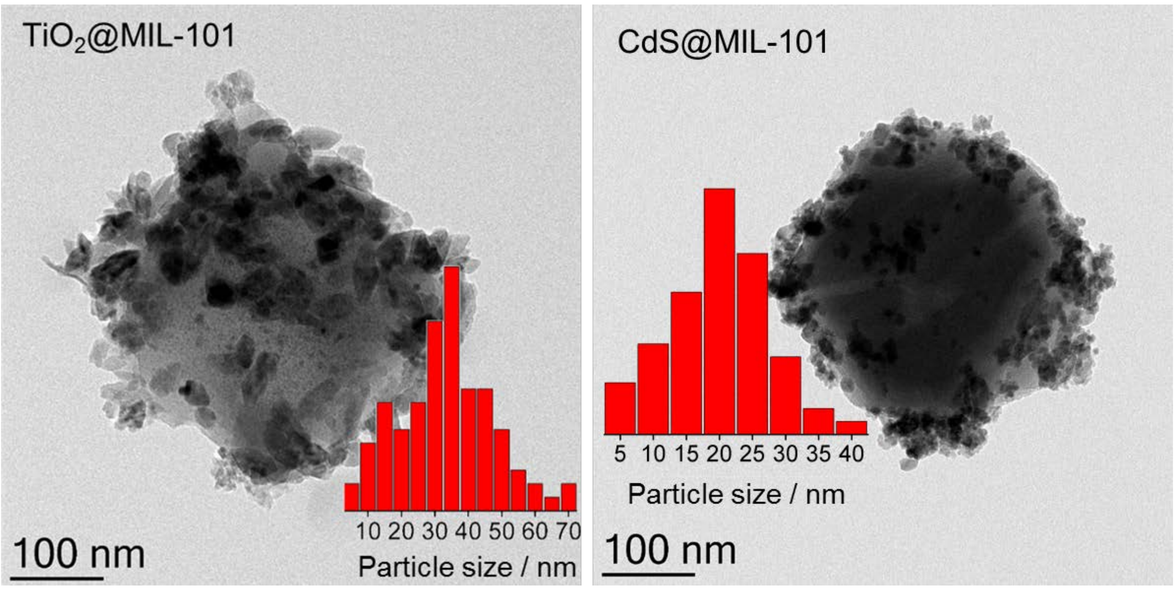

Figure S7. TEM micrographs of TiO_2@MIL-101 and CdS@MIL-101 with the respective particle size distribution.

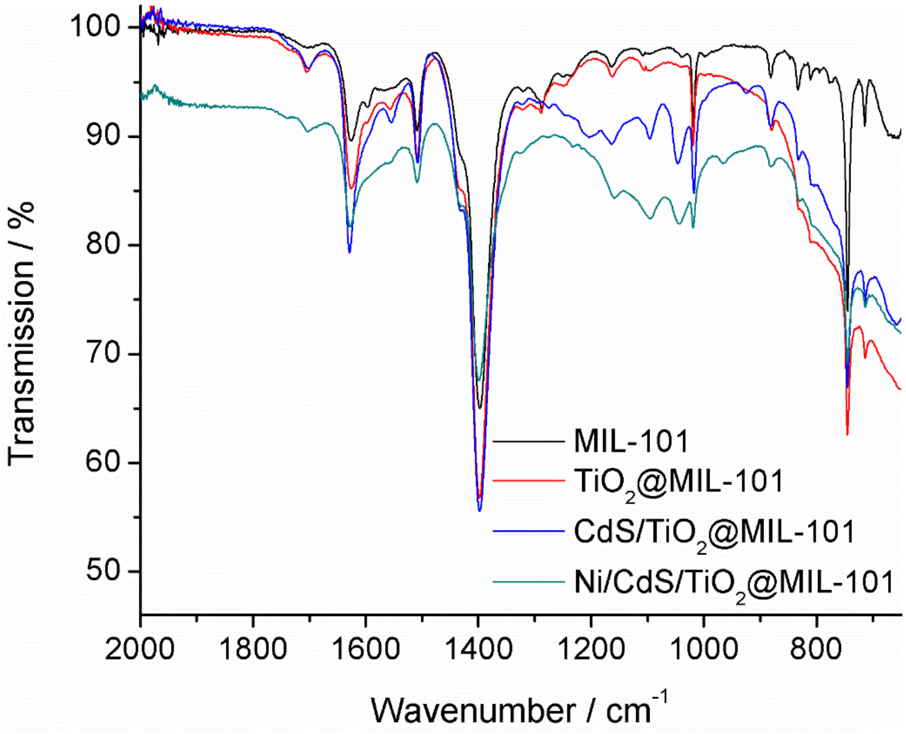

Figure S8. FTIR spectra of MIL-101, TiO_2@MIL-101, CdS/TiO_2@MIL-101, and Ni/CdS/TiO_2@MIL-101.

Table S2. Linear fitting parameters and R^2-values (squared correlation coefficient) of the TCSPC traces for the lifetime determination of excited CdS in TRPL studies. The IRF has not been taken into account in the data analysis. Fluorescence lifetimes of CdS catalysts supported on MIL-101 are given.

Compound	Slope [1/ns]	Stand. error slope [1/ns]	R^2-value	Lifetime [ns]	Lifetime error [ns]
CdS@MIL-101	-3.001	0.018	0.99881	0.333	0.002
CdS/TiO_2@MIL-101	-3.346	0.043	0.99131	0.299	0.004
Ni/CdS/TiO_2@MIL-101	-4.238	0.032	0.99711	0.236	0.002

Photocatalytic Experiments

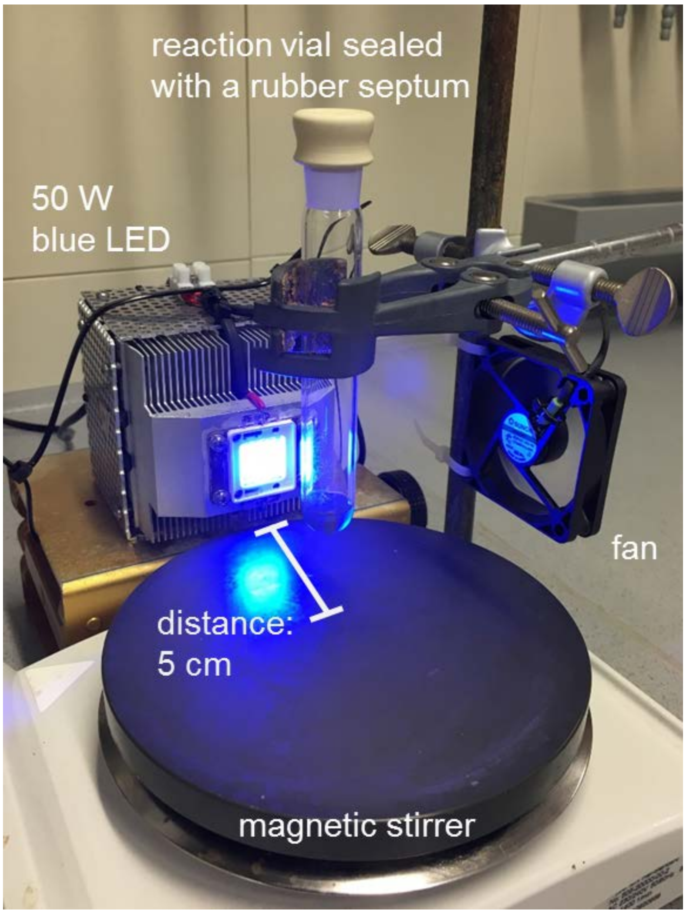

Figure S9. Experimental setup for photocatalytic experiments. The reaction vials sealed with a rubber septum were illuminated by a 50 W blue LED (470 nm, distance 5 cm, ~15000 lx), stirred magnetically, and cooled by a fan.

We performed control experiments to investigate whether O_2 is inserted into the reaction vials by diffusion through the rubber septa during catalysis. Therefore, we prepared several experiments in a nitrogen-filled glovebox using the same amount of catalyst, substrate, and solvent as described in the supplementary methods section and sealed the reaction vials with a greased glass plug. The yields of the reactions prepared in the glove box were equal to the yields prepared according to the supplementary methods section using a rubber septum. Consequently, no entry of O_2 was observed, which would have influenced the reactions (for example the yields). Additionally, no entry of O_2 was observed during the analysis of the evolved amount of H_2 by GC-TDC.

Table S3. Solvent screening for the photocatalytic dehydrogenation of benzyl alcohol.[a]

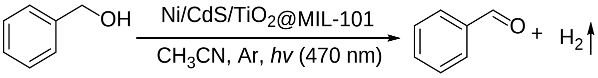

Entry	Solvent	Yield[b] [%]
1	Diglyme	14
2	**Acetonitrile**	**53**
3	Toluene	34
4	Tetrahydrofurane	12
5	Dimethoxyethane	15
6	1,4-Dioxane	6
7	No solvent	33

[a] Reaction conditions: 0.20 mmol Benzyl alcohol, 0.5 mg Ni/CdS/TiO_2@MIL-101, Ar, 0.30 mL solvent, 27 °C, 20 h, 470 nm blue LED 50 W. [b] Determined by GC using n-dodecane as internal standard.

Table S4. Screening of the Ni amount for the photocatalytic dehydrogenation of benzyl alcohol.[a]

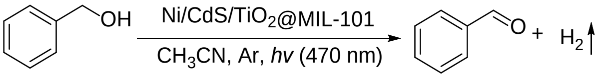

Entry	Catalyst[c]	Yield[b] [%]
1	Ni/CdS/TiO_2@MIL-101 (2 wt% Ni)	64
2	**Ni/CdS/TiO_2@MIL-101 (4 wt% Ni)**	**73**
3	Ni/CdS/TiO_2@MIL-101 (6 wt% Ni)	52

[a] Reaction conditions: 0.3 mmol benzyl alcohol, 0.5 mg catalyst, 0.5 mL solvent, Ar, 24 h, 27 °C, 470 nm blue LED 50 W. [b] Determined by GC using n-dodecane as internal standard. [c] The Ni content was calculated based on the amount of precursor.

Table S5. Catalyst screening for the photocatalytic dehydrogenation of benzyl alcohol.[a]

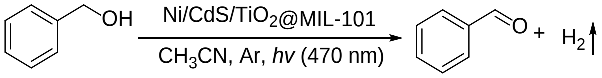

Entry	Catalyst	Yield[b] [%]
1	**$Ni/CdS/TiO_2$@MIL-101**	**73**
2	$Pd/CdS/TiO_2$@MIL-101	16
3	$Pt/CdS/TiO_2$@MIL-101	21
4	$Au/CdS/TiO_2$@MIL-101	8
5	CdS/TiO_2@MIL-101	13
6	CdS@MIL-101	6
7	Ni/CdS@MIL-101	29
8	Ni/TiO_2@MIL-101	0
9	MIL-101	0
10	CdS[c]	5
11	Ni/CdS[c]	15
12	Ni/CdS[c] + TiO_2[d]	10
13	Ni/TiO_2	0
14	Ni + CdS[c] + TiO_2[d]	6
15	$Ni/CdS/TiO_2$[d]	21
16	TiO_2 (P25)	0

[a] Reaction conditions: 0.3 mmol benzyl alcohol, 0.5 mg catalyst, 0.5 mL solvent, Ar, 24 h, 27 °C, 470 nm blue LED 50 W. [b] Determined by GC using n-dodecane as internal standard. [c] Commercial available cubic CdS. [d] Commercial available TiO_2 (anatase).

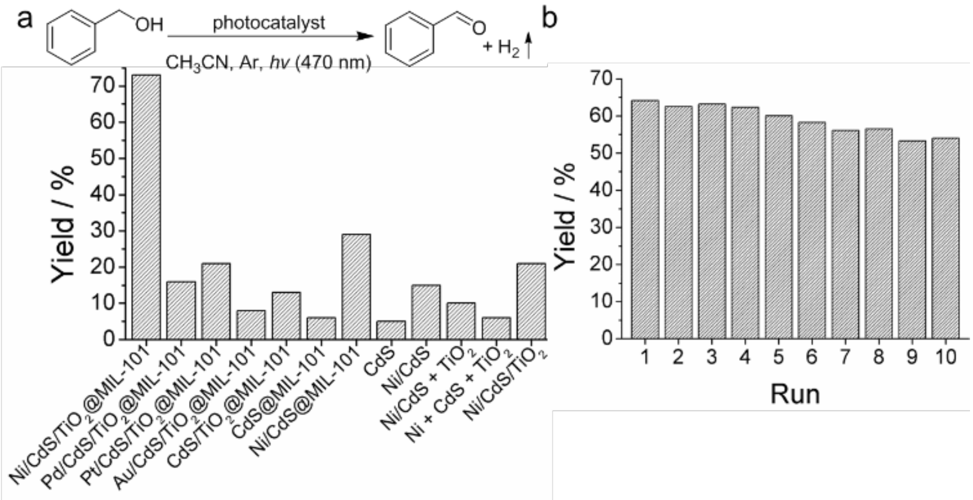

Figure S10. a) Comparison of different photocatalysts for the dehydrogenation of benzyl alcohol. The yields were determined by gas chromatography (GC) using n-dodecane as internal standard. b) Reusability of the Ni/CdS/TiO2@MIL-101 catalyst with an activity decrease of less than 10 % after ten runs resulting from the purification procedure of the catalyst between the runs.

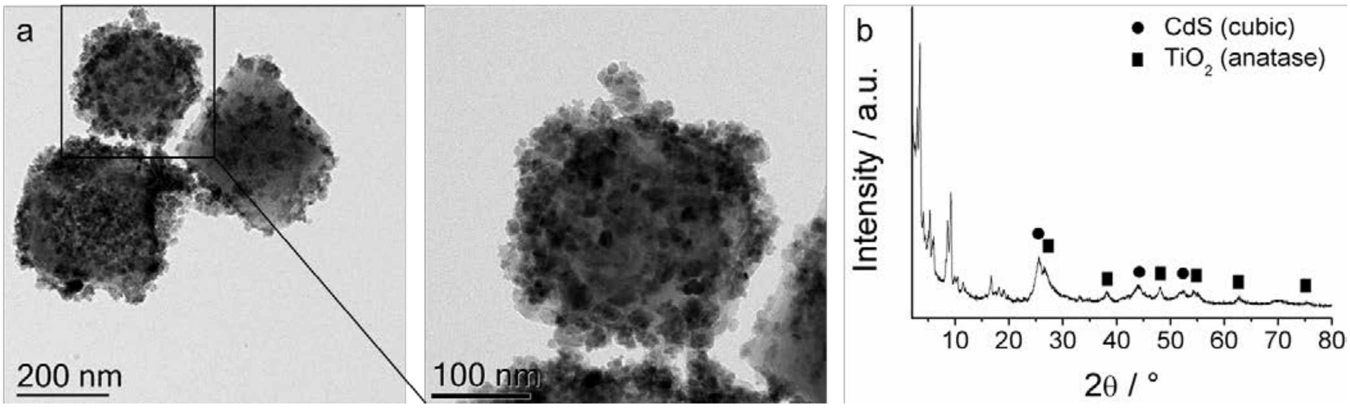

Figure S11. a) TEM micrographs of the Ni/CdS/TiO_2@MIL-101 catalyst reused for the photocatalytic dehydrogenation of benzyl alcohol for ten runs. b) XRD analysis of the reused catalyst.

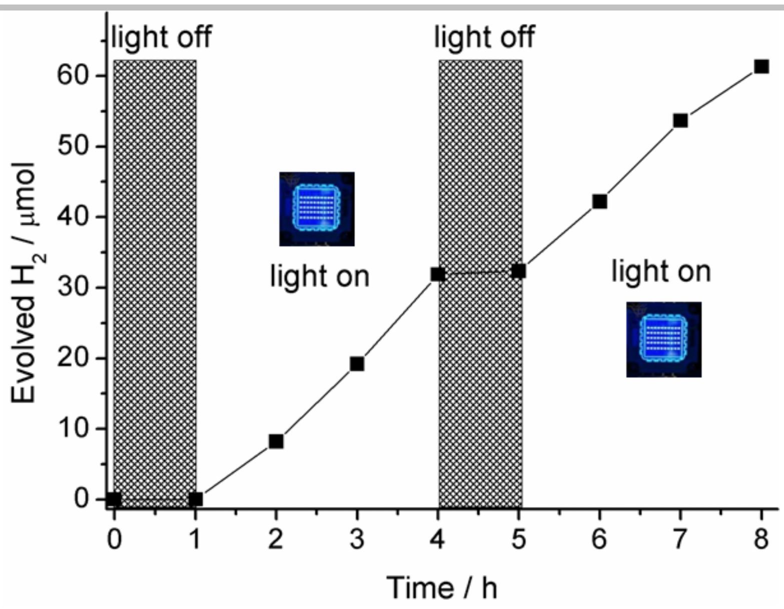

Figure S12. Light on/off experiment. Hydrogen evolution from benzyl alcohol was only observed under light illumination (4.0 mg Ni/CdS/TiO_2@MIL-101, 0.3 mmol benzyl alcohol, 0.3 mL CH_3CN, Ar, 50 W blue LED).

Table S6. Photocatalytic dehydrogenation of additional alcohols.[a]

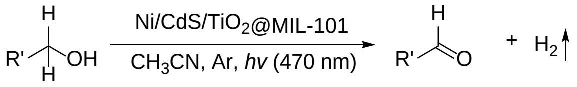

Entry	Product	R	Yield[b] [%]
1	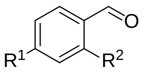	R^1 = OMe, R^2 = H	>99
2		R^1 = H, R^2 = OMe	93
3		R^1 = Me, R^2 = H	>99
4		R^1 = H, R^2 = Me	82
5		R^1 = F, R^2 = H	87
6		R^1 = Cl, R^2 = H	>99
7[c]		R^1 = H, R^2 = Cl	87
8[c]		R^1 = Br, R^2 = H	96
9[c]		R^1 = OH, R^2 = H	83
10		R^1 = H, R^2 = OH	87
11[d]		R^1 = H, R^2 = CF_3	89
12[c]	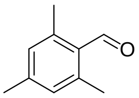		78
13	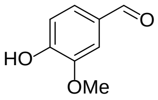		85
14[d]	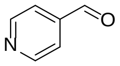		92
15[d]	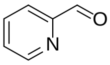		83
16[e]	acetone		64[f]

[a] Reaction conditions: 0.1 mmol alcohol, 0.6 mg Ni/CdS/TiO_2@MIL-101, Ar, 0.3 mL CH_3CN, 27 °C, 24 h, 470 nm blue LED 50 W. [b] Determined by GC using n-dodecane as internal standard. [c] 1.2 mg Ni/CdS/TiO_2@MIL-101. [d] 1.2 mg Ni/CdS/TiO_2@MIL-101, 48 h. [e] Without solvent, 72 h. [f] Determined by the evolved amount of H_2 using methane as internal standard (GC-TCD).

Table S7. Hydrogen generation via photocatalytic dehydrogenation of alcohols.[a]

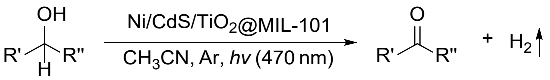

Entry	Product	R	Yield[b] [µmol]	H_2[c] [µmol]
1	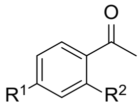	R^1 = H, R^2 = H	97	92
2		R^1 = OMe, R^2 = H	96	88
3		R^1 = Cl, R^2 = H	97	85
4	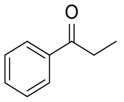		93	77
5	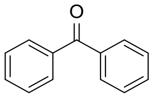		88	78
6	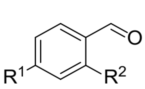	R^1 = H, R^2 = H	>99	93
7		R^1 = H, R^2 = H	10[d]	0[d]
8		R^1 = Me, R^2 = H	>99	94
9		R^1 = H, R^2 = NH_2	96	84
10		R^1 = OH, R^2 = H	83	71

[a] Reaction conditions: 0.1 mmol alcohol, 0.6 mg Ni/CdS/TiO_2@MIL-101, Ar, 0.3 mL CH_3CN, 27 °C, 24 h, 470 nm blue LED 50 W. [b] Determined by GC using n-dodecane as internal standard. [c] Determined using methane as internal standard (GC-TCD). [d] Without inert atmosphere.

Table S8. Screening of the alcohol:amine ratio for the synthesis of imines.[a]

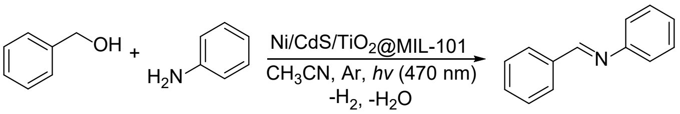

Entry	alcohol:amine	Yield[b] [%]
1	1:1	36
2	1.1:1	41
3	1.2:1	49
4	**1.3:1**	**66**
5	1.4:1	65

[a] 0.1 mmol aniline, benzyl alcohol, 1.5 mg Ni/CdS/TiO_2@MIL-101, Ar, 0.15 mL CH_3CN, 27 °C, 30 h, 470 nm blue LED 50 W. [b] Determined by GC using n-decane as internal standard.

Table S9. Hydrogen liberation during the photocatalytic synthesis of imines from alcohols an amines.[a]

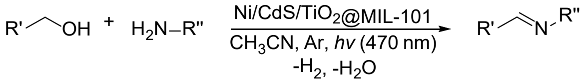

Entry	Product	R	Yield[b] [%]	H_2[c] [µmol]
1	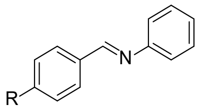	R = H	92	113
2		R = H	50[d]	0[d]
3		R = Me	86	107
4		R = Cl	88	95
5	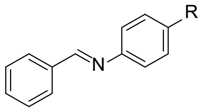	R = Me	88	107
6		R = OMe	93	117
7	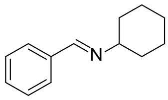		87	113

[a] Reaction conditions: 0.1 mmol amine, 0.13 mmol alcohol, 1.5 mg Ni/CdS/TiO_2@MIL-101, Ar, 0.15 mL CH_3CN, 27 °C, 48 h, 470 nm blue LED 50 W. [b] Determined by GC using n-decane as internal standard. [c] Determined using methane as internal standard (GC-TCD). The benzyl alcohol derivates (0.13 mmol) were completely oxidized to the corresponding aldehydes. [d] Without inert atmosphere.

Theoretical Procedures

The aim of the Density Functional Theory (DFT) calculations that we report in this supplemental information is to check in a transparent model calculation whether there is a difference in the strength with which a benzyl alcohol molecule binds to a Ni and a Pd particle. We believe that this comparison is most meaningful when the metal particles have a similar geometry. Therefore, we chose to compare the strength with which one benzyl alcohol molecule (C_7H_8O) binds to either Ni_{13} or Pd_{13}, with the latter having similar geometries that result from a basic icosahedral motive.

Our calculations use the TURBOMOLE[S3] program package. Geometry optimizations (GO) serve to find reasonable nanoparticle structures. All GOs of the model system were carried out with the Perdew-Burke-Ernzerhof (PBE)[S4,S5] generalized gradient approximation (GGA) and the def2-TZVP[S6] basis set. The same basis set was also used in all calculations with a hybrid exchange-correlation (xc) functional (see below). All our calculations take *van-der-Waals'* interactions into account via the scheme of Grimme.[S7]

Metals with d-electrons are challenging for many exchange-correlation energy approximations, because the inaccuracies of semi-local functionals affect localized and delocalized orbitals quite differently. One-electron self-interaction[S8], e.g., depends sensitively on orbital localization.[S9] Hence, studying systems containing Ni and/or Pd requires special care.[S10] To make sure that the qualitative conclusions that we draw here are not affected by such errors, we check whether the trends that we observe with the PBE GGA are reproduced by the Becke-3-parameter-Lee-Yang-Parr (B3LYP)[S11,S12] hybrid xc functional that cancels the self-interaction error partially due to its fraction of Fock exchange.

Table S10. Total energy $E_{\mathrm{tot}}^{\mathrm{xc}}$ of one benzyl alcohol (C_7H_8O), the bare metal particles (Ni_{13}(ico), Pd_{13}(ico)) and the combined system Ni_{13}/C_7H_8O and Pd_{13}/C_7H_8O, respectively. Binding energies $\Delta E_{\mathrm{B}}^{\mathrm{xc}}$ are calculated based on the total energy differences according to equation (1) as described in the text. All numbers are in eV.

	$E_{\mathrm{tot}}^{\mathrm{PBE}}$	$\Delta E_{\mathrm{B}}^{\mathrm{PBE}}$	$E_{\mathrm{tot}}^{\mathrm{B3LYP}}$	$\Delta E_{\mathrm{B}}^{\mathrm{B3LYP}}$
C_7H_8O	-9427.9455	–	-9434.3790	–
Ni_{13}(ico)	-533506.0785	–	-533554.0148	–
Pd_{13}(ico)[a]	-45270.8245	–	-45250.4232	–
Pd_{13}/C_7H_8O(S13a)[a,b]	-54701.2921	-2.52	-54685.8137	-1.01

Pd_{13}/C_7H_8O(S13c)[a,b]	-54701.2740	-2.50	–	–
Ni_{13}/C_7H_8O(S13b)[b]	-542937.0146	-2.99	-542989.5710	-1.18
Ni_{13}/C_7H_8O(S13d)[b]	-542936.9670	-2.94	–	–
Pd_{13}/C_7H_8O(3a)[a,c,d1]	-54701.4167	-2.65	–	–
Pd_{13}/C_7H_8O[a,d2]	-54701.4140	-2.64	–	–
Ni_{13}/C_7H_8O(3b)[c,d1]	-542937.1477	-3.12	–	–
Ni_{13}/C_7H_8O[c,d2]	-542937.1368	-3.11	–	–

[a] relativistic Pd-effective-core-potential[S13]

[b] (S13x) refers to Figure S13 a, b, c, d

[c] (3x) refers to Figure 3 a, b

[d1] relaxed lowest energy structure from DFT BOMD

[d2] relaxed second lowest energy structure from DFT BOMD

We started by doing GOs for one benzyl alcohol molecule and the 13-atom Ni and Pd clusters separately. Table S10 shows the corresponding total energies. Different structural isomers are reported in the literature for Ni_{13}[S10,S14,S15] and Pd_{13}[S10,S16,S17]. We started from the stable structures reported in refs. [S14] and [S10] for Ni_{13} and Pd_{13}, respectively. From those we chose the icosahedral structure for both MNP clusters and relaxed the structure. Previous calculations found the icosahedral geometry as the Ni_{13}(ico) ground state.[S10,S14] For Pd_{13}, the icosahedral geometry is stable as well, but PBE and PBE0 calculations favor a bilayered structure and a geometry showing *c3v* symmetry by circa 124 meV and 26 meV, respectively.[S10,S16] In order to have a comparison on the same metal geometry, we chose the icosahedral geometry for Pd_{13} as the basis of our study. This choice is further motivated by unpublished DFT Born-Oppenheimer-Molecular-Dynamics (BOMD) room-temperature data obtained by some of us in the context of another study that shows that an icosahedral Pd_{13} cluster is stabilized by solvent molecules. Thus, we consider the icosahedral structure the more relevant one for the present study.

When determining the electronic structure of small Ni and Pd clusters, one must further take into account that they can show a non-zero magnetic moment.[S10,S14,S15,S16,S17,S18,S19,S20,S21,S22] For Pd_{13}(ico) both PBE and PBE0 predict a spin magnetic moment of 8 μ_B for the ground state. For Ni_{13}(ico) the situation is different. PBE prefers 8 μB, yet PBE0 yields a higher magnetic state of 16 μ_B. Our results for both MNP clusters agree with refs. [S10, S14, S16] within the margins of comparability and reproducibility. In our study, we used the semi-empirical Becke-3-parameter-Lee-Yang-Parr (B3LYP)[S11,S12] hybrid functional, which also lead to 16 μ_B ground state. The magnetic, high spin state predicted by hybrid functionals (PBE0, B3LYP), seems to conform with recent X-ray magnetic circular dichroism spectroscopy experiments of cationic Ni_{13}^+ that were independently reported by Langenberg et al.[S18] and Meyer et al.[S19]. Prior to these, however, Stern-Gerlach studies[S20,S21] on Ni_{13} predicted a lower total magnetic moment. For our calculation of the binding energies we therefore in each case used the lowest energy structures that we found.

Finally, we modeled a joint system, determined its total energy ($E_{\mathrm{tot}}^{\mathrm{xc}}$) and calculated the binding energy ($\Delta E_{\mathrm{B}}^{\mathrm{xc}}$) via

$$\Delta E_{\mathrm{B}}^{\mathrm{xc}}\,(\mathrm{MNP}_{13}/\mathrm{C}_7\mathrm{H}_8\mathrm{O}) = E_{\mathrm{tot}}^{\mathrm{xc}}\,(\mathrm{MNP}_{13}/\mathrm{C}_7\mathrm{H}_8\mathrm{O}) - E_{\mathrm{tot}}^{\mathrm{xc}}\,(\mathrm{MNP}_{13}) - E_{\mathrm{tot}}^{\mathrm{xc}}\,(\mathrm{C}_7\mathrm{H}_8\mathrm{O}), \qquad (1)$$

where *xc* refers to the functional (here PBE and later B3LYP), MNP_{13} to either Ni_{13}(ico) or Pd_{13}(ico) and MNP_{13}/C_7H_8O to the joint system. For each structure we carried out a set of GOs with fixed spin magnetic moments (in μ_B) in the range of [0,2,...,10] to determine its magnetic ground state. In this system, we started from a geometry in which the benzyl alcohol's benzene ring was close to the MNP and relaxed these initial structure (with PBE). We used different starting geometries, with the functional group (-OH) pointing towards or away from the MNP, respectively (Figure S13).

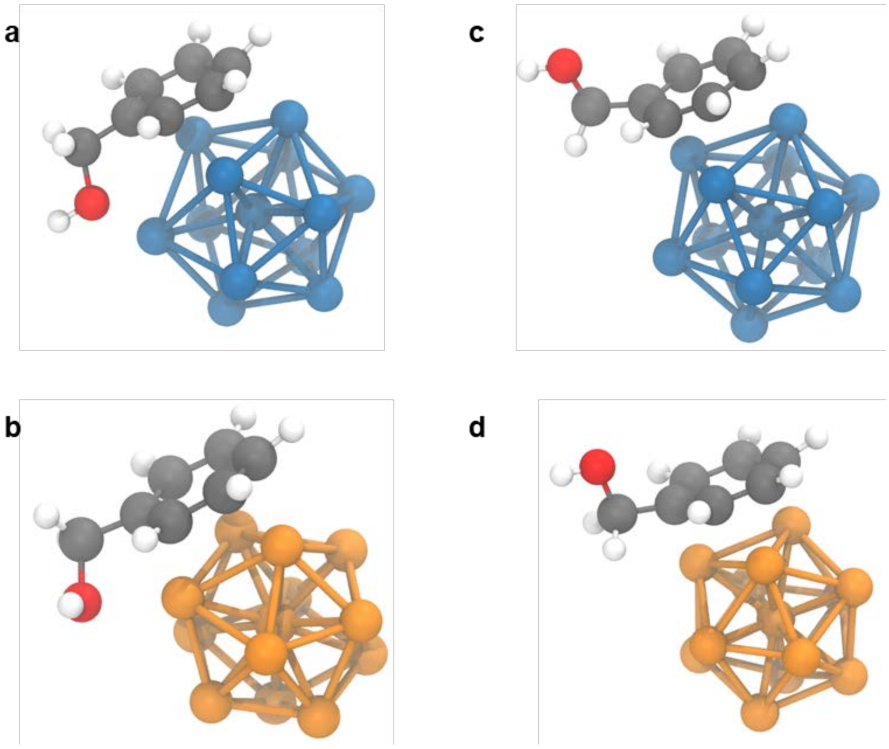

Figure S13. Relaxed structures with different arrangements of the functional group (-OH) of benzyl alcohol with respect to (top) Pd_{13}(ico) and (bottom) Ni_{13}(ico).

We found that with PBE the former is slightly preferred by both Ni_{13}/C_7H_8O and Pd_{13}/C_7H_8O by some 50 meV and only a few meV, respectively. The lowest energy configurations, corresponding to Figure S13 (a, b), showed a binding energy of 2.99 eV (Ni_{13}/C_7H_8O (8 μ_B)) and 2.52 eV (Pd_{13}/C_7H_8O (4 μ_B)), i.e., a difference of ca. 0.4 eV. Furthermore, comparing the magnetic moments of the joint system to the bare 13-atom MNP clusters using the PBE functional shows a quenching of the magnetic moment for Pd_{13}/C_7H_8O (4 μ_B), but not for Ni_{13}/C_7H_8O (8 μ_B).

To check whether the observed trend in binding energy is robust we also computed the electronic structure with B3LYP. To this end, we kept the two aforementioned lowest energy geometries fixed (Figure S13 (a, b)) and carried out a ground state calculation. The spin magnetic moment (in μ_B) for these calculations was varied in the range of [0,2,...,8] and [0,2,...,16] for Pd_{13}/C_7H_8O and Ni_{13}/C_7H_8O, respectively. Our B3LYP ground state calculations yielded a binding energy of 1.18 eV (Ni_{13}/C_7H_8O degenerate 8 μ_B and 10 μ_B state) and 1.01 eV (Pd_{13}/C_7H_8O (4 μ_B)), respectively. For fixed geometries we thus find smaller binding energies with the hybrid functional, but the trend of stronger binding to Ni_{13} is confirmed. The hybrid calculation also confirms the quenching of the magnetic moment for the Pd system, yet also predicts a reduction of the spin to a degenerate 8 and 10 μ_B state for the Ni system. An in-depth analysis of the magnetic moment for small MNP clusters will be part of a future study.

Finally, in order to check whether our locally optimized structures are realistic and to take into account potential temperature effects, we carried out a DFT BOMD simulation with a Nosé-Hoover thermostat.[S23,S24] For this we used the following setup: The thermostat temperature was 298.15 K and the PBE xc functional was employed in combination with the def2-SVP[S25] basis set. The presence of the substrate alters the relative permittivity (ε_R=13.5)[S26] of the medium. We took this shift into account via the conductor-like screening model.[S27] Based on our GO calculations, we chose a fixed spin magnetic moment of 8 μ_B and 4 μ_B for the Ni and Pd system, respectively. The relaxation time equaled approximately 13 fs (560 a.u.) and 9.3 fs (400 a.u.) for Pd_{13}/C_7H_8O and Ni_{13}/C_7H_8O, respectively. The time step was some 1.9 fs (80 a.u.) and the total simulation time was circa 3 ps, which was sufficient to observe several low energy structures. We extracted the two lowest energy structures from these BOMD calculations and further relaxed them with the same PBE setup as before. As a result, we found that Ni_{13}/C_7H_8O (8 μ_B) is bound by -3.11 to -3.12 eV and Pd_{13}/C_7H_8O (4 μ_B) by -2.64 to -2.65 eV. Thus, the binding energies observed for these new structures are larger than for the locally optimized ones, but the trend of stronger binding to Ni is again robust. The lowest energy conformations, i.e. those corresponding to -3.12 and -2.65 eV, are depicted in the main manuscript (Figure 3).

References

[S1] J. Hermannsdörfer, M. Friedrich, R. Kempe, *Chem. Eur. J.* **2013**, *19*, 13652–13657.

[S2] D. Tilgner, R. Kempe, *Chem. Eur. J.* **2017**, *23*, 3184–3190.

[S3] TURBMOLE V7.3 **2018**, a development of University of Karlsruhe and Forschungszentrum Karlsruhe GmbH, 1989-2018.

[S4] J. P. Perdew, K. Burke, M. Ernzerhof, *Phys. Rev. Lett.* **1996**, *77*, 3865-3868.

[S5] J. P. Perdew, K. Burke, M. Ernzerhof, *Phys. Rev. Lett.* **1997**, *78*, 1396.

[S6] A. Weigend, R. Ahlrichs, *Phys. Chem. Chem. Phys.* **2005**, *7*, 3297–3305.

[S7] S. Grimme, *Inc. J. Comput. Chem.* **2004**, *25*, 1463–1473.

[S8] J. P. Perdew, Alex Zunger, *Phys. Rev. B* **1981**, *23*, 5048-5079.

[S9] T. Körzdörfer, S. Kümmel, N. Marom, L. Kronik, *Phys. Rev. B* **2009**, *79*, 201205.

[S10] L. Leppert, R. Kempe, S. Kümmel, *Phys. Chem. Chem. Phys.* **2015**, *17*, 26140-26148.

[S11] A. D. Becke, *J. Chem. Phys.* **1993**, *98*, 5648-5652.

[S12] P.J. Stephens, F. J. Devlin, C. F. Chabalowski, M. J. Frisch, *J. Phys. Chem.* **1994**, *98*, 11623-11627.

[S13] D. Andrae, U. Haeussermann, M. Dolg, H. Stoll, H. Preuss, *Theor. Chim. Acta* **1990**, *77*, 123-141.

[S14] G. L. Gutsev, C. W. Weatherford, K. G. Belay, B. R. Ramachandran, P. Jena, *J. Chem. Phys*. **2013**, *138*, 164303.

[S15] J. P. Chou, C. R. Hsing, C. M. Wei, C. Cheng, C. M. Chang, *J. Phys.: Condens. Matter* **2013**, *25*, 125305.

[S16] A. M. Köster, P. Calaminici, E. Orgaz, D. R. Roy, J. U. Reveles, S. N. Khanna, *J. Am. Chem. Soc*. **2011**, *133*, 12192-12196.

[S17] B. Fresch, H.-G. Boyen, F. Remacle, *Nanoscale* **2012**, *4*, 4138–4147.

[S18] A. Langenberg, K. Hirsch, A. Ławicki, V. Zamudio-Bayer, M. Niemeyer, P. Chmiela, B. Langbehn, A. Terasaki, B. v. Issendorff, J. T. Lau, *Phys. Rev. B* **2014**, *90*, 184420.

[S19] J. Meyer, M. Tomber, T. van Wüllen, G. Niedner-Schattenburg, S. Peredkob, W. Eberhardt, M. Neeb, S. Palutke, M. Martins, W. Wurth, *J. Chem. Phys*. **2015**, *143*, 104302.

[S20] M. B. Knickelbein, *J. Chem. Phys*. **2002**, *116*, 9703-9711.

[S21] S. E. Apsel, J. W. Emmert, J. Deng, L. A. Bloomfield, *Phys. Rev. Lett*. **1996**, *76*, 1441-1444.

[S22] A. J. Cox, J. G. Louderback, S. E. Apsel, L. A. Bloomfield, *Phys. Rev. B* **1994**, *49*, 12295-12298.

[S23] W. G. Hoover, *Phys. Rev. A* **1985**, *31*, 1695–1697.

[S24] S. Nosé, *J. Chem. Phys*. **1984**, *81*, 511–519.

[S25] A. Schäfer, H. Horn, R. Ahlrichs, *J. Chem. Phys*. **1992**, *97*, 2571–2577.

[S26] Ch. Wohlfart, Landolt-Börnstein (Supplement to IV/6), **2008**, *17*, 396-396.

[S27] A. Klamt, G. Schuurmann, *J. Chem. Soc.* **1993**, *2*, 799–805.

Publication 3

Visible Ligh-driven Dehydrogenation of Benzylamine under Liberation of H_2

Reprinted from
ChemCatChem **12**, 4593-4599 (2020),
with the permission of Wiley-VCH Verlag GmbH & Co. KGaA.

Mara Klarner[1], Sebastian Hammon[2], Sebastian Feulner[3],
Stephan Kümmel[2], Lothar Kador[3], and Rhett Kempe[1]

[1] Inorganic Chemistry II, Catalyst Design, University of Bayreuth, Bayreuth 95440, Germany

[2] Theoretical Physics IV, University of Bayreuth, Bayreuth 95440, Germany

[3] Institute of Physics, Bayreuth Institute of Macromolecule Research (BIMF), University of Bayreuth, Bayreuth 95440, Germany

My contribution

M. Klarner was the lead contributor to the publication.

S. Kümmel and S. Hammon conceived the theoretical study on the binding of benzylamine to different metal co-catalysts in a model. I performed the corresponding computational density functional theory study and associated simulations. S. Kümmel and myself were involved in scientific discussions. S. Kümmel supervised the theoretical study.

M. Klarner and R. Kempe designed the experiments. M. Klarner synthesized and characterized the photocatalyst. The catalytic reactions and the associated analytics were carried out by M. Klarner. S. Feulner performed the fluorescence lifetime studies. L. Kador was involved in scientific discussions. R. Kempe supervised the experimental part of this work and was continuously involved in the scientific discussions.

M. Klarner and R. Kempe conceived the structure of the manuscript. M. Klarner wrote large parts of the manuscript. L. Kador was involved in the correction of the manuscript. R. Kempe and M. Klarner finalized the experiment-related text of the manuscript together. I wrote the first version of the part of the manuscript that describes the computational study. S. Kümmel and myself finalized the theory-related text of the manuscript together.

ChemCatChem
Full Papers
doi.org/10.1002/cctc.202000329
Chemistry Europe
European Chemical Societies Publishing

Visible Light-driven Dehydrogenation of Benzylamine under Liberation of H_2

Mara Klarner,[a] Sebastian Hammon,[b] Sebastian Feulner,[c] Stephan Kümmel,[b] Lothar Kador,[c] and Rhett Kempe*[a]

The visible light-driven transformation of chemical compounds in combination with the liberation of H_2 is highly attractive. Herein, we report on a photocatalyst that allows the acceptorless dehydrogenation of benzylamine. Upon light absorption, free charge carriers are generated and used for the concerted imine formation and liberation of H_2. Our photocatalyst consists of CdS as a light harvesting semiconductor supported on colloidal metal-organic framework crystallites. The decoration with co-catalytic nickel nanoparticles promotes hydrogen evolution and, in addition, stabilizes the CdS component under irradiation.

Introduction

The solar-driven upgrading of organic compounds is a promising and sustainable way to produce value-added products.[1] The simultaneous liberation of H_2 during such upgrading processes generates an additional, highly attractive byproduct. Meanwhile, a well investigated approach is the photocatalytic acceptorless dehydrogenation of alcohols (alcohol splitting) to yield carbonyl compounds (Scheme 1, top).[2] In a similar way, amines may be transformed into imines and H_2 (Scheme 1, bottom). The photocatalytic amine dehydrogenation described so far requires sacrificial agents, mostly molecular oxygen (aerobic amine oxidation). The visible light-mediated aerobic amine oxidation is catalyzed by semiconductor materials including CdS,[3] graphitic carbon nitride,[4] Nb_2O_5,[5] WS_2,[6] WO_3[7] and bismuth oxyhalides.[8] Zhao and coworkers developed a Ni/CdS catalyst system for the visible light-driven H_2 generation from water in combination with the coupling of amines.[9] Furthermore, heterojunction photocatalysts,[10] plasmonic composite catalysts[11] and MOF-based photocatalysts[12] are described to yield homocoupled imines via aerobic amine oxidation. The transformation of two different amines into a non-symmetric imine is more challenging, requiring high temperatures and oxygen pressure.[13]

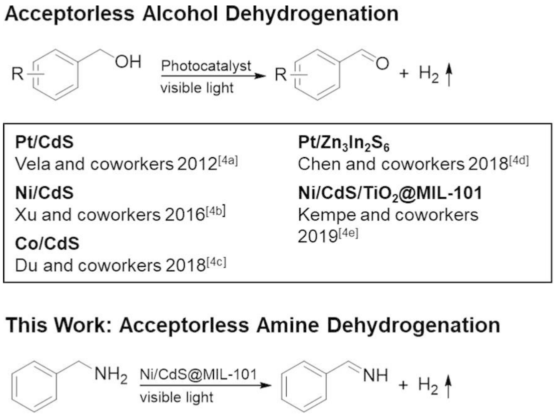

Scheme 1. State of the art in visible light-mediated photocatalytic dehydrogenation of alcohols with liberation of H_2 (alcohol splitting) and the acceptorless dehydrogenation of benzylamine (amine splitting) introduced here.

Herein, we report on the photocatalytic and visible light-driven acceptorless dehydrogenation of benzylamine (amine splitting). The reaction proceeds additive-free, without requiring an electron acceptor, and involves amine oxidation towards an imine in combination with liberation of one equivalent of H_2. The synthesis of non-symmetric imines is possible by using a second, non-benzylic amine that is not dehydrogenated by the photocatalyst. To accomplish amine splitting, we developed a novel metal-organic framework-based photocatalyst system (Ni/CdS@MIL-101).

Ni/CdS@MIL-101 is composed of three components. a) The metal organic framework (MOF) known as MIL-101(Cr) is used as the visible light inactive support material that acts as a molecular sponge permitting the semiconductor and catalyst synthesis and determines the overall size of the photocatalyst for efficient recycling.[14] b) CdS is the visible light absorbing semiconductor material. c) Nickel nanoparticles are an efficient

---

[a] M. Klarner, Prof. Dr. R. Kempe
Inorganic Chemistry II
University of Bayreuth
Universitätsstraße 30, 95440 Bayreuth (Germany)
E-mail: kempe@uni-bayreuth.de
[b] S. Hammon, Prof. Dr. S. Kümmel
Theoretical Physics IV
University of Bayreuth
Universitätsstraße 30, 95447 Bayreuth (Germany)
[c] S. Feulner, Prof. Dr. L. Kador
Institute of Physics, Bayreuth Institute of Macromolecule Research (BIMF)
University of Bayreuth
Universitätsstraße 30, 95447 Bayreuth (Germany)

Supporting information for this article is available on the WWW under https://doi.org/10.1002/cctc.202000329

co-catalyst for H_2 evolution and enhance the stability of CdS under photocatalytic conditions since the oxidation of sulfide to sulfate is prevented. Fluorescence lifetime measurements indicate a faster electron transfer from the conduction band of CdS to the Ni particles in comparison to nanoparticles of noble metals such as Pd or Pt. Thereby, the probability of charge recombination within the semiconductor is reduced. In addition, DFT calculations suggest a stronger substrate binding of the amine to the Ni than to Pd nanoparticles.

Results and Discussion

The photocatalytically inactive MOF MIL-101 with its characteristic pore structure (Supporting Information, Figure S2a) was shown to have a surface area of 2700 m^2/g.[15] The MIL-101 crystallite size, between 100 and 300 nm, is desirable for the generation of active and reusable core-shell catalysts. The MIL-101 crystallites are small enough to exhibit a proper outer surface area for the modification with photoactive components.[16] This is combined with the easy separation of the colloidal photocatalyst, since the crystallites are, on the other hand, large enough to ensure recyclability by centrifugation. The highly porous and size optimized support material can be selectively loaded with precursor molecules permitting the catalyst synthesis. The outer surface of single MIL-101 crystallites is decorated with visible light-absorbing CdS particles by a simple solvothermal route. Cadmium acetate is infiltrated into MIL-101 in dimethyl sulfoxide as sulfur source and crystallizes as cubic CdS under solvothermal conditions at 180 °C to yield CdS@MIL-101.[17] Transmission electron microscopy revealed the arrangement of CdS particles with an average size between 20 and 30 nm on the structure determining core MIL-101 (Scheme 2; Supporting Information, Figure S4). The gas phase infiltration of volatile metal-organic precursors into the porous CdS@MIL-101 composite material allows for the generation of metal nanoparticles, denoted as M/CdS@MIL-101. For the modification with nickel nanoparticles, bis(cyclopentadienyl) nickel(II) $[Ni(C_5H_5)_2]$ was infiltrated at room temperature by applying static vacuum and subsequently reducing to Ni_0 at 90 °C and 10 bar H_2.[18] We modified CdS@MIL-101 with different amounts of nickel, 1 wt.%, 5 wt.%, and 10 wt.%. $(\eta_3$-Allyl)$(\eta_5$-cyclopentadienyl)-palladium(II) $[Pd(C_3H_5)(C_5H_5)]$ was used to generate 5 wt.% Pd_0 nanoparticles by sublimation at 32 °C in dynamic vacuum and reduction at 70 °C and 70 bar H_2.[19] The modification with 5 wt.% Pt_0 proceeds via the gas phase loading of trimethyl-(methylcyclopentadienyl)-palladium(IV) $[Me_3Pt(CH_3\text{-}C_5H_4)]$ into the pores of CdS@MIL-101 at 37 °C in static vacuum, followed by a reduction step at 80 °C and 50 bar H_2.[20] TEM analysis (Scheme 2; Supporting Information, Figure S3) indicated a homogeneous distribution of metallic nanoparticles smaller than 2 nm which are located on the CdS particles, forming an interface with the visible light-absorbing semiconducting material. The metal content of M_5CdS@MIL-101 catalysts (theoretically 5 wt.%) was examined by inductively coupled plasma optical emission spectroscopy (ICP-OES) and found to be 5.1 wt.% Ni, 5.2 wt.% Pd, and 4.9 wt.% Pt, respectively (Supporting Information, Table S1). The calculated weight percentage of CdS is 45 wt.% for each catalyst material. The final M/CdS@MIL-101 core-shell composite showed the original octahedral shape determined by the MIL-101. The metal nanoparticles are assumed to serve as an electron reservoir, since a directed electron transfer from the conduction band of the semiconductor CdS across the semiconductor/nanoparticle interface has been postulated.[21] Scheme 2 presents the general photocatalytic concept of M/CdS@MIL-101: An electron-hole pair is generated upon visible light excitation of CdS. The electron is transferred from the conduction band (CB) of CdS to a metal particle by the built-in electric field, thereby reducing the possibility of charge recombination. Subsequently, spatially separated redox reactions can be catalyzed. Electrons reduce protons for molecular hydrogen generation at the co-catalytic nanoparticles and, simultaneously, holes in the CdS valence band are consumed by oxidizing substrates.

For determining the absorbance characteristics of Ni_5CdS@MIL-101, we performed diffuse-reflectance ultraviolet-

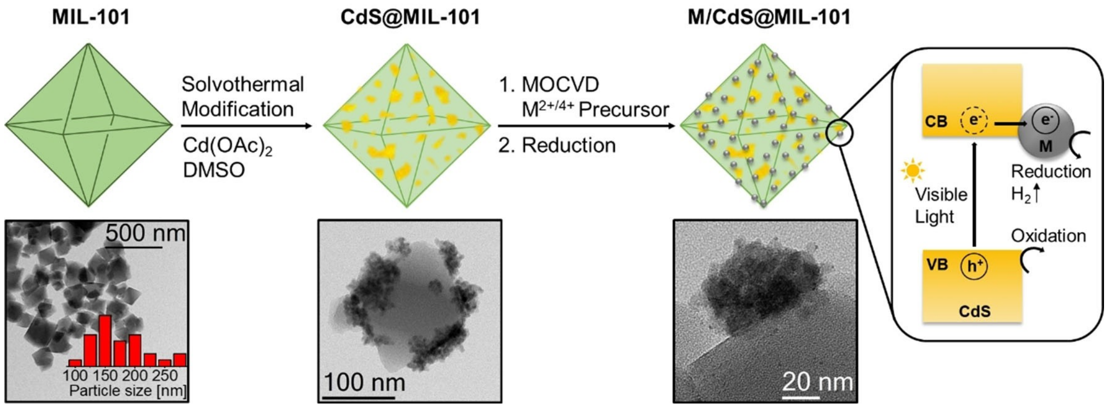

Scheme 2. Synthesis of the photocatalyst M/CdS@MIL-101. The decoration with CdS semiconductor particles proceeds via a solvothermal modification. The metal precursor (Ni: $[Ni(C_5H_5)_2]$; Pd: $[Pd(C_3H_5)(C_5H_5)]$; Pt: $[Me_3Pt(CH_3\text{–}C_5H_4)]$) is infiltrated into MIL-101 (green) by gas phase deposition and reduced by hydrogen treatment. In the semiconductor CdS (yellow) an electron is promoted from the valence band (VB) to the conduction band (CB) by the absorption of visible light. After the directed electron transfer towards the metal particles (grey), spatially separated redox reactions can be catalyzed.

visible spectroscopy (DRS) between 350 and 700 nm. As compared to bare MIL-101 absorbing around 600 and 450 nm, an increased absorption was observed for the dark yellow CdS@MIL-101 (Supporting Information, Figure S4a). Upon generating the photoactive compound, the characteristic absorbance of MIL-101 is extinguished. Photons of wavelengths smaller than 510 nm are predominantly absorbed, corresponding to the band gap of the semiconductor CdS. With the Munk-Kubelka equation, the optical band gap of CdS was determined as 2.44 eV, in agreement with the literature value for cubic CdS (Supporting Information, Figure S4b). The photocatalyst Ni_5CdS@MIL-101 exhibited nearly constant absorbance throughout the visible range. We examined the surface area and the pore size distribution of the different compounds during synthesis of the photocatalyst by nitrogen physisorption measurements. The modification of porous MIL-101 with CdS results in a significant decrease of the initial surface area by 53 %. Further modification with Ni nanoparticles leads only to a minor additional decrease of the surface area to 1040 m^2/g. X-ray powder diffractometry (PXRD) reveals the exclusive formation of cubic CdS particles (Supporting Information, Figure S8a) showing reflections at 26.5°, 43.9°, and 51.9° (2θ). The reflections from 2° to 20° (2θ) are assigned to the preserved MIL-101 core. X-ray photoelectron spectroscopy (XPS) indicated the formation of metallic Ni nanoparticles (Supporting Information, Figure S5). The major peak within the S2p region at a binding energy of 161.5 eV is assigned to metallic sulfide (CdS). Traces of metal sulfate were identified at a binding energy of 169 eV; they are ascribed to surface oxidation of CdS due to the handling in air. The XPS survey shows characteristic elemental signals for Cr, O, and C of the MIL-101 support material and additional signals for Cd, S, and Ni, which form the photoactive shell. The homogeneous distribution of Ni particles on the CdS@MIL-101 material was confirmed by energy dispersive X-ray (EDX) elemental mapping (Supporting Information, Figure S6). Furthermore, we performed Fourier-transform infrared spectroscopy (FT-IR) of Ni_5CdS@MIL-101 and the intermediate materials during synthesis (Supporting Information, Figure S7a). Due to the surface modification with the light harvesting CdS, MIL-101 signals are reduced between 700 and 2000 cm^{-1}. A total weight loss of 42 % was observed for the Ni_5CdS@MIL-101 photocatalyst as compared to 72 % for MIL-101 in thermogravimetric analysis (TGA) (Supporting Information, Figure S7b). By covering the MOF core with the photocatalytic active shell, the temperature stability of the system is enhanced.

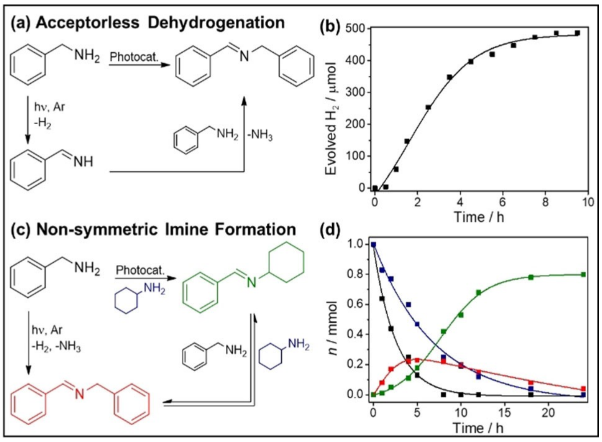

Figure 1. (a) Acceptorless dehydrogenation of benzylamine. (b) H_2 liberation from benzylamine (1 mmol) is observed under visible light illumination and quantified by GC-TCD. (c) Non-symmetric imine formation by cross-coupling benzylamine and cyclohexylamine. (d) Kinetic study (color code refers to (c)).

Next, we performed the photocatalytic acceptorless dehydrogenation of benzylamine via liberation of molecular H_2. Thereby, the intermediate aldimine reacts with a second equivalent of benzylamine in a condensation reaction to yield the homocoupled product *N*-benzyl-1-phenylmethanimine (Figure 1a). The elimination of gaseous ammonia was verified by gas chromatography (thermal conductive detector, GC-TCD). The flat band potential of CdS is sufficiently positive (VB 1.7 V vs NHE)[22] to thermodynamically allow for the oxidation of benzylamine (standard reduction potential 0.9 V vs NHE).[23] The photocatalytic amine dehydrogenation by Ni_5CdS@MIL-101 was performed under an inert-gas atmosphere at room temperature without the use of any additives or acceptor molecules. In the presence of co-catalytic Ni nanoparticles, the dehydrogenation of benzylamine proceeds with quantitative yield, whereas the neat CdS@MIL-101 leads to the formation of the tertiary amine as a byproduct (Table 1, Entry 1, 2). We confirmed the equimolar liberation of molecular H_2 by analyzing the reaction headspace via GC-TCD (Figure 1b). Switching the light on and off verified the release of H_2 only under visible light illumination (Supporting Information, Figure S10). The reusability of Ni_5CdS@MIL-101 photocatalyst was investigated by the acceptorless dehydrogenation of benzylamine. We performed five consecutive runs without a remarkable loss of activity (Supporting Information, Figure S11).

We also developed an approach to access non-symmetric imines using a second, non-benzylic amine which is not dehydrogenated by the photocatalyst under the given conditions. Figure 1c describes the cross-coupling of benzylamine and cyclohexylamine via the dehydrogenation of benzylamine and subsequent reversible transimination to yield the hetero-coupled *N*-cyclohexyl-1-phenylmethanimine (Figure 1c, d). This exchange is a non-photocatalytic equilibrium reaction, in which one equivalent of benzylamine is liberated and fed back into

Table 1. Photocatalytic acceptorless dehydrogenation of benzylamine.[a]

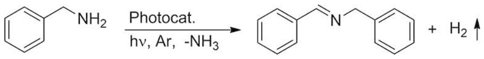

	Catalyst	Yield [%][b]	Yield H_2 [%][c]
1	Ni_5CdS@MIL-101	99	98
2	CdS@MIL-101	62	59
3	Without hν	0	0
4	Without catalyst	0	0

[a] 1 mmol benzylamine, 1.5 mL MeCN, 10 h, 5 mg catalyst, rt, Ar, 470 nm blue LED (50 W). [b] Determined by GC using n-dodecane as an internal standard. [c] Quantified by GC-TDC using methane as an internal standard.

the dehydrogenation cycle. Under visible light illumination, the equilibrium is shifted towards the non-symmetric imine, guaranteeing its predominant formation (Supporting Information, Table S5).

We synthesized the $Ni_xCdS@MIL-101$ catalyst systems with different Ni contents (x equal to 1, 5, 10 wt.% Ni) to investigate the influence of the co-catalytic nanoparticles on the dehydrogenative cross-coupling. To convert 1 mmol of substrates under optimized reaction conditions, 5 mg $Ni_5CdS@MIL-101$ were suspended in 1.5 ml ethanol and illuminated with a 50 W blue LED (470 nm) (Supporting Information, Figure S1, Table S3 and S4).

CdS@MIL-101 loaded with 5 wt.% Ni showed the best catalytic performance yielding 74% heterocoupled product **1** and 7% homocoupled product **2** (Table 2, Entry 2). With increasing Ni content, the nanoparticles covering the CdS crystals reduce the light absorbance and, thereby, the generation of free charge carriers resulting in 17% of **1** and 37% of **2** (Table 2, Entry 3). With 1 wt.% Ni, the photocatalytic activity is similar to neat CdS@MIL-101 (Table 2, Entry 1). The MIL-101 support is essential, since Ni-modified commercial CdS shows a significantly lower activity (Table 2, Entry 4). Also, the unmodified CdS@MIL-101 shows a lower catalytic activity (Table 2, Entry 5) underlining the importance of Ni nanoparticles which was already observed for the formation of the homocoupled product *N*-benzyl-1-phenylmethanimine **2**. We found no photocatalytic activity without the light-harvesting CdS component in both Ni@MIL-101 and the neat support MIL-101 (Table 2, Entries 6, 7). The modification with the noble metals Pd and Pt as co-catalysts leads mainly to the formation of the homocoupled product **2** (Table 2, Entries 8, 9). This fact highlights the superior performance of co-catalytic non-noble Ni nanoparticles. The composite material $Ni_5CdS@MIL-101$ catalyzes the cross-coupling of amines as shown by several control experiments: Without the catalyst and without visible light illumination no conversion of the substrates occurs(Table 2, Entries 10, 11). Interestingly, a significantly reduced yield is observed in air (Table 2, Entry 12).

Next, we studied the stability of the semiconducting CdS component of $Ni_5CdS@MIL-101$ under photocatalytic conditions. The corrosion of CdS is a frequently discussed phenomenon and a main challenge in the use of such photocatalysts.[24] Recently, DiMeglio and co-workers reported on the benzylamine mediated oxidation of sulfide during the non-aqueous dehydrogenation of benzylamine with O_2 as a sacrificial agent.[25] The standard reduction potential of benzylamine thermodynamically allows for the oxidation of CdS via the formation of the amine-radical cation. In a typical photocatalytic set-up, the photocatalysts $Ni_5CdS@MIL-101$ and CdS@MIL-101 were illuminated in the presence of benzylamine and ethanol as solvent in an inert gas atmosphere.

The pre-catalytic CdS@MIL-101 exhibits one major sulfur signal at $^2P_{3/2}$ 161.5 eV (86%) corresponding to metal sulfide and a small signal for metal sulfate at $^2P_{3/2}$ 168.7 eV (14%) (Figure 2, (1) and (2)). Post-catalytic PXRD analysis indicates the formation of oxidized sulfur species due to the presence of several reflections besides those of cubic CdS (Supporting Information, Figure S8). XPS analysis in the S^2p region confirms an increase in surface sulfate to 51%. The modification with Ni nanoparticles improves the stability of the CdS component since no corrosion effects are observed in PXRD. The ratio of CdS (94%) to $CdSO_4$ (6%) is constant for pre- and post-catalytic $Ni_5CdS@MIL-101$ (Figure 2, (3) and (4)). We performed several control experiments without either visible light illumination, or the presence of benzylamine or solvent and, in addition, in dry

Table 2. Photocatalytic dehydrogenation of benzylamine and cross-coupling with cyclohexylamine. Comparison of different Ni contents, different metal nanoparticles and different reaction conditions.[a]

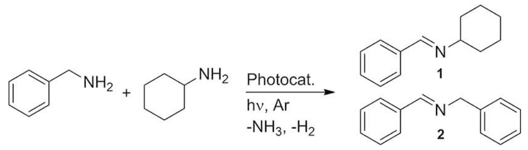

	Catalyst	Metal [wt %][b]	Yield 1 [%][c]	Yield 2 [%][c,d]
1	$Ni_1CdS@MIL-101$	1	45	12
2	$Ni_5CdS@MIL-101$	5.1[e]	74	7
3	$Ni_{10}CdS@MIL-101$	10	17	37
4	Ni@CdS[f]	5	18	4
5	CdS@MIL-101	–	42	17
6	Ni@MIL-101	5	0	0
7	MIL-101	–	0	0
8	$Pd_5CdS@MIL-101$	5.2[e]	8	34
9	$Pt_5CdS@MIL-101$	4.9[e]	7	51
10	Without hν	5.1[e]	0	0
11	Without catalyst	–	0	0
12	Ambient air	5.1[e]	11	23

[a] 1 mmol benzylamine, 1 mmol cyclohexylamine, 1.5 mL EtOH, 5 mg catalyst, 470 nm blue LED (50 W), 20 h, rt, Ar. [b] Co-catalytic metal nanoparticles (Ni, Pd, Pt). [c] Determined by GC using n-dodecane as an internal standard. [d] Referred to 0.5 mmol. [e] Determined by ICP-OES analysis. [f] Commercial CdS (Alfa Aesar).

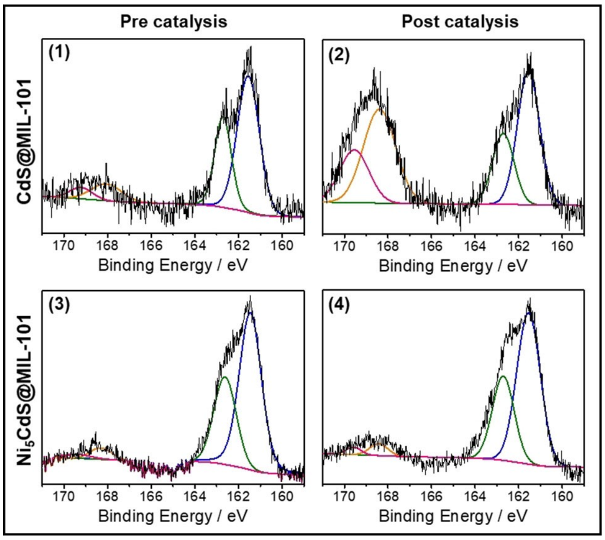

Figure 2. XPS studies of $Ni_5CdS@MIL-101$ and CdS@MIL-101 demonstrating the enhanced photocatalytic stability of CdS in the presence of Ni nanoparticles. $Ni_5CdS@MIL-101$ does not show significant degradation of the surface of CdS [(3), (4)], whereas CdS in CdS@MIL-101 is oxidized under photocatalytic conditions [(1), (2)]. For details see text.

acetonitrile. PXRD analysis of post-catalytic Ni_5CdS@MIL-101 materials showed no evidence for CdS corrosion in all these cases, which supports the idea of benzylamine-mediated sulfide oxidation in an oxygen-containing solvent (Supporting Information, Figure S8). The observed stability of CdS is decisive for the catalytic recyclability of Ni_5CdS@MIL-101. Further experiments on Pd_5CdS@MIL-101 and Pt_5CdS@MIL-101 photocatalysts revealed that the supposed stabilizing effect of metal nanoparticles on the CdS semiconductor occurs also with these noble metals.

The directed electron transfer from photo-excited CdS across the semiconductor-metal interface to Ni nanoparticles was investigated with fluorescence lifetime imaging microscopy in the frequency domain (FD-FLIM). A custom-built apparatus was used with a semiconductor laser at 487 nm and modulation frequencies between 110 and 155 MHz (adapted from Ref. [26]). The combination of the semiconductor material CdS with metallic particles opens up an additional decay channel of charge carriers in the conduction band of CdS. By absorbing visible light, an electron-hole pair is generated in the CdS component which can recombine after an intrinsic lifetime by emitting a photon. FD-FLIM data are conveniently plotted in the so-called polar-plot representation, where the quadrature component of the normalized fluorescence signal is plotted versus the component which is in phase with the excitation. Single-exponential decays correspond to data on a characteristic semi-circle with radius 0.5 around the point (0.5; 0) in this plot. Data points within the semi-circle, on the other hand, represent fluorescence decays featuring more than one lifetime component and can be linearly decomposed in the complex plane.[27] The photoluminescence lifetime of neat CdS supported on MIL-101 is determined by drawing a straight line through the data points in the polar plot and extrapolating it to the intersections with the semicircle (Figure 3a). Two lifetime components are extracted which are independent of the modulation frequency (Supporting Information, Figure S9). The shorter lifetime is interpreted as the luminescence lifetime of CdS, whereas the longer one is ascribed to the luminescence of the MIL-101. The position of the data points on the straight line represents the relative contributions of the two lifetime components to the luminescence signal. With increasing Ni content, the CdS lifetime gradually shortens from 115 ps (CdS@MIL-101) to 97 ps (Ni_1CdS@MIL-101), 67 ps (Ni_5CdS@MIL-101) and 11 ps ($Ni_{10}CdS$@MIL-101), respectively, verifying the directed electron transfer (Figure 3a-d). The relative variation of these lifetimes is reliable; the absolute numbers are subject to an uncertainty of about a factor two to three, however, given the comparatively low modulation frequencies. In accordance with the observed photocatalytic activity, the efficiency of the charge transfer increases with the Ni content. The charge carrier separation over two different catalyst components leads to the enhanced photocatalytic activity of Ni/CdS@MIL-101 in redox reactions. Comparing the 3d metal Ni with the noble metals Pd and Pt, the lifetime of neat CdS is most strongly affected by neighboring Ni particles, indicating faster electron transfer to Ni particles than to either Pd or Pt (Figure 3c, e, f). Comparing catalyst systems with 5 wt.% of the three metals, the lifetime of neat CdS is reduced from 115 ps to 108 ps (Pd_5CdS@MIL-101), 92 ps (Pt_5CdS@MIL-101) and 67 ps (Ni_5CdS@MIL-101). This result underlines the superior performance of Ni particles in the discussed photocatalytic reactions.

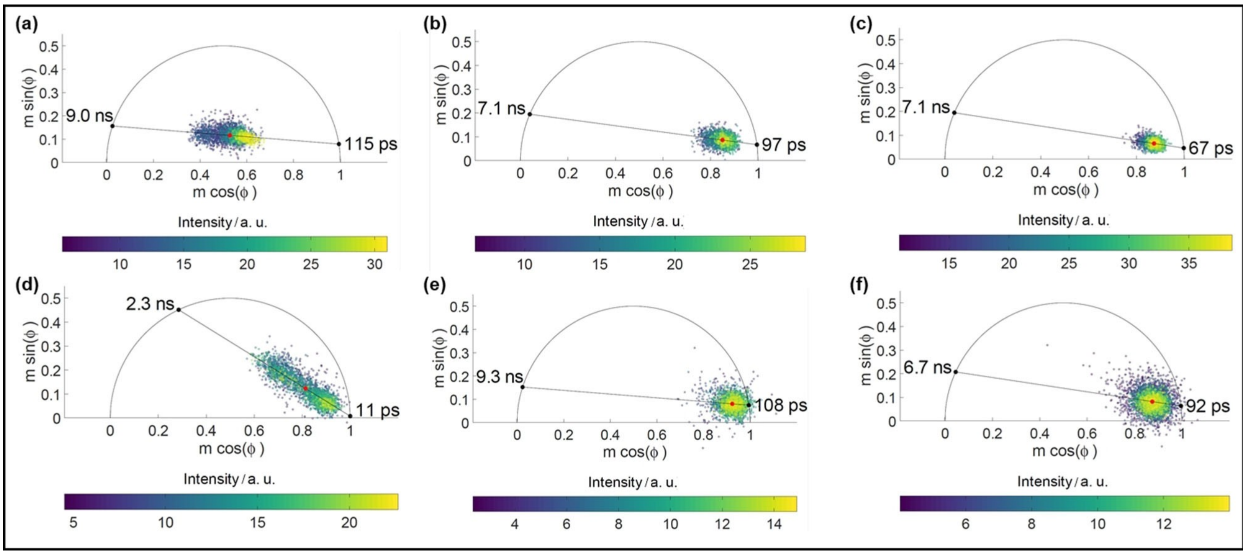

Figure 3. Fluorescence lifetime studies of MIL-101 supported catalysts confirming the directed electron transfer from excited CdS to Ni nanoparticles. Polar-plot representations of the data for Ni_xCdS@MIL-101 and M_5CdS@MIL-101: (a) neat CdS, (b) 1 wt.% Ni, (c) 5 wt.% Ni, (d) 10 wt.% Ni, (e) 5 wt.% Pd and (f) 5 wt.% Pt. The fluorescence lifetime of CdS decreases with increasing Ni content (right end point of the straight line on the semi-circle). It also depends on the metal nanoparticle (Ni, Pd, Pt; 5 wt.%) indicating an influence of the latter on the electron transfer efficiency. Data points correspond to diffraction-limited spots on the sample within an area of size 10×10 μm, the red dot indicating their center of mass. The fluorescence intensity of each spot is color-coded. The modulation frequency of the laser was 110 MHz. For further details see text.

In addition to a faster electron transfer from CdS to Ni in comparison to Pd or Pt particles, another reason for the superior photocatalytic performance of Ni/CdS@MIL-101 may be the interaction or binding of benzylamine with the metal nanoparticles. As a straightforward test we computed the binding energy of benzylamine to the metal nanoparticles. While this type of calculation can be performed using density functional theory (DFT) in principle, it requires careful considerations in practice: The structure of metal particles in general is difficult to determine due to the existence of many isomers of similar energy,[28] yet it may influence binding energies. Furthermore, common exchange-correlation approximations may reach their accuracy limits for d-electron systems.[29] For these reasons, we focused on 13-atom clusters of Ni and Pd as two representative test cases. Both form similar and stable cluster geometries, such as the icosahedron.[28,30] Our calculations suggest that the icosahedral structure is arguably the most relevant one for Ni_{13} and Pd_{13} at room temperature in solution (Supporting Information, Theoretical Procedure). Therefore, we investigated the binding energy of one benzylamine molecule to one 13-atom metal cluster (Ni_{13} or Pd_{13}) by computing the electronic and geometric structure using TURBOMOLE[31] (Supporting Information, Theoretical Procedure). We checked for possible limitations of the predictive power of the DFT calculations due to the presence of d-electrons by computing the binding energies with different exchange-correlation functionals.[32] In particular, the importance of localization and self-interaction was investigated by using functionals with different amounts of exact exchange.

We found the general trend that benzylamine binds stronger to Ni_{13} than to Pd_{13} by several hundred meV (Supporting Information, Table S8). The lowest energy geometries are depicted in Figure 4. This result correlates with a previous study on the binding energy of benzyl alcohol to Ni_{13} and Pd_{13}.[17a] Furthermore, we calculated the binding energy for the dehydrogenated intermediate (C_7H_7N). This intermediate also shows a higher binding energy to Ni_{13} than to Pd_{13}, yet overall slightly lower than benzylamine (Supporting Information, Theoretical Procedure).

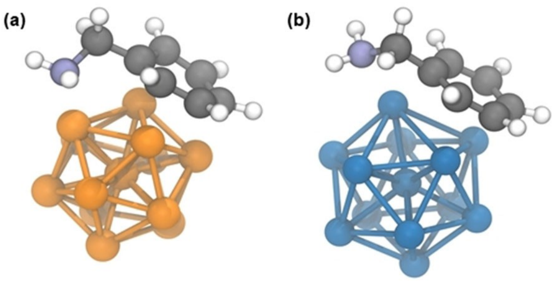

Figure 4. Lowest energy geometries obtained from Born-Oppenheimer DFT molecular dynamics simulations in which a benzylamine molecule binds to a 13-atom Pd icosahedral particle (a) and a 13-atom Ni icosahedral particle (b).

Conclusion

In conclusion, we have reported the first example of photocatalytic, visible light-driven acceptorless amine dehydrogenation (amine splitting). The noble metal-free photocatalyst Ni/CdS@MIL-101 oxidizes benzylamine with the liberation of one equivalent of H_2 most efficiently. The synthesis of non-symmetric imines is possible by adding a second amine which is not dehydrogenated by the photocatalyst under the given conditions. The MOF-supported colloidal photocatalyst is composed of the visible light-absorbing semiconductor CdS and Ni nanoparticles. We confirmed the directed electron transfer from the conduction band of CdS to metallic nanoparticles (Ni, Pd and Pt) and observed a faster electron transfer to the abundant non-noble metal Ni. The co-catalytic Ni (as well as Pd and Pt) also enhances the stability of CdS against photocorrosion in the presence of benzylamine. In addition, DFT calculations reveal a stronger binding of benzylamine to Ni than to Pd clusters.

Acknowledgements

This work was supported by the German Research Foundation (DFG SFB 840, B1). The authors also acknowledge the support of the Bavarian Polymer Institute (University of Bayreuth, KeyLab Electron and Optical Microscopy, KeyLab Theory and Simulation) and the initiative Solar Technologies go Hybrid. We thank Florian Puchtler (XRD) and Prof. Dr. Sven Hüttner (XPS). Furthermore, we thank the Elite Network Bavaria and the DAAD (Bayreuth-Melbourne Colloid/Polymer Network) for financial and other support. Open access funding enabled and organized by Projekt DEAL.

Conflict of Interest

The authors declare no conflict of interest.

Keywords: hydrogen generation · MOF · nickel · amines · photocatalysis

[1] G. Han, Y.-H. Jin, R. A. Burgess, N. E. Dickenson, X.-M. Cao, Y. Sun, *J. Am. Chem. Soc.* **2017**, *139*, 15584–15587.

[2] a) T. P. A. Ruberu, N. C. Nelson, I. I. Slowing, J. Vela, *J. Phys. Chem. Lett.* **2012**, *3*, 2798–2802; b) Z. Chai, T.-T. Zeng, Q. Li, L.-Q. Lu, W.-J. Xiao, D. Xu, *J. Am. Chem. Soc.* **2016**, *138*, 10128–10131; c) D. Jiang, X. Chen, Z. Zhang, L. Zhang, Y. Wang, Z. Sun, R. M. Irfan, P. Du, *J. Catal.* **2018**, *357*, 147–153; d) S. Meng, X. Ye, J. Zhang, X. Fu, S. Chen, *J. Catal.* **2018**, *367*, 159–170; e) D. Tilgner, M. Klarner, S. Hammon, M. Friedrich, A. Verch, N. de Jonge, S. Kümmel, R. Kempe, *Aust. J. Chem.* **2019**, *72*, 842–847; f) T. Mitkina, C. Stanglmair, W. Setzer, M. Gruber, H. Kisch, B. Koenig, *Org. Biomol. Chem.* **2012**, *10*, 3556–3561; g) K. Imamura, H. Tsukahara, K. Hamamichi, N. Seto, K. Hasimoto, H. Kominami, *Appl. Catal. A* **2013**, *450*, 28–33.

[3] a) W. Zhao, C. Liu, L. Cao, X. Yin, H. Xu, B. Zhang, *RSC Adv.* **2013**, *3*, 22944–22948; b) R. Wu, S. Wang, Y. Zhou, J. Long, F. Dong, W. Zhang, *ACS Appl. Nano Mater.* **2019**, *2*, 6818–6827.

[4] a) F. Su, S. C. Mathew, L. Möhlmann, M. Antonietti, X. Wang, S. Blechert, *Angew. Chem. Int. Ed.* **2011**, *50*, 657–660; *Angew. Chem.* **2011**, *123*, 683–

686; b) A. Kumar, P. Kumar, C. Joshi, S. Ponnada, A. K. Pathak, A. Ali, B. Sreedhar, S. L. Jain, *Green Chem.* **2016**, *18*, 2514–2521.

[5] S. Furukawa, Y. Ohno, T. Shishido, K. Teramura, T. Tanaka, *ACS Catal.* **2011**, *1*, 1150–1153.

[6] a) F. Raza, J. H. Park, H.-R. Lee, H.-I. Kim, S.-J. Jeon, J.-H. Kim, *ACS Catal.* **2016**, *6*, 2754–2759; b) H. Liang, B.-Q. Zhang, J.-M. Song, *ChemCatChem* **2019**, *11*, 6288–6294.

[7] N. Zhang, X. Li, H. Ye, S. Chen, H. Ju, D. Liu, Y. Lin, W. Ye, C. Wang, Q. Xu, J. Zhu, L. Song, J. Jiang, Y. Xiong, *J. Am. Chem. Soc.* **2016**, *138*, 8928–8935.

[8] A. Han, H. Zhang, G.-K. Chuah, S. Jaenicke, *Appl. Catal. B* **2017**, *219*, 269–275.

[9] W. Yu, D. Zhang, X. Guo, C. Song, Z. Zhao, *Catal. Sci. Technol.* **2018**, *8*, 5148–5154.

[10] a) S. Samanta, S. Khilari, D. Pradhan, R. Srivastava, *ACS Sustainable Chem. Eng.* **2017**, *5*, 2562–2577; b) K. Zhang, H. Su, H. Wang, J. Zhang, S. Zhao, W. Lei, X. Wei, X. Li, J. Chen, *Adv. Sci.* **2018**, *5*, 1800062.

[11] a) S. Naya, K. Kimura, H. Tada, *ACS Catal.* **2013**, *3*, 10–13; b) S. Sarina, H. Zhu, E. Jaatinen, Q. Xiao, H. Liu, J. Jia, C. Chen, J. Zhao, *J. Am. Chem. Soc.* **2013**, *135*, 5793–5801; c) H. Chen, C. Liu, M. Wang, C. Zhang, N. Luo, Y. Wang, H. Abroshan, G. Li, F. Wang, *ACS Catal.* **2017**, *7*, 3632–3638.

[12] a) D. Sun, L. Ye, Z. Li, *Appl. Catal. B* **2015**, *164*, 428–432; b) H. Liu, C. Xu, D. Li, H.-L. Jiang, *Angew. Chem. Int. Ed.* **2018**, *57*, 5379–5383; *Angew. Chem.* **2018**, *130*, 5477–5481.

[13] a) A. Grirrane, A. Corma, H. Garcia, *J. Catal.* **2009**, *264*, 138–144; b) L. Liu, S. Zhang, X. Fu, C.-H. Yan, *Chem. Commun.* **2011**, *47*, 10148–10150; c) X. Qiu, C. Len, R. Luque, Y. Li, *ChemSusChem* **2014**, *7*, 1684–1688; d) M. Largeron, M.-B. Fleury, *Chem. Eur. J.* **2015**, *21*, 3815–3820.

[14] a) D. Tilgner, M. Friedrich, J. Hermannsdörfer, R. Kempe, *ChemCatChem*, **2015**, *7*, 3916–3922; b) D. Tilgner, R. Kempe, *Chem. Eur. J.* **2017**, *23*, 3184–3190; c) D. Tilgner, M. Friedrich, A. Verch, N. de Jonge, R. Kempe, *ChemPhotoChem* **2018**, *2*, 349–352; d) D. Tilgner, M. Klarner, S. Hammon, M. Friedrich, A. Verch, N. de Jonge, S. Kümmel, R. Kempe, *Aust. J. Chem.* **2019**, *72*, 842–847.

[15] G. Ferey, C. Mellot-Draznieks, C. Serre, F. Millange, J. Dutour, S. Surble, I. Margiolaki, *Science* **2005**, *309*, 2040–2042.

[16] J. Hermannsdörfer, M. Friedrich, R. Kempe, *Chem. Eur. J.* **2013**, *19*, 13652–13657.

[17] a) D. Tilgner, M. Klarner, S. Hammon, M. Friedrich, A. Verch, N. de Jonge, S. Kümmel, R. Kempe, *Aust. J. Chem.* **2019**, *72*, 842–847; b) Y. Wang, Y. Zhang, Z. Jiang, G. Jiang, Z. Zhao, Q. Wu, Y. Liu, Q. Xu, A. Duan, C. Xu, *Appl. Catal. B* **2016**, *185*, 307–314; c) J. He, Z. Yan, J. Wang, J. Xie, L. Jiang, Y. Shi, F. Yuan, F. Yu, Y. Sun, *Chem. Commun.* **2013**, *49*, 6761–6763; d) D. Ding, Z. Jiang, J. Jin, J. Li, D. Ji, Y. Zhang, L. Zan, *J. Catal.* **2019**, *375*, 21–31.

[18] J. Hermannsdörfer, M. Friedrich, N. Miyajima, R. Albuquerque, S. Kümmel, R. Kempe, *Angew. Chem. Int. Ed.* **2012**, *51*, 11473–11477; *Angew. Chem.* **2012**, *124*, 11640–11644.

[19] J. Hermannsdörfer, R. Kempe, *Chem. Eur. J.* **2011**, *17*, 8071–8077.

[20] S. Proch, J. Hermannsdörfer, R. Kempe, C. Kern, A. Jess, L. Seyfarth, J. Senker, *Chem. Eur. J.* **2008**, *14*, 8204–8212.

[21] a) T. Simon, N. Bouchonville, M. J. Berr, A. Vaneski, A. Adrovic, D. Volbers, R. Wyrwich, M. Döblinger, A. S. Susha, A. L. Rogach, F. Jäckel, J. K. Stolarczyk, J. Feldmann, *Nat. Mater.* **2014**, *13*, 1013–1018; b) Y. Xu, R. Xu, *Appl. Surf. Sci.* **2015**, *351*, 779–793; c) S. Cao, C.-J- Wang, X.-J. Lv, Y. Chen, W.-F. Fu, *Appl. Catal. B* **2015**, *162*, 381–391; d) Z. Chai, T.-T. Zeng, Q. Li, L.-Q. Lu, W.-J. Xiao, D. Xu, *J. Am. Chem. Soc.* **2016**, *138*, 10128–10131; e) G. Han, Y.-H. Jin, R. A. Burgess, N. E. Dickenson, X.-M. Cao, Y. Sun, *J. Am. Chem. Soc.* **2017**, *139*, 15584–15587.

[22] A. J. Bard, M. S. Wrigthon, *J. Electrochem. Sci. Technol.* **1977**, *124*, 1706–1710.

[23] K. Ohkubo, T. Nanjo, S. Fukuzumi, *Bull. Chem. Soc. Jpn.* **2006**, *79*, 1489–1500.

[24] a) A. Henglein, *Ber. Bunsenges. Phys. Chem.* **1982**, *86*, 301–305; b) D. Meissner, C. Brenndorf, R. Memming, *Appl. Surf. Sci.* **1987**, *27*, 423–436; c) Y. H. Hsieh, C. P. Huang, *Colloids Surf.* **1991**, *53*, 275–295.

[25] J. L. DiMeglio, B. M. Bartlett, *Chem. Mater.* **2017**, *29*, 7579–7586.

[26] S. Zahner, L. Kador, K. R. Allakhverdiev, E. Yu. Salaev, M. F. Huseyinoğlu, *J. Appl. Phys.* **2014**, *115*, 043504.

[27] a) G. I. Redford, R. M. Clegg, *J. Fluoresc.* **2005**, *15*, 805–815; b) M. A. Digman, V. R. Caiolfa, M. Zamai, E. Gratton, *Biophys. J.* **2008**, *94*, L14-L16.

[28] L. Leppert, R. Kempe, S. Kümmel, *Phys. Chem. Chem. Phys.* **2015**, *17*, 26140–26148.

[29] T. Schmidt, S. Kümmel, *Computation* **2016**, *4*, 33-1–33-15.

[30] a) G. L. Gutsev, C. W. Weatherford, K. G. Belay, B. R. Ramachandran, P. Jena, *J. Chem. Phys.* **2013**, *138*, 164303; b) J. P. Chou, C. R. Hsing, C. M. Wei, C. Cheng, C. M. Chang, *J. Phys. Condens. Matter* **2013**, *25*, 125305; c) A. M. Köster, P. Calaminici, E. Orgaz, D. R. Roy, J. U. Reveles, S. N. Khanna, *J. Am. Chem. Soc.* **2011**, *133*, 12192–12196; d) B. Fresch, H.-G. Boyen, F. Remacle, *Nanoscale* **2012**, *4*, 4138–4147.

[31] TURBMOLE V7.3 **2018**, (University of Karlsruhe and Forschungszentrum Karlsruhe GmbH, Karlsruhe, Germany).

[32] a) J. P. Perdew, K. Burke, M. Ernzerhof, *Phys. Rev. Lett.* **1996**, *77*, 3865–3868; b) J. P. Perdew, K. Burke, M. Ernzerhof, *Phys. Rev. Lett.* **1997**, *78*, 1396; c) J. P. Perdew, M. Ernzerhof, *J. Chem. Phys.* **1996**, *105*, 9982; d) C. Adamo, V. Barone *J. Chem. Phys.* **1999**, *110*, 6158; e) A. D. Becke, *J. Chem. Phys.* **1993**, *98*, 5648–5652; f) P. J. Stephens, F. J. Devlin, C. F. Chabalowski, M. J. Frisch, *J. Phys. Chem.* **1994**, *98*, 11623–11627; g) J. Tao, J. P. Perdew, V. N. Staroverov, G. E. Scuseria, *Phys. Rev. Lett.* **2003**, *91*, 146401; h) V. N. Staroverov, G. E. Scuseria, J. Tao, J. P. Perdew, *J. Chem. Phys.* **2003**, *119*, 12129–12137; i) V. N. Staroverov, G. E. Scuseria, J. Tao, J. P. Perdew, *J. Chem. Phys.* **2004**, *121*, 11507–11507; j) J. Sun, A. Ruzsinszky, J. P. Perdew, *Phys. Rev. Lett.* **2015**, *115*, 036402.

Manuscript received: February 25, 2020
Revised manuscript received: June 4, 2020
Accepted manuscript online: June 5, 2020
Version of record online: July 17, 2020

ChemCatChem

Supporting Information

Visible Light-driven Dehydrogenation of Benzylamine under Liberation of H_2

Mara Klarner, Sebastian Hammon, Sebastian Feulner, Stephan Kümmel, Lothar Kador, and Rhett Kempe*

Supporting Information

Visible Light-Driven Dehydrogenation of Benzylamine under Liberation of H_2

Mara Klarner, Sebastian Hammon, Sebastian Feulner, Stefan Kümmel, Lothar Kador, and Rhett Kempe

Table of Contents

Experimental Procedures

General Methods

All chemicals and solvents were purchased commercially from chemical suppliers with purity over 95 % and used without further purification. Ethanol was degassed by three consecutive *freeze-pump-thaw*-cycles. Benzylamine (Merck) was vacuum distilled and stored under argon. All manipulations including air or moisture sensitive compounds were carried out under dry and oxygen-free argon atmosphere (Schlenk techniques) or in a nitrogen-filled glovebox (mBraun 120) with a high-capacity recirculator (below 0.1 ppm of oxygen and water).

Reduction of precursor compounds were carried out with Parr Instrument stainless steel autoclaves N-MT5 300 mL equipped with heating mantles and temperature controller. Solvothermal syntheses were performed in a muffle furnace (Nabertherm) with programmable temperature ramps. Inductively coupled plasma optical emission spectroscopy (ICP-OES) was carried out according to standard protocol digestion (4 mL HNO_3/HCl 3:1, microwave irradiation, 25 min, 195 °C) with a Vista-Pro radial (Varian). Fourier transform infrared (FTIR) spectroscopy measurements were performed with a Cary 630 FTIR spectrometer (Agilent Technologies) over a range from 2000 cm^{-1} to 700 cm^{-1}. Thermogravimetric analysis was performed from 30 °C to 700 °C (10 °C min^{-1}) using a TGA/SDTA 851^e (Mettler) under nitrogen atmosphere. Gas chromatography (GC) analyses were performed using an Agilent Technologies 6850 gas chromatograph equipped with a flame ionization detector (FID) and a MN Optima 17 capillary column (30.0 m x 0.32 mm x 0.25 µm) using n-dodecane as internal standard. GC-MS analyses were performed using an Agilent Technologies 6890 gas chromatograph with a MN-MS HP-5 capillary column (30.0 m x 0.32 mm x 0.25 µm) and a coupled mass spectrometer as detector. Gas mixtures were analyzed using a 6890N gas chromatograph (Agilent Technologies) equipped with an Agilent special Plot + Molsieve capillary column (30.0 m x 0.32 mm x 0.25 µm). Methane was used as internal standard. Nitrogen physisorption isotherms were determined at -196 °C using a Nova 2000e (Quantachrome) apparatus. Specific surface areas were calculated by using p/p_0-values from 0.05-0.3 by the BET model. Specific total pore volumes were determined by DFT calculations (N_2 at -196 °C on silica (cylindric pore, NLDFT equilibrium model)). Transmission electron microscopy (TEM) measurements were carried out using a LEO 922o microscope (Zeiss, 200 kV) equipped with a LaB6 electron source and an omega energy filter. The samples were suspended in chloroform and sonicated for 2 min. 2 µL of the suspension were placed on a CF200-Cu-grid (Electron Microscopy Sciences) and allowed to dry. EDX (energy dispersive X-ray spectroscopy) measurements were performed by using a Zeiss Ultra Plus with an acceleration voltage of 20 kV. The sample coating with platinum (1.3 µm) was performed with a Sputter Coater 208HR (Cressington). Diffuse reflectance ultraviolet-visible spectra were measured using a CARY 300 (Agilent Technologies) with an Ulbricht sphere in the range of 350 to 700 nm. For optical band gap determination, a tauc plot was used applying the Munk-Kubelka equation. X-ray powder diffraction (XRD) analysis in the range of 2-80 °2θ was performed using a XPERT-PRO diffractometer (Panalytical) ($Cu_{K\alpha}$ radiation, 1.54178 Å) in θ-2θ geometry with a position sensitive detector. The reference card number for comparison is 01-080-0019 for CdS. X-ray photoelectron spectroscopy (XPS) was performed using a PHI Versa Probe III instrument of Physical Electronics. As X-ray source a monochromatic $Al_{K\alpha}$ with a spot size of 100 µm (24.5 W) was used. The kinetic pass energy of the photoelectrons was determined with a hemispheric analyzer (45°) set to pass energy of 26 eV for high-resolution spectra. Photoluminescence studies were conducted with a custom-built confocal fluorescence lifetime imaging microscope operating in the frequency domain (FD-FLIM). It is equipped with an amplitude-modulated cw diode laser at 488 nm (Toptica; iBEAM-SMART-488-S) with adjustable output power (set to 20 mW) and a miniature photomultiplier module (Hamamatsu H10721-01) as detector. The microscope objective is a Leica PL FLUOTAR L (100× / 0.75). Modulation frequencies between 110 MHz and 155 MHz were used. Data acquisition was performed with an integration time of 30 ms per data point. The sample was flushed with nitrogen gas for minimizing photobleaching effects. Samples are prepared by spin coating thin films of powder material dispersed in a polystyrene (Mw 200k g/mol) matrix on cover slips (26 mm x 20 mm x 200 µm). 2 mg of the sample material were suspended in a polystyrene / toluene solution (300 µL, 185 mg/mL). Spin coating was performed at 750 rpm for 15 s, 1500 rpm for 30 s, 3000 rpm for 60 s.

Material Synthesis

Synthesis of MIL-101

The synthesis was carried out according to a previous work to obtain an average crystallite size of 180 nm.[S1] Chromium(III) nitrate nonahydrate (480 mg, 1.20 mmol), terephthalic acid (198 mg, 1.20 mmol), hydrofluoric acid 46 wt% (10 µL, 0.228 mmol) and deionized H_2O (12.00 mL) were sealed in a 23 mL teflon-lined hydrothermal autoclave. The mixture was heated for 8 h at 220 °C (3.3 °C min^{-1}). The reaction mixture was cooled down fast to 160 °C and slowly to 30 °C (cooling rate: 2.7 °C h^{-1}). Excessively crystallized terephthalic acid was removed by filtration over a pore 3 filter. The product was separated from the aqueous solution by centrifugation (1800 rpm, 45 min), refluxed in ethanol/water (90/10 vol.-%) for 12 h, and centrifugalized (1800 rpm, 45 min) to remove the CrOOH impurities and to separate the MIL-101 crystals with different size distribution. The green MIL-101 was dried under vacuum (10^{-4} mbar, 85 °C, 24 h).

BET: 2700 m^2 g^{-1}.

PXRD: (°2θ) 2.78, 3.26, 3.41, 3.94, 4.30, 4.84, 5.13, 5.59, 5.85, 6.24, 6.48, 8.10, 8.40, 8.58, 8.86, 9.02, 9.71, 9.86, 10.30, 11.22, 16.50.

Synthesis of CdS@MIL-101

The synthesis was carried out according to a modified literature procedure.[S2] 400 mg MIL-101 was suspended in 35 mL of dimethyl sulfoxide in a 125 mL teflon-lined hydrothermal autoclave. 600 mg (2.25 mmol) of $Cd(OAc)_2 \cdot 2\ H_2O$ cadmium(II) acetate dihydrate was added and the reaction mixture was stirred for 2 h. The mixture was heated at 180 °C for 10 h (heating rate: 2.5 °C min^{-1}). After cooling down to room temperature, the resulting CdS@MIL-101 was separated by filtration and washed with ethanol. The material was combined with 40 mL of ethanol and heated at 100 °C for 10 h (heating rate: 1.2 °C min^{-1}) in a 125 mL Teflon-lined hydrothermal autoclave. After cooling down, the material was separated by filtration and dried under vacuum (10^{-4} mbar, 85 °C, 24 h).

Synthesis of Ni_xCdS@MIL-101, Ni@MIL-101[S3]

100 mg dry CdS@MIL-101 was placed in a two-chamber-tube with $Ni(Cp)_2$ bis(cyclopentadienyl)nickel(II) (16.6 mg, 0.088 mmol, 5 wt.%) separated by a glass frit. The gas phase infiltration of the Ni precursor occurred at room temperature (25 °C) in static vacuum (10^{-4} mbar) for 20 h. The reduction of the Ni precursor was performed under hydrogen atmosphere (10 bar H_2) at 90 °C for 20 h in a Parr Instruments steel autoclave. The resulting Ni_5CdS@MIL-101 was evacuated (10^{-4} mbar, 85 °C, 20 h) in order to remove former metal ligand residue. The weight percentage of nickel (x wt.%) was varied by the amount of $Ni(Cp)_2$ to yield Ni_xCdS@MIL-101.

Synthesis of Pd_5CdS@MIL-101[S3]

100 mg CdS@MIL-101 were placed in a two-chamber-tube with (Cp)Pd(allyl) allyl(cyclopentadienyl)palladium(II) (10.2 mg, 0.048 mmol, 5 wt.%) separated by a glass frit. The gas phase infiltration of the Pd precursor occurred at 32 °C in dynamic vacuum (10^{-4} mbar) for 24 h. The reduction of the Pd precursor was performed at 70 bar H_2 and 70 °C for 24 h. The resulting Pd_5CdS@MIL-101 was evacuated (10^{-4} mbar, 85 °C, 20 h) in order to remove former metal ligand residue.

Synthesis of Pt_5CdS@MIL-101[S4]

100 mg CdS@MIL-101 were placed in a two-chamber-tube with $(Me)_3Pt(Cp')$ trimethyl(methylcyclopentadienyl)platinum(IV) (8.2 mg, 0.026 mmol, 5 wt.%) separated by a glass frit. The gas phase infiltration of the Pt precursor occurred at 37 °C in static vacuum (10^{-4} mbar) for 20 h. The reduction of the Pt precursor was performed at 50 bar H_2 and 80 °C

for 24 h. The resulting Pt_5CdS@MIL-101 was evacuated (10^{-4} mbar, 85 °C, 20 h) in order to remove former metal ligand residue.

Synthesis of *N*-cyclohexyl-1-phenylmethanimine (compound **1**)

1020 µL (10 mmol) benzaldehyde were stirred in a round bottom flask, then 1146 µL (10 mmol) cyclohexylamine were added dropwise. After 15 min, the turbid emulsion was diluted with 10 mL diethyl ether and dried over $NaSO_4$. After removing the solvent under reduced pressure, the product was obtained as yellow oil.

^1H NMR: (300 MHz, $CDCl_3$) δ 8.32 (s, 1H); 7.73-7.71 (t, 2H); 7.41-7.39 (t, 3H); 3.25-3.15 (quint, 1H); 1.87-1.59 (m, 7H); 1.41-1.29 (m, 3H).

Synthesis of *N*-benzyl-1-phenylmethanimine (compound **2**)

1020 µL (10 mmol) benzaldehyde were stirred in a round bottom flask, then 1090 µL (10 mmol) benzylamine were added dropwise. The turbid emulsion was diluted with 10 mL diethyl ether and dried over $NaSO_4$. After removing the solvent under reduced pressure, the product was obtained as colorless oil.

^1H NMR: (300 MHz, $CDCl_3$) δ 8.32 (s, 1H); 7.83-7,79 (m, 2H); 7.47-7.25 (m, 8H); 4.77 (s, 2H).

General Procedure for Photocatalytic Experiments

A 50 mL reaction vial was charged with a magnetic stir bar, Ni_xCdS@MIL-101 catalyst (5 mg), benzylamine (109 µL, 1 mmol) and cyclohexylamine (115 µL, 1 mmol). The vial was sealed with a rubber septum, evacuated to remove the air atmosphere and flushed with argon. Dry and degassed solvent (1.5 mL) was added, then the vial was further purged with argon for 1 min and connected to a wash bottle to generate an open reaction system under inert atmosphere. The vial was illuminated for 20 h by a 50 W blue LED (470 nm, distance 2 cm, ~15000 lx) and cooled by a fan (Figure S1). The reaction temperature was measured to be 27 °C. N-dodecane (100 µL, 0.44 mmol) was added as internal standard and the catalyst was separated from the reaction solution by centrifugation (9000 rpm, 9 min) before quantitative analysis by GC. The amount of H_2 evolved from benzylamine (109 µL, 1 mmol) was determined by injecting 500 µL of methane as internal standard in a sealed reaction vial before LED illumination. The gas phase of the reaction was analyzed by GC-TDC. Acetonitrile (1.5 mL) was chosen as solvent for quantifying the H_2 liberation from benzylamine to preclude the H_2 generation by the oxidation of ethanol.

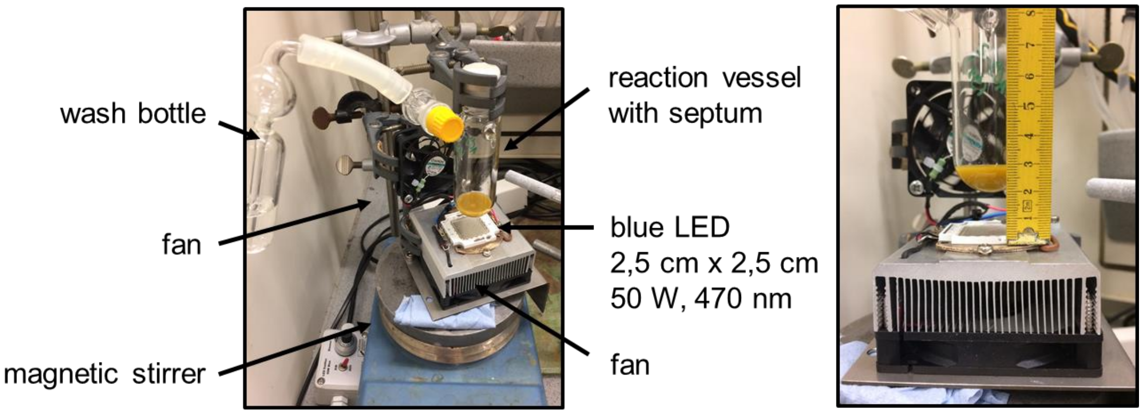

Figure S1 Experimental set-up for photocatalytic experiments. The reaction mixture is illuminated by a 50 W blue LED (470 nm) from below.

Kinetic study of the cross coupling of benzylamine and cyclohexylamine

The general procedure for photocatalytic experiments was applied. A 50 mL reaction vial was charged with 5 mg Ni_5CdS@MIL-101 catalyst, benzylamine (109 µL, 1 mmol) and cyclohexylamine (115 µL, 1 mmol). The vial was sealed, evacuated to remove the air atmosphere and flushed with argon, before dry and degassed ethanol (1.5 mL) was added. A single photocatalytic reaction was performed for each time interval of the kinetic study. Therefor the period of illumination by a 50 W blue LED (470 nm, distance 2 cm, ~15000 lx) was varied. N-dodecane (100 µL, 0.44 mmol) was added as internal standard and the catalyst was separated from the reaction solution by centrifugation (9000 rpm, 9 min) before quantitative analysis by GC.

Evaluating the photocatalytic stability of catalysts

The general procedure for photocatalytic experiments was applied. A 50 mL reaction vial was charged with 5 mg catalyst, benzylamine (109 µL, 1 mmol) and cyclohexylamine (115 µL, 1 mmol). The vial was sealed, evacuated to remove the air atmosphere and flushed with argon, before dry and degassed solvent (1.5 mL) was added. The vial was illuminated for 48 h by a 50 W blue LED (470 nm, distance 2 cm, ~15000 lx). The catalyst was separated from the reaction solution by centrifugation (9000 rpm, 9 min), washed with ethanol and dried in vacuum before analysis by PXRD and XPS. The post-photocatalysis solutions were analyzed for leached Cd und Ni by ICP-OES. Samples were prepared by removing volatile organic compounds in vacuum and diluting in 5 % nitric acid solution. The leaching of Ni_5CdS@MIL-101 and CdS@MIL-101 was determined to be < 50 ppm (Cd) and < 12 ppm (Ni).

Recyclability study of Ni_5CdS@MIL-101

For the recyclability study, a 50 mL reaction vial was charged with a magnetic stir bar, Ni_5CdS@MIL-101 catalyst (5 mg) and benzylamine (109 µL, 1 mmol). The vial was sealed with a rubber septum, evacuated to remove the air atmosphere, and flushed with argon. Dry and degassed acetonitrile (1.5 mL) was added, then the vial was further purged with argon for 1 min. The vial was illuminated for 3 h by a 50 W blue LED (470 nm, distance 2 cm, ~15000 lx) and cooled by a fan. N-dodecane (100 µL, 0.44 mmol) was added as internal standard and the catalyst was separated from the reaction solution by centrifugation (9000 rpm, 9 min) before quantitative analysis by GC. The amount of evolved H_2 was determined by injecting 500 µL of methane as internal standard in a sealed reaction vial before LED illumination. The gas phase of the reaction was analyzed by GC-TDC. Ni_5CdS@MIL-101 catalyst was purified in acetonitrile and ethanol (washing, centrifuging at 9000 rmp, 9 min) three times between the runs.

Material Characterization

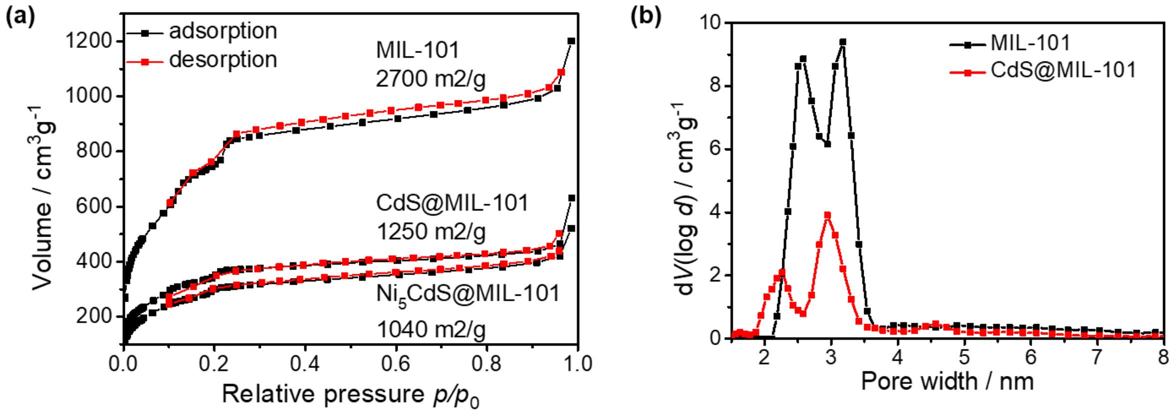

Figure S2 (a) N2-physisorptions isotherms of MIL-101, CdS@MIL-101 and Ni_5CdS@MIL-101 with respective surface areas determined by BET-model (0.05-0.3 p/p_0). (b) Pore size distribution of MIL-101 compared to CdS@MIL-101.

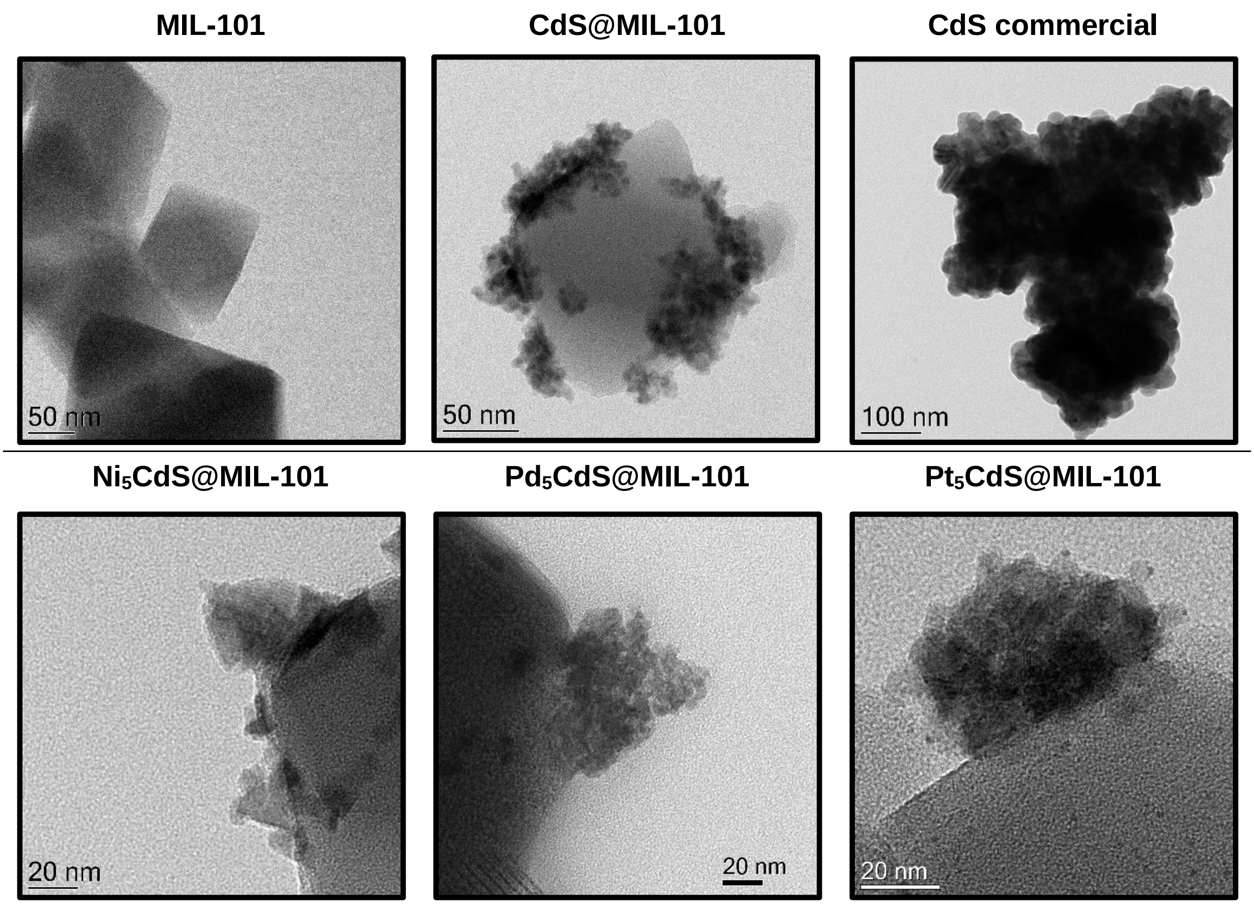

Figure S3 TEM analysis of as-synthesized octahedral-shaped MIL-101 and CdS@MIL-101 showing the core-shell morphology. For comparison TEM analysis of commercial CdS (Alfa Aesar) was performed. TEM analysis of Ni_5CdS@MIL-101, Pd_5CdS@MIL-101 and Pt_5CdS@MIL-101.

Table S1 ICP-OES analysis of CdS@MIL-101, Ni_5CdS@MIL-101, Pd_5CdS@MIL-101 und Pt_5CdS@MIL-101 with contents given in wt.%.

Compound	Cr	Cd	CdS[a]	Ni	Pd	Pt
CdS@MIL-101	11.7	36.3	46.6	-	-	-
Ni_5CdS@MIL-101	9.8	34.9	44.9	5.1		
Pd_5CdS@MIL-101	8.9	35.5	45.6	-	5.2	-
Pt_5CdS@MIL-101	8.4	35.4	45.5	-	-	4.9

[a] Calculated based on Cd content.

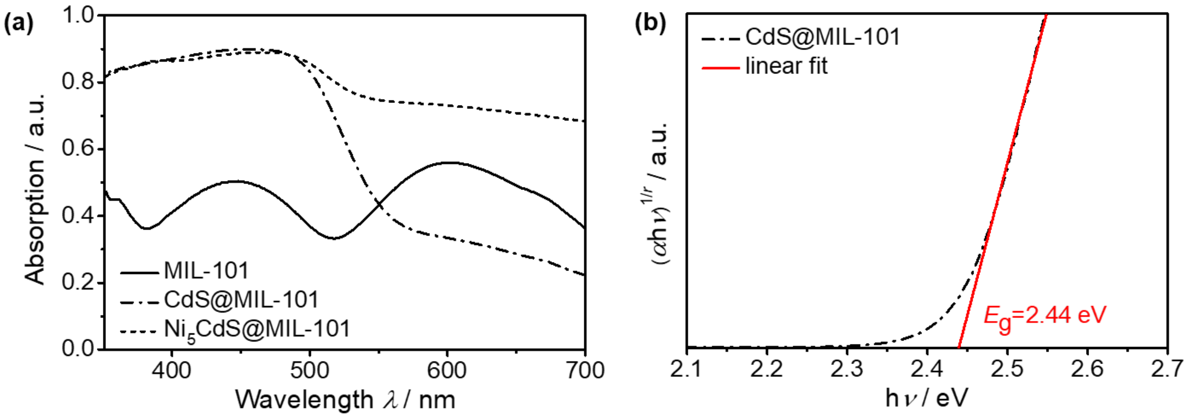

Figure S4 (a) Diffuse reflectance spectra of MIL-101, CdS@MIL-101 and Ni_5CdS@MIL-101 in the range of 350-700 nm. (b) Tauc plot for CdS@MIL-101 (applying the Munk-Kubelka equation).

Table S2 Linear fitting parameters and R^2-value (squared correlation coefficient) for the optical band gap determination by the tauc plot (see Figure S4).

	Intercept	Stand. error intercept	Slope	Stand. error slope	R^2-value
CdS@MIL-101	-885.5	14.9	363.1	5.9	0.99602

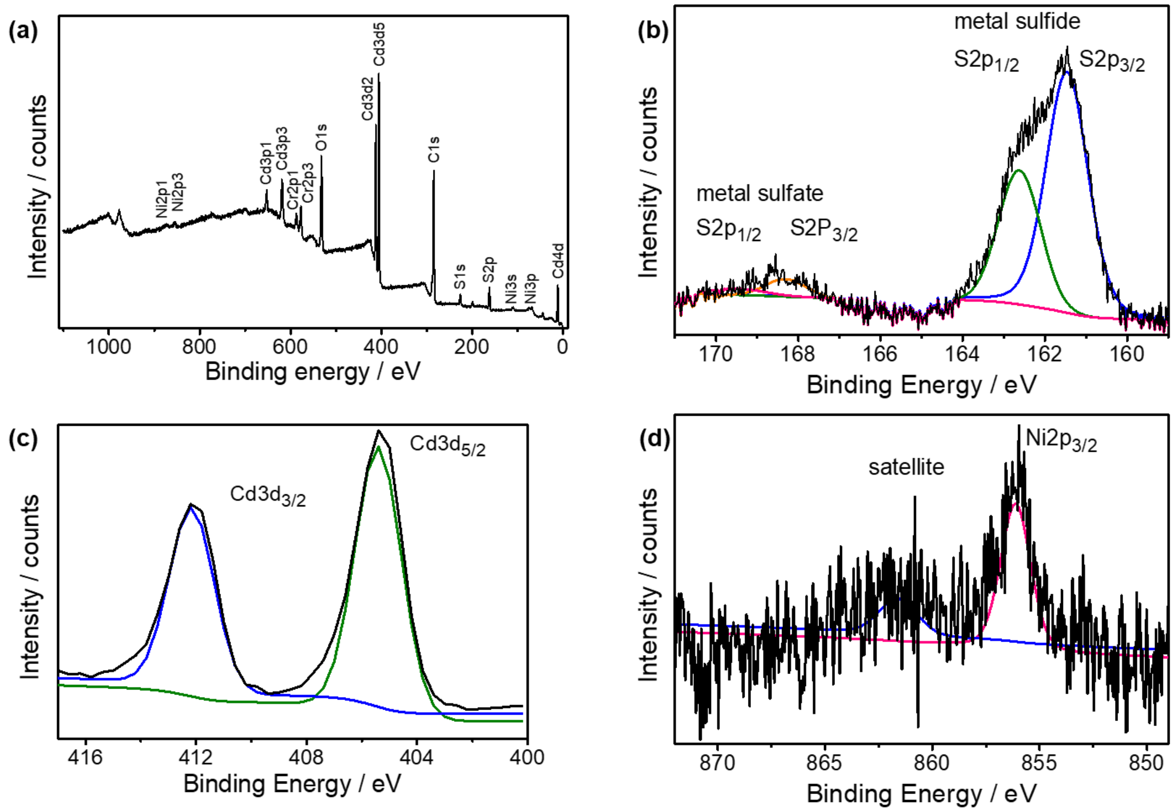

Figure S5 XPS spectra of Ni_5CdS@MIL-101. (a) Survey spectrum, (b) the S2p region, (c) the Cd3d region and (d) the Ni2p region in detail.

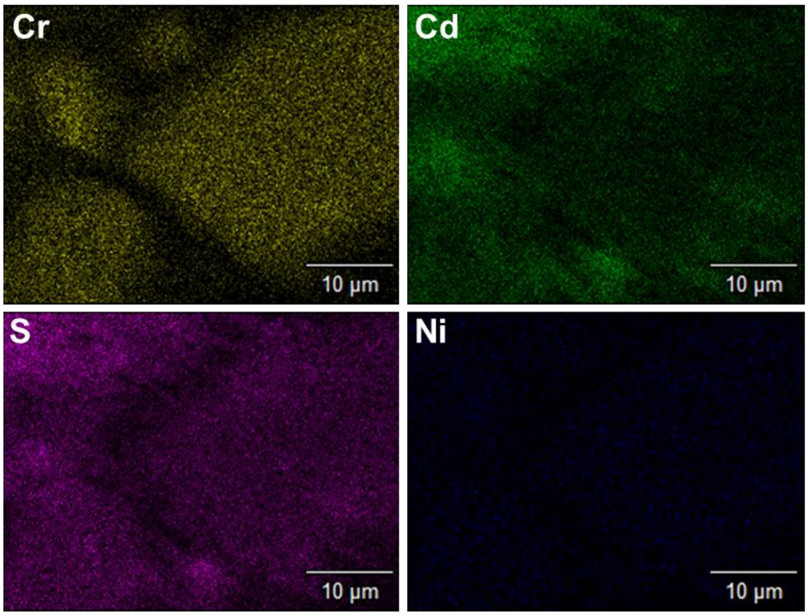

Figure S6 EDX elemental mapping of Ni_5CdS@MIL-101 shows the deposition of CdS on MIL-101 crystals and homogeneously distributed Ni particles.

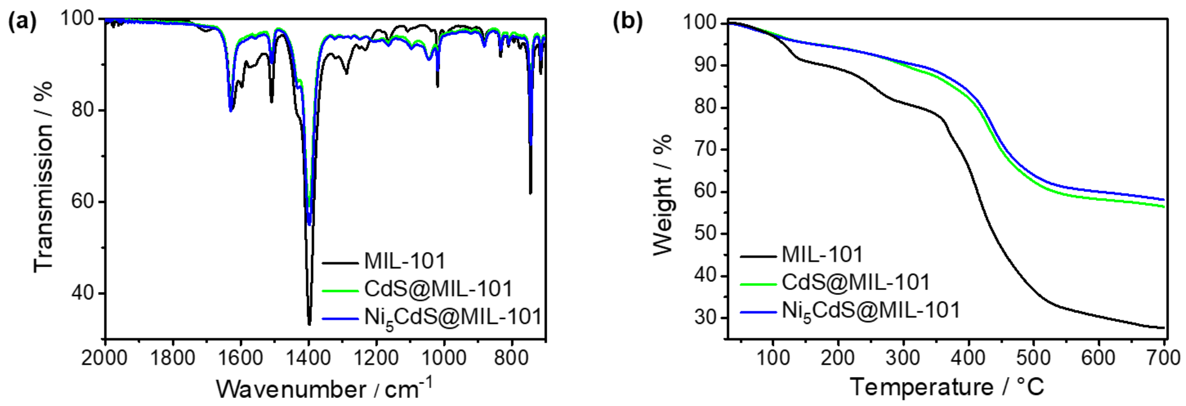

Figure S7 (a) FT-IR spectra and (b) thermogravimetric analysis of MIL-101, CdS@MIL-101 and Ni$_5$CdS@MIL-101.

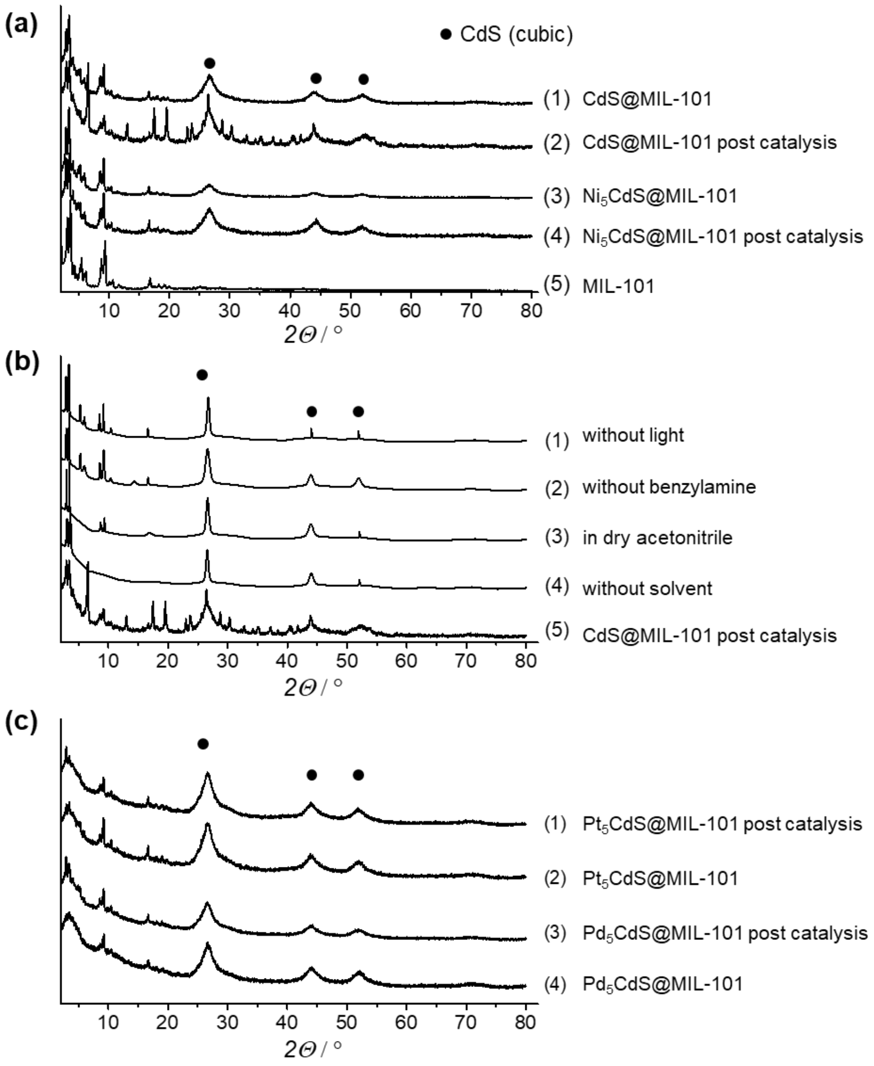

Figure S8 XRD of CdS@MIL-101 catalysts to evaluate the stability of CdS. (a) Ni$_5$CdS@MIL-101 and CdS@MIL-101 catalysts pre and post catalysis (1)-(4) compared to neat MIL-101 (5). (b) CdS@MIL-101 catalyst exposed to different catalytic conditions: (1) without light, (2) without benzylamine, (3) in dry acetonitrile, (4) without solvent, (5) standard catalytic conditions. (c) Pt$_5$CdS@MIL-101 and Pd$_5$CdS@MIL-101 catalysts pre and post catalysis (1)-(4).

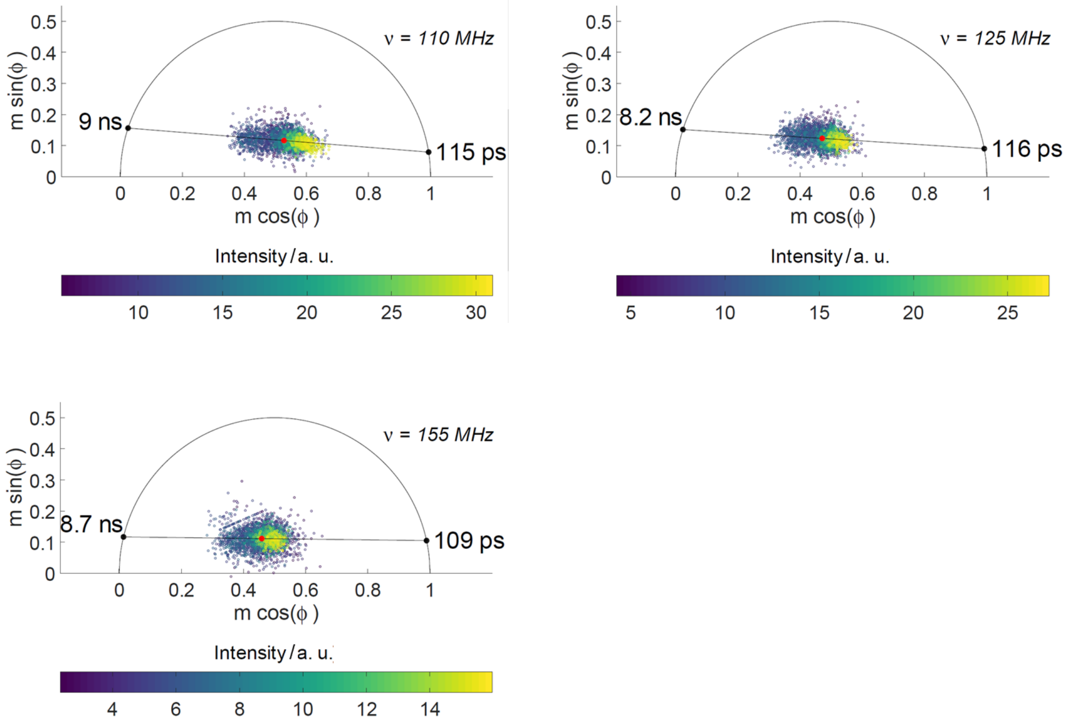

Figure S9 Fluorescence lifetime measurements in the frequency domain performed on neat CdS@MIL-101 at modulation frequencies of 110 MHz, 125 MHz, and 155 MHz confirm that the results do not depend on the laser modulation frequency within the experimental error.

Photocatalytic Experiments

Table S3 Solvent screening for the photocatalytic non-symmetric coupling of benzylamine and cyclohexylamine.[a]

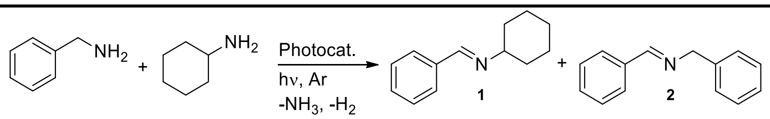

Entry	Solvent	Yield 1 [%] [b]	Yield 2 [%] [b, c]
1	acetonitrile	26	53
2	methanol	13	31
3	**ethanol**	**74**	**7**
4	tetrahydrofuran	8	28
5	toluene	29	34
6	hexane	26	48
7	dimethylformamide	19	13
8	pyridine	17	11
9	dimethoxyethane	7	51
10	no solvent	34	22

[a] 1 mmol benzylamine, 1 mmol cyclohexylamine, 1.5 mL solvent, 5 mg Ni_5CdS@MIL-101, 470 nm blue LED (50 W), 20 h, rt, Ar. [b] Determined by GC using n-dodecane as an internal standard. [c] Referred to 0.5 mmol.

Table S4 Screening of the amount of solvent and amount of catalyst for the photocatalytic coupling of benzylamine and cyclohexylamine.[a]

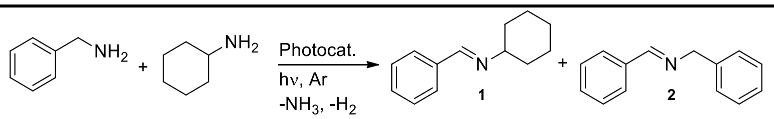

Entry	Ethanol [mL]	Catalyst [mg]	Yield 1 [%] [b]	Yield 2 [%] [b, c]
1	0.5	5	34	6
2	1	5	52	6
3	**1.5**	**5**	**74**	**7**
4	2	5	60	10
5	3	5	2	41
6	1.5	2	54	11
7	**1.5**	**5**	**74**	**7**
8	1.5	7	65	12
9	1.5	10	57	14

[a] 1 mmol benzylamine, 1 mmol cyclohexylamine, different volumes of ethanol, different amount of $Ni_5CdS@MIL-101$, 470 nm blue LED (50 W), 20 h, rt, Ar. [b] Determined by GC using n-dodecane as an internal standard. [c] Referred to 0.5 mmol.

Table S5 Reversible transimination of homocoupled *N*-benzyl-1-phenylmethan-imine with cyclohexylamine to yield *N*-cyclohexyyl-1-phenylmethanimine applying different reaction conditions.[a]

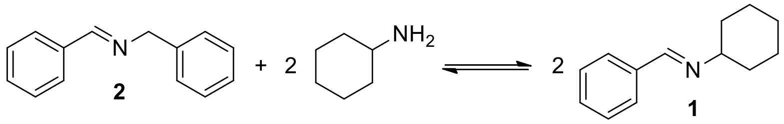

	Yield 1 [%] [b]	Free benzylamine [%]
CdS@MIL-101	67	0
$Ni_5CdS@MIL-101$	80	0
Without hν	26	31
Without catalyst	28	28

[a] 0.5 mmol **2**, 1 mmol cyclohexylamine, 1.5 mL EtOH, 20 h, 5 mg catalyst, rt, Ar, 470 nm blue LED (50 W). [b] Determined by GC using n-dodecane as an internal standard.

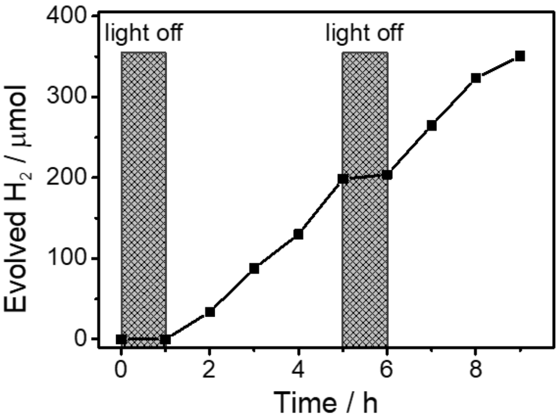

Figure S10 Photocatalytic H_2 generation from benzylamine by $Ni_5CdS@MIL-101$ during a light on/off experiment.[a] H_2 evolution was just observed under visible light illumination. [a] 1 mmol benzylamine, 5 mg $Ni_5CdS@MIL-101$, 1.5 mL acetonitrile, 500 µL methane, 470 nm blue LED (50 W), rt, Ar.

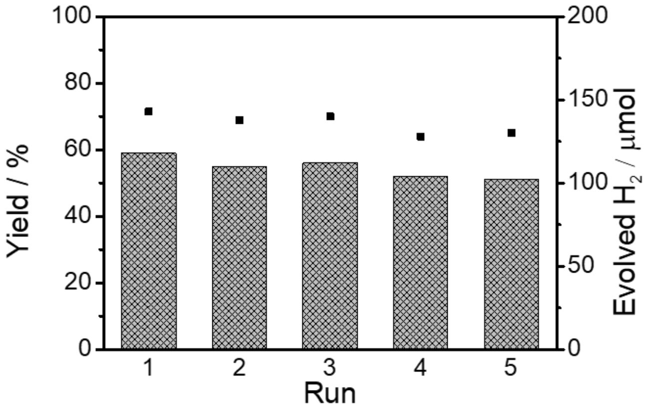

Figure S11 Recycling study of $Ni_5CdS@MIL\text{-}101$ in the photocatalytic acceptorless dehydrogenation of benzylamine.[a] No remarkable loss of activity was observed for five successive runs. [a] 1 mmol benzylamine, 5 mg $Ni_5CdS@MIL\text{-}101$, 1.5 mL acetonitrile, 500 µL methane, 3 h, 470 nm blue LED (50 W), rt, Ar, closed system.

Theoretical Procedures

The molecular model that we studied contained benzylamine (C_7H_9N) and the intermediate (C_7H_7N), respectively, in combination with either one Ni_{13} or Pd_{13} cluster (cp. Figure 4). The joint organometallic system is denoted MNP_{13}/C_7H_9N and MNP_{13}/C_7H_7N, respectively, with MNP_{13} referring to the metal nanoparticle Ni_{13} or Pd_{13}. Our computational procedure follows the line of our previous work.[S5] We used the TURBOMOLE[S6] program package for our Density Functional Theory (DFT) study. We performed geometry optimizations (GO) to obtain reliable molecular structures. All GOs and further electronic ground state calculations utilized the def2-TZVP[S7] basis set. All our calculations considered van-der-Waals' interactions via the scheme of Grimme.[S8] Dealing with transition metal particles requires a careful choice of the xc energy functional, as pointed out in the main manuscript. The Coulomb energy (Hartree term) that is present in DFT,[S9] contains a self-interaction energy contribution that is generally more prominent in localized than in delocalized electronic states.[S10] It is one of the responsibilities of the exchange-correlation (xc) energy functional to compensate for that spurious energy contribution.[S11] In practice, *e.g.*, hybrid xc approximations partly remove self-interaction by including exact Fock exchange fractionally. Dealing with Ni_{13} and Pd_{13} is further complicated by the fact that their ground state is spin-polarized,[S12- S16] which is a more general finding for transition metal clusters.[S13-S22] Consequently, the introduction of a certain amount of Fock exchange might also lead to an overestimation of the spin-polarization and spin magnetic moment, respectively. For this reason, we complemented our Perdew-Burke-Ernzerhof (PBE)[S23] generalized gradient approximation (GGA) calculations with further using three hybrid xc functionals containing different percentages of Fock exchange: The TPSSh[S24] (10%), B3LYP[S25] (20%) and PBE0[S26] (25%). Additionally, we checked our results with TPSS[S27] and SCAN[S28] and thus, incorporated xc functionals from the meta-GGA rung. We determined the spin multiplicity of the ground state for each xc functional. For the latter, the most stable spin state was found by calculating a set of GO or ground state calculations with fixed multiplicities of a pertinent range (see below).

Starting our investigation, we performed GOs for benzylamine, the intermediate and both metal clusters (Ni_{13}, Pd_{13}) to obtain reliable structures and total energies of each. The total energies E_{tot}^{xc} are reported in Table S6 and S7 for the organic molecules and clusters, respectively, and were used to calculate the binding energies of the joint systems thereafter. Our calculations and further, yet unpublished data strongly suggest that the icosahedral structure is arguably the most relevant one for Ni_{13} and Pd_{13} at room temperature in solution. Thus, we started from an icosahedral metal geometry for both clusters. See [S5] for a discussion of structural isomers of the metal particles. Table S7 additionally features the spin magnetic moment $\mu^{(xc)}$ of the corresponding electronic ground state (predicted by a certain xc functional); *e.g.* a spin moment of 8 μ_{B} corresponds to a spin multiplicity $m = 9$, whereas $m = 2S + 1$ and S denotes the spin quantum number.

Table S6. Total energy E_{tot}^{xc} for the singlet ground state of one benzylamine (C_7H_9N) and the intermediate (C_7H_7N) in dependence of the xc functional approximation.

xc	$E_{\mathrm{tot}}^{xc}(C_7H_9N)$ [eV]	$E_{\mathrm{tot}}^{xc}(C_7H_7N)$ [eV]
PBE	-8887.3941	-8854.5669
PBE0	-8888.3540	-8855.2789
B3LYP	-8893.5866	-8860.6359
TPSS	-8900.6394	-8867.5979
TPSSh	-8899.7185	-8866.6023
SCAN	-8894.8616	-8861.8326

Table S7. Total energy E_{tot}^{xc} and spin magnetic moment μ^{xc} for the corresponding ground state of icosahedral Ni_{13} and icosahedral Pd_{13} in dependence of the xc functional. A relativistic core-potential[S13] was used for Pd.

xc	$E_{\mathrm{tot}}^{xc}(Ni_{13})$ [eV]	$\mu^{xc}(Ni_{13})$ [μ_{B}]	$E_{\mathrm{tot}}^{xc}(Pd_{13})$ [eV]	$\mu_{\mathrm{B}}^{xc}(Pd_{13})$ [μ_{B}]
PBE	-533506.0785	8	-45270.8245	8
PBE0	-533493.3678	16	-45254.5648	8
B3LYP	-533554.0148	16	-45250.4232	8
TPSS	-533604.0066	8	-45249.6988	8
TPSSh	-533587.3274	8	-45244.9208	8
SCAN	-533632.9777	8	-45273.0666	8

For the icosahedral Pd_{13} all xc functionals predicted a spin magnetic moment of 8 μ_B for the ground state, agreeing with related previous studies.[S12,S15,S16] The situation for the icosahedral Ni_{13}, however, proved to be more delicate, as the holistic finding of previous DFT studies already indicated.[S5,S12,S13,S29] Our PBE GGA, meta-GGA (TPSS, SCAN) and hybrid TPSSh calculations predicted 8 μ_B. Yet, both hybrid functionals containing a larger amount of Fock exchange (PBE0, B3LYP) preferred a higher magnetic state of 16 μ_B. As discussed previously,[S5] the magnetic, high spin state predicted by hybrid functionals (PBE0, B3LYP), seems to conform with recent X-ray magnetic circular dichroism spectroscopy experiments of cationic Ni_{13}^+ that were independently reported by Langenberg *et al.* and Meyer *et al.*.[S17,S18] Prior to these, however, Stern-Gerlach studies on Ni_{13} predicted a lower total magnetic moment.[S19,S20]

In order to obtain realistic structures that also incorporate potential temperature effects, we utilized DFT Born-Oppenheimer Molecular Dynamics (BOMD) simulations with a Nosé-Hoover thermostat[S30] for our model system. Our BOMD setup was the following: The temperature was set to 298 K. We employed the PBE (GGA) in combination with the def2-SVP[S31] basis set. The Conductor-like Screening Model[S32] (COSMO) considers the change of the relative permittivity ε_R of the medium caused by the presence of a substrate. We used COSMO for benzylamine (ε_R=4.6).[S33] Based on first PBE GO test calculations that indicated a reduction of the magnetic moment for Pd_{13}/C_7H_9N, but not for Ni_{13}/C_7H_9N, we chose a fixed spin magnetic moment of 8 μ_B and 4 μ_B, respectively. Furthermore, we fixed 8 μ_B for Ni_{13}/C_7H_9N and 2 μ_B for Pd_{13}/C_7H_7N, since similar calculations implied a further quenching of the magnetic moment. The relaxation time equaled approximately 560 a.u. (13.0 fs) and 400 a.u. (9.3 fs) for systems containing Pd_{13} and Ni_{13}, respectively. We chose a time step of 80 a.u (1.9 fs). The total simulation time was circa 6 ps, which was enough to observe several low energy structures in all calculations. We extracted those structures that corresponded to the most prominent energy minima of the BOMD simulation (*i.e.*, 4 structures for Ni_{13}/C_7H_9N, Pd_{13}/C_7H_9N, Ni_{13}/C_7H_7N and 5 for Pd_{13}/C_7H_7N). For these structures, we carried out GOs to further relax them and to determine their magnetic ground state. For the latter, we carried out a set of GOs with PBE and fixed spin magnetic moments (in μ_B) in the range of [0,2,…,10] for each of these structures. Finally, we determined the binding energy (E_B^{xc}) for each structure by subtracting the total energies (E_{tot}^{xc}) of the bare systems (see Table S6, S7; here first for C_7H_9N and later C_7H_7N):

$$E_B^{xc}\,(MNP_{13}/C_7H_9N) = E_{tot}^{xc}\,(MNP_{13}/C_7H_9N) - E_{tot}^{xc}\,(MNP_{13}) - E_{tot}^{xc}\,(C_7H_9N), \quad (1)$$

xc refers to PBE (GGA) here and further below to the rest of the aforementioned functionals. As a result, we found with PBE that Ni_{13}/C_7H_9N (8 μ_B) is bound by -3.54 to -3.55 eV and Pd_{13}/C_7H_9N (4 μ_B) by -2.73 to -2.75 eV. In the BOMD simulation, we started from a geometry in which the benzylamine's benzene ring was close to the MNP_{13} and the functional group

(-NH_2) was pointing away from the MNP_{13}. An additional finding was that during these BOMD simulations, the functional group aligned towards Ni_{13} and Pd_{13}, respectively, and further resided in that orientation. The lowest energy geometries, *i.e.*, those corresponding to -3.55 and -2.75 eV, are depicted in the main manuscript (Figure 4), which clearly show an orientation of the functional group towards the metal clusters.

To check whether the observed trend in binding energy is robust, we also computed the electronic structure with PBE0, B3LYP, TPSSh, TPSS and SCAN. For this purpose, we kept the two lowest energy geometries fixed and carried out ground state calculations. We determined the ground state by varying the magnetic moment (in μ_B) in the range of $[0,2,\ldots,\mu^{xc}(MNP_{13}) + 2]$ (μ^{xc} according to Table ST2, *e.g.* $\mu^{PBE0}(Ni_{13})=16\ \mu_B$).

Table S8. Total energies E_{tot}^{xc}, binding energies E_B^{xc} and spin magnetic moments μ^{xc} for the corresponding ground states of MNP_{13}/C_7H_9N in dependence of the xc functional. The difference in binding energy $\Delta E_B^{xc} = E_B^{xc}(Ni_{13}/C_7H_9N) – E_B^{xc}(Pd_{13}/C_7H_9N)$. A relativistic core-potential[S13] was used for Pd. An energetically degenerated state w.r.t. magnetic moment is indicated by two entries.

	Ni_{13}/C_7H_9N			**Pd_{13}/C_7H_9N**			
xc	E_{tot}^{xc} [eV]	E_B^{xc} [eV]	μ^{xc} [μ_B]	E_{tot}^{xc} [eV]	E_B^{xc} [eV]	μ^{xc} [μ_B]	**ΔE_B^{xc} [eV]**
PBE	-542397.0177	-3.55	8	-54160.9728	-2.75	4	-0.70
PBE0	-542383.5580	-1.84	14	-54145.0317	-2.11	6	0.27
B3LYP	-542449.2869	-1.69	8	-54145.0658	-1.06	6	-0.63
TPSS	-542508.4642	-3.82	8	-54153.1524	-2.81	4	-1.01
TPSSh	-542490.7932	-3.75	8	-54147.2927	-2.65	4, 6	-1.10
SCAN	-542531.5333	-3.69	8	-54170.8508	-2.92	4, 6	-0.77

Table S8 shows the results of our study: We calculated the difference in binding energy by $\Delta E_B^{xc} = E_B^{xc}(Ni_{13}/C_7H_9N) – E_B^{xc}(Pd_{13}/C_7H_9N)$ to find a potential preference of the binding of benzylamine to one of the metal clusters. We found the general trend that benzylamine binds more strongly to Ni_{13} than to Pd_{13} by several hundred meV, yet with the exception for PBE0. However, we believe that the very high spin state ($\mu^{PBE0}(Ni_{13})=14\ \mu_B$) is responsible for that outlier. We consider that the true binding is more accurately represented by the other xc functionals. Furthermore, these functionals (B3LYP, TPSS, TPSSh, SCAN) confirmed our results for PBE qualitatively. We therefore consider using PBE to be enough in the study of the intermediate (C_7H_7N). We then calculated the binding energies for the intermediate following the exact same procedure as for benzylamine. The trend that emerged from our GO calculations with PBE is that Ni_{13}/C_7H_7N (8 μ_B) is bound by -3.48 to -3.54 eV and Pd_{13}/C_7H_9N (2 μ_B) by -3.08 to -3.12 eV. In conclusion, the intermediate binds stronger to Ni_{13} than to Pd_{13}, yet overall slightly weaker compared to benzylamine.

References

[S1] J. Hermannsdörfer, M. Friedrich, R. Kempe, *Chem. Eur. J.* **2013**, *19*, 13652-13657.

[S2] D. Tilgner, M. Klarner, S. Hammon, M. Friedrich, A. Verch, N. de Jonge, S. Kümmel, R. Kempe, *Austr. J. Chem.* **2019**, *72*, 842-847.

[S3] J. Hermannsdörfer, M. Friedrich, N. Miyajima, R. Q. Albuquerque, S. Kümmel, R. Kempe, *Angew. Chem. Int. Ed.* **2012**, *51*, 11473–11477.

[S4] S. Proch, J. Herrmannsdörfer, R. Kempe, C. Kern, A. Jess, L. Seyfarth, J. Senker, *Chem. - A Eur. J.* **2008**, *14*, 8204–8212.

[S5] D. Tilgner, M. Klarner, S. Hammon, M. Friedrich, A. Verch, N. de Jonge, S. Kümmel, R. Kempe, *Austr. J. Chem*. **2019**, *72*, 842-847

[S6] TURBMOLE°V7.3 **2018**, (University of Karlsruhe and Forschungszentrum Karlsruhe GmbH, Karlsruhe, Germany).

[S7] A. Weigend, R. Ahlrichs, *Phys. Chem. Chem. Phys*. **2005**, *7*, 3297–3305.

[S8] S. Grimme, *Inc. J. Comput. Chem*. **2004**, *25*, 1463–1473.

[S9] W. Kohn, L. J. Sham, *Phys. Rev*. **1965**, *140,* A1133.

[S10] T. Körzdörfer, S. Kümmel, N. Marom, L. Kronik, *Phys. Rev. B* **2009**, *79*, 201205.

[S11] J. P. Perdew, Alex Zunger, *Phys. Rev. B* **1981**, *23*, 5048-5079.

[S12] L. Leppert, R. Kempe, S. Kümmel, *Phys. Chem. Chem. Phys.* **2015**, *17*, 26140-26148.

[S13] G. L. Gutsev, C. W. Weatherford, K. G. Belay, B. R. Ramachandran, P. Jena, *J. Chem. Phys.* **2013**, *138*, 164303.

[S14] J. P. Chou, C. R. Hsing, C. M. Wei, C. Cheng, C. M. Chang, *J. Phys.: Condens. Matter* **2013**, *25*, 125305.

[S15] A. M. Köster, P. Calaminici, E. Orgaz, D. R. Roy, J. U. Reveles, S. N. Khanna, *J. Am. Chem. Soc*. **2011**, *133*, 12192-12196.

[S16] B. Fresch, H.-G. Boyen, F. Remacle, *Nanoscale* **2012**, *4*, 4138–4147.

[S17] A. Langenberg, K. Hirsch, A. Ławicki, V. Zamudio-Bayer, M. Niemeyer, P. Chmiela, B. Langbehn, A. Terasaki, B. v. Issendorff, J. T. Lau, *Phys. Rev. B* **2014**, *90*, 184420.

[S18] J. Meyer, M. Tomber, T. van Wüllen, G. Niedner-Schattenburg, S. Peredkob, W. Eberhardt, M. Neeb, S. Palutke, M. Martins, W. Wurth, *J. Chem. Phys*. **2015**, *143*, 104302.

[S29] M. B. Knickelbein, *J. Chem. Phys.* **2002**, *116*, 9703-9711.

[S20] S. E. Apsel, J. W. Emmert, J. Deng, L. A. Bloomfield, *Phys. Rev. Lett*. **1996**, *76*, 1441-1444.

[S21] A. J. Cox, J. G. Louderback, S. E. Apsel, L. A. Bloomfield, *Phys. Rev. B* **1994**, *49*, 12295-12298.

[S22] M. Martins, W. Wurth *J. Phys.: Condens. Matter* **2016**, *28*, 503002.

[S23] a) J. P. Perdew, K. Burke, M. Ernzerhof, *Phys. Rev. Lett*. **1996**, *77*, 3865-3868; b) J. P. Perdew, K. Burke, M. Ernzerhof, *Phys. Rev. Lett*. **1997**, *78*, 1396.

[S24] a) V. N. Staroverov, G. E. Scuseria, J. Tao, J. P. Perdew, *J. Chem. Phys.* **2003**, *119*, 12129–12137; b) V. N. Staroverov, G. E. Scuseria, J. Tao, J. P. Perdew, *J. Chem. Phys*. **2004**, *121*, 11507–11507.

[S25] a) A. D. Becke, *J. Chem. Phys*. **1993**, *98*, 5648-5652; b) P.J. Stephens, F. J. Devlin, C. F. Chabalowski, M. J. Frisch, *J. Phys. Chem.* **1994**, *98*, 11623-11627.

[S26] a) J. P. Perdew, Matthias Ernzerhof, *J. Chem. Phys*. **1996**, *105*, 9982; b) C. Adamo, V. Barone *J. Chem. Phys.* **1999**, *110*, 6158.

[S27] J. Tao, J. P. Perdew, V. N. Staroverov, G. E. Scuseria, *Phys. Rev. Lett*. **2003**, *91*, 146401.

[S28] J. Sun; A. Ruzsinszky; J. P. Perdew., *Phys. Rev. Lett*. **2015**, *115*, 036402.

[S29] R. Singh, P. Kroll, *Phys. Rev. B* **2008**, *78*, 245404.

[S30] a) W. G. Hoover, *Phys. Rev. A* **1985**, *31*, 1695–1697; b) S. Nosé, *J. Chem. Phys*. **1984**, *81*, 511–519.

[S31] A. Schäfer, H. Horn, R. Ahlrichs, *J. Chem. Phys*. **1992**, *97*, 2571–2577.

[S32] A. Klamt, G. Schuurmann, *J. Chem. Soc*. **1993**, *2*, 799–805.

[S33] A. A. Maryott, E. R. Smith, *National Bureau of Standards*, **1951**, 26.

Publication 4

Combining Metal Nanoparticles with an Ir(III) Photosensitizer

reprinted from
The Journal of Physical Chemistry C **125**, 25765-25773 (2021)
with the permission of the American Chemical Society.

Sebastian Hammon[1,2], Mara Klarner[3], Martin Friedrich[3], Gerald Hörner[4], Birgit Weber[4], Jürgen Senker[5], Rhett Kempe[3], Thiago Branquinho de Queiroz[2], and Stephan Kümmel[1]

[1] Theoretical Physics IV, University of Bayreuth, 95440 Bayreuth, Germany
[2] Centro de Ciencias Naturais e Humanas, Universidade Federal do ABC, Santo André, São Paulo 09210-580, Brazil
[3] Department of Chemistry, Inorganic Chemistry II – Sustainable Chemistry Centre, University of Bayreuth, 95440 Bayreuth, Germany
[4] Department of Chemistry, Inorganic Chemistry IV, University of Bayreuth, 95440 Bayreuth, Germany
[5] Department of Chemistry, Inorganic Chemistry III, University of Bayreuth, 95440 Bayreuth, Germany

---

My contribution

M. Klarner and I equally contributed to the article. S. Kümmel, T. Branquinho de Queiroz and S. Hammon conceived the theoretical study on the combined model of photocatalyst and different metal co-catalysts. I performed the corresponding computational density functional theory study and associated simulations. S. Kümmel and T. Branquinho de Queiroz co-supervised the theoretical study and were continuously involved in the scientific discussions. T. Branquinho de Queiroz introduced me to the practical aspects in particular of the range-separated hybrid functional calculations and their handling in QChem.

M. Klarner and R. Kempe designed the experiments. M. Klarner synthesized and characterized the different photocatalysts. M. Friedrich initially designed the photocatalyst and did some preliminary work regarding the catalytic application and NMR experiments in collaboration with J. Senker. G. Hörner carried out computational calculations of the grafting of the L1 ligand onto the secondary building unit and together with B. Weber commented on the scientific discussion. R. Kempe supervised the experimental part of this work and was continuously involved in the scientific discussions.

Myself and S. Kümmel conceived the structure of the manuscript and wrote all of the text describing my calculations and the introduction, discussion, and conclusion. M. Klarner wrote the section describing the experimental work. G. Hörner wrote the part of the manuscript describing the grafting simulations. R. Kempe contributed to the manuscript text. T. Branquinho de Queiroz made detailed suggestions concerning the manuscript text. B. Weber and J. Senker proofread the manuscript.

THE JOURNAL OF
PHYSICAL
CHEMISTRY C
A JOURNAL OF THE AMERICAN CHEMICAL SOCIETY

pubs.acs.org/JPCC Article

Combining Metal Nanoparticles with an Ir(III) Photosensitizer

Sebastian Hammon, Mara Klarner, Gerald Hörner, Birgit Weber, Martin Friedrich, Jürgen Senker, Rhett Kempe,* Thiago Branquinho de Queiroz, and Stephan Kümmel*

Cite This: J. Phys. Chem. C 2021, 125, 25765−25773

Read Online

ACCESS | Metrics & More | Article Recommendations | SI Supporting Information

ABSTRACT: We report on a new photocatalytic system that consists of an iridium-based photosensitizer that has been encapsulated into the pores of the metal−organic framework (MOF) MIL-101, which have then been loaded with metal nanoparticles. Loading with Ni leads to substantially increased photocatalytic hydrogen evolution rates, whereas loading with Pt and Pd leads to only a small increase or none at all, respectively. These experimental findings triggered us to theoretically study the combination of the photosensitizer and metal cluster in detail. Time-dependent density functional theory calculations with an optimally tuned range-separated hybrid functional show that the optical excitations of systems, in which the iridium-based photosensitizer is combined with a metal cluster, involve a pronounced charge transfer from the metal to the photosensitizer. Density functional calculations show that the binding energy between the photosensitizer and the metal cluster is considerably larger for Ni than for Pd and Pt.

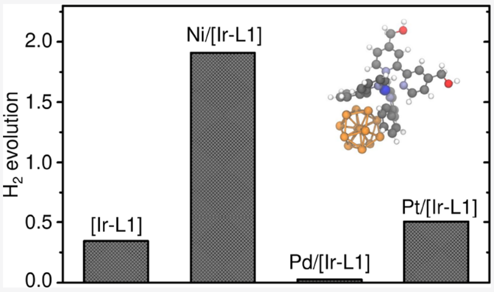

1. INTRODUCTION

Photocatalysis is one of the processes that have the potential to make an important contribution to meeting mankind's energy needs sustainably, e.g., by generating hydrogen that can replace fossil fuels. There has thus been a great interest in the photophysical properties of 2-phenylpyridyl- (ppy) and/or 2,2′-bipyridyl- (bpy) ligand-based Ir(III) photosensitizers, and insights have been gained from theoretical and experimental efforts in recent years.[1−9] It has been shown that these sensitizers have a lowest triplet state (T_1) that is associated with a long-lived charge separation. The latter can facilitate redox reactions that ultimately lead to the generation of hydrogen. In such triplet photosensitizers, the triplet excitations can rapidly be accessed after optical excitation through intersystem crossing, as the central Ir atom introduces a pronounced spin−orbit coupling, and the lowest triplet excitation T_1 is reached through internal conversion. Generally, T_1 is long-lived, e.g., with a photoluminescence (PL) lifetime of $\tau_{PL} \approx 0.1-14\ \mu s$ for most heteroleptic Ir photosensitizers.[9] The electronic nature of T_1 can usually be characterized as ligand-centered, metal−ligand to ligand charge transfer (MLLCT) or a varying mix of both.[9] $[Ir(bpy)(ppy)_2]^+$ (named Ir-L0 in the following) is a prime example of such a redox-active triplet photosensitizer, since it exhibits a long-lived T_1 (τ_{PL} = 370 ns in degassed tetrahydrofuran (THF))[10] with a distinct Ir/ppy → bpy charge-transfer character, designated as MLLCT(bpy).[4,5,10,11]

In the present study, which combines first experiments with a detailed theoretical study, we discuss that metal nanoparticles (MNPs) can modify the properties of a photosensitizer and substantially enhance the hydrogen evolution rate. We confined a visible light photosensitizer with the $[Ir(bpy)(ppy)_2]^+$ motif (cf. Figure 1, named Ir-L1 in the following) into MIL-101, which was subsequently loaded with Ni, Pd, and Pt nanoparticles. Upon loading with Ni, we observe a significantly enhanced photocatalytic activity for hydrogen evolution, whereas Pt and Pd lead to just a small enhancement or none at all, respectively. Relying on density functional theory (DFT) and time-dependent (TD) DFT with a range-separated hybrid functional[12−15] and a range-separation parameter that is determined by nonempirical optimal tuning,[8,16−27] we analyze how the presence of metal particles changes the electronic structure and the excitations of the photosensitizer. We find that there is a strong electronic interaction between the metal particles and the Ir-L1 in the ground state, with a clear trend in the binding affinity between the MNPs and Ir-L1: In the model systems that we studied, the Ni particle binds considerably stronger to Ir-L1 than Pd and Pt. The presence of the metals also substantially changes the character of the excitations. The absorption spectrum shows many densely lying excitations, and we find clear signatures of a charge transfer from the MNP to the Ir-L1 in the optical transitions. We discuss possible differences between the mechanisms of hydrogen evolution in the MNP-loaded samples and the mechanism discussed above

Received: June 29, 2021
Revised: October 27, 2021
Published: November 12, 2021

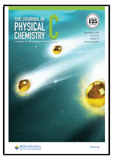

https://doi.org/10.1021/acs.jpcc.1c05756
J. Phys. Chem. C 2021, 125, 25765−25773

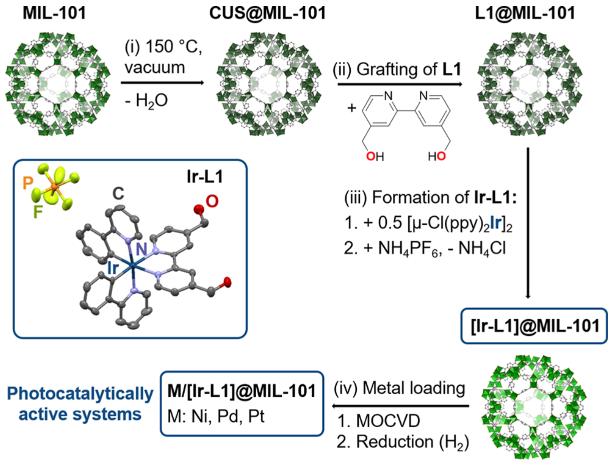

Figure 1. Synthesis of M/[Ir-L1]@MIL-101 by the ship-in-a-bottle approach. Step (i): CUS@MIL-101 is generated by removing auxiliary H_2O ligands from the SBU. Step (ii): After grafting the ligand L1 to CUS@MIL-101, step (iii): the iridium dimer [(μ-Cl)(ppy$_2$)Ir]$_2$ was added for the Ir-L1 complex formation. The anion was exchanged by noncoordinating hexafluorophosphate. Step (iv): For metal-loaded catalysts, a suitable metal precursor was infiltrated into MIL-101 by metal−organic chemical vapor deposition (MOCVD) and reduced by H_2 treatment. The molecular structure of Ir-L1 was determined by X-ray single crystal structure analysis. For crystallographic data and complex characterization, see SI.

for the bare Ir(III) photosensitizer and put our findings into perspective in the concluding section.

2. SYNTHESIS AND HYDROGEN EVOLUTION

The three-dimensional metal−organic framework MIL-101(Cr) is made from the linkage of terephthalic acid and secondary building units (SBUs, Cr_3O) where two out of three Cr^{3+} cations exhibit an accessible coordinatively unsaturated site (CUS).[28] The activated host material CUS@MIL-101 is yielded by the removal of auxiliary water ligands and, thereafter, can engage in adsorption processes of guest molecules.

In recent years, the grafting of various alcohols to Lewis-acidic coordinatively unsaturated Cr^{3+} sites was demonstrated.[29−32] Hence, we designed a bipyridyl ligand L1 that contains hydroxyl groups in the backbone and allows homogeneously distributed grafting to CUS. This serves as a basis for the targeted encapsulation of an iridium photosensitizer with an Ir-L0 motif within MIL-101 following a ship-in-a-bottle approach. We compared the new heteroleptic iridium photosensitizer Ir-L1 (cf. Figure 1) to the established [Ir(dtbbpy)(ppy)$_2$]$^+$ (4,4′-di-*tert*-butyl-2,2′-bipyridyl, named Ir-L2) in means of optical absorption characteristics and redox potentials, two crucial factors for efficient photocatalysis, and found no significant differences, as shown in the Supporting Information (SI)). The theoretical comparison with Ir-L0 further corroborates the photocatalytic functionality of Ir-L1, as discussed in the section Ir-L1 Triplet Photosensitizer.[33] Therefore, we consider the photosensitizer Ir-L1 suitable for our study on a confined photocatalyst system. The composite material M/[Ir-L1]@MIL-101 was synthesized along a four-step route as outlined in Figure 1 (M: Ni, Pd, Pt).

Step (i): The activated form of the host material CUS@MIL-101 was generated from native MIL-101 by removal of up to two molecules of water per SBU, which originated from the hydrothermal synthesis of MIL-101.[28] Therefore, MIL-101 was heated to 150 °C in vacuum for 12 h, resulting in CUS@MIL-101 crystallites with an intact octahedral shape (cf. SI, Figure S4(a)). Compared to as-synthesized MIL-101, no significant changes in crystallinity were observed (cf. SI, Figure S4(b)).

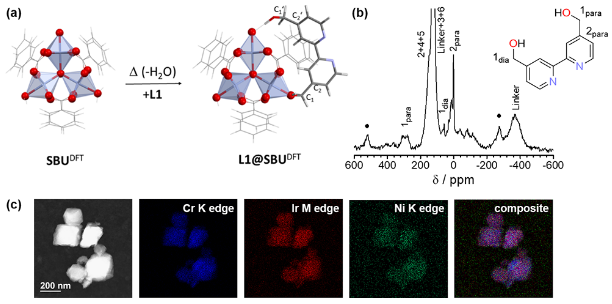

Figure 2. (a) DFT optimized structures of a truncated model of SBU^{DFT} and of its adduct $L1@SBU^{DFT}$; diagnostic ^{13}C MAS NMR carbon sites are highlighted. (b) ^{13}C MAS NMR spectrum of L1@MIL-101 including assignments; spinning side bands were marked with a dot. (c) HAADF-STEM of Ni/[Ir-L1]@MIL-101 and representative EDX elemental maps of Cr, Ir, and Ni. Additionally, overlapped element maps are given.

Step (ii): In order to ensure a homogeneous distribution of the bulky iridium complex Ir-L1 (∼13.3 × 10.0 Å), we followed a ship-in-a-bottle approach: The 2,2′-bipyridyl-4,4′-dimethanol ligand L1 was homogeneously grafted to the activated MOF through coordination at the unsaturated Cr^{3+} sites of the SBU as monitored by Fourier transform IR (FT-IR) and magic angle spinning (MAS) nuclear magnetic resonance (NMR) spectroscopy (cf. Figure 2(a)). The assignments of ^{13}C MAS NMR shifts were made by a comparative study of MIL-101, L1, and Ir-L1. Paramagnetic MAS NMR previously proved a very useful tool for identifying coordination species,[34] revealing diagnostic hyperfine shifts for C atoms close to paramagnetic centers. Accordingly, the MAS NMR spectra of MIL-101 showed massive negative paramagnetic shifts for the skeletal terephthalic linker (−370 ppm) as compared to noncoordinated molecules (cf. Figure 2(b)). In keeping with this finding, the paramagnetic shift for C1 (1_{para} 292 ppm) and C2 (2_{para} 2 ppm) signals of the grafted ligand L1 gave clear evidence for the successful incorporation of the ligand at defined sites of the SBU (cf. Figure 2(b) and SI, Figure S6(a,b)). A diamagnetic shift for C1 (1_{dia} 58 ppm) indicated the coordination of the ligand by one hydroxyl group only. For further interpretation of the MAS NMR shifts, the grafting process of L1 was analyzed with DFT methods (cf. SI for details). Truncated models of the trinuclear SBU (cf. Figure 2(a)) have been optimized in the native form (SBU^{DFT}) and in the ligand-grafted form concomitant with partial dehydration ($L1@SBU^{DFT}$). Incorporation of L1 via coordination at the open coordination site of Cr^{3+} accommodates the cleft between neighboring terephthalic moieties. L1 is found well-suited to bind via strong hydrogen bonding at a second site of the same SBU. The dis-symmetric interaction with two different Lewis sites of only one of the hydroxyl groups in the ligand backbone of L1 thus well-matches the outcomes of ^{13}C MAS NMR spectra. In keeping with this, computation of $L1@SBU^{DFT}$ reveals small but significant Mulliken spin densities ρ at C1 and C2 (with $\rho(C1) \ll \rho(C2)$) but none

https://doi.org/10.1021/acs.jpcc.1c05756
J. Phys. Chem. C 2021, 125, 25765−25773

at the H-bridged ligand arm at C1′ and C2′. Two-point anchoring of L1 at one single SBU as in optimized L1@SBU^{DFT} serves to fix the pyridine moieties of L1 in a close-to-coplanar *cis*-arrangement, which is suitable for on-site construction of the Ir photosensitizer. IR spectra computed of grafted L1@SBU^{DFT} qualitatively match the experimental data (cf. SI, Figure S15).

Step (iii): On-site formation of the Ir-L1 complex was achieved by adding a $[(\mu\text{-Cl})(\text{ppy})_2\text{Ir}]_2$ dimer with predisposed Ir(ppy)_2 units and incorporation of noncoordinating hexafluorophosphate through anion metathesis to yield [Ir-L1]@MIL-101. The successful encapsulation of the Ir photosensitizer within the MOF pores was corroborated by FT-IR spectroscopy (cf. SI, Figure S8) and MAS NMR spectroscopy (cf. SI, Figure S6(c,d)). In contrast to ligand grafting, the ^{13}C MAS NMR spectrum of [Ir-L1]@MIL-101 did not indicate direct grafting via Cr^{3+} sites, since signals were observed only within the typical diamagnetic shift region (0−180 ppm). In particular, there were no signs of dis-symmetric attachment. We believe that the formation of the sterically demanding Ir-L1 photosensitizer within the mesopores of MIL-101 was associated with the decoordination of L1 from the Cr^{3+} sites.

High-angle annular dark-field scanning transmission electron microscopy (HAADF-STEM) images indicated a homogeneous distribution of Ir in the MOF crystallites (cf. Figure 2(c)). Analysis via inductively coupled plasma optical emission spectroscopy revealed the presence of 5.8 wt.% Ir due to Ir-L1 encapsulated in MIL-101, which corresponds to 0.3 μmol(Ir) mg^{-1}(MIL-101). Diffuse-reflectance ultraviolet−visible spectroscopy of yellow-green [Ir-L1]@MIL-101 showed absorption at wavelengths below 600 nm (see SI, Figure S9). This finding is highly consistent with the optical absorption properties of Ir-L1, which strongly absorbs at wavelengths $\lambda < 525$ nm (2.36 eV).

We investigated this photocatalyst [Ir-L1]@MIL-101 for the proton reduction from water using triethylamine as a sacrificial agent. For this purpose, degassed H_2O and triethylamine were dissolved in degassed THF, the photocatalyst was added, and the slurry was illuminated with a blue LED (470 nm, 50 W). Discontinuous headspace analysis through gas chromatography quantified the amount of H_2 evolved after 6 h, from which the H_2 evolution rate per hour was calculated. [Ir-L1]@MIL-101 was found to produce about 0.34 $\mu\text{mol}(H_2)\ h^{-1}\ \mu\text{mol}(\text{Ir})^{-1}$ at the selected reaction condition, i.e., the photoreaction was slightly superstoichiometric after 6 h. Confinement of the photosensitizer Ir-L1 affects its photophysical properties. We report an investigation of the stability of [Ir-L1]@MIL-101 in the SI.

Time-resolved luminescence spectroscopy of [Ir-L1]@MIL-101 demonstrated a multiexponential PL decay with lifetime components in the time range of only a few nanoseconds, while Ir-L1 gave leading decay components in the time range of several hundreds of nanoseconds (see SI, Figure S13 and Table S2). Thus, the composite [Ir-L1]@MIL-101 opens deactivation pathways for Ir-L1 that can be related to its confinement, steric distortion, and/or the open-shell skeleton of the MOF. Nevertheless, and in spite of the reduced excited-state lifetime, confined [Ir-L1]@MIL-101 still is active toward photochemical hydrogen production.

Step (iv): Incorporation of group 10 MNPs (Ni, Pd, Pt; 5 wt.%) within the pores of [Ir-L1]@MIL-101 was achieved by a metal−organic chemical vapor deposition approach with suitable precursors and on-site reduction to metallic nanoparticles by hydrogen treatment (cf. SI, Table S1).

Exemplarily, we recorded a HAADF-STEM image and representative energy-dispersive X-ray spectroscopy (EDX) elemental maps of Ni/[Ir-L1]@MIL-101 (cf. Figure 2(c)). The spatial distribution of Cr atoms matched the octahedral shape of the MIL-101 crystallites, which was obviously retained throughout all modifications. Ir and Ni are likewise detected homogeneously distributed over the MOF.

The additional presence of group 10 MNPs did not significantly alter the PL of (non-metal-loaded) [Ir-L1]@MIL-101, except for a small increase in the PL lifetime (see SI, Figure S13 and Table S2).

Regarding the photocatalytic activity (cf. Figure 3), palladium almost entirely quenches the hydrogen evolution (0.03 $\mu\text{mol}(H_2)\ h^{-1}\ \mu\text{mol}(\text{Ir})^{-1}$). Loading with the well-established reduction (co)catalyst Pt leaves the activity largely unaffected (0.51 $\mu\text{mol}(H_2)\ h^{-1}\ \mu\text{mol}(\text{Ir})^{-1}$). It was surprising to find the 3d metal nickel boosting the hydrogen evolution rate by a factor of 5.6 to 1.91 $\mu\text{mol}(H_2)\ h^{-1}\ \mu\text{mol}(\text{Ir})^{-1}$, thereby outperforming the established precious metals (cf. Figure 3).

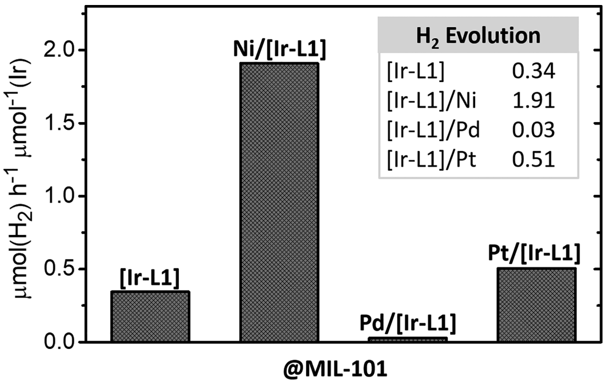

Figure 3. Hydrogen evolution rate for the photocatalytic proton reduction from water for [Ir-L1]@MIL-101 and M/[Ir-L1]@MIL-101 (M: Ni, Pd, Pt). For the general procedure for photocatalytic experiments, see SI.

In conclusion, the distinction in cocatalytic efficiency cannot be correlated with effects of Ni, Pd, and Pt on the photoluminescence of the [Ir-L1]@MIL-101. However, we see a clear qualitative effect of the metal element itself. The MOF stabilizes the metal nanoparticles without blocking their surface and ensures the spatial proximity of the metal and the photosensitizer. The proximity of the metal can be expected to have an effect on electron transfer and energy transfer between the metal and the photosensitizer and thus affect the catalytic activity. Our experiments show a highly beneficial effect for the 3d metal nickel. In the following, we take steps to understanding this effect better via computational analysis.

3. ANALYSIS OF THE ELECTRONIC STRUCTURE AND EXCITATIONS

For further understanding we have performed a computational analysis of key elements of the experimental system, with a focus on the combination of Ir-L1 with Ni, Pd, and Pt and the corresponding charge-transfer properties.

3.1. Ir-L1 Triplet Photosensitizer.

As a first step, we checked whether adding the anchor groups to the photosensitizer leads to any unexpected effects. We calculated the optical absorption spectra of the Ir-L1 structure that underlies the experiments and the basic motif Ir-L0, which is an intensively studied triplet photosensitizer (cf. Introduction). The former differs from the latter by the anchor group ($-CH_2OH$) that is attached to the bpy ligand. Figure 4 shows that the spectra calculated with TDDFT[35,36] (cf. SI, Computation Details) are qualitatively very similar. The strongest vis singlet excitations of both complexes are located around ~3 eV. The brightest one of Ir-L1 (S_4, 3.03 eV) shows a slightly increased oscillator strength (0.1023) compared to the brightest one of Ir-L0 (2.99 eV, 0.0886). Note that in this and all following figures, we folded the calculated oscillator strengths with Gaussians to guide the eye (scale on the left edge of the figure), whereas the oscillator strength itself was plotted on a scale of [0, 0.2].

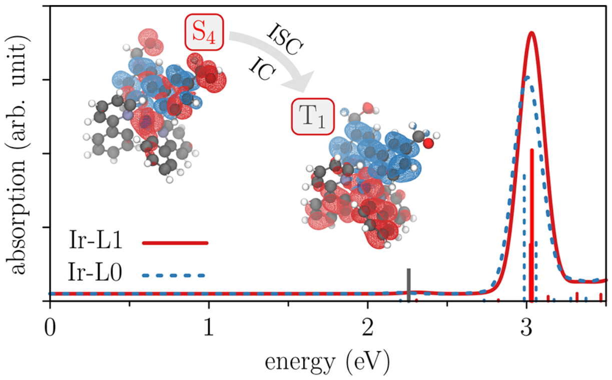

Figure 4. Vis absorption spectrum of the modified Ir-L1 and the standard Ir-L0: The excitation spectra were calculated using TDDFT with the nonempirical optimally tuned ωPBE (ω_{opt}(Ir-L1) = 0.16 bohr^{-1}, ω_{opt}(Ir-L0) = 0.16 bohr^{-1}). The relative oscillator strength is indicated by the height of the vertical red and blue bars for Ir-L1 and Ir-L0, respectively. T_1(Ir-L1) is marked by the single gray bar. For a better visualization, the spectrum is shifted vertically by a constant of 0.02 arb. unit. Inset: Difference densities for the brightest singlet S_4 (3.03 eV) and the lowest triplet excitation T_1 (2.26 eV), with schematic allusion to intersystem crossing and internal conversion. See the main text for details about the difference densities.

We also calculated the electronic difference densities of the singlet and triplet excitations, respectively, with the singlet ground state, as depicted in the inset of Figure 4 for the brightest excitation S_4(Ir-L1) and T_1(Ir-L1). T_1 shows a clear long-range MLLCT(bpy) character, as illustrated by the red and blue wireframes that indicate negative (area of electron lack) and positive (gain) in these and the following difference densities. An isovalue of 0.0005 a_0^{-3} was used in the plots of the difference densities throughout the paper. The MLLCT(bpy) of Ir-L1 is qualitatively very similar to the one of Ir-L0 (cf. SI, Figure S17). In total, Ir-L1 inherits the key photophysical properties of Ir-L0 and can function as a triplet photosensitizer via the previously discussed mechanism.[25] The findings from the calculations are thus in line with the experimental observations that also point to a negligible influence of the anchor groups (SI, Figure S2).

3.2. Influence of Metal Nanoparticles on Ir-L1. As studying the complete system of Ir-L1 and an MNP inside MIL-101 with first-principles methods is computationally unfeasible and the main electronic effects are expected to occur in the interaction between the metals and Ir-L1, we are studying a model system that contains a 13-atom metal cluster (M_{13} = Ni_{13}, Pd_{13}, Pt_{13}) and one Ir-L1 molecule. Obviously, the 13-atom clusters are smaller than the nanoparticles that fill the MOF pores in the experiments,[37] but given the computational restrictions, we consider 13-atom clusters minimalistic structures that are suitable for studying the metal−Ir-L1 interaction for several reasons: They are known to form a variety of stable isomers,[38−47] and similar geometries occur for all three metals. This allows the different metals to be compared on a similar structural basis. Furthermore, we have generally observed in Born−Oppenheimer DFT molecular dynamics[48,49] (BOMD) simulations at room temperature that 13-atom metal clusters can adapt their structure to their environment, e.g., when they are in solution or bind to a molecule. Therefore, versatile aspects of a possible interaction between the metal cluster and Ir-L1 can be captured. Finally, the choice is also supported by the finding that all three M_{13} bind to Ir-L1 (see below) and may thus be interpreted to represent a small subsystem inside a pore.

Note that transition metal clusters require special attention with respect to the choice of the exchange-correlation approximation, because the partially localized d-orbitals are prone to be affected by self-interaction errors, and different density functionals are sensitive to this problem to different degrees.[50] For the reasons discussed in refs 51 and 52, we used the semilocal generalized gradient approximation Perdew−Burke−Ernzerhof[53,54] (PBE) for DFT geometry optimizations, to calculate binding energies and for BOMD simulations, and the optimally tuned range-separated hybrid functional ωPBE,[55,56] composed of PBE exchange in the short-range, exact exchange in the long-range, and PBE correlation, to compute photophysical properties such as the photoabsorption spectrum (cf. SI, Analysis of the electronic structure and excitations). All calculations using PBE and ωPBE were carried out with the TURBOMOLE[57] and QCHEM[58] code, respectively.

For determining the structures of the combined metal−Ir-L1 systems, we performed a BOMD simulation at room temperature for each system M_{13}/[Ir-L1] employing the def2-SVP basis set.[59] We started from an icosahedral structure for all three metal clusters, and initially, M_{13} had been displaced from $(ppy)_2$ by a distance of ~7 Å^{-1} between the centers of gravity of M_{13} and Ir-L1. We observed that all three metal clusters were "drawn" into the gap between the two ligands (cf. Figure 5). Ni_{13} and Pt_{13} retained their icosahedral structures, whereas Pt_{13} assumed different geometries in the course of the simulation. We propagated each system for about 4 ps and then determined the energetically most favorable structure of each run by checking the total energy data. We

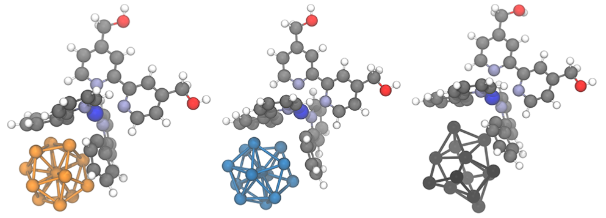
(a) Ni_{13}/[Ir-L1] (b) Pd_{13}/[Ir-L1] (c) Pt_{13}/[Ir-L1]

Figure 5. Molecular structures used to study the direct influence of the metals on the photophysical properties: (a) Ni_{13}/[Ir-L1], (b) Pd_{13}/[Ir-L1], (c) Pt_{13}/[Ir-L1].

further relaxed the thus-found structures in geometry optimizations using PBE with van der Waals corrections (DFT-D3)[60] and the def2-TZVP basis set.[61] The resulting geometries are depicted in Figure 5 and served as the basis for the following calculations.

We calculated the binding energy between the metal clusters and Ir-L1 by taking the difference of the total energies of the separated and the combined systems, using the fully relaxed structures. With a binding energy of −5.76 eV, Ni_{13}/[Ir-L1] is more strongly bound than Pd_{13}/[Ir-L1] (−4.72 eV) and Pt_{13}/[Ir-L1] (−3.39 eV). The binding energy is thus an observable in which the Ni-based system differs noticeably from the Pt- and Pd-based ones.

The pronounced binding energy that is observed in all cases also indicates that there is substantial interaction between the metals and Ir-L1. Analyzing the density of states of M_{13}/[Ir-L1] corroborates this finding. If there would be no interaction between the constituents of a system, then the density of states of the combined system would result from summing up the density of states of the separate subsystems. Our calculations, however, show that the DOS of M_{13}/[Ir-L1] can neither quantitatively nor qualitatively be understood from the superposition of the densities of states of M_{13} and Ir-L1. This is discussed in greater detail in the SI (cf. Figure S18), and reassuringly, this observation is not specific to a particular exchange-correlation approximation, as both PBE and ωPBE consistently yield the same trend (cf. SI, Figure S18(a) and S19(a)).

One might wonder whether our observation of a pronounced interaction between Ir-L1 and the metal clusters is specific just for the 13-atom clusters. Therefore, we have repeated the analysis for the considerably larger system Ni_{38}/[Ir-L1]. In the SI, we show that also for this larger system, the density of states clearly shows a pronounced electronic interaction between the metal particle and the photosensitizer. We further show (Figure S22) that the highest occupied orbital is delocalized in a qualitatively similar way over Ir-L1 and the metal for both the small and the larger cluster. Thus, the above conclusions are not specific to just small clusters.

The potentially most interesting observable in the context of photocatalytic activity is the photoabsorption spectrum. Analogously to the previous reasoning about the density of states, the absorption spectrum of M_{13}/[Ir-L1] would result from the superposition of the individual spectra of Ir-L1 and M_{13} if the interaction between the constituents would be negligible. Figure 6 compares the absorption spectra of M_{13}/[Ir-L1] to those of the individual molecular components, and the superposition of the latter. We applied a Gaussian broadening of 0.08 eV to guide the eye. Panel (a) depicts the data for Ni_{13}/[Ir-L1], panel (b) depicts the data for Pd_{13}/[Ir-L1], and panel (c) depicts the data for Pt_{13}/[Ir-L1]. The superposition, labeled M_{13} + Ir-L1 in Figure 6, is the sum of the individual spectra of M_{13} and Ir-L1. As M_{13}/[Ir-L1] and M_{13} have a spin-polarized ground state (cf. SI, Table S4), the labeling of the excitations in Figure 6 and the following discussion need extra explanation. For the bare Ir-L1 system, an excitation that preserves the spin leads to a singlet state, and we therefore denoted such excitations with S, and the ones in which one spin was flipped were denoted with T. A spin-conserving excitation of, for example, M_{13}/[Ir-L1] does not lead to a singlet state but keeps the magnetic moment that is introduced by the metal particle. Nevertheless, we continue to label spin-conserving excitations with S and spin-flip excitation with T to ease the comparison between the spectrum of the combined system M_{13}/[Ir-L1] and the spectra of the separate constituents. In the SI, we present the details about the spin configurations. In order to put this comparison on a firm footing, we paid attention to two aspects: (i) We calculated the spectrum of M_{13} and Ir-L1 (separately) in the fixed structure as they are in M_{13}/[Ir-L1] (cf. Figure 5) to avoid spectral differences that are just a consequence of structural differences. (ii) Due to its implicit density dependency, the optimally tuned range-separation parameter ω_{opt} is system-specific and,

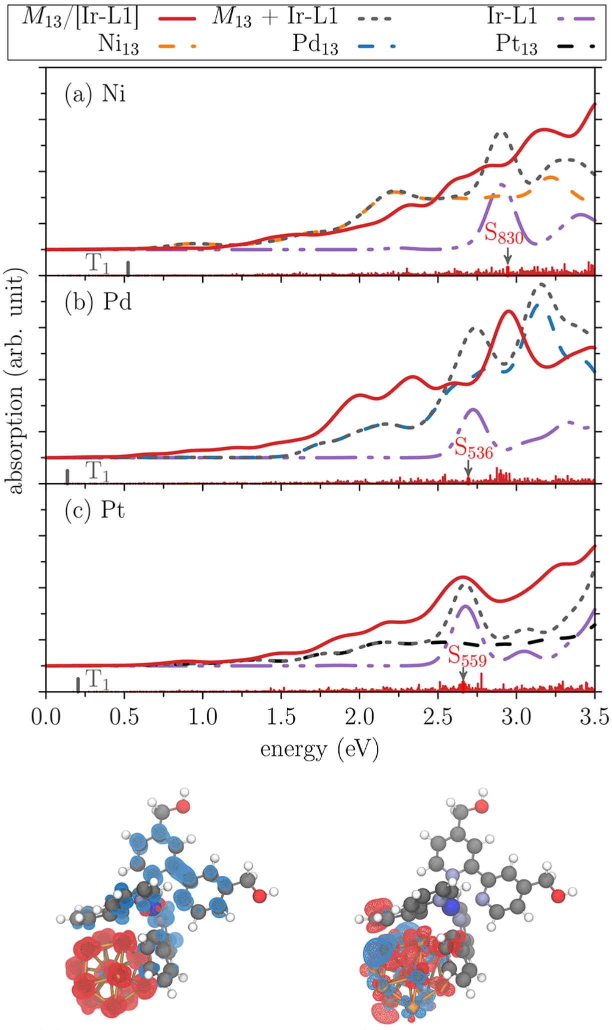

(d) S_{830}: 2.94 eV, 0.0079 (e) T_1: 0.52 eV, 0.0

Figure 6. Top: Vis absorption spectrum of M_{13}/[Ir-L1], M_{13}, Ir-L1, and the superposition M_{13} + Ir-L1. The spectra were obtained from TDDFT with ωPBE. Vertical red bars and the single gray bar show the relative oscillator strength and lowest spin-flip excitation for M_{13}/[Ir-L1], respectively. All absorption spectra are shifted vertically by 0.24 arb. unit for easy distinction from the horizontal axis. The spectra depicted in panels (a–c) each use the optimally tuned ω_{opt} of the respective M_{13}/[Ir-L1]. (a) Ni_{13}/[Ir-L1] (ω_{opt} = 0.14 $bohr^{-1}$). (b) Pd_{13}/[Ir-L1] (ω_{opt} = 0.12 $bohr^{-1}$). (c) Pt_{13}/[Ir-L1] (ω_{opt} = 0.11 $bohr^{-1}$). Bottom: Difference densities of selected excitations of Ni_{13}/[Ir-L1] with the given energy and oscillator strength (marked in (a)). (d) The difference density of the optical excitation S_{830} shows a metal particle to ligand charge transfer. (e) Difference density of the lowest spin-flip excitation, which we denote by T_1 in analogy to the previous section.

thus, differs for M_{13}/[Ir-L1], M_{13}, and Ir-L1 (cf. SI, Table S4). To eliminate these exchange-correlation-functional-related differences, we used $\omega_{\mathrm{opt}}(M_{13}/[\mathrm{Ir\text{-}L1}])$ to calculate the absorption spectrum of M_{13} and Ir-L1 in (i). For this reason, the absorption spectra of Ir-L1 shown in Figure 6 differ from each other and the one of Figure 4. The noticeable red shift is mostly due to the smaller range-separation parameter and not geometry-related. Figure 6 clearly shows that the superposition of the absorption spectra of M_{13} and Ir-L1 cannot explain the spectra of the combined systems M_{13}/[Ir-L1] for any of the systems.

When comparing the spectra of the M_{13}/[Ir-L1] systems to the one of the bare Ir-L1, one notices pronounced differences in all cases: (i) The vis photoabsorption of M_{13}/[Ir-L1] is overall larger than the one of Ir-L1. (ii) When one compares the oscillator strength of the brightest excitation of M_{13}/[Ir-L1] to the oscillator strength of the brightest excitation of Ir-L1, one notices that it decreases by approximately 1 order of magnitude upon addition of the metal. (iii) On the other hand, the number of excited states increases enormously. Figure S23 in the SI shows that this is directly due to the metal clusters. These results clearly show that all three metals influence the photoabsorption process significantly.

In order to analyze the situation further, we computed the difference densities between the most relevant electronic excitations and the ground state. Figures S24−S26 in the SI show these difference densities for the 30 excitations with the highest oscillator strength in the energy range up to 3.2 eV. (We chose the value 3.2 eV as the upper limit, because this is approximately the threshold between vis and UV.) These difference densities reveal that for all three metals, the metal cluster takes on the role of an electron donor and charge is transferred to Ir-L1. The metal particle to ligand charge transfer extends over the whole Ir complex; however, the trend of a long-range charge-transfer $M_{13} \rightarrow$ bpy is also noticeable for all M_{13}/[Ir-L1] (cf. SI, Figure S24, e.g., S_{485}, S_{813}, S_{947} of Ni_{13}/[Ir-L1]; Figure S25, S_{356}, S_{649}, S_{747} of Pd_{13}/[Ir-L1]; Figure S26, S_{451}, S_{559}, S_{747} of Pt_{13}/[Ir-L1]). This long-range charge-transfer character is shown exemplary for S_{830} of Ni_{13}/[Ir-L1] in Figure 6(d). S_{830} shows overlap with the main peak of Ir-L1 in Figure 6(a), and the comparison to Figure 4 clearly demonstrates that the addition of the metal cluster changes the excitation mechanism. We found qualitatively similar features for Pd_{13}/[Ir-L1] (cf. S_{536}) and Pt_{13}/[Ir-L1] (cf. S_{559}). The metal particle to ligand charge-transfer process in the M_{13}/[Ir-L1] systems is particularly pronounced for excitation energies above ~2.3 eV and extends to 3.2 eV and further into the UV. Excitations of similar character can also be found at lower energies but less frequently and with a lower oscillator strength (e.g., S_{245}(Ni_{13}/[Ir-L1]): 1.62 eV, 0.003). In summary, our calculated photoabsorption spectra show that all three metals have a pronounced influence on the photoabsorption process and, compared to the bare Ir-L1 system, change the charge-transfer characteristics.

We also investigated in how far the interaction between the metal cluster and the Ir-L1 depends on their relative spatial proximity. To this end, we calculated photoabsorption spectra for a series of structures in which we successively increased the distance between the center of mass of the metal cluster and Ir-L1 in steps of a few bohr while keeping other structural features fixed. The metal particles have a noticeable influence on the photoabsorption up to distances that are about 10 bohr larger than the equilibrium distance. This shows that our findings can be expected to hold on more general grounds and are not specific to a particular binding geometry. The calculations also show a qualitative trend that the interaction persists more pronouncedly for the Ni_{13} cluster than for the other metals (Figure S28).

Finally, we took a look at the lowest spin-flip excitation of M_{13}/[Ir-L1], in analogy to the analysis of T_1(Ir-L1) in Figure 4. Panel (e) in Figure 6 depicts the difference density for the exemplary case of the lowest spin-flip transition of Ni_{13}/[Ir-L1]. In contrast to the situation for the bare Ir-L1 there is little charge-transfer character in this excitation: the difference density is predominantly localized on the metal cluster (cf. SI, Figure S27).

4. DISCUSSION AND CONCLUSION

We have reported the synthesis of a new photocatalytic system in which a heteroleptic Ir(III) photosensitizer has been encapsulated in the pores of MIL-101, which have then been loaded with three different metals. This setup ensures spatial proximity between the photosensitizer and the metals. In comparison to the bare photosensitizer, loading with Pd strongly reduces the hydrogen evolution rate, loading with Pt slightly increases it, and loading with the earth-abundant metal Ni significantly increases the rate by a factor of more than five.

Understanding the mechanism behind this effect is challenging because of the difficulty to obtain insight into the processes within the pores in situ. Based on the experimental results, it is difficult to disentangle in how far the effect is directly related to photophysical and photochemical properties and in how far it may depend on other phenomena, e.g., ones of steric nature. In order to take first steps toward an understanding, we have done a detailed theoretical−computational investigation of the photosensitizer in combination with Ni, Pd, and Pt clusters. The calculations show a strong interaction between all of the metals and the photosensitizer. The presence of the metal clusters changes the photoabsorption significantly: Instead of the few excitations with large oscillator strength that characterize the bare photosensitizer, the combination with the metal leads to a very dense excitation spectrum covering a broader range of energies. We have analyzed many of the excitations in detail via difference densities and found that for the combined systems, many of the optically active excitations involve a charge transfer from the metal to the photosensitizer ligands. It is conceivable that this can play a role in the photophysics and chemistry.

However, we did not find any substantial, qualitative differences between the combination of the photosensitizer with the three different metals with respect to the electronic excitations. Taking into account the finding that the lowest spin-flip excitation does not have charge-transfer character when the photosensitizer is combined with the metal particles, one might speculate that the photophysical mechanism for the M_{13}/[Ir-L1] systems differs from the one in the bare Ir-L1 sensitizer: In the latter, accessing the triplet state is beneficial, because it leads to a long-lived charge-separated state. In the former, accessing the spin-flipped state may be detrimental, because the excitations in which the spin does not change show charge-transfer character, whereas the spin-flipped state does not. The presence of heavier atoms in the Pt and Pd metal particles may lead to a stronger spin orbit coupling than for the Ni system and thus a higher probability to end up in the spin-flipped and, therefore, unfavorable noncharge separated

https://doi.org/10.1021/acs.jpcc.1c05756
J. Phys. Chem. C 2021, 125, 25765−25773

state. Such a reasoning could explain the larger hydrogen evolution rate of Ni, but of course, other explanations are also possible. For example, it is conceivable that the different hydrogen evolution rates are not directly related to differences in the photophysical properties but have other reasons. Our calculations revealed, for example, that the binding between the Ni cluster and the photosensitizer is much stronger than the binding between the photosensitizer and the Pd and Pt cluster. This may influence the spatial arrangement of the constituents in the pore and thus also the hydrogen evolution rate.

In summary, our work is a proof of concept showing in a combination of experiment and theory that the spatial proximity of metal particles and a photosensitizer leads to significant interaction and potentially interesting effects. Further work will be needed to reach a detailed understanding of the photophysics and chemistry of these complex systems and to further explore the possibilities that such systems offer in practice. The increased hydrogen evolution rates that we observe for the combination of Ni with Ir-L1 are a strong incentive for further studies in this direction.

■ ASSOCIATED CONTENT

Supporting Information

The Supporting Information is available free of charge at https://pubs.acs.org/doi/10.1021/acs.jpcc.1c05756.

> Detailed description of the experimental procedures and methods; the material synthesis; the material and catalyst characterization of Ir-L1 and M/[Ir-L1]@MIL-101, and additional information in relation to the grafting process of the L1 ligand. Computational details about the DFT and TDDFT calculations for the metal cluster−photosensitizer systems and additional results such as the density of states, TDDFT absorption spectra and difference densities, and their dependence on the distance between M_{13} and Ir-L1 (PDF)

■ AUTHOR INFORMATION

Corresponding Authors

Rhett Kempe − *Department of Chemistry, Inorganic Chemistry II − Sustainable Chemistry Centre, University Bayreuth, Bayreuth D-95447, Germany;* orcid.org/0000-0002-9138-4155; Email: kempe@uni-bayreuth.de

Stephan Kümmel − *Department of Physics, Theoretical Physics IV, University of Bayreuth, Bayreuth D-95447, Germany;* orcid.org/0000-0001-5914-6635; Email: stephan.kuemmel@uni-bayreuth.de

Authors

Sebastian Hammon − *Department of Physics, Theoretical Physics IV, University of Bayreuth, Bayreuth D-95447, Germany; Centro de Ciencias Naturais e Humanas, Universidade Federal do ABC, Santo André, São Paulo 09210-580, Brazil*

Mara Klarner − *Department of Chemistry, Inorganic Chemistry II − Sustainable Chemistry Centre, University Bayreuth, Bayreuth D-95447, Germany*

Gerald Hörner − *Department of Chemistry, Inorganic Chemistry IV, University Bayreuth, Bayreuth D-95447, Germany;* orcid.org/0000-0002-3883-2879

Birgit Weber − *Department of Chemistry, Inorganic Chemistry IV, University Bayreuth, Bayreuth D-95447, Germany;* orcid.org/0000-0002-9861-9447

Martin Friedrich − *Department of Chemistry, Inorganic Chemistry II − Sustainable Chemistry Centre, University Bayreuth, Bayreuth D-95447, Germany*

Jürgen Senker − *Department of Chemistry, Inorganic Chemistry III, University Bayreuth, Bayreuth D-95447, Germany;* orcid.org/0000-0002-7278-7952

Thiago Branquinho de Queiroz − *Centro de Ciencias Naturais e Humanas, Universidade Federal do ABC, Santo André, São Paulo 09210-580, Brazil;* orcid.org/0000-0003-3775-954X

Complete contact information is available at: https://pubs.acs.org/10.1021/acs.jpcc.1c05756

Notes

The authors declare no competing financial interest.

■ ACKNOWLEDGMENTS

We acknowledge stimulating discussions with Prof. Dr. Lothar Kador. Financial support from the German Research Foundation (DFG SFB 840, B1), from the Bavarian State Ministry of Science, Research, and the Arts for the Collaborative Research Network "Solar Technologies go Hybrid", and from the Bavarian Polymer Institute (KeyLab Electron and Optical Microscopy, KeyLab Theory and Simulation in terms of computing resources) is gratefully acknowledged.

■ REFERENCES

(1) Goldsmith, J. I.; Hudson, W. R.; Lowry, M. S.; Anderson, T. H.; Bernhard, S. Discovery and high-throughput screening of heteroleptic iridium complexes for photoinduced hydrogen production. *J. Am. Chem. Soc.* **2005**, *127*, 7502−7510.

(2) Tinker, L.; McDaniel, N.; Curtin, P.; Smith, C.; Ireland, M.; Bernhard, S. Visible Light Induced Catalytic Water Reduction without an Electron Relay. *Chem. - Eur. J.* **2007**, *13*, 8726−8732.

(3) Curtin, P. N.; Tinker, L. L.; Burgess, C. M.; Cline, E. D.; Bernhard, S. Structure-activity correlations among iridium(III) photosensitizers in a robust water-reducing system. *Inorg. Chem.* **2009**, *48*, 10498−10506.

(4) Wu, S. H.; Ling, J. W.; Lai, S. H.; Huang, M. J.; Cheng, C. H.; Chen, I. C. Dynamics of the excited states of $[Ir(ppy)_2bpy]^+$ with triple phosphorescence. *J. Phys. Chem. A* **2010**, *114*, 10339−10344.

(5) Gärtner, F.; Denurra, S.; Losse, S.; Neubauer, A.; Boddien, A.; Gopinathan, A.; Spannenberg, A.; Junge, H.; Lochbrunner, S.; Blug, M.; et al. Synthesis and characterization of new iridium photosensitizers for catalytic hydrogen generation from water. *Chem. - Eur. J.* **2012**, *18*, 3220−3225.

(6) Bokarev, S. I.; Bokareva, O. S.; Kühn, O. Electronic excitation spectrum of the photosensitizer $[Ir(ppy)_2(bpy)]^+$. *J. Chem. Phys.* **2012**, *136*, 214305.

(7) Bokarev, S. I.; Hollmann, D.; Pazidis, A.; Neubauer, A.; Radnik, J.; Kühn, O.; Lochbrunner, S.; Junge, H.; Beller, M.; Brückner, A. Spin density distribution after electron transfer from triethylamine to an $[Ir(ppy)_2(bpy)]^+$ photosensitizer during photocatalytic water reduction. *Phys. Chem. Chem. Phys.* **2014**, *16*, 4789−4796.

(8) Bokareva, O. S.; Möhle, T.; Neubauer, A.; Bokarev, S. I.; Lochbrunner, S.; Kühn, O. Chemical Tuning and Absorption Properties of Iridium Photosensitizers for Photocatalytic Applications. *Inorganics* **2017**, *5*, 23.

(9) DiLuzio, S.; Mdluli, V.; Connell, T. U.; Lewis, J.; VanBenschoten, V.; Bernhard, S. High-Throughput Screening and Automated Data-Driven Analysis of the Triplet Photophysical

Properties of Structurally Diverse, Heteroleptic Iridium(III) Complexes. *J. Am. Chem. Soc.* **2021**, *143*, 1179−1194.

(10) Neubauer, A.; Grell, G.; Friedrich, A.; Bokarev, S. I.; Schwarzbach, P.; Gärtner, F.; Surkus, A. E.; Junge, H.; Beller, M.; Kühn, O.; et al. Electron- and energy-transfer processes in a photocatalytic system based on an Ir(III)-photosensitizer and an iron catalyst. *J. Phys. Chem. Lett.* **2014**, *5*, 1355−1360.

(11) Wilde, A. P.; King, K. A.; Watts, R. J. Resolution and analysis of the components in dual emission of mixed-chelate/ortho-metalate complexes of iridium(III). *J. Phys. Chem.* **1991**, *95*, 629−634.

(12) Savin, A. On degeneracy, near-degeneracy and density functional theory. *Theor. Comput. Chem.* **1996**, *4*, 327−357.

(13) Baer, R.; Neuhauser, D. Density Functional Theory with Correct Long-Range Asymptotic Behavior. *Phys. Rev. Lett.* **2005**, *94*, 043002.

(14) Gill, P. M. W.; Adamson, R. D.; Pople, J. A. Coulomb-attenuated exchange energy density functionals. *Mol. Phys.* **1996**, *88*, 1005−1009.

(15) Iikura, H.; Tsuneda, T.; Yanai, T.; Hirao, K. A long-range correction scheme for generalized-gradient-approximation exchange functionals. *J. Chem. Phys.* **2001**, *115*, 3540−3544.

(16) Levy, M.; Perdew, J. P.; Sahni, V. Exact differential equation for the density and ionization energy of a many-particle system. *Phys. Rev. A: At., Mol., Opt. Phys.* **1984**, *30*, 2745−2748.

(17) Stein, T.; Kronik, L.; Baer, R. Prediction of charge-transfer excitations in coumarin-based dyes using a range-separated functional tuned from first principles. *J. Am. Chem. Soc.* **2009**, *131*, 2818.

(18) Autschbach, J. Charge-transfer excitations and time-dependent density functional theory: Problems and some proposed solutions. *ChemPhysChem* **2009**, *10*, 1757−1760.

(19) Baer, R.; Livshits, E.; Salzner, U. Tuned Range-Separated Hybrids in Density Functional Theory. *Annu. Rev. Phys. Chem.* **2010**, *61*, 85−109.

(20) Kronik, L.; Stein, T.; Refaely-Abramson, S.; Baer, R. Excitation Gaps of Finite-Sized Systems from Optimally Tuned Range-Separated Hybrid Functionals. *J. Chem. Theory Comput.* **2012**, *8*, 1515−1531.

(21) Zheng, Z.; Phillips, H.; Geva, E.; Dunietz, B. D. Ab Initio Study of the Emissive Charge-Transfer States of Solvated Chromophore-Functionalized Silsesquioxanes. *J. Am. Chem. Soc.* **2012**, *134*, 6944−6947.

(22) Zheng, Z.; Geva, E.; Dunietz, B. D. Solvated Charge Transfer States of Functionalized Anthracene and Tetracyanoethylene Dimers: A Computational Study Based on a Range Separated Hybrid Functional and Charge Constrained Self-Consistent Field with Switching Gaussian Polarized Continuum Models. *J. Chem. Theory Comput.* **2013**, *9*, 1125.

(23) Phillips, H.; Zheng, Z.; Geva, E.; Dunietz, B. D. Orbital gap predictions for rational design of organic photovoltaic materials. *Org. Electron.* **2014**, *15*, 1509.

(24) Karolewski, A.; Stein, T.; Baer, R.; Kümmel, S. Communication: Tailoring the optical gap in light-harvesting molecules. *J. Chem. Phys.* **2011**, *134*, 151101.

(25) Bokarev, S. I.; Bokareva, O. S.; Kühn, O. A theoretical perspective on charge transfer in photocatalysis. The example of Ir-based systems. *Coord. Chem. Rev.* **2015**, *304−305*, 133−145.

(26) De Queiroz, T. B.; Kümmel, S. Tuned range separated hybrid functionals for solvated low bandgap oligomers. *J. Chem. Phys.* **2015**, *143*, 034101.

(27) Kümmel, S. Charge-Transfer Excitations: A Challenge for Time-Dependent Density Functional Theory That Has Been Met. *Adv. Energy Mater.* **2017**, *7*, 1700440.

(28) Férey, G.; Mellot-Draznieks, C.; Serre, C.; Millange, F.; Dutour, J.; Surblé, S.; Margiolaki, I. A Chromium Terephthalate-Based Solid with Unusually Large Pore Volumes and Surface Area. *Science* **2005**, *309*, 2040−2042.

(29) Vimont, A.; Goupil, J. M.; Lavalley, J. C.; Daturi, M.; Surblé, S.; Serre, C.; Millange, F.; Férey, G.; Audebrand, N. Investigation of acid sites in a zeotypic giant pores chromium(III) carboxylate. *J. Am. Chem. Soc.* **2006**, *128*, 3218−3227.

(30) Vimont, A.; Leclerc, H.; Maugé, F.; Daturi, M.; Lavalley, J. C.; Surblé, S.; Serre, C.; Férey, G. Creation of controlled Brønsted acidity on a zeotypic mesoporous chromium(III) carboxylate by grafting water and alcohol molecules. *J. Phys. Chem. C* **2007**, *111*, 383−388.

(31) Wickenheisser, M.; Jeremias, F.; Henninger, S. K.; Janiak, C. Grafting of hydrophilic ethylene glycols or ethylenediamine on coordinatively unsaturated metal sites in MIL-100(Cr) for improved water adsorption characteristics. *Inorg. Chim. Acta* **2013**, *407*, 145−152.

(32) Saha, B. B.; El-Sharkawy, I. I.; Miyazaki, T.; Koyama, S.; Henninger, S. K.; Herbst, A.; Janiak, C. Ethanol adsorption onto metal organic framework: Theory and experiments. *Energy* **2015**, *79*, 363−370.

(33) Condie, A. G.; Gonzalez-Gomez, J. C.; Stephenson, C. R. J. Visible-light photoredox catalysis: Aza-Henry reactions via C-H functionalization. *J. Am. Chem. Soc.* **2010**, *132*, 1464−1465.

(34) Wittmann, T.; Mondal, A.; Tschense, C. B.; Wittmann, J. J.; Klimm, O.; Siegel, R.; Corzilius, B.; Weber, B.; Kaupp, M.; Senker, J. Probing Interactions of N-Donor Molecules with Open Metal Sites within Paramagnetic Cr-MIL-101: A Solid-State NMR Spectroscopic and Density Functional Theory Study. *J. Am. Chem. Soc.* **2018**, *140*, 2135−2144.

(35) Casida, M. E. Time-Dependent Density Functional Response Theory for Molecules. *Recent Advances in Density Functional Methods* **1995**, *1*, 155−192.

(36) Casida, M. E. Propagator corrections to adiabatic time-dependent density-functional theory linear response theory. *J. Chem. Phys.* **2005**, *122*, 054111.

(37) Hermannsdörfer, J.; Friedrich, M.; Miyajima, N.; Albuquerque, R. Q.; Kümmel, S.; Kempe, R. Ni/Pd@MIL-101: Synergistic Catalysis with Cavity-Conform Ni/Pd Nanoparticles. *Angew. Chem., Int. Ed.* **2012**, *51*, 11473−11477.

(38) Nava, P.; Sierka, M.; Ahlrichs, R. Density functional study of palladium clusters. *Phys. Chem. Chem. Phys.* **2003**, *5*, 3372−3381.

(39) Aprà, E.; Fortunelli, A. Density-functional calculations on platinum nanoclusters: Pt_{13}, Pt_{38}, and Pt_{55}. *J. Phys. Chem. A* **2003**, *107*, 2934−2942.

(40) Wang, L.-L.; Johnson, D. D. Density functional study of structural trends for late-transition-metal 13-atom clusters. *Phys. Rev. B: Condens. Matter Mater. Phys.* **2007**, *75*, 235405.

(41) Piotrowski, M. J.; Piquini, P.; Da Silva, J. L. F. Density functional theory investigation of 3d, 4d, and 5d 13-atom metal clusters. *Phys. Rev. B: Condens. Matter Mater. Phys.* **2010**, *81*, 155446.

(42) Köster, A. M.; Calaminici, P.; Orgaz, E.; Roy, D. R.; Reveles, J. U.; Khanna, S. N. On the ground state of Pd_{13}. *J. Am. Chem. Soc.* **2011**, *133*, 12192−12196.

(43) Chaves, A. S.; Rondina, G. G.; Piotrowski, M. J.; Tereshchuk, P.; Da Silva, J. L. The role of charge states in the atomic structure of Cu_n and Pt_n (n = 2−14 atoms) clusters: A DFT investigation. *J. Phys. Chem. A* **2014**, *118*, 10813−10821.

(44) Leppert, L.; Kempe, R.; Kümmel, S. Hydrogen binding energies and electronic structure of Ni-Pd particles: a clue to their special catalytic properties. *Phys. Chem. Chem. Phys.* **2015**, *17*, 26140−26148.

(45) Piotrowski, M. J.; Ungureanu, C. G.; Tereshchuk, P.; Batista, K. E. A.; Chaves, A. S.; Guedes-Sobrinho, D.; Da Silva, J. L. F. Theoretical Study of the Structural, Energetic, and Electronic Properties of 55-Atom Metal Nanoclusters: A DFT Investigation within van der Waals Corrections, Spin-Orbit Coupling, and PBE+U of 42 Metal Systems. *J. Phys. Chem. C* **2016**, *120*, 28844−28856.

(46) Chaves, A. S.; Piotrowski, M. J.; Da Silva, J. L. Evolution of the structural, energetic, and electronic properties of the 3d, 4d, and 5d transition-metal clusters (30 TM_n systems for n = 2−15): A density functional theory investigation. *Phys. Chem. Chem. Phys.* **2017**, *19*, 15484−15502.

(47) Van Den Bossche, M. DFTB-Assisted Global Structure Optimization of 13- and 55-Atom Late Transition Metal Clusters. *J. Phys. Chem. A* **2019**, *123*, 3038−3045.

(48) Nosé, S. A unified formulation of the constant temperature molecular dynamics methods. *J. Chem. Phys.* **1984**, *81*, 511−519.

(49) Hoover, W. G. Canonical dynamics: Equilibrium phase-space distributions. *Phys. Rev. A: At., Mol., Opt. Phys.* **1985**, *31*, 1695−1697.

(50) Schmidt, T.; Kümmel, S. The Influence of One-Electron Self-Interaction on d-Electrons. *Computation* **2016**, *4*, 33.

(51) Tilgner, D.; Klarner, M.; Hammon, S.; Friedrich, M.; Verch, A.; de Jonge, N.; Kümmel, S.; Kempe, R. H2-Generation from Alcohols by the MOF-Based Noble Metal-Free Photocatalyst Ni/CdS/TiO_2@MIL-101. *Aust. J. Chem.* **2019**, *72*, 842−847.

(52) Klarner, M.; Hammon, S.; Feulner, S.; Kümmel, S.; Kador, L.; Kempe, R. Visible Light-driven Dehydrogenation of Benzylamine under Liberation of H_2. *ChemCatChem* **2020**, *12*, 4593−4599.

(53) Perdew, J. P.; Burke, K.; Ernzerhof, M. Generalized Gradient Approximation Made Simple. *Phys. Rev. Lett.* **1996**, *77*, 3865−3868.

(54) Perdew, J. P.; Burke, K.; Ernzerhof, M. Generalized Gradient Approximation Made Simple [Physical Review Letters 77, 3865 (1996)]. *Phys. Rev. Lett.* **1997**, *78*, 1396.

(55) Rohrdanz, M. A.; Herbert, J. M. Simultaneous benchmarking of ground- and excited-state properties with long-range-corrected density functional theory. *J. Chem. Phys.* **2008**, *129*, 034107.

(56) Henderson, T. M.; Janesko, B. G.; Scuseria, G. E. Generalized gradient approximation model exchange holes for range-separated hybrids. *J. Chem. Phys.* **2008**, *128*, 194105.

(57) TURBOMOLE V7.4 2019, a development of University of Karlsruhe and Forschungszentrum Karlsruhe GmbH, 1989−2007, TURBOMOLE GmbH, since 2007; available from http://www.turbomole.org.

(58) Shao, Y.; Gan, Z.; Epifanovsky, E.; Gilbert, A. T.; Wormit, M.; Kussmann, J.; Lange, A. W.; Behn, A.; Deng, J.; Feng, X.; et al. Advances in molecular quantum chemistry contained in the Q-Chem 4 program package. *Mol. Phys.* **2015**, *113*, 184−215.

(59) Schäfer, A.; Horn, H.; Ahlrichs, R. Fully optimized contracted Gaussian basis sets for atoms Li to Kr. *J. Chem. Phys.* **1992**, *97*, 2571−2577.

(60) Grimme, S. Accurate description of van der Waals complexes by density functional theory including empirical corrections. *J. Comput. Chem.* **2004**, *25*, 1463−1473.

(61) Weigend, F.; Ahlrichs, R. Balanced basis sets of split valence, triple zeta valence and quadruple zeta valence quality for H to Rn: Design and assessment of accuracy. *Phys. Chem. Chem. Phys.* **2005**, *7*, 3297−3305.

https://doi.org/10.1021/acs.jpcc.1c05756
J. Phys. Chem. C 2021, 125, 25765−25773

Supporting Information

Combining Metal Nanoparticles with an Ir(III) Photosensitizer

Sebastian Hammon,[†,‡] Mara Klarner,[¶] Gerald Hörner,[§] Birgit Weber,[§] Martin Friedrich,[¶] Jürgen Senker,[||] Rhett Kempe,[*,¶] Thiago Branquinho de Queiroz,[‡] and Stephan Kümmel[*,†]

† Department of Physics, Theoretical Physics IV, University of Bayreuth, Universitätsstraße 30, Bayreuth D-95447, Germany

‡ Centro de Ciencias Naturais e Humanas, Universidade Federal do ABC, Av. dos Estados, Santo André, São Paulo 09210-580, Brazil

¶ Department of Chemistry, Inorganic Chemistry II – Sustainable Chemistry Centre, University of Bayreuth, Universitätsstraße 30, Bayreuth D-95447, Germany

§ Department of Chemistry, Inorganic Chemistry IV, University of Bayreuth, Universitätsstraße 30, Bayreuth D-95447, Germany

|| Department of Chemistry, Inorganic Chemistry III, University of Bayreuth, Universitätsstraße 30, Bayreuth D-95447, Germany

*E-mail: kempe@uni-bayreuth.de; stephan.kuemmel@uni-bayreuth.de

Table of Contents

Synthesis and Hydrogen Evolution

General Methods

All chemicals and solvents were purchased commercially from chemical suppliers with purity over 95 % and used without further purification. All manipulations including air or moisture sensitive compounds were carried out under dry and oxygen-free argon atmosphere (Schlenk techniques) or in a nitrogen-filled glovebox (mBraun 120) with a high-capacity recirculator (below 0.1 ppm of oxygen and water).

Reduction of precursor compounds were carried out with Parr Instrument stainless steel autoclaves N-MT5 300 mL equipped with heating mantles and temperature controller. Solvothermal syntheses were performed in a muffle furnace (Nabertherm) with programmable temperature ramps. Inductively coupled plasma optical emission spectroscopy (ICP-OES) was carried out according to standard protocol digestion (4 mL HNO_3/HCl 3:1, microwave irradiation, 25 min, 195 °C) with a Vista-Pro radial (Varian). Elemental analyses were performed by using an Elementar Vario EL III. NMR spectra were measured using a Bruker Avance III HD 500 MHz spectrometer. Chemical shifts are reported in ppm relative to the deuterated solvent. ^{13}C MAS spectra were acquired on a Bruker Avance III HD spectrometer (9.4 Tesla) using a 1.9 mm triple resonance probe and a spinning speed of 40 kHz or 12.5 kHz. A Hahn-echo pulse sequence with an interpulse distance of 25 µs and 80 µs (one rotor period) was applied for background suppression, respectively. Due to fast spinning hetero-nuclear proton broadband decoupling did not have an influence on the spectral resolution and was thus omitted. The 90° pulse length and recycle delay were set to 2.0 µs and 50 ms, respectively. The average temperature in the rotor at ν_{rot} = 40 kHz was determined to 325 K by referencing with $Pb(NO_3)$. The spin−lattice relaxation times T_1 were obtained with the inversion recovery method with a recycle delay of 0.3 s and time increments ranging from 0.5 to 256 ms. The $^{13}C-^{1}H$ REDOR-type recoupling experiments were performed with two 180° pulses on the ^{1}H channel at the center of each of the two rotation periods (τ_{deph} = 50 µs) while a 180° pulse was applied on the ^{13}C at the center of the two rotation periods. ^{1}H and ^{13}C 180° pulse lengths are 2.8 and 4 µs, respectively. Fourier transform infrared (FT-IR) spectroscopy measurements were performed with a JASCO FT-IR 6100 spectrometer in the range 4000 cm^{-1} to 700 cm^{-1} with a resolution of 4 cm^{-1} an a N_2 flow. Gas mixtures were analyzed using a 6890N gas chromatograph (Agilent Technologies) equipped with an Agilent special Plot + Molsieve capillary column (30.0 m x 0.32 mm x 0.25 µm). Methane was used as internal standard. Nitrogen physisorption isotherms were determined at -196 °C using a Nova 2000e (Quantachrome) apparatus. Specific surface areas were calculated by using p/p_0-values from 0.05-0.3 by the BET model. Specific total pore volumes were determined by DFT calculations (N_2 at -196 °C on silica (cylindric pore, NLDFT equilibrium model)). Transmission electron microscopy (TEM) measurements were carried out using a LEO 922O microscope (Zeiss, 200 kV). The samples were suspended in chloroform and sonicated for 5 min. 2 µL of the suspension were placed on a CF200-Cu-grid or a LC200-Cu-grid (Electron Microscopy Sciences) and allowed to dry. High-angle annular dark-field scanning transmission electron microscopy (HAADF-STEM) measurements were performed using a ARM200F (JEOL, 200 kV) equipped with aspherical aberration corrector (CEOS) and an energy-dispersed X-ray analysis (EDX) system (JEOL). Diffuse reflectance ultraviolet-visible spectra were measured using a CARY 300 (Agilent Technologies) with an Ulbricht sphere in the range 400 nm to 750 nm. UV-vis spectra were measured on a CARY 60 (Agilent Technologies). Fluorescence spectra in the were recorded on a JASCO FP8300 spectrofluorometer with an excitation wavelength of 420 nm. Excitation and emission bandwidth were set to 10 nm, response time to 0.1 s and the scan speed to 200 nm/min. Cyclic voltametric measurements were carried out in solution under moisture and oxygen-free conditions using a three-electrode assembly connected to a potentiostat (Model 263A, EG&G Princeton Applied Research) at a scanning rate of 100 mV s^{-1}. A solution of tetra-*n*-butylammonium hexafluorophosphate in acetonitrile with a concentration of 0.1 M was used as the electrolyte solution. As working electrode, a platinum disk electrode in the respective solution of iridium complex dissolved in acetonitrile was used. A platinum wire in the electrolyte solution and $Ag/AgNO_3$ in acetonitrile (0.1 M) were used as counter and reference electrodes, respectively. Each measurement was calibrated by the internal standard ferrocene/ferrocenium. X-ray crystal structure analysis was performed with a STOE STADIVARI [(λ(Mo-K_α) = 0.71073 Å] equipped with an Oxford Cryostream low temperature unit. Structure solution and refinement were achieved with SIR97[S1], SHELXL-2014[S2] and WinGX.[S3] The structure was visualized using Mercury 4.1.3.[S4] Powder X-ray powder diffraction (PXRD) analysis in the range of 2-80 °2θ was performed using a STOE STADI-P diffractometer (CuKα radiation, 1.54178 Å) in θ-2θ geometry with a position sensitive detector. The samples were sealed in glass capillaries (mark-tubes, Hilgenberg, No. 10, diameter 0.7mm) in inert atmosphere.

Time-resolved photoluminescence studies were carried out with a fluorescence lifetime imaging microscope (FLIM) MicroTime200 (Pico Quant). It is equipped with a picosecond diode laser (405 nm) with adjustable output power (set to 0.5 µW), a dichroic filter 405rdc-UF3 and a longpass filter 561 nm. The optical core is an inverted microscope IX 73 (Olympus) with a confocal unit and a piezo stage for z stacks. The data were recorded with a water immersion objective (60×, NA 1.2.). A single-photon counting APD module (SPAD) is used. Data acquisition is based on time-correlated single photon counting (TCSPC) performed by a TimeHarp 260 Pico board (Pico Quant). Samples are prepared by spin coating thin films of powder material dispersed in a polystyrene (Mw 200k g/mol) matrix on cover slips (Ø 18 mm). 2 mg of the sample are suspended in a degassed polystyrene / toluene solution (300 µL, 200 mg/mL). Spin coating is performed at 1500 rpm for 90 s under inert gas atmosphere.

Material Synthesis

Dimethyl(2,2‘-bipyridine)-4,4‘-dicarboxylate

4,4‘-Dicarboxy-2,2‘-bipyridine (488 mg, 2 mmol) was suspended in methanol (80 mL) and 20 drops of 96 % H_2SO_4 were added. After refluxing for 20 h, the reaction mixture was poured into 100 ml of water and the pH was carefully adjusted to pH 8 using a NaOH solution. Afterwards the mixture was extracted three times with 100 mL DCM and the combined organic layers were dried over $NaSO_4$. The solvent was evaporated to yield a white, crystalline solid.

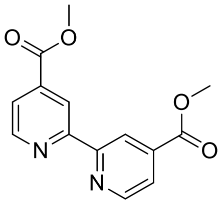

FW ($C_{14}H_{12}N_2O_4$) = 272.26 g mol^{-1}

Yield 467 mg (1.72 mmol, 86%)

^{1}H-NMR ($CDCl_3$, 500 MHz) δ = 8.96 (s, 2H, pyr-3-CH), 8.87 (d, 2H, pyr-6-CH, J = 4.90 Hz), 7.90 (dd, 2H, pyr-5-CH, J = 4.90 Hz), 4.00 (s, 6H, O-CH_3) ppm.

2,2‘-Bipyridine-4,4‘-dimethanol: **L1**

Dimethyl(2,2’-bipyridine)-4,4’-dicarboxylate (467 mg, 1.72 mmol, 1 eq) was dissolved in 2 mL methanol and 50 mL DCM and $NaBH_4$ (519 mg, 13.7 mmol, 8 eq) was added. The reaction was heated to reflux for 20 h. Another portion of $NaBH_4$ (519 mg, 13.7 mmol, 8 eq) was added and the solution was heated to reflux for another 20 h. Afterward, the solvent was removed, and the residue dissolved in 100 mL of water. This solution was extracted three times with 100 mL of ethyl acetate. The combined organic layers were dried over $NaSO_4$ and the solvent removed to obtain the white, crystalline ligand L1.

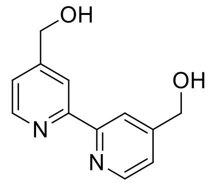

FW ($C_{12}H_{12}N_2O_2$) = 216.24 g mol^{-1}

Yield 263 mg (1.22 mmol, 71%)

^{1}H-NMR (Methanol-d_4, 500 MHz) δ = 8.58 (d, 2H, pyr-6-CH, J = 5.05 Hz), 8.26 (s, 2H, pyr-3-CH), 7.43 (d, 2H, pyr-5-CH, J = 5.05 Hz), 4.74 (s, 4H; CH_2) ppm.

^{13}C-NMR (Methanol-d_4, 125 MHz) δ = 157.34, 154.45, 150.30, 122.82, 120.31, 63.74 ppm.

[(µ-Chloro)(di-2-phenylpyridine)iridium(III)]-dimer

$IrCl_3 \cdot x\ H_2O$ (256 mg, 0.81 mmol, 1 eq) was dissolved in 3 mL H_2O and 18 mL 2-ethoxyethanol and subsequently degassed by bubbling argon through the solution. After addition of 2-phenylpyridine (255 µL, 1.78 mmol, 2.2 eq, ppy) the reaction was heated to reflux for 20 h under inert atmosphere, whereby a yellow solid precipitated. After cooling, the mixture was washed twice with 20 mL diethyl ether. The yellow precipitate was filtrated off and washed another time with diethyl ether. The solid was dried under vacuum.

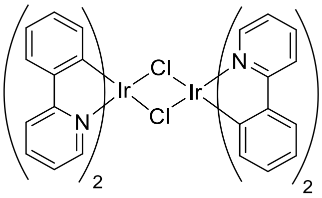

FW ($C_{44}H_{32}Cl_2N_4Ir_2$) = 1072.10 g mol^{-1}

Yield 327 mg (0.43 mmol, 53 %)

^{1}H-NMR ($CDCl_3$, 500 MHz) δ = 9.25 (d, 4H J = 5.82 Hz), 7.88 (d, 4H, J = 8.09 Hz), 7.74 (t, 4H, J = 7.70 Hz), 7.49 (d, 4H, J = 7.72 Hz), 6.76 (q, 8H, J = 7.61 Hz), 6.57 (t, 4H, J = 7.49 Hz), 5.94 (d, 4H, J = 7.72 Hz) ppm.

^{13}C-NMR ($CDCl_3$, 125 MHz) δ = 168.53, 151.67, 145.33, 143.68, 136.13, 130.56, 129.08, 123.63, 122.09, 121.29, 118.36 ppm.

2,2’-Bipyridine-4,4‘-(di-*tert*-butyl)bis(2-phenylpyridine)iridium(III)hexafluorophosphate[S5]: **Ir-L2**

[(μ-Cl)(ppy)$_2$Ir(III)]$_2$ (100 mg, 0.093 mmol, 1 eq) was dissolved in 1mL H_2O and 3 mL 2-ethoxyethanol. 4,4’-*di-tert-butyl*-2,2’-bipyridine (50 mg, 0.186 mmol, 2 eq, dtbbpy) was added and the reaction mixture was refluxed for 20 h. After cooling to room temperature, the solution was poured on an aqueous solution of ammonium hexafluorophosphate (1 g, 6.13 mmol, in 10 mL H_2O). The precipitating solid was filtered off, washed with H_2O, and dried under vacuum, yielding a yellow-orange powder denoted as [(dtbbpy)(ppy)$_2$IrPF$_6$].

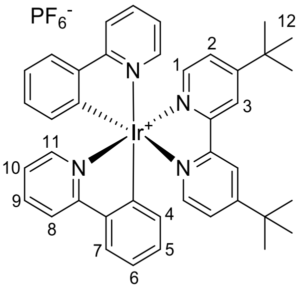

FW ($C_{40}H_{40}F_6IrN_4P$) = 913.95 g mol^{-1}

Yield 146 mg (0.160 mmol, 86 %)

^{1}H-NMR (Methanol-d$_4$, 500 MHz) δ = 8.9 (d, 2H, CH-1, J = 4.83 Hz), 8.28 (dd, 2H, CH-11, J = 8.33, 1.42 Hz), 8.04 (d, 2H, CH-2, J = 4.83 Hz), 7.98 (dt, 2H, CH-10, J = 8.44, 0.7 Hz), 7.92 (dd, 2H, CH-5, J = 8.0, 1.1 Hz), 7.83 (d, 2H, CH-7, J = 4.43 Hz), 7.74 (dd, 2H, CH-2, J = 4.83 Hz), 7.15 (dt, 2H, CH-9, J = 8.44, 0.7 Hz), 7.06 (dt, 2H, CH-4, J = 5.0, 1.4 Hz), 6.99 (dt, 2H, CH-6, J = 8.0, 1.4 Hz), 6.37 (dd, 2H, CH-8, J = 7.7, 1.0 Hz), 1.44 (s, 18H, CH3-12) ppm.

^{13}C-NMR (Methanol-d$_4$, 125 MHz) δ = 168.2, 164.6, 155.9, 150.8, 149.3, 144.3, 139.0, 131.9, 130.5, 125.5, 124.9, 123.7, 122.9, 122.6, 120.0, 35.8, 29.9 ppm.

(2,2’-Bipyridine-4,4’-dimethanol)bis(2-phenylpyridine)iridium(III)hexafluorophosphate: **Ir-L1**

[(μ-Cl)(ppy)$_2$Ir(III)]$_2$ (100 mg, 0.093 mmol, 1 eq) was dissolved in 1mL H_2O and 3 mL 2-ethoxyethanol. 2,2’-Bipyridine-4,4’-diyldimethanol (40.2 mg, 0.186 mmol, 2 eq) was added and the reaction mixture was refluxed for 20 h. After cooling to room temperature, the solution was poured an aqueous solution of ammonium hexafluorophosphate (1 g, 6.13 mmol, in 10 mL H_2O). The precipitating solid Ir-L1 was filtered off, washed with H_2O, and dried under vacuum, yielding a yellow-orange powder. Suitable crystals for single crystal

X-Ray analysis were yielded by vapor phase diffusion technique, using acetone and ether as solvents.

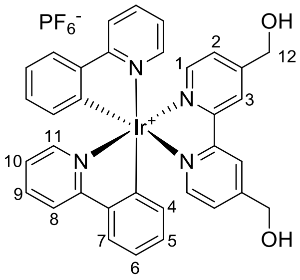

FW ($C_{34}H_{28}F_6IrN_4O_2P$ + C_3H_6O) = 861.81 g mol^{-1} (+ 58.08 g mol^{-1})

Elemental analysis C 48.31, H 3.73 N 6.09; found: C 48.20, H 3.61, N 6.06 %.

Yield 141 mg (0.164 mmol, 88 %)

^{1}H-NMR (Methanol-d_4, 500 MHz) δ = 8.61 (d, 2H, CH-1, J = 4.83 Hz), 7.82 (dd, 2H, CH-11, J = 8.33, 1.42 Hz), 7.77 (d, 2H, CH-2, J = 4.83 Hz), 7.73 (dt, 2H, CH-10, J = 8.44, 0.7 Hz), 7.67 (dd, 2H, CH-5, J = 8.0, 1.1 Hz), 7.61 (d, 2H, CH-7, J = 4.43 Hz), 7.47 (dd, 2H, CH-2, J = 4.83 Hz), 7.28 (dt, 2H, CH-9, J = 8.44, 0.7 Hz), 6.97 (dt, 2H, CH-4, J = 5.0, 1.4 Hz), 6.85 (dt, 2H, CH-6, J = 8.0, 1.4 Hz), 6.24 (dd, 2H, CH-8, J = 7.7, 1.0 Hz), 4.84 (s, 4H, CH_2-12) ppm.

^{13}C-NMR (Methanol-d_4, 125 MHz) δ = 168.2, 164.6, 155.9, 150.8, 149.3, 144.3, 139.0, 131.9, 130.5, 125.5, 124.9, 123.7, 122.9, 122.6, 120.0, 65.9 ppm.

Crystallographic Data

of (2,2'-Bipyridine-4,4'-dimethanol)bis(2-phenylpyridine)iridium(III)hexafluorophosphate

Crystals suitable for X-ray analysis were grown from a saturated solution of the compound in acetone.

Deposition Number: 2083161

Compound	Ir-L1 (t632apma)
Formula	$C_{34}H_{28}F_6IrN_4O_2P$ + C_3H_6O
Formula weight	919.85
Crystal system	triclinic
Space group	P-1
a / Å	9.5070(4)
b / Å	14.0350(6)
c / Å	14.2210(6)
α / °	67.234(3)
β / °	82.061(3)
γ / °	89.857(3)
Cell volume / Å^3	1730.22(13)
Z	2
Crystal size / mm^3	0.18*0.17*0.14
Habit	block
Color	yellow
Density / gcm^{-1}	1.766
T / K	133
Theta range	1.57-26.665
Unique reflections	6935
Observed reflections [I>2s(I)]	6071
Parameters	474
wR2 all data	0.0639
R [I>2s(I)]	0.0264

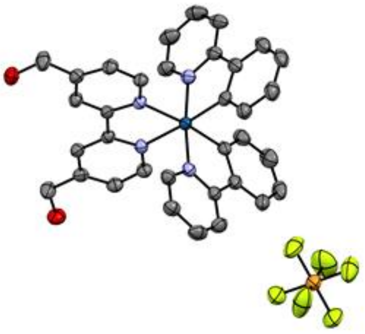

Synthesis of MIL-101

Chromium(III)nitrate nonahydrate (800 mg, 2 mmol) and terephthalic acid (332 mg, 2 mmol) were dissolved in a 0.05 M tetramethylammonium hydroxide solution (10 mL). The mixture was sealed in a 23 mL containing, Teflon-lined hydrothermal autoclave. The autoclave was heated to 180 °C (heating rate: 2.6 °C min^{-1}), the temperature was kept for 24 h and slowly cooled down to 30 °C within 12 hours (cooling rate: 0.2 °C min^{-1}). Excessively crystallized terephthalic acid was removed by filtration over a pore 3 filter. The green slurry was again filtered using a fine pore paper filter. MIL-101 was dried under vacuum (10^{-4} mbar, 85 °C, 24 h).

Generation of coordinatively unsaturated sites in MIL-101 (CUS@MIL-101)[S6]

400 mg of MIL-101 were stirred at 150 °C and dynamic vacuum (10^{-4} mbar) for 12 hours. The resulting material denoted as CUS@MIL-101 was handled under exclusion of water and oxygen.

Grafting of (2,2‘-Bipyridine)-4,4‘-diyldimethanol: L1@MIL-101

2,2‘-Bipyridine-4,4‘-dimethanol (21.6 mg, 0.1 mmol) was dissolved in 8 mL of dry methyl *tert*-butyl ether. This solution was added to CUS@MIL-101 (400 mg) under inert atmosphere and stirred at reflux for 20 h. The solid was filtered off, washed with methyl *tert*-butyl ether, and dried under vacuum. The material is denoted as L1@MIL-101.

Synthesis of [Ir-L1]@MIL-101

L1@MIL-101 (400 mg) was suspended in 8 mL 1,2-dichloroethane and $[(\mu\text{-Cl})(ppy)_2Ir(III)]_2$ (53.6 mg, 0.05 mmol) was added. The suspension was heated to reflux temperature and stirred for 48 h. The resulting [Ir-L1-Cl]@MIL-101 was filtered off using a small-pore paper filter and dried under vacuum. The material was added to a solution of ammonium hexafluorophosphate (1 g, 6.13 mmol, in 10 mL H_2O) and stirred for 10 minutes at room temperature. The solid [Ir-L1-PF_6]@MIL-101 (abbreviated as [Ir-L1]@MIL-101) was filtered off using a small-pored paper filter and dried in vacuum.

Synthesis of Ni/[Ir-L1]@MIL-101[S7]

100 mg dry [Ir-L1]@MIL-101 were placed in a two-chamber-tube with $[Ni(Cp)_2]$ bis(cyclopentadienyl)nickel(II) (16.6 mg, 0.088 mmol, 5 wt.%) separated by a glass frit. The gas phase infiltration of the Ni precursor occurred at room temperature (25 °C) in static vacuum (10^{-4} mbar) for 20 h. The reduction of the Ni precursor was performed under

hydrogen atmosphere (10 bar H_2) at 90 °C for 20 h in a Parr Instruments steel autoclave. The resulting Ni/[Ir-L1]@MIL-101 was evacuated (10^{-4} mbar, 85 °C, 20 h) to remove former metal ligand residue.

Synthesis of Pd/[Ir-L1]@MIL-101[S7]

100 mg dry [Ir-L1]@MIL-101 were placed in a two-chamber-tube with [(Cp)Pd(allyl)] allyl(cyclopentadienyl)palladium(II) (10.2 mg, 0.048 mmol, 5 wt.%) separated by a glass frit. The gas phase infiltration of the Pd precursor occurred at 32 °C in dynamic vacuum (10^{-4} mbar) for 24 h. The reduction of the Pd precursor was performed at 70 bar H_2 and 70 °C for 24 h. The resulting Pd/[Ir-L1]@MIL-101 was evacuated (10^{-4} mbar, 85 °C, 20 h) to remove former metal ligand residue.

Synthesis of Pt/[Ir-L1]@MIL-101[S8]

100 mg dry [Ir-L1]@MIL-101 were placed in a two-chamber-tube with [$(Me)_3$Pt(Cp')] trimethyl(methylcyclopentadienyl)platinum(IV) (8.2 mg, 0.026 mmol, 5 wt.%) separated by a glass frit. The gas phase infiltration of the Pt precursor occurred at 37 °C in static vacuum (10^{-4} mbar) for 20 h. The reduction of the Pt precursor was performed at 50 bar H_2 and 80 °C for 24 h. The resulting Pt/[Ir-L1]@MIL-101 was evacuated (10^{-4} mbar, 85 °C, 20 h) to remove former metal ligand residue.

General Procedure for Photocatalytic Experiments

In a typical experiment, M/[Ir-L1]@MIL-101 (x mg, 2 μmol Ir, ideally 5 wt.% Ir) catalyst was placed in a 10 mL Schlenk tube and sealed with a rubber septum and flushed with argon after evacuation. Then, degassed THF (1000 μL), degassed H_2O (100 μL, 5.55 mmol) and triethylamine (100 μL, 0.72 mmol) were added to the vial. To analyze the reaction headspace by gas chromatography, methane (500 μL) was injected as internal standard. The Schlenk tube was illuminated by a 50 W blue LED (470 nm, distance 2 cm, ~15000 lx). The reaction temperature was regulated by fans to 27 °C. The amount of H_2 evolved was determined by analyzing 500 μL of the reaction headspace by GC-TDC.

Recyclability of the embedded photosensitizer [Ir-L1]@MIL-101

Reaction conditions

N-phenyl-1,2,3,4-tetrahydroisoquinoline + nitromethane
2 mol% [Ir-L1]@MIL-101
0.025 mmol (5.2 mg) N-Phenyl-1,2,3,4-Tetryhydroisoquinolin
18.6 mmol (1 ml) CH_3NO_2

in 10 ml Schlenk tube + O_2 balloon
50 W blue LED (470 nm) at room temperature for 30 min

Yield: reaction mixture was centrifugated (7000 rpm, 7 min)
nitromethane was removed from solution in vacuum,
50 µl MeCN were added
residue was dissolved in $CDCl_3$
turnover was determined by ^1H NMR

Recyclability: catalyst was washed with nitromethane twice and once with dry THF
solvents were removed in vacuum

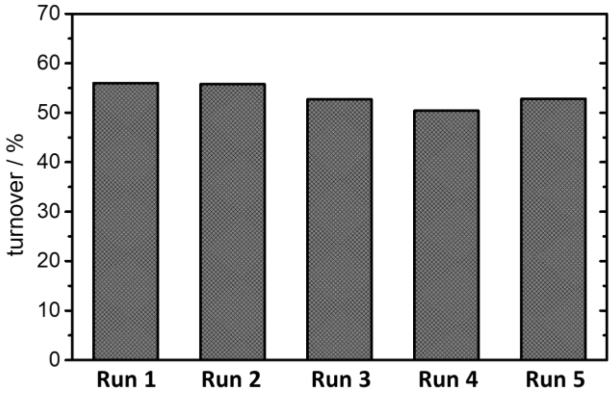

Figure S1. Recyclability demonstration for the [Ir-L1]@MIL-101 system.

Computational Details

DFT calculations were performed using ORCA2.9.1.[S9] Large TZVP basis sets were used throughout.[S10] A truncated trinuclear chromium(III) cluster was chosen as a model of the extended structure of MIL-101; ligand L1 was added to hemi- and fully hydrated SBU^{DFT}, to receive optimized hybrids L1@SBU^{DFT} and L1@ SBU^{DFT} (hyd.). The structures of the (ligand modified) chromium(III) clusters were optimized with the generalized gradient approximation functional BP86[S11]; numerical frequency calculations were performed in order to extract the IR spectra of the received minima and to prove the optimized structures to be stationary points; it is noted that an (apparent) imaginary mode was detected at very low frequency in SBU^{DFT}, owing to a skeleton torsion. Dispersion contributions were approximated using Grimme’s DFT-D3 atom pairwise dispersion corrections of the parent BP86 functional.[S12] Solvent effects were accounted for in a dielectric continuum approach (COSMO), parametrized for MeCN.[S13] The dielectric solvent cage was included, in order to suppress artificial bond contraction due to uncompensated Coulomb attraction between anions and cations.

Material Characterization

Complex Characterization of Ir-L1

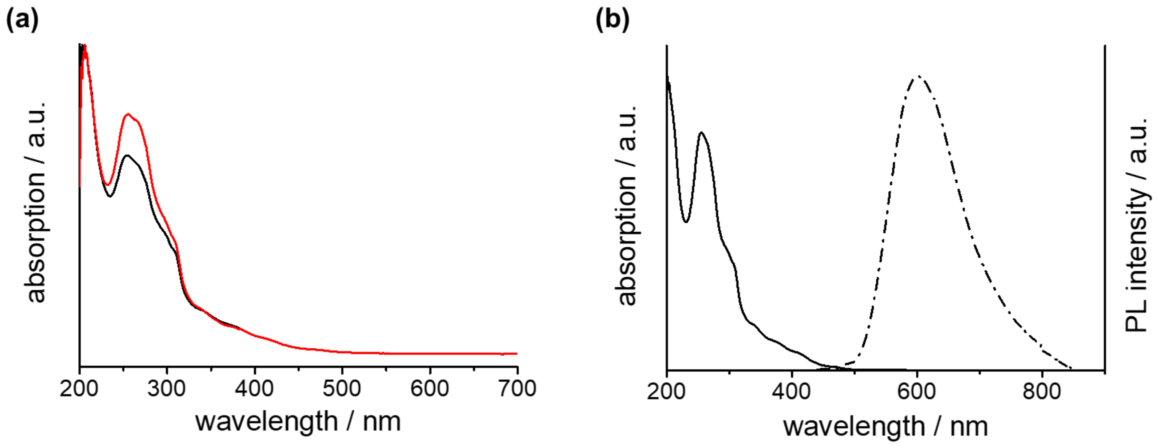

Figure S2. (a) UV-vis absorption spectra of Ir-L1 (black) compared to Ir-L2 (red) in the range of 200-700 nm. (b) Absorption and photoluminescence emission (excitation 420 nm) of Ir-L1.

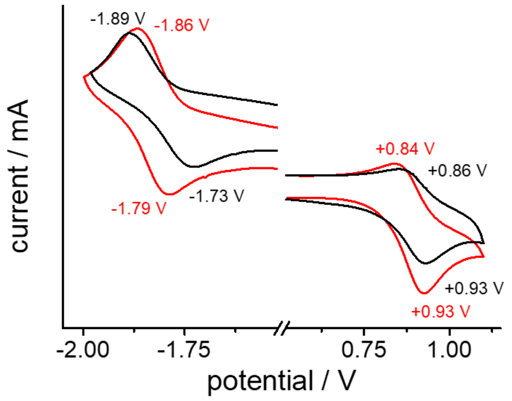

Figure S3. Cyclic voltammogram of Ir-L1 (black) compared to Ir-L2 (red).

Catalyst Characterization of M/Ir-L1@MIL-101

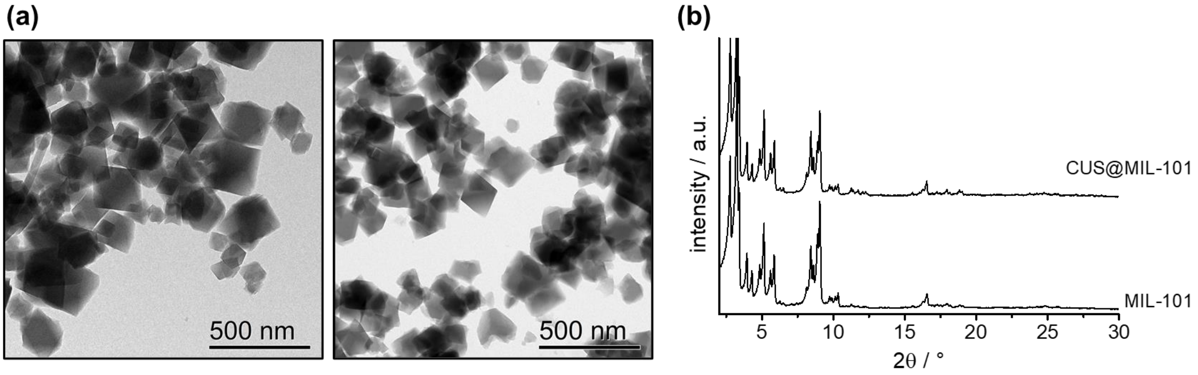

Figure S4. (a) TEM images of as-synthesized MIL-101 (left) and after the successful generation of CUS@MIL-101 at 150 °C in vacuum for 12 hours, showing the same morphology. (b) Powder XRD patterns of MIL-101 and CUS@MIL-101. No changes in crystallinity due to generation of CUS were observed.

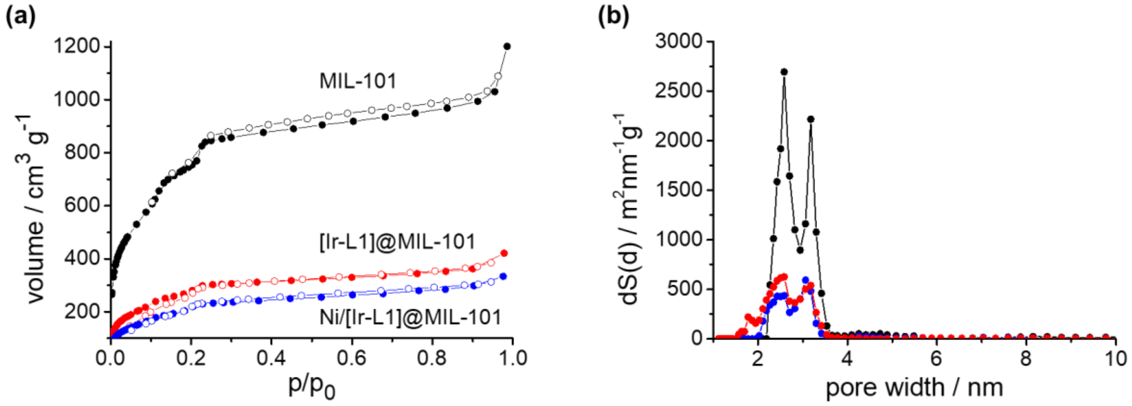

Figure S5. (a) N_2-physisorption isotherms of MIL-101 (2750 m^2/g), [Ir-L1]@MIL-101 (1000 m^2/g) and Ni/[Ir-L1]@MIL-101 (750 m^2/g) with respective surface areas determined by BET-model (0.05-0.3 p/p_0). Adsorption is depicted in filled dots, desorption in rings. (b) Pore size distribution of MIL-101 compared to [Ir-L1]@MIL-101 and Ni/[Ir-L1]@MIL-101.

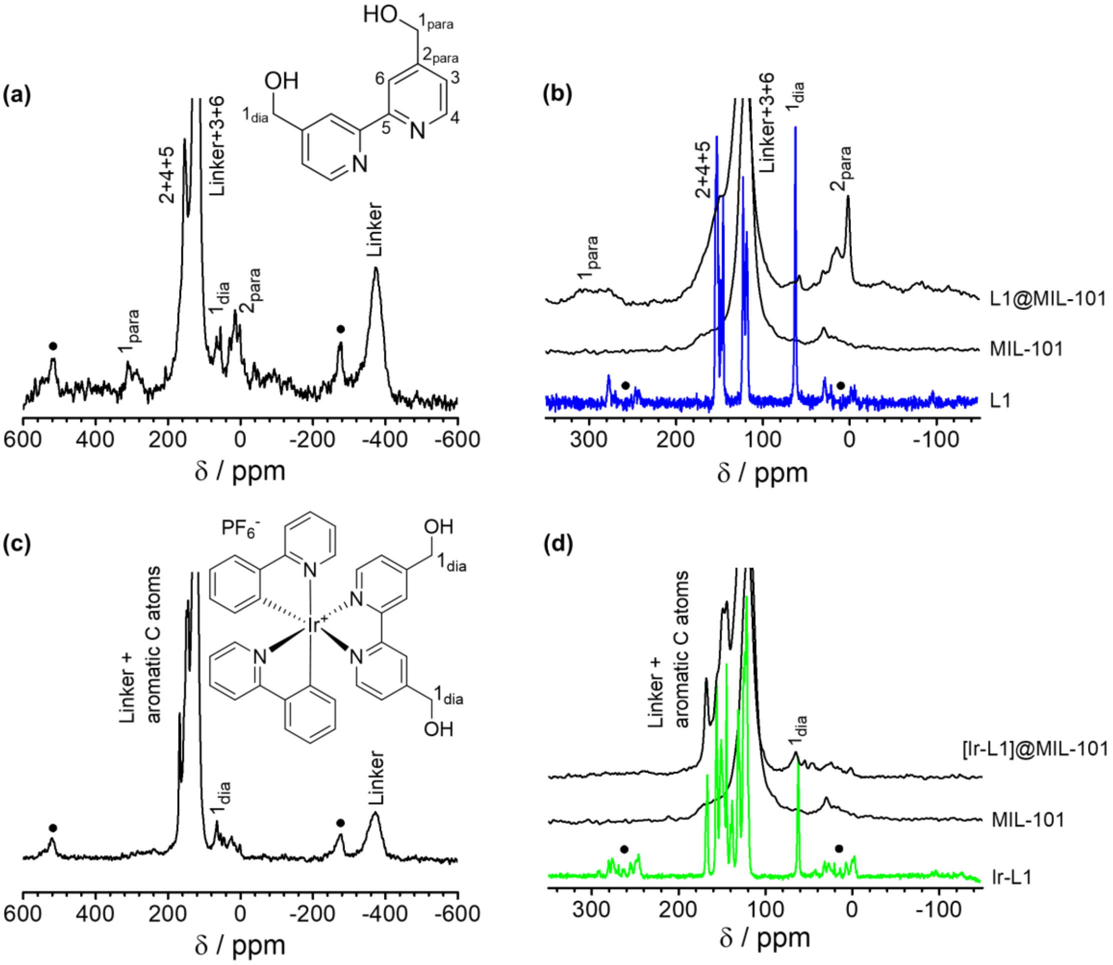

Figure S6. ^{13}C MAS NMR spectra monitoring the L1 grafting and the Ir-L1 complex formation including assignments; spinning side bands are marked with a dot (12.5 kHz or 40 kHz); signals assigned to the terephthalic acid of MIL-101 are marked as linker: (a) L1@MIL-101 and (b) L1, MIL-101 and L1@MIL-101 for comparison. (c) [Ir-L1]@MIL-101 and (d) Ir-L1, MIL-101 and Ir-L1@MIL-101 for comparison.

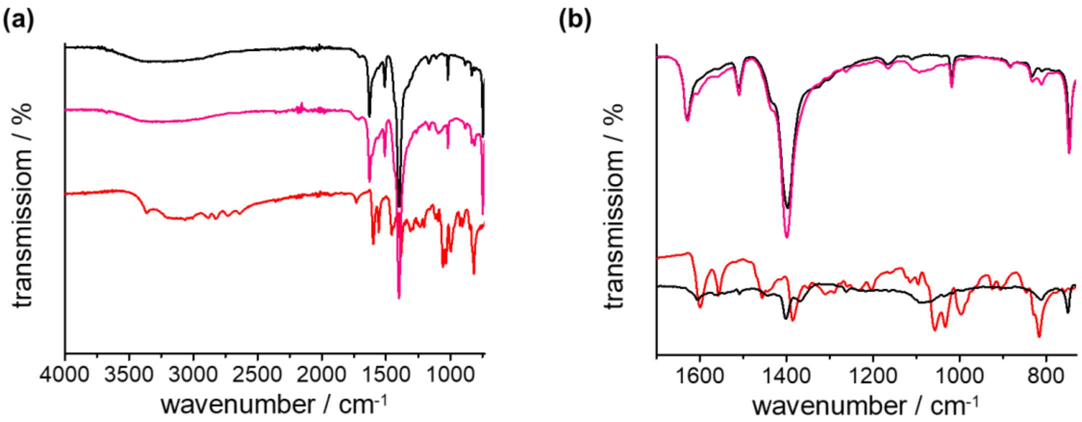

Figure S7. (a) FT-IR spectra of MIL-101 (black), L1@MIL-101 (pink) and L1 (red) in the range of 4000 cm^{-1} to 730 cm^{-1}. (b) In the range of 1700 to 730 cm^{-1}, an overlay of and L1@MIL-101 and MIL-101 is made. In comparison, the difference spectrum (black) of those and the L1 ligand are shown.

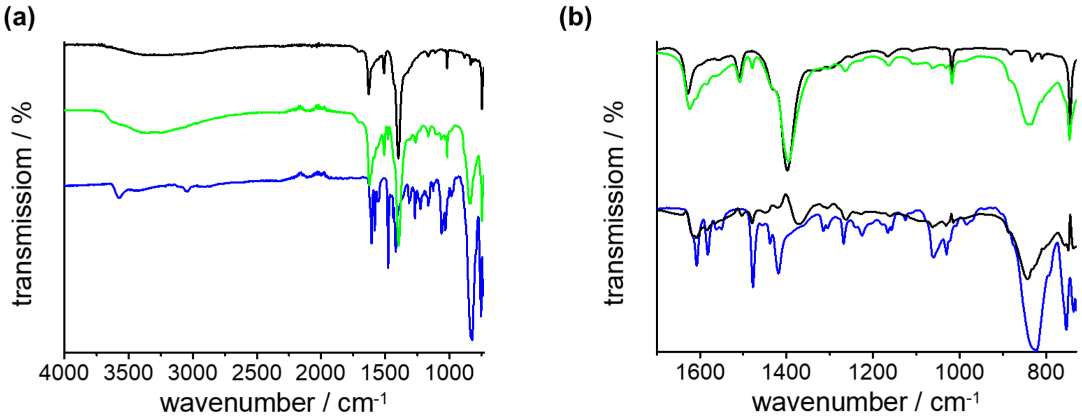

Figure S8. (a) FT-IR spectra of MIL-101 (black), [Ir-L1]@MIL-101 (green) and Ir-L1 (blue) in the range of 4000 to 730 cm^{-1}. (b) In the range of 1700 to 730 cm^{-1}, an overlay of and [Ir-L1]@MIL-101 and MIL-101 is made. In comparison, the difference spectrum of those (black) and the Ir-L1 complex are shown.

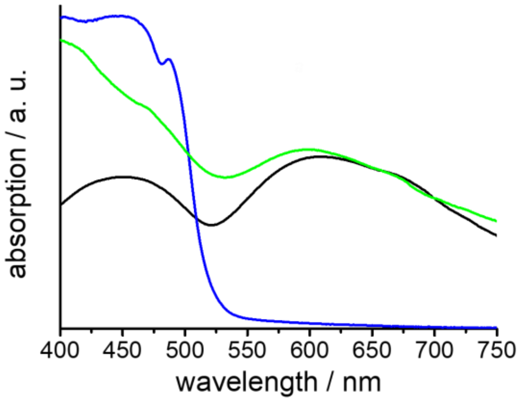

Figure S9. Diffuse reflectance spectra of MIL-101 (black), Ir-L1 (blue) and [Ir-L1]@MIL-101 (green) in the range of 400-750 nm.

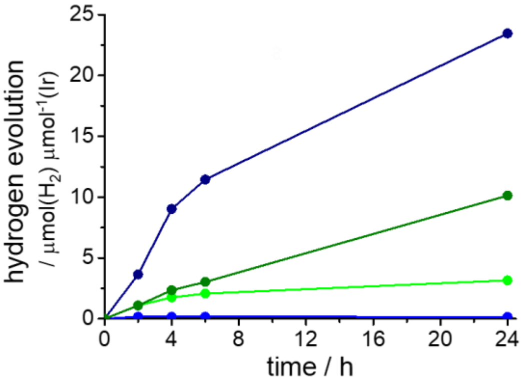

Figure S10. Hydrogen evolution over time; molecular hydrogen was detected by GC-TDC with methane as internal standard: H_2 evolution for [Ir-L1]@MIL-101 (green), Ni/[I-L1r]@MIL-101 (dark blue), Pd/[Ir-L1]@MIL-101 (blue) and Pt/[Ir-L1]@MIL-101 (dark green) over 24 h.

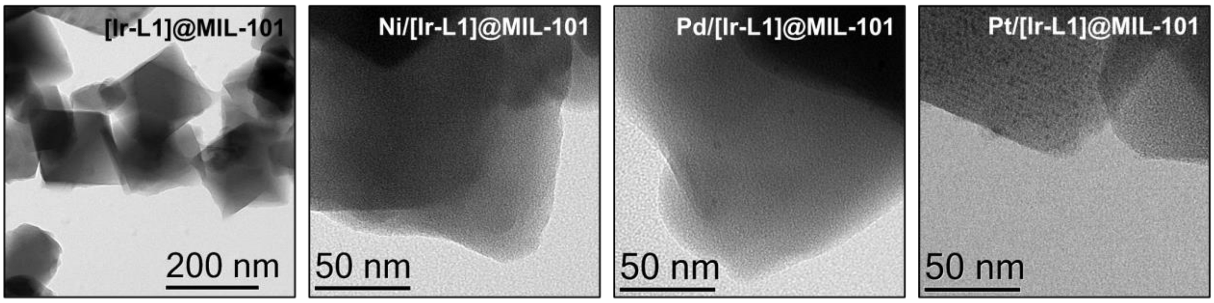

Figure S11. TEM images of [Ir-L1]@MIL-101, Ni/[Ir-L1]@MIL-101, Pd/[Ir-L1]@MIL-101 and Pt/[Ir-L1]@MIL-101.

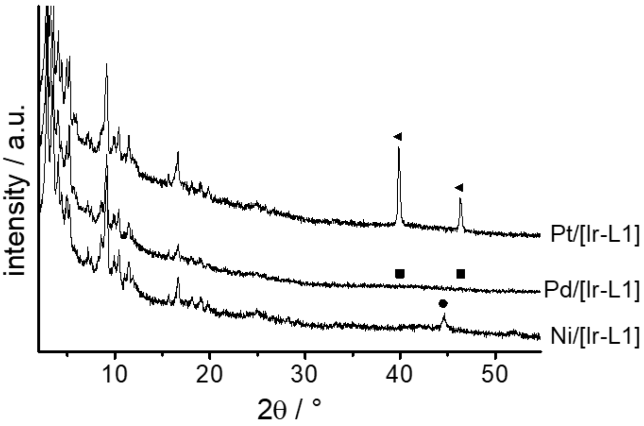

Figure S12. Powder XRD of Ni/[Ir-L1]@MIL-101, Pd/[Ir-L1]@MIL-101 and Pt/[Ir-1]@MIL-101 for comparison. Highlighted reflexes for cubic Ni(0) (circle), cubic Pd(0) (square), cubic Pt(0) triangle.

Table S1. ICP-OES analysis of [Ir-L1]@MIL-101 and M/[Ir-L1]@MIL-101 (M=Ni, Pd, Pt) with contents given in wt.%.

Compound	**Ir**	**Ni**	**Pd**	**Pt**
[**Ir**-L1]@MIL-101	5.83	-	-	-
Ni/[**Ir**-L1]@MIL-101	4.59	5.09		
Pd/[**Ir**-L1]@MIL-101	5.05	-	5.11	-
Pt/[**Ir**-L1]@MIL-101	4.81	-	-	6.30

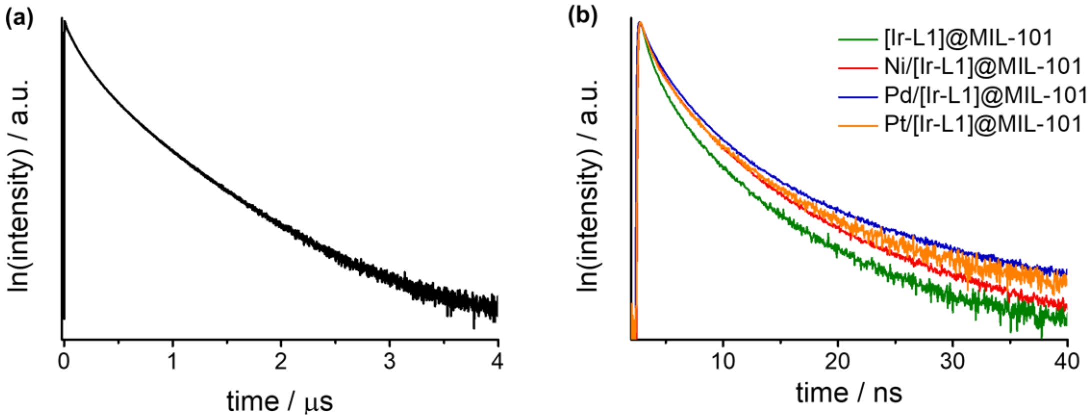

Figure S13. TRPL studies of (a) Ir-L1 and (b) MIL-101 supported catalysts [Ir-L1]@MIL-101, Ni/[Ir-L1]@MIL-101, Pd/[Ir-L1]@MIL-101 and Pt/[Ir-L1]@MIL-101 at excitation wavelength 405 nm. Normalized TCSPC traces are in semi-log representation.

Table S2. Lifetime determination by fitting the TCSPC traces of excited Ir-L1 in TRPL studies. Curves were fitted with a 4-fold exponential decay function. The IRF has not been taken into account in the data analysis.

Compound	**Fluorescence lifetime / ns**	**Amplitude / a. u.**
Ir-L1	121	107
	297	63
	42	23
	569	10
[Ir-L1]@MIL-101	1.70	11
	0.56	8.5
	4.70	4.1
	16.00	0.22
Ni/[Ir-L1]@MIL-101	2.59	40
	0.83	28
	7.00	8.3
	29.00	0.44
Pd/[Ir-1]@MIL-101	2.81	39
	1.00	28
	8.30	7.3
	34.00	0.68
Pt/[Ir-1]@MIL-101	2.10	5.7
	0.66	3.2
	5.80	2.0
	23.00	0.12

Additional Figures, Tables and IR spectra of L1@SBU^{DFT} from DFT

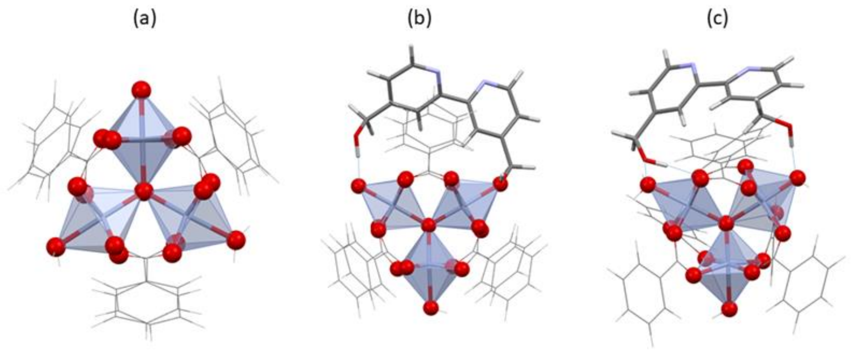

SBU^{DFT} **L1@SBU^{DFT}** hydrated **L1@SBU^{DFT}**

Figure S14. Optimized structures of (a) the trinuclear truncated MOF model (SBU^{DFT}), (b) the adduct L1@SBU^{DFT} of ligand L1 with mono-dehydrated SBU^{DFT}. Alternative scenarios imply trans-configured donor moieties of L1 that are significantly disfavored on our level of approximation (Δ(*cis-trans*) = 5.5 kJ mol^{-1} = 0.057 eV. (c) The adduct of L1 with the fully hydrated SBUDFT; corner-linked CrO6 octahedra given in blue; hydrogen bonding is highlighted as dashed lines.

Harmonic frequencies computed for the SBU^{DFT} well match the energy and intensity of asymmetric and symmetric CO stretching modes located at ca. 1600 cm^{-1} (198.4 meV) and 1400 cm^{-1} (173.6 meV) in the experimental IR spectra, respectively (cf. Fig. S15)

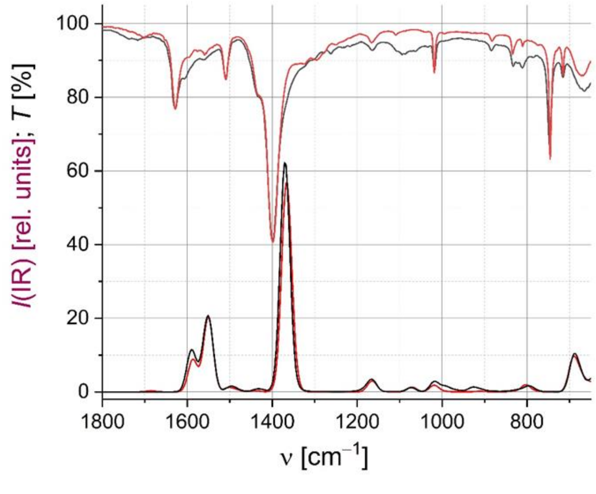

Figure S15. Comparison of experimental and computed IR spectra. (Top; transmission T) Spectra of MIL-101 (top; red) and L1@MIL-101 (top; black). (Bottom; *I*(IR)) Spectra of the model SBU^{DFT} (red) and L1@SBU^{DFT} (black).

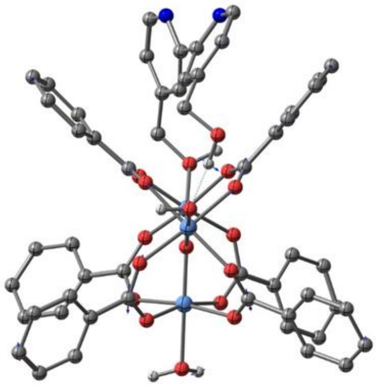

Figure S16. Diagnostic IR mode of the hybrid L1@SBU^{DFT} at *v* = 1557 cm^{-1}; arrows denote direction of prominent displacements (an animation of the mode is available in gif-format as Electronic Supporting Information.)

Evidently in the truncated models, the threefold symmetry of the solid state structure is conserved as are individual bond lengths within the chromium(III) coordination spheres (cf. Table S3).

Table S3. Pertinent metrical data of chromium(III) inner coordination and hydrogen bonding [Å] in DFT optimized structures.[a]

	X-ray [b]	**SBU^{DFT}**	**L1@SBU^{DFT}**	**L1@SBU^{DFT} (hyd)**
Cr(1)-O$_{eq}$	1.971(8)	1.985(15)	1.979(15)	1.992(20)
Cr(1)-O$_{ax}$	2.025	2.152	2.153	2.123
Cr(1)-O$_{cen}$	1.897	1.874	1.876	1.890
Cr(2)-O$_{eq}$	1.978(5)	2.004(5)	1.998(5)	2.002(10)
Cr(2)-O$_{ax}$	2.058	2.053	1.935	1.935
Cr(2)-O$_{cen}$	1.886	1.904	1.976	1.979
Cr(3)-O$_{eq}$	1.965(10)	1.989(15)	1.983(15)	1.988(15)
Cr(3)-O$_{ax}$	2.067	2.147	2.142	2.133
Cr(3)-O$_{cen}$	1.899	1.873	1.878	1.877
Cr(1)-O$_{ax}$H···O(H)-C(1)	--	--	--	1.670
Cr(1)-O$_{eq}$···HO-C(1)	--	--	--	1.837
Cr(2)-O$_{ax}$···HO-C(1')	--	--	1.592	1.638

[a] BP86/TZVP level of theory; [b] crystal data (unpublished)

Analysis of the Electronic Structure and Excitations

In the following we present additional information and details about the calculations that are reported in the section “Analysis of the electronic structure and excitations” of the main paper.

Computational Details

Small transition metal clusters such as M_{13} can prefer spin-polarized electronic ground states[S14,S15,S16,S17,S18]. To find the most stable spin state of a system, we ran a set of density functional (DFT) geometry optimizations (GO) or ground state calculations with a fixed spin magnetic moment m_s of a pertinent interval and evaluated the total energy. The interval for, e.g., M_{13}/[Ir-L1], was chosen according to the preferred magnetic moment of M_{13} stated below in terms of [0, 2, …, $m_s(M_{13})$ + 2] μ_B. All geometry optimizations used the Perdew-Burke-Ernzerhof[S19,S20] (PBE) exchange-correlation functional with van-der-Waals corrections (DFT-D3)[S21] and the def2-TZVP basis set[S22]. The binding energies E_B of M_{13}/[Ir-L1] were computed from the difference of the molecular total energies E_{tot} obtained from ground state DFT calculations (PBE-D3 + def2-TZVP):

$$E_{\mathrm{B}}(M_{13}/[\mathrm{Ir\text{-}L1}]) = E_{\mathrm{tot}}(M_{13}/[\mathrm{Ir\text{-}L1}]) - E_{\mathrm{tot}}(M_{13}) - E_{\mathrm{tot}}(\mathrm{Ir\text{-}L1})\,. \qquad (S1)$$

The def2-ecp effective core potential was used for Pd, Pt and Ir in combination with the def2 basis sets[S22]. The ground state calculations utilized the relaxed PBE-D3 geometries of the respective system. Note that the relaxed structures of M_{13}/[Ir-L1] were obtained according to the procedure given in the main manuscript.

The relaxed structures of Ni_{13}/[Ir-L1] and Pd_{13}/[Ir-L1] showed an icosahedral (ico) structure of the metal clusters (cf. main manuscript, Fig. 5 panel (a) and (b)). PBE(-D3) predicts 8 μ_B for the vacuum structure of both Ni_{13}(ico) and Pd_{13}(ico)[S14,S15,S16,S23]. Furthermore, PBE(-D3) favors 4 μ_B for the structure seen for Pt_{13} (cf. Fig. 5 panel (c)), which is consistent with one that was reported in Ref. S24. For further discussions on structural isomers of M_{13}, we refer to Ref. S14 and references therein. Table S4 lists the spin magnetic moment of the ground state of all systems studied in the section regarding the analysis of the electronic structure and excitations. Reassuringly, PBE and the tuned range-separated hybrid ωPBE (see below) yielded the same spin magnetic moment for each system. This consistency check has special relevance for the Ni systems, since some hybrid exchange-correlation functionals predict a higher spin magnetic moment for Ni_{13}[S23,S25,S26]. For a discussion on the spin magnetic moment of Ni_{13}, see Ref. S25 and S26. A series of concluding comments regarding spin-polarized systems: A spin moment of, e.g., 8 μ_B corresponds to a spin multiplicity $M = 9$ (nonet state), whereas $M = 2S + 1$ and S denotes the spin quantum number. For example, our DFT calculations predict a spin magnetic moment of 8 μ_B for Ni_{13}/[Ir-L1]. Thus, the optical (spin-conserving) excitations are nonet → nonet transitions. The spin-flip excitation to the next lower magnetic moment (6 μ_B) is a nonet → septet transition. To ease the comparison between all spin-conserving and spin-flip excitations (as further explained in the main manuscript), we refer to these uniformly as S_n and T_n, respectively, with n being the n'th excitation.

DFT Born-Oppenheimer molecular dynamics (BOMD) simulations with a Nosé-Hoover thermostat[S27,S28] of M_{13}/[Ir-L1] utilized the PBE exchange-correlation functional in combination with the def2-SVP basis set[S29] (M_{13}=Ni_{13}, Pd_{13}, Pt_{13}). We used a thermostat temperature of 298 K and a time step of 80 a.u. (≈ 1.94 fs). The total simulation time was circa 4 ps and the relaxation time equaled 560 a.u. (≈ 13.55 fs) for Pt_{13}/[Ir-L1] and 400 a.u. (≈ 9.68 fs) for both Pd_{13}/[Ir-L1] and Ni_{13}/[Ir-L1]. For the BOMD simulations of M_{13}/[Ir-L1] we chose a fixed spin magnetic moment of 8 μ_B for the Ni, 4 μ_B for the Pd and 2 μ_B for the Pt system. These choices were based on the spin magnetic moment of the electronic ground state that we determined for preliminary structures of M_{13}/[Ir-L1] by running a set of DFT geometry optimizations, as explained above.

Table S4. Spin magnetic moment m_s of the electronic ground state of different molecular systems obtained from DFT ground state calculations. PBE and ωPBE using the non-empirically optimized range-separation parameter ω_{opt} of each system consistently yield the same m_s. ω_{opt} was obtained according to Eq. S2. The ground state calculations utilized the relaxed PBE-D3 geometries of the respective system.

System	m_s (μ_B)	ω_{opt} (bohr^{-1})
Ir-L1	0	0.16
Ir-L0	0	0.16
Ni_{13}	8	0.18
Pd_{13}	8	0.17
Pt_{13}	4	0.17
Ni_{13}/[Ir-L1]	8	0.14
Pd_{13}/[Ir-L1]	4	0.12
Pt_{13}/[Ir-L1]	2	0.11

Range-separated hybrid exchange-correlation functionals typically split the Coulomb operator ($1/r$) into a short- and long-range term[S30,S31]. This is implemented here by the error function $erf(r\omega)$ in terms of $1/r = [1 - erf(r\omega)]/r + erf\,(r\omega)/r$, with ω being the range-separation parameter[S32,S33]. We employed the version of ωPBE[S34,S35] that uses pure semi-local PBE exchange in the short-range, exact Hartree-Fock exchange only in the long-range and PBE correlation without range-separation. Note that all calculations utilizing ωPBE were carried out in a generalized Kohn-Sham (GKS) framework as implemented by QCHEM[S36]. In this study, the non-empirical tuning process of ωPBE aims to satisfy the DFT version of Koopmans' theorem[S37], since it usually leads to a trustworthy description of photophysical properties (cf. main manuscript, Introduction). The theorem establishes a physical meaning of the highest occupied Kohn-Sham eigenvalue ϵ_{HOMO} in exact ground state DFT, which also holds within GKS[S38]. It rigorously guarantees that $-\epsilon_{\mathrm{HOMO}}(N)$ equals the first vertical ionization energy $IP(N)$ of an N-electron system. $IP(N)$ is defined as the difference between the total energy E_{tot} of the cationic and neutral system (for "frozen" core positions), $IP(N) = E_{\mathrm{tot}}(N-1) - E_{\mathrm{tot}}(N)$. To obey as closely as possible to the latter, we tune the range-separation parameter such that ω_{opt} minimizes $J(\omega)$ of

$$J^2(\omega) = [IP^{\omega}(N) + \epsilon_{\mathrm{HOMO}}(N)]^2 + [IP^{\omega}(N+1) + \epsilon_{\mathrm{HOMO}}(N+1)]^2. \qquad (S2)$$

To this end, we iterate through an interval for ω in discrete steps of 0.01 bohr^{-1} and compute the electronic ground state of the neutral (N), cationic ($N-1$) and anionic ($N+1$) system for each value of the interval within the structure of the neutral system. These yielded ϵ_{HOMO} and the total energies needed to calculate IP^{ω} from the definition above. The ground state calculations of Ir-L0, Ir-L1, M_{13} utilized the def2-TZVP basis set and M_{13}/[Ir-L1] used def2-SVP. Table S4 contains the optimally tuned ω_{opt} of molecular systems studied with ωPBE in the main manuscript.

Excitation spectra and densities were obtained from linear response time-dependent DFT (TDDFT) calculations in the Casida formalism[S39,S40]. For this, we used ωPBE and the LANL2DZ basis set in combination with the LANL2DZ-ecp effective core potential for Ni, Pd, Pt and Ir as provided by QCHEM[S36]. For better visualization, absorption spectra were obtained by convoluting the TDDFT excitation spectra with a Gaussian of width 0.08 eV. Note that we also tested the accuracy of the Tamm-Dancoff approximation[S41] (TDA) by calculating the excitation spectra of M_{13}/[Ir-L1] (within their equilibrium geometry). This test showed that the TDA yields the qualitatively same trend as the full linear-response TDDFT calculation for the excitation spectrum and excitation densities. For this reason, the study on the distance dependency of the interaction between the metal nanoparticles and the Ir photosensitizer was carried out within the TDA. Spin-flip excitations of M_{13}/[Ir-L1] were also obtained within the TDA for technical reasons within QChem.

Each of the M_{13} exhibits a characteristically dense excitation spectrum (cf. Fig. S23). Consequently, it is necessary to calculate several hundred and up to about 1000 excitations only for the VIS excitation spectrum of M_{13} and M_{13}/[Ir-L1], respectively. This in turn means that an increasingly elaborate diagonalization is necessary to obtain the roots of the Casida matrix equations. Note that this can be a more general bottleneck to obtaining UV excitation spectra of systems containing (transition) metal clusters from Casida linear response TDDFT calculations.

All calculations using the range-separated hybrid ωPBE and generalized gradient approximation PBE(-D3) were carried out with the QCHEM[S36] and TURBOMOLE[S42] code, respectively.

Ir-L0 Triplet Photosensitizer

Figure S17 shows the electronic difference density of the lowest triplet excitation T_1 and the ground state of $[Ir(bpy)(ppy)_2]^+$ (named Ir-L0) obtained from TDDFT. For this calculation, the range-separated hybrid exchange-correlation functional ωPBE and the LANL2DZ basis set were used. The red and blue wireframes indicate negative (electron lack) and positive (gain) areas in the difference densities presented in this section, respectively.

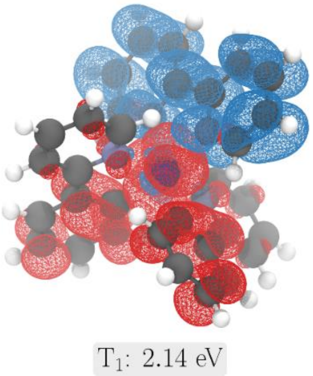

Figure S17. Electronic difference density of T_1 of $[Ir(bpy)(ppy)_2]^+$ (Ir-L0). Obtained from a TDDFT calculation with the non-empirical optimally tuned ωPBE (ω_{opt}(Ir-L0)=0.16 bohr^{-1}). See main text for details.

Density of States of M_{13}/[Ir-L1]

We compared the density of states (DOS) of M_{13}/[Ir-L1] to that of its molecular constituents M_{13} and Ir-L1. The DOS is (approximately) computed from the Kohn-Sham ground state eigenvalues. Figure S18 shows the DOS of M_{13}/[Ir-L1], M_{13} and Ir-L1 obtained from a DFT ground state calculation with ωPBE and LANL2DZ (Ni_{13}/[Ir-L1] panel (a), Pd_{13}/[Ir-L1] panel (b), Pt_{13}/[Ir-L1] panel (c)). For better visualization, the eigenvalue spectrum was convoluted with a Gaussian of width 0.08 eV. Analogous to the comparison of absorption spectra discussed in the main manuscript, we paid attention to two aspects: (i) We calculated the ground state of M_{13} and Ir-L1 (separately) in the fixed structure as they are in M_{13}/[Ir-L1] (cf. main manuscript, Fig. 3). This eliminates effects that would just be due to structural differences. (ii) To eliminate exchange-correlation functional related differences, we used the optimally tuned range-separation parameter, ω_{opt}, of M_{13}/[Ir-L1] also to calculate the DOS of M_{13} and Ir-L1 in (i). Following these considerations, Figure S18 clearly shows that the total spectra differ from the respective individual spectra. In particular, the DOS of M_{13}/[Ir-L1] shows no overlap with that of the respective metal cluster for energies approximately higher than -8 eV. Therefore, the DOS of M_{13}/[Ir-L1] cannot even be explained qualitatively from the superposition of M_{13} and Ir-L1. Reassuringly, calculating the DOS of M_{13}/[Ir-L1] with the generalized gradient approximation PBE consistently yields the same trend as the range-separated hybrid functional ωPBE, as shown exemplarily for Ni_{13}/[Ir-L1] in Fig. S19. Note that consideration (i) was also applied for the calculations with PBE. The confirmation by another class of exchange-correlation functionals shows the robustness of our results.

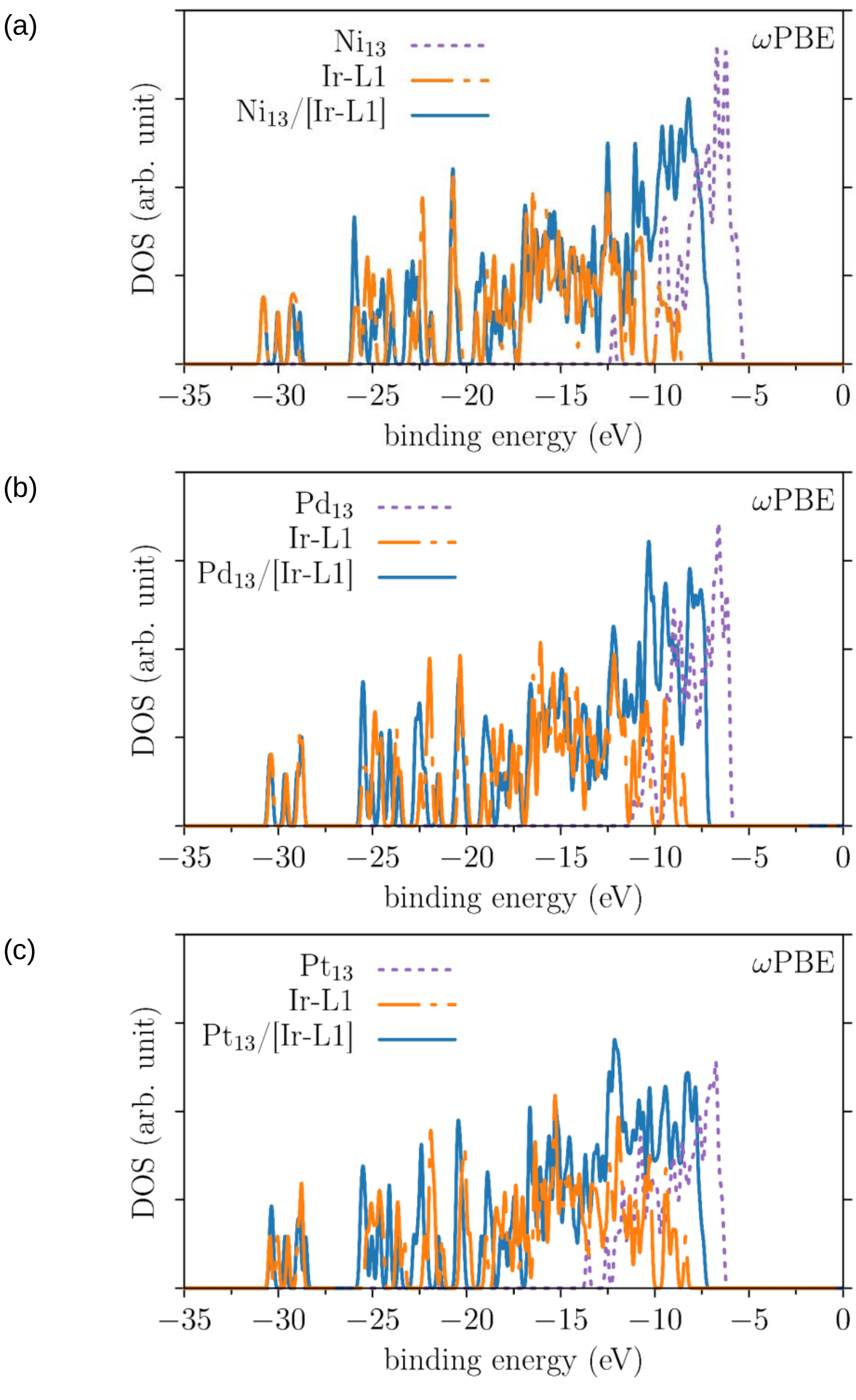

Figure S18. Theoretical density of states of M_{13}/[Ir-L1], M_{13} and Ir-L1 obtained from DFT ground state calculations with the non-empirical optimally tuned ωPBE. (a) Comparison for Ni_{13}/[Ir-L1]. The respective calculations used ω_{opt}=0.14 bohr^{-1}, as explained in the main text. (b) Pd_{13}/[Ir-L1] (ω_{opt}=0.12 bohr^{-1}). (c) Pt_{13}/[Ir-L1] (ω_{opt}=0.11 bohr^{-1}).

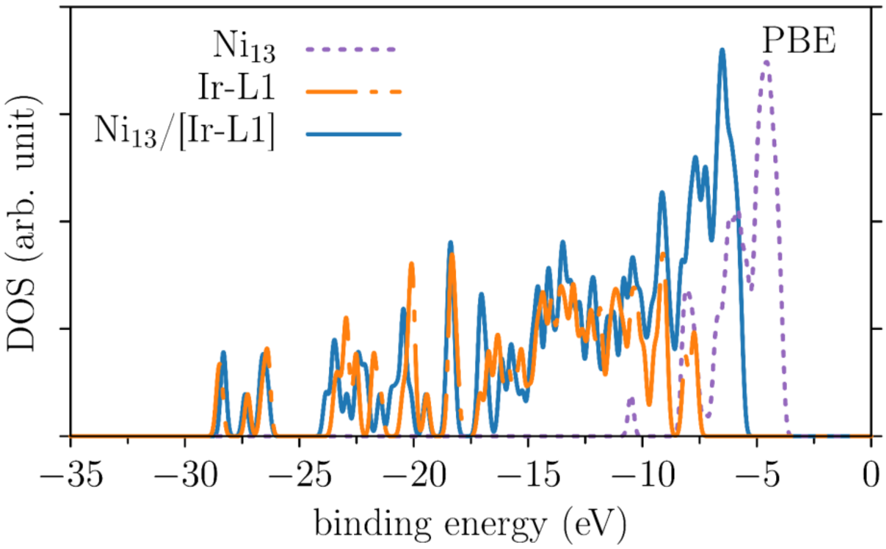

Figure S19. Theoretical density of states of Ni_{13}/[Ir-L1], M_{13} and Ir-L1 obtained from DFT ground state calculations with PBE. See main text for details.

Density of States of Ni_{38}/[Ir-L1]

In order to make sure that these findings are not special only for the 13-atom clusters we also studied a considerably larger system, Ni_{38}, in combination with Ir-L1. To this end we started from a 38-atom cluster geometry from Ref. S23 that corresponds to a cut-out of the bulk structure and optimized it using the PBE functional and the def2-SVP basis set. We then placed the Ir-L1 complex in the vicinity of the metal cluster and optimized the geometry of the combined system. We again observe that the metal cluster and the photosensitizer approach each other during the optimization, i.e., the way in which the geometries evolve already suggests that there is an interaction. Fig. S20 shows the final lowest energy geometry.

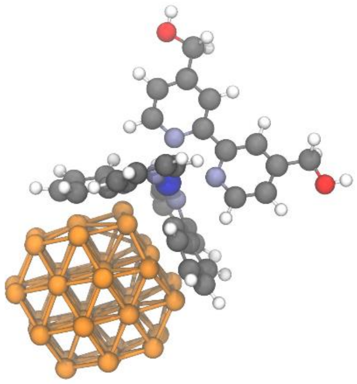

Figure S20. Optimized geometry of Ni_{38}/[Ir-L1]. See main text for details.

We then analyzed the Kohn-Sham DOS in the same way as for Ni_{13}/[Ir-L1], i.e., we compare the DOS of the combined system with the DOS of the subsystems. The results are depicted in Fig. S21. For the sake of clarity, we also show the sum of the two independently calculated

DOS (line labeled Ir-L1 + Ni_{38}). The figure shows that the DOS of the combined system differs markedly from the sum of the two independent DOS. This clearly confirms that also for the larger metal particle there is a pronounced interaction between the photosensitizer and the metal.

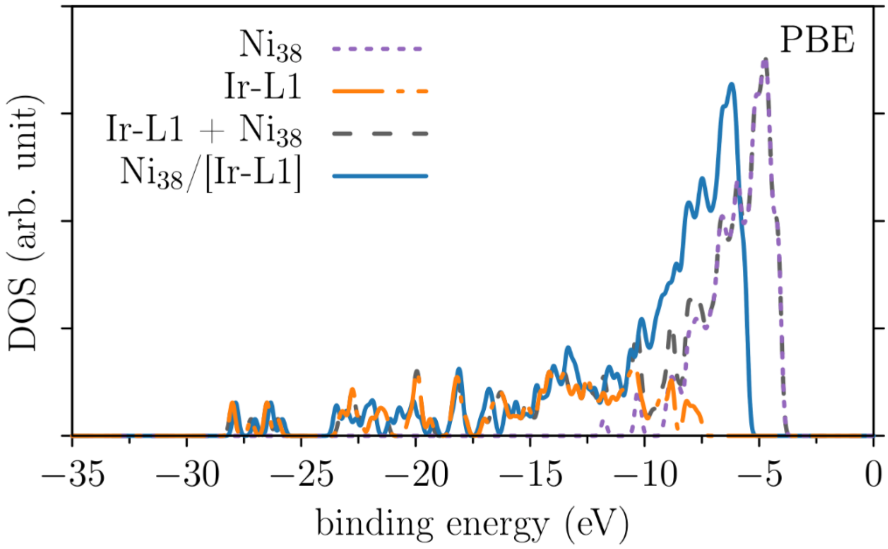

Figure S21. Theoretical density of states of Ni_{38}/[Ir-L1], N_{38}, Ir-L1, and the sum of the independently computed DOS of Ir-L1 and Ni_{38} obtained from DFT ground state calculations with PBE. See main text for details.

Finally, a plot of the highest occupied orbitals, shown in Fig. S22 for Ni_{13}/[Ir-L1] and Ni_{38}/[Ir-L1], further confirms the significant interaction: The orbital (as well as lower ones that are not shown in the plot) spreads over both the Ir-L1 and the metal particle, i.e., electron density is truly shared between the two systems.

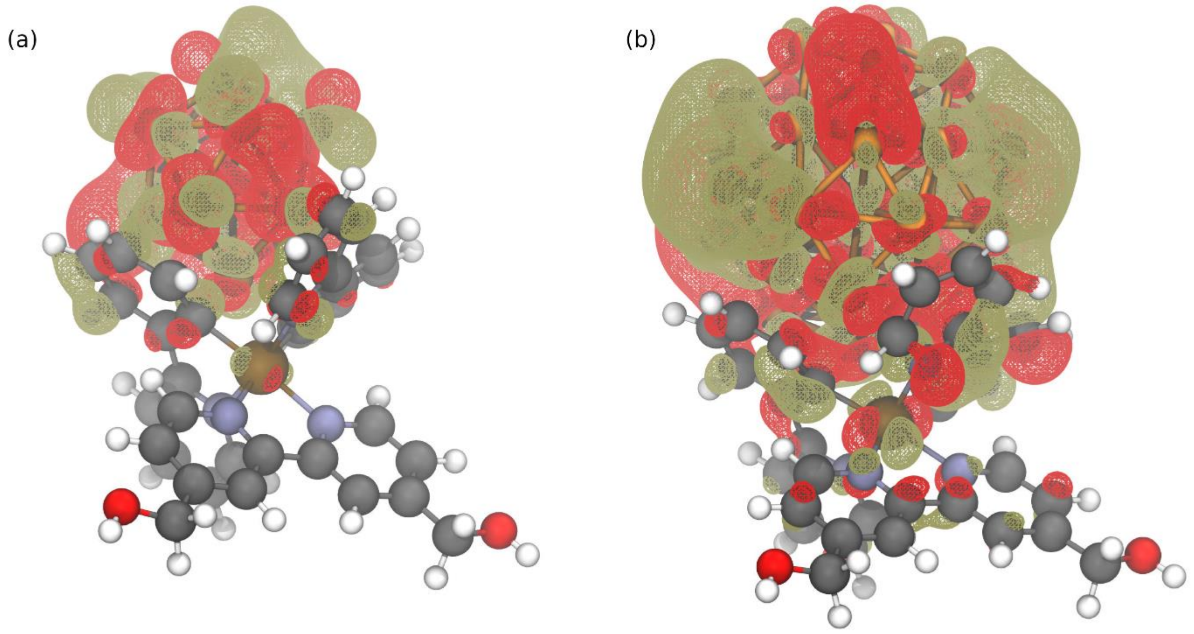

Figure S22. Isosurface plots of the highest-occupied orbital (in one spin channel, with PBE) for Ir-L1 in combination with Ni_{13} (a) and Ni_{38} (b). See main text for details.

Absorption Spectra of M_{13}

Figure S23 shows the gas-phase absorption spectra of M_{13} obtained from TDDFT calculations with ωPBE. The non-empirically optimized range-separation parameter of the respective 13-atom metal cluster was used (cf. Table S1). The absorption spectra were obtained by convoluting the TDDFT excitation spectra with a Gaussian of width 0.08 eV.

To avoid misunderstandings, it should be noted that the absorption spectra of each M_{13} (Fig. S23) differ from those shown in the main manuscript (Fig. 5), since a different range-separation parameter was used in each case. Due to using the optimally tuned range-separation parameter of each M_{13} cluster, the absorption spectra shown here are more accurate compared to those of Fig. 5. Therefore, the absorption spectra shown in Fig. S23 should be considered for, e.g., the comparison with the gas-phase experiment of M_{13}.

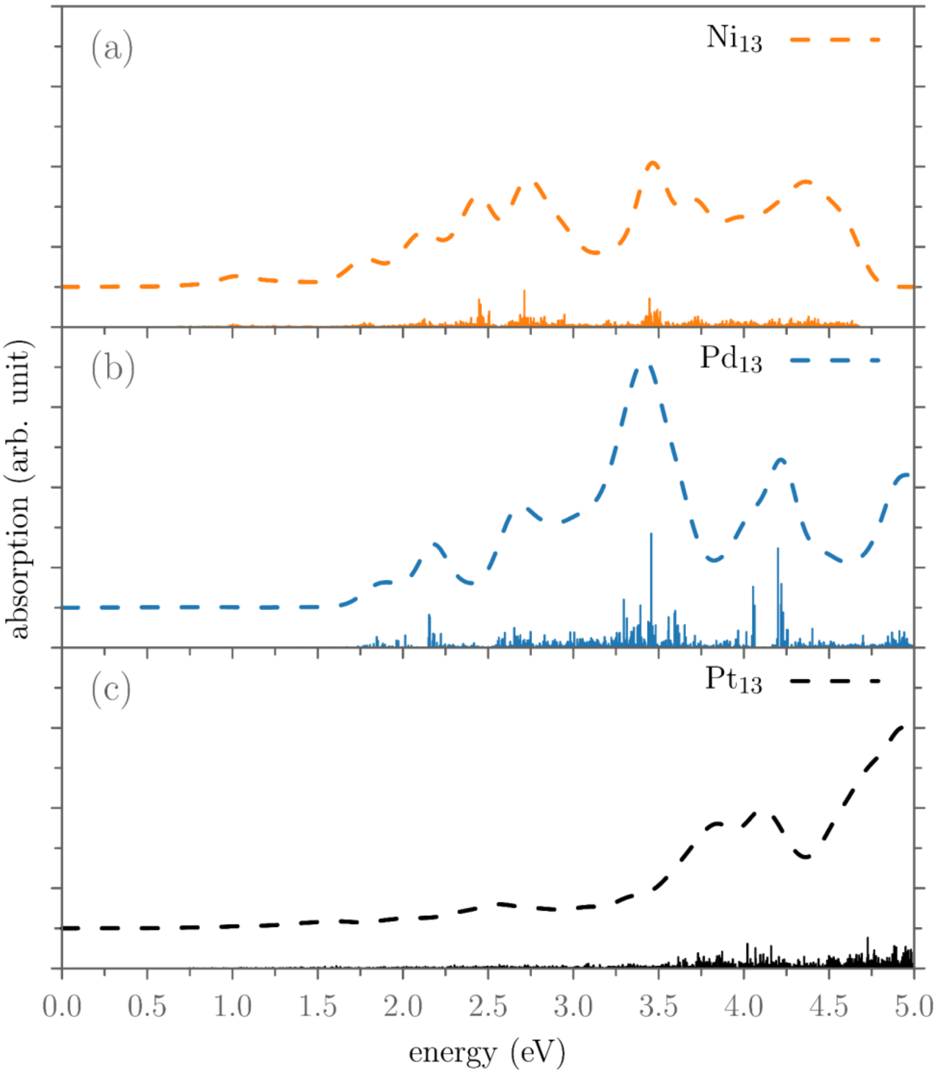

Figure S23. Theoretical absorption spectrum of M_{13}. The excitation spectra are obtained from TDDFT calculations with the non-empirical optimally tuned ωPBE, plotted on a scale of [0,2.4] arb. unit. For better visualization, all absorption spectra are shifted vertically by 0.3 arb. units. Vertical bars show the relative oscillator strength, plotted on a second scale of [0,0.2] (labels and tick marks omitted). Spectra of M_{13} with the optimally tuned ω_{opt} of each M_{13}: (a) Ni_{13} (ω_{opt}=0.18 bohr^{-1}) (b) Pd_{13} (ω_{opt}=0.17 bohr^{-1}). (c) Pt_{13} (ω_{opt}=0.17 bohr^{-1}).

Excitation Difference Densities of M_{13}/[Ir-L1]

The difference densities of the 30 excitations with the highest oscillator strength up to 3.2 eV and the ground state are shown in Fig. S24 for Ni_{13}/[Ir-L1], in Fig. S25 for Pd_{13}/[Ir-L1] and in Fig. S26 for Pt_{13}/[Ir-L1]. The red and tan wireframes indicate areas of electron lack and gain, respectively. For further details, see main manuscript.

Figure S27 shows the difference density of the lowest spin-flip excitation and the ground state of M_{13}/[Ir-L1]: For Ni_{13}/[Ir-L1] (panel (a)) this is a nonet → septet transition, for Pd_{13}/[Ir-L1] (panel (b)) a quintet → triplet and for Pt_{13}/[Ir-L1] (panel (c)) a triplet → singlet.

The study on the distance dependency of the interaction between the metal nanoparticles and the Ir photosensitizer showed differences between the metal clusters, as further discussed in the main manuscript. To this end, M_{13} was successively displaced from Ir-L1 along the line connecting their centers of mass, starting from the equilibrium position. Following this procedure, we expected that the metal particle to ligand charge-transfer observed in the equilibrium position (cf. Figs. S24-S26) will successively decrease. At the same time, the excitation character should become successively more similar to those of the separate components of M_{13}/[Ir-L1]. Finally, at a certain distance, the interaction should become negligible and the photophysical observables should be directly explainable by a superposition of those of the constituents. It was particular instructive to analyze an additional separation between 7 and 10 bohr, as difference between the metal particles became evident: Firstly, the difference densities of the excitations indicated that the metal particle → ligand charge-transfer remains most pronounced for Ni_{13}/[Ir-L1] compared to Pd_{13} and Pt_{13}. The fading interaction is reflected by the excitation character becoming more similar to that of the bare components: The intramolecular charge-transfer character of the bare Ir-L1 becomes more pronounced again and/or the excitation is (partly) localized on the metal particle or not at all. Secondly, the influence of Pt_{13} subsided more strongly compared to Ni_{13} and Pd_{13} and is probably already negligible for an additional distance of about 10 bohr. These latter changes can be seen in the difference densities of M_{13}/[Ir-L1] depicted in Fig. S28. We exemplarily show the five excitations with the highest oscillator strength up to 3.2 eV of M_{13}/[Ir-L1] for an additional distance of 10 bohr. Note that we also checked the following five excitations with lower oscillator strengths, which further confirm the addressed changes of the excitation character. At an additional distance of ca. 15 bohr, the interaction between Ir-L1 and both Ni_{13} and Pd_{13} became fully negligible.

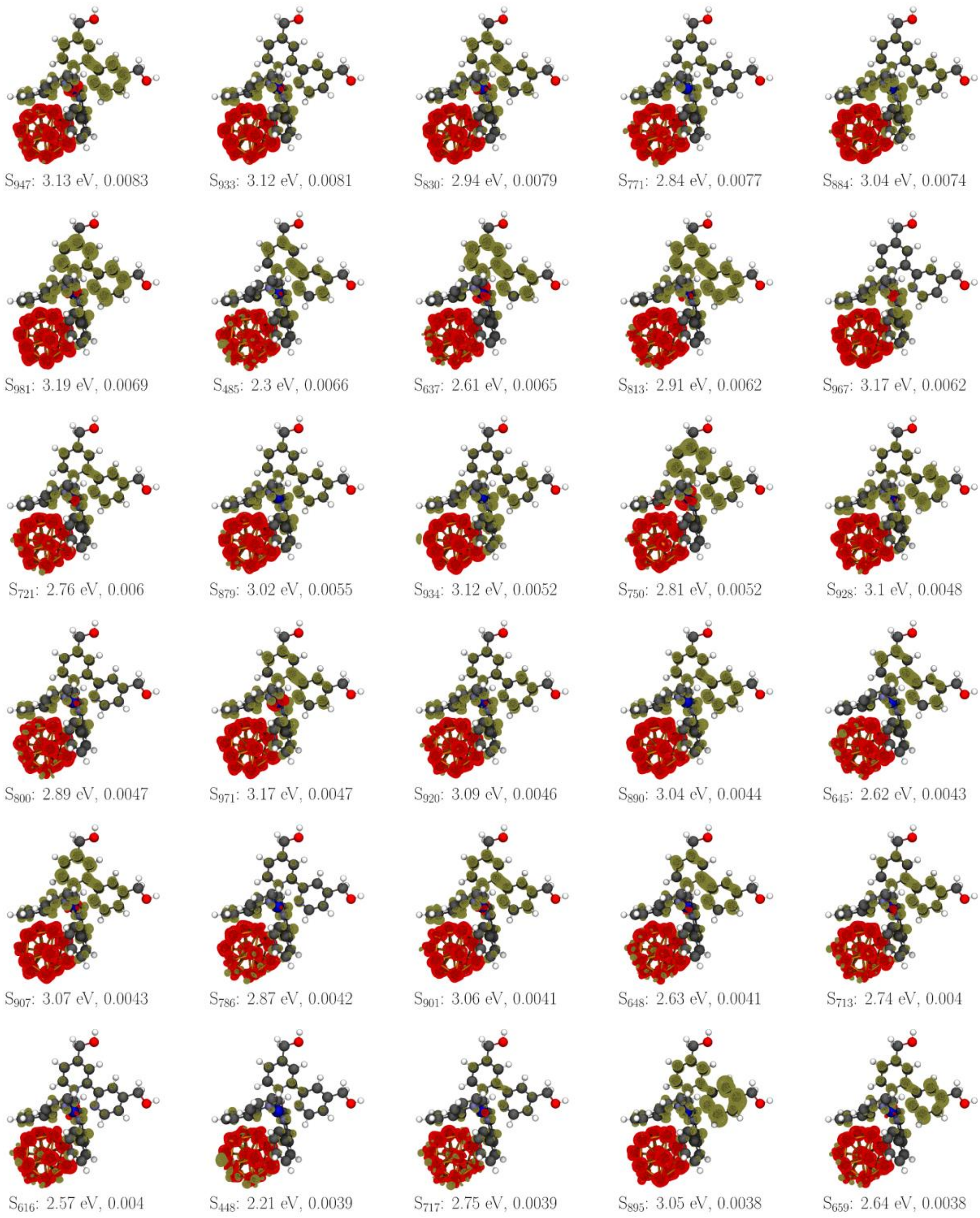

S_{947}: 3.13 eV, 0.0083
S_{933}: 3.12 eV, 0.0081
S_{830}: 2.94 eV, 0.0079
S_{771}: 2.84 eV, 0.0077
S_{884}: 3.04 eV, 0.0074

S_{981}: 3.19 eV, 0.0069
S_{485}: 2.3 eV, 0.0066
S_{637}: 2.61 eV, 0.0065
S_{813}: 2.91 eV, 0.0062
S_{967}: 3.17 eV, 0.0062

S_{721}: 2.76 eV, 0.006
S_{879}: 3.02 eV, 0.0055
S_{934}: 3.12 eV, 0.0052
S_{750}: 2.81 eV, 0.0052
S_{928}: 3.1 eV, 0.0048

S_{800}: 2.89 eV, 0.0047
S_{971}: 3.17 eV, 0.0047
S_{920}: 3.09 eV, 0.0046
S_{890}: 3.04 eV, 0.0044
S_{645}: 2.62 eV, 0.0043

S_{907}: 3.07 eV, 0.0043
S_{786}: 2.87 eV, 0.0042
S_{901}: 3.06 eV, 0.0041
S_{648}: 2.63 eV, 0.0041
S_{713}: 2.74 eV, 0.004

S_{616}: 2.57 eV, 0.004
S_{448}: 2.21 eV, 0.0039
S_{717}: 2.75 eV, 0.0039
S_{895}: 3.05 eV, 0.0038
S_{659}: 2.64 eV, 0.0038

Figure S24. Difference density of optical excitations and the ground state of Ni_{13}/[Ir-L1] obtained from TDDFT with ωPBE (ω_{opt}=0.14 bohr^{-1}). The *n*'th (spin-conserving) excitation S_n is stated with its energy and oscillator strength. See main text for details.

S_{636}: 2.88 eV, 0.015
S_{649}: 2.9 eV, 0.013
S_{668}: 2.93 eV, 0.01
S_{682}: 2.96 eV, 0.0096
S_{652}: 2.9 eV, 0.0094
S_{644}: 2.89 eV, 0.0093
S_{467}: 2.54 eV, 0.0088
S_{660}: 2.92 eV, 0.0082
S_{612}: 2.83 eV, 0.0081
S_{670}: 2.94 eV, 0.008
S_{461}: 2.53 eV, 0.0064
S_{356}: 2.26 eV, 0.0059
S_{397}: 2.37 eV, 0.0052
S_{747}: 3.07 eV, 0.0051
S_{536}: 2.69 eV, 0.005
S_{735}: 3.05 eV, 0.005
S_{658}: 2.92 eV, 0.0049
S_{781}: 3.13 eV, 0.0047
S_{468}: 2.54 eV, 0.0047
S_{382}: 2.33 eV, 0.0045
S_{629}: 2.86 eV, 0.0044
S_{716}: 3.02 eV, 0.0044
S_{540}: 2.7 eV, 0.0042
S_{699}: 2.99 eV, 0.0042
S_{663}: 2.92 eV, 0.0041
S_{764}: 3.1 eV, 0.004
S_{419}: 2.43 eV, 0.0039
S_{287}: 2.04 eV, 0.0039
S_{336}: 2.2 eV, 0.0038
S_{654}: 2.91 eV, 0.0037

Figure S25. Difference density of optical excitations and the ground state of Pd_{13}/[Ir-L1] obtained from TDDFT with ωPBE (ω_{opt}=0.12 bohr^{-1}). The *n*'th (spin-conserving) excitation S_n is stated with its energy and oscillator strength.

S_{606}: 2.78 eV, 0.018
S_{501}: 2.51 eV, 0.0095
S_{559}: 2.66 eV, 0.0093
S_{599}: 2.75 eV, 0.0078
S_{565}: 2.68 eV, 0.0073
S_{669}: 2.92 eV, 0.0072
S_{551}: 2.64 eV, 0.0072
S_{563}: 2.67 eV, 0.0072
S_{451}: 2.38 eV, 0.0068
S_{548}: 2.64 eV, 0.0067
S_{574}: 2.7 eV, 0.0067
S_{730}: 3.04 eV, 0.006
S_{510}: 2.53 eV, 0.0057
S_{515}: 2.55 eV, 0.0056
S_{517}: 2.55 eV, 0.0051
S_{794}: 3.15 eV, 0.0051
S_{535}: 2.6 eV, 0.005
S_{713}: 3 eV, 0.0048
S_{568}: 2.68 eV, 0.0046
S_{373}: 2.15 eV, 0.0046
S_{804}: 3.17 eV, 0.0043
S_{798}: 3.16 eV, 0.0043
S_{769}: 3.11 eV, 0.0043
S_{380}: 2.17 eV, 0.0041
S_{382}: 2.18 eV, 0.0041
S_{263}: 1.8 eV, 0.004
S_{189}: 1.52 eV, 0.0039
S_{513}: 2.54 eV, 0.0039
S_{582}: 2.72 eV, 0.0038
S_{434}: 2.33 eV, 0.0038

Figure S26. Difference density of optical excitations and the ground state of Pt$_{13}$/[Ir-L1] obtained from TDDFT with ωPBE (ω_{opt}=0.11 bohr^{-1}). The *n*'th (spin-conserving) excitation S_n is stated with its energy and oscillator strength.

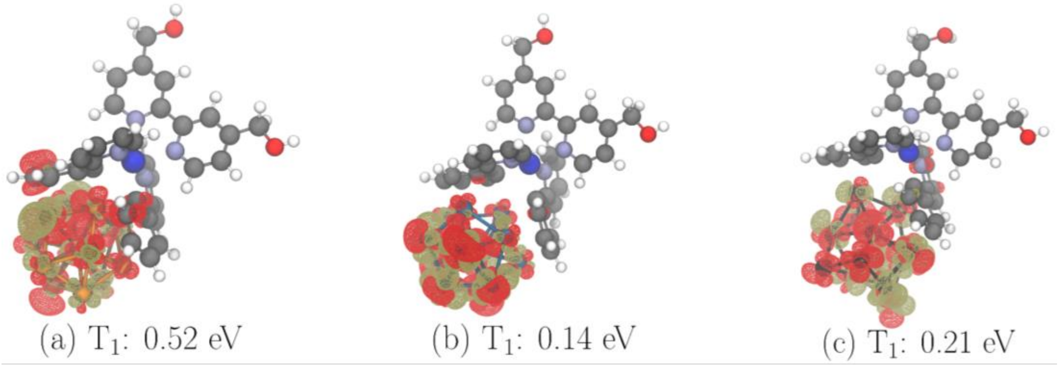

(a) T_1: 0.52 eV (b) T_1: 0.14 eV (c) T_1: 0.21 eV

Figure S27. Difference density of the lowest spin-flip excitation (labeled T_1) of M_{13}/[Ir-L1] with the given energy obtained from TDDFT (TDA) with the optimally tuned ωPBE. Ni_{13}/[Ir-L1] (ω_{opt}=0.14 bohr^{-1}) is shown in panel (a), Pd_{13}/[Ir-L1] (ω_{opt}=0.12 bohr^{-1}) in panel (b) and Pt_{13}/[Ir-L1] (ω_{opt}=0.11 bohr^{-1}) in panel (c). See main text for details.

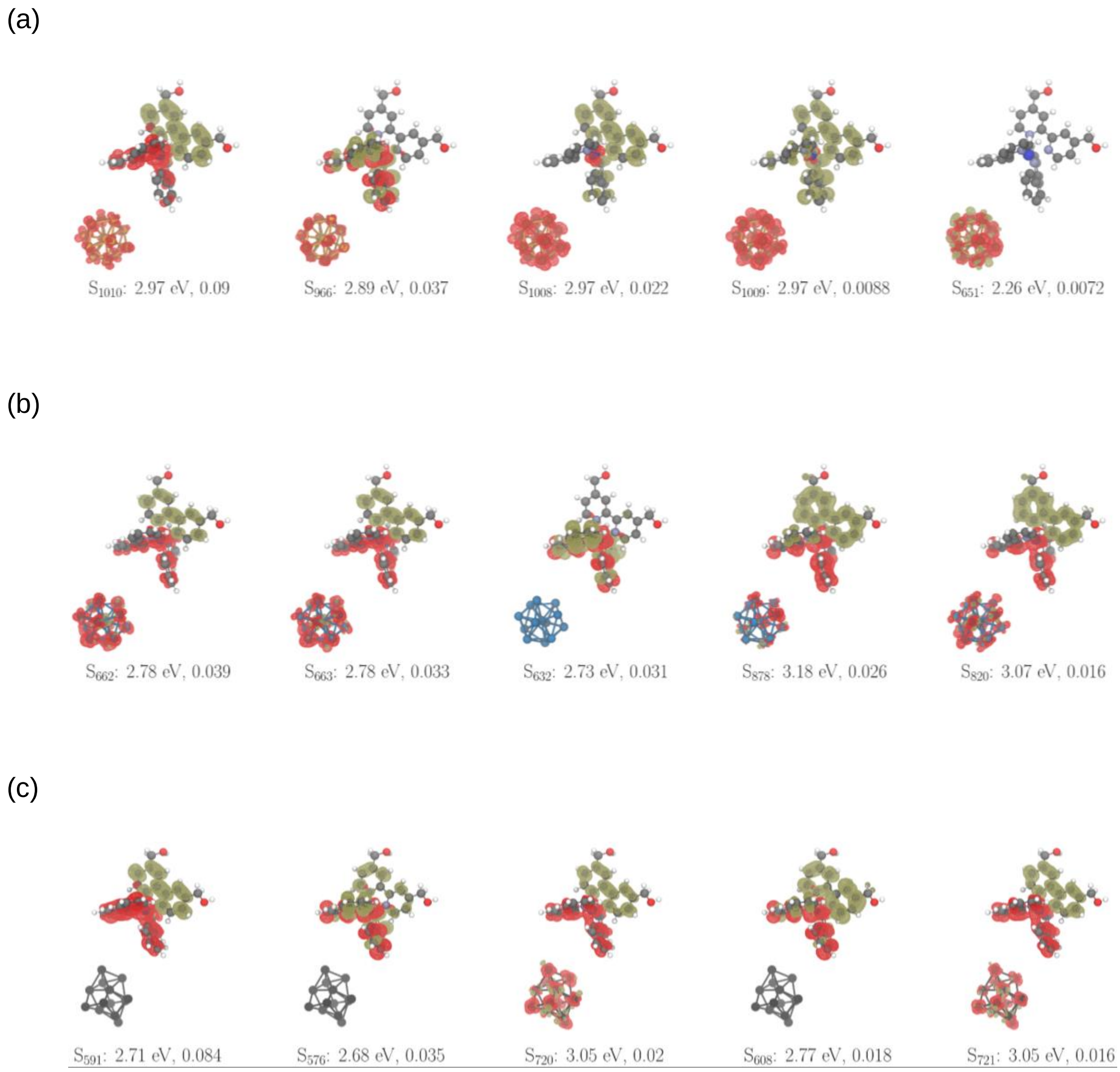

Figure S28. Difference density of optical excitations and the ground state of M_{13}/[Ir-L1] obtained from TDDFT (TDA) with ωPBE. Starting from the equilibrium position, M_{13} was displaced from Ir-L1 by 10 bohr along the line connecting their centers of mass. Ni_{13}/[Ir-L1] (ω_{opt}=0.14 bohr^{-1}) is shown in panel (a), Pd_{13}/[Ir-L1] (ω_{opt}=0.12 bohr^{-1}) in panel (b) and Pt_{13}/[Ir-L1] (ω_{opt}=0.11 bohr^{-1}) in panel (c). The n'th (spin-conserving) excitation S_n is given with energy and oscillator strength. See main text for details.

References

[S1] A. Altomare, M. C. Burla, M. Camalli, G.L. Cascarano, C. Giacovazzo, A. Guagliardi, A.G.G. Moliterni, G. Polidoli, R. Spagna, *J. Appl. Cryst.* **1999**, *32*, 115-119.

[S2] G. M. Sheldrick, *Acta Crystallogr. Sect. C Struct. Chem*. **2015**, *C71*, 3–8.

[S3] L. J. Farrugia, *J. Appl. Cryst.* **1999**, *32*, 837-838.

[S4] C. F. Macrae, P. R. Edgington, P. McCabe, E. Pidcock, G. P. Shields, R. Taylor, M. Towler, J. van de Streek, *J. Appl. Crystallogr*. **2006**, *39*, 453–457.

[S5] A. G. Condie, J. C. Gonzáles-Gómez, C. R. J. Stephenson, *J. Am. Chem. Soc.* **2010**, *132*, 1464-1465.

[S6] Y. K. Hwang, D.-Y. Hong, J.-S. Chang, S. H. Jhung, Y.-K. Seo, J. Kim, A. Vimont, M. Daturi, C. Serre, G. Férey, *Angew. Chem. Int. Ed.* **2008**, *47*, 4144–4148.

[S7] J. Hermannsdörfer, M. Friedrich, N. Miyajima, R. Q. Albuquerque, S. Kümmel, R. Kempe, *Angew. Chem. Int. Ed.* **2012**, *51*, 11473–11477.

[S8] S. Proch, J. Herrmannsdörfer, R. Kempe, C. Kern, A. Jess, L. Seyfarth, J. Senker, *Chem. Eur. J.* **2008**, *14*, 8204–8212.

[S9] F. Neese, *WIREs Comput. Mol. Sci.* **2012**, *2,* 73–78.

[S10] A. Schäfer, H. Horn. R. Ahlrichs, *J. Chem. Phys.* **1992**, *97*, 2571-2577.

[S11] A. Becke, *Phys. Rev. A* **1988**, *38*, 3098-3100.

[S12] S. Grimme, J. Antony, S. Ehrlich, H. Krieg, *J. Chem. Phys.* **2010**, *132*, 154104; S. Grimme, S. Ehrlich, L. Goerigk, *J. Comput. Chem*. **2011**, *32*, 1456–1465.

[S13] A. Klamt, G. Schüürmann, *J. Chem. Soc. Perkin. Trans. 2* **1993**, 799-805.

[S14] M. J. Piotrowski, P. Piquini, J. L. Da Silva, *Phys. Rev. B* **2010**, *81*, 155446

[S15] A. M. Köster, P. Calaminici, E. Orgaz, D. R. Roy, J. U. Reveles, S. N. Khanna, *J. Am. Chem. Soc.* **2011**, *133*, 12192–12196

[S16] A. S. Chaves, M. J. Piotrowski, J. L. Da Silva, *Chem. Phys.* **2017**, *19*, 15484–15502

[S17] M. J. Piotrowski, C. G. Ungureanu, P. Tereshchuk, K. E. Batista, A. S. Chaves, D. Guedes-Sobrinho, J. L. Da Silva, *J. Phys. Chem. C* **2016**, *120*, 28844–28856

[S18] M. Van Den Bossche, *J. Phys. Chem. A* **2019**, *123*, 3038–3045

[S19] J. P. Perdew, K. Burke, M. Ernzerhof, *Phys. Rev. Lett.* **1996**, *77*, 3865–3868

[S20] J. P. Perdew, K. Burke, M. Ernzerhof, *Phys. Rev. Lett.* **1997**, *78*, 1396–1396

[S21] S. Grimme, *J. Comput. Chem.* **2004**, *25*, 1463–1473

[S22] F. Weigend, R. Ahlrichs, *Phys. Chem. Chem. Phys.* **2005**, *7*, 3297–3305

[S23] L. Leppert, R. Kempe, S. Kümmel*, Phys. Chem. Chem. Phys.* **2015**, *17*, 26140–26148

[S24] L. L. Wang, D. D. Johnson, *Phys. Rev. B* **2007**, *75*, 1700440

[S25] D. Tilgner, M. Klarner, S. Hammon, M. Friedrich, A. Verch, N. de Jonge, S. Kümmel, R. Kempe, *Austr. J. Chem.* **2019**, *72*, 842–847

[S26] M. Klarner, S. Hammon, S. Feulner, S. Kümmel, L. Kador, R. Kempe *ChemCatChem.* **2020**, *12*, 4593–4599

[S27] S. Nosé, *J. Chem. Phys.* **1984**, *81*, 511–519.

[S28] W.G. Hoover, *Phys. Rev. A* **1985**, *31*, 1695–1697

[S29] A. Schäfer, H. Horn, R. Ahlrichs, *J. Chem. Phys.* **1992**, *97*, 2571–2577

[S30] A. Savin, *Theor. Comput. Chem.* **1996,** *4,* 327–357.

[S31] R. Baer, D. Neuhauser, *Phys. Rev. Lett.* **2005**, *94*, 043002

[S32] P. M. W. Gill, R. D. Adamson, J. A. Pople, *Mol. Phys.* **1996**, *88*, 1005–1009.

[S33] H. Iikura, T. Tsuneda, T. Yanai, K. Hirao, *J. Chem. Phys.* **2001**, *115*, 3540–3544

[S34] T. M. Henderson, B. G. Janesko, G. E. Scuseria, *J. Chem. Phys.* **2008**, *128*, 194105

[S35] M. A. Rohrdanz, J. M. Herbert, *J. Chem. Phys.* **2008**, *129*, 034107

[S36] Y. Shao, Z. Gan, E. Epifanovsky, A. T. Gilbert, M. Wormit, J. Kussmann, A. W. Lange, A. Behn, J. Deng, X. Feng, *Mol. Phys.* **2015**, *113*, 184–215

[S37] M. Levy, J. P. Perdew, V. Sahni, *Phys. Rev. A* **1984**, *30*, 2745–2748

[S38] R. Baer, E. Livshits, U. Salzner, *Annu. Rev. Phys. Chem.* **2010**, *61*, 85–109

[S39] M. E. Casida, *Recent Advances in Density Functional Methods* **1995,** 155–192

[S40] M. E. Casida, *J. Chem. Phys.* **2005**, *122*, 054111

[S41] S. Hirata, M. Head-Gordon, *Chem. Phys. Lett.* **1999,** *314,* 291–299

[S42] TURBOMOLE V7.4, **2019**

Publication 5

Pump-Probe Photoemission Simulated in Real Time: Revealing Many-Particle Signatures

Reprinted with permission from
Physical Review A **104**, 012815 (2021)

Sebastian Hammon and Stephan Kümmel

Theoretical Physics IV, University of Bayreuth, 95440 Bayreuth, Germany

My contribution

I am the first author of this paper and did all numerical calculations and simulations. During my M.Sc. thesis I had been introduced to several of the computational techniques by Matthias Dauth, and had helpful discussions on the BTDFT code with Ingo Schelter, both of whom are mentioned in the acknowledgment. Myself and S. Kümmel discussed the project repeatedly and wrote the manuscript together with frequent discussions.

Publ. 5

PHYSICAL REVIEW A **104**, 012815 (2021)

Pump-probe photoemission simulated in real time: Revealing many-particle signatures

Sebastian Hammon and Stephan Kümmel[*]
Theoretical Physics IV, University of Bayreuth, 95447 Bayreuth, Germany

(Received 6 May 2021; revised 28 June 2021; accepted 9 July 2021; published 27 July 2021)

We simulate the photoemission from an electronically excited system by computing the escape of electron density in real space using time-dependent density functional theory in real time. We show that for a one-electron system, the angular resolved photoemission after an initial excitation can be interpreted as the mapping of a previously unoccupied orbital. For the molecule perylene-3,4,9,10-tetracarboxylic dianhydride, the angular resolved photoemission (ARPES) calculated after a preceding pump pulse reveals signatures of the many-particle character of the first electronic excitation: The photoemission results from more than one time-dependent orbital, and comparing the ARPES pattern to a particle-hole analysis of the first electronic excitation confirms that the excitation does not just correspond to one electron having been moved into a previously empty orbital, but is a superposition of several single-particle excitations.

DOI: 10.1103/PhysRevA.104.012815

I. INTRODUCTION: PROBING ELECTRONIC STRUCTURE BY PHOTOEMISSION

Photoemission spectroscopy is one of the important techniques for obtaining insight into the electronic structure of condensed matter. For the simplest case of an atom or molecule in the gas phase, its basic principle is conveyed by the equation

$$E_{\mathrm{kin}} = \frac{\boldsymbol{p}^2}{2m} = \frac{\hbar^2\boldsymbol{k}^2}{2m} = \hbar\omega - |E_{\mathrm{B}}| \qquad (1)$$

that expresses the measured kinetic energy E_{kin} of the emitted electron as the difference between the known energy of the exciting photon of frequency ω and the initially unknown electron binding energy E_{B}. Here, $\hbar$ is Planck's constant, m is the electron mass, and $\boldsymbol{p}$ denotes the electron's momentum. In practice, photoemission experiments are often interpreted by relating the photoemission peaks to single-particle eigenvalues and orbitals. This amounts to identifying E_{B} with a single-particle eigenvalue. In the context of Hartree-Fock theory, this approach rests on Koopman's theorem [1]. In density functional theory (DFT), the question of the physical interpretability of the Kohn-Sham or generalized Kohn-Sham eigenvalues can depend strongly on the chosen exchange-correlation approximation [2–6]. Yet, the DFT-based single-particle interpretation of photoemission experiments has been very successful, especially for organic semiconductors [7–22].

Not withstanding this success, it is well known that the physical interpretation of the density of states from single-particle theories is intrinsically of approximative nature [23,24], as condensed matter systems consist of interacting particles. Many-body interaction (W) effects can be taken into account, e.g., by Green's function (G) methods [25]. The GW method [26] in different variants [27–29], specifically quasiparticle self-consistent GW [30], is widely used to calculate photoemission observables. Green's function approaches that go beyond the GW approximation have also been demonstrated to capture exciton physics and allow one to calculate time-resolved and angle-resolved photoemission [31].

The Dyson orbital is a formally exact quantity related to photoemission. Signatures of the differences between molecular orbitals and Dyson orbitals have been found even for otherwise benevolent organic semiconductor molecules such as perylene-3,4,9,10-tetracarboxylic dianhydride (PTCDA) [32]. The question in how far photoemission can be interpreted in terms of single-particle concepts, and when many-particle effects are so prominent that they cannot be ignored, is therefore not only of interest from a theoretical point of view, but is also of importance for the proper interpretation of experimental data. The present paper aims at contributing to this understanding from the perspective of time-dependent density functional theory (TDDFT).

The particular focus of our work is on photoemission in a pump-probe setup, i.e., a photoemission process in which a system is excited by a first electromagnetic pulse that does not lead to ionization, and then by a second pulse, which leads to ionization. Experimentally this situation has been realized in different ways, and we refer to Refs. [33–35] for just a few exemplary references for solid state, atomic, and molecular realizations, respectively. Different approaches, often using model Hamiltonians, have been developed to theoretically describe this situation; Refs. [36,37] serve to point out again just two well-known examples from a vast range of publications.

Our work here is about the first-principles simulation of such processes using TDDFT in the real-time approach. Real-time simulations of photoemission are attractive because no fitting of model parameters to experimental data is required, i.e., the approach is first principles and thus has predictive power. At the same time, real-time TDDFT

---

[*] Corresponding author: stephan.kuemmel@uni-bayreuth.de, http://www.tp4.uni-bayreuth.de/en

can be made computationally efficient [38–53] so that simulations for systems with many electrons are possible. Different methods have been proposed to simulate photoemission with TDDFT [42,54–60] and have revealed, e.g., that such calculations can accurately predict even difficult observables such as circular dichroism signals [61], which are of increasing interest experimentally [62]. In the present paper we use real-time TDDFT to simulate photoemission from excited systems in the above-mentioned pump-probe scenario.

In Sec. II, we explain our simulation method. Section III is devoted to a proof of principle. By solving the time-dependent Schrödinger equation for a one-electron system we demonstrate that the real-time ARPES simulation allows us to map excited states. In Sec. IV, we then compute pump-probe photoemission from the PTCDA molecule, a frequently studied model organic semiconductor. We show that here, photoemission from the excited molecule shows signatures of more than one molecular orbital. This is in line with interpreting the many-particle excitation as a superposition of several single-particle contributions. The result demonstrates that the notion of one electron being emitted from one orbital has its limits, that TDDFT in real time allows us to go beyond this single-particle interpretation of photoemission, and that ARPES can reveal such features. We offer conclusions in Sec. V.

II. REAL-TIME TDDFT SETUP FOR SIMULATING PHOTOEMISSION FROM ELECTRONICALLY EXCITED SYSTEMS

We calculate photoemission as a dynamical process in real time. The key elements of the process are captured in a single calculation that simulates the excitation and ionization dynamics that eventually lead to the emission and angle-resolved detection of the photoelectrons.

First, we calculate the ground state of the N-electron system self-consistently. Starting from that ground state, we solve the time-dependent Kohn-Sham (KS) equations in real time, i.e., we find the solutions of the equations

$$i\hbar\frac{\partial}{\partial t}\varphi_j(\boldsymbol{r},t)=\left[-\frac{\hbar^2}{2m}\nabla^2+v_{\mathrm{KS}}(\boldsymbol{r},t)\right]\varphi_j(\boldsymbol{r},t) \qquad (2)$$

by numerical propagation for $j = 1,\dots,N$. Here, φ_j denotes the jth KS orbital, i the imaginary number, and $v_{\mathrm{KS}}(\boldsymbol{r},t)$ the local KS potential

$$v_{\mathrm{KS}}(\boldsymbol{r},t)=v_{\mathrm{H}}(\boldsymbol{r},t)+v_{\mathrm{xc}}(\boldsymbol{r},t)+v_{\mathrm{ext}}(\boldsymbol{r})+v_{\mathrm{dip}}(\boldsymbol{r},t) \qquad (3)$$

that consists of the Hartree v_{H}, exchange correlation (XC) v_{xc}, and the external potential. For clarity, we split the latter in the contribution from the nuclei v_{ext}, which we assume to be static, and the time-dependent potential v_{dip} that represents the light field in the dipole approximation. Direct ionization out of the ground state can be simulated using one electric field represented by the potential

$$v_{\mathrm{dip}}(\boldsymbol{r},t)=e\sin(\omega t)f(t)\boldsymbol{E}_0\cdot\boldsymbol{r}. \qquad (4)$$

Here, e denotes the elementary charge, $\boldsymbol{E}_0$ is the (constant) laser polarization, ω is the frequency of the radiation, and $f(t)$ describes the temporal pulse shape, which in our simulations was chosen as detailed in Appendix B, Eq. (B1). One obtains the time-dependent density $n(\boldsymbol{r},t)$ from the sum

$$n(\boldsymbol{r},t)=\sum_{j=1}^{N}|\varphi_j(\boldsymbol{r},t)|^2. \qquad (5)$$

From the time-dependent orbitals one can compute the approximate probability of finding a photoelectron at a specific point in space, denoted as the detection point $\boldsymbol{R}_D$. This approach has first been put forward pragmatically [55]. In later work, it has been justified in more detail [57–59]. As the previous derivations differ to some extent, we shortly summarize our view of the theory in the following.

Under the action of the time-dependent potential v_{dip}, an occupied orbital $\varphi_j(\boldsymbol{r},t)$ of Eq. (2) can evolve such that parts of it become an outgoing wave packet. At a point $\mathbf{R}_D$ that is far away from the system's center, one can write this wave packet as a superposition of plane waves

$$\varphi_j(\boldsymbol{R}_D,t)=\int c_j(\boldsymbol{k})e^{i(\boldsymbol{k}\cdot\boldsymbol{R}_D-\omega_k t)}\,d^3k. \qquad (6)$$

The plane wave expansion is valid under the assumption that the ionizing dipole field has either been switched off by the time that the wave packet arrives at $\boldsymbol{R}_D$, or that the field strength is negligibly small. In this case, k and ω_k are related by the dispersion relation for free particles,

$$\omega_k=\frac{\hbar}{2m}k^2. \qquad (7)$$

As the plane waves are the eigenstates of the momentum operator, $|c_j(\boldsymbol{k})|^2$ is the probability of detecting the momentum $\hbar\boldsymbol{k}$ in the outgoing wave packet. For obtaining the coefficient $c_j(\boldsymbol{k})$ one performs a Fourier transform of $\varphi_j(\boldsymbol{R}_D,t)$ to the frequency domain:

$$\begin{aligned}\varphi_j(\boldsymbol{R}_D,\omega)&=\int_{-\infty}^{\infty}e^{i\omega t}\,dt\int c_j(\boldsymbol{k})e^{i(\boldsymbol{k}\cdot\boldsymbol{R}_D-\omega_k t)}\,d^3k\\&=\int c_j(\boldsymbol{k})e^{i\boldsymbol{k}\cdot\boldsymbol{R}_D}\,d^3k\int_{-\infty}^{\infty}e^{i(\omega-\omega_k)t}\,dt\\&=2\pi\int c_j(\boldsymbol{k})e^{i\boldsymbol{k}\cdot\boldsymbol{R}_D}\delta(\omega-\omega_k)\,d^3k.\end{aligned} \qquad (8)$$

The Dirac δ on the right-hand side indicates that only one specific value of ω_k contributes to the wave packet at $\boldsymbol{R}_D$. Via the dispersion relation Eq. (7) this relates to one unique value of $k > 0$. Furthermore, far from the system's center the plane waves will be purely outgoing in the radial direction, i.e., the direction of $\boldsymbol{k}$ is fixed by the direction of the detection point $\boldsymbol{R}_D$, $\boldsymbol{k}/k=\boldsymbol{R}_D/R_D$. The vector $\boldsymbol{k}$ is thus uniquely specified.

This analysis of Eq. (8) shows that $\varphi_j(\boldsymbol{R}_D,\omega)$ is proportional to $c_j(\boldsymbol{k}_\omega)$, with $k_\omega=\sqrt{2m\omega/\hbar}$. One can convert the probability from frequency to kinetic energy units via

$$|\varphi_j(\boldsymbol{R}_D,\omega)|^2=|\varphi_j(\boldsymbol{R}_D,E_{\mathrm{kin}}/\hbar)|^2. \qquad (9)$$

Under the assumption that Kohn-Sham particles can be identified with electrons, the total probability for detecting an electron with momentum $\hbar\boldsymbol{k}$ at the point $\boldsymbol{R}_D$ is given by summing up the probabilities for all outgoing wave packets, i.e., summing the contributions from all occupied Kohn-Sham orbitals. Therefore, a measure for the total probability

$I(\boldsymbol{R}_D, E_{\mathrm{kin}})$ of finding a photoelectron with kinetic energy E_{kin} at $\boldsymbol{R}_D$ is

$$I(\boldsymbol{R}_D, E_{\mathrm{kin}}) \propto \sum_{j=1}^{N} |\varphi_j(\boldsymbol{R}_D, E_{\mathrm{kin}}/\hbar)|^2. \tag{10}$$

Before we proceed to discuss how Eq. (10) is used in practice, we discuss its theoretical foundations. Interpreting the occupied Kohn-Sham orbitals is an approximation, but one that can well be justified: Chong *et al.* [2] have shown that the occupied Kohn-Sham eigenvalues resulting from an accurate XC potential are very good approximations to ionization potentials. It has further been argued that for systematic reasons [11,63], DFT eigenvalues can well approximate relaxed ionization energies. For molecules with a complicated electronic structure, e.g., orbitals localized on different length scales, this may require advanced functional approximations [4,14]. (For our study here, we explain further down why our XC approximations are justified.) It has also been argued on general grounds that DFT orbitals can approximate Dyson orbitals [32,64], and photoemission experiments have confirmed such interpretations [9]. Thus, the DFT-based interpretation of photoemission is an approximate but nevertheless powerful point of view that complements the perspective of traditional quasiparticle theory. Practical implementations of the latter, e.g., in the form of the GW approximation, come with their own set of approximations, leading to different variants of GW with potentially differing results [26–29,65–67]. The common basis and unifying perspective can be seen in the Dyson equation. Especially the generalized Kohn-Sham formalism, which for orbital-dependent XC functionals leads to a nonmultiplicative potential, establishes a formal similarity to the nonlocal self-energy of traditional many-particle theory (see, e.g., Refs. [6,14] for recent overviews focusing on molecules and organic semiconductors).

Equation (10) is our basis for computing ARPES spectra and their relative intensities. The molecule of interest is subjected to a time-dependent dipole field that liberates some density. Numerically, we assure that this liberation is possible by representing the time-dependent orbitals on large numerical grids in real space. The time-dependent Kohn-Sham orbitals are recorded as functions of time on a set of spatially fixed detection points $\{\boldsymbol{R}_D\}$ placed on a hemisphere around the system's center. Carefully tailored absorbing boundaries make sure that reflections at the grid boundaries are minimized (see Appendix B) and thus do not contribute noticeably to the recorded signals. The recorded values of $\varphi_j(\boldsymbol{R}_D, t)$ are numerically Fourier transformed into the frequency domain and the photoemission intensity at each point $\boldsymbol{R}_D$ on the hemisphere is calculated via Eq. (10).

In the present study we want to simulate photoemission from an excited system, and therefore extend the above-described scheme in the following way. We first determine the dipole-allowed electronic excitation energies of the system that we want to study in a separate, initial linear response calculation. Any linear response technique can be used here, e.g., one could resort to the well-known Casida [68] or Sternheimer [69,70] TDDFT methods. In this work, we stay with the real-time approach also for this task and use the well-established boost excitation [38]. The resulting linear-response signal is evaluated with the advanced technique that has been described in full detail in Ref. [51]. From it we obtain the excitation energies and the corresponding transition dipole moments and transition densities accurately.

We then start the actual simulation of the pump-probe photoemission process by exciting the system, which initially is in its ground state, with a first potential

$$v_{\mathrm{pump}}(\boldsymbol{r}, t) = e \sin(\omega_{\mathrm{L},1} t) f_1(t) \boldsymbol{E}_{0,1} \cdot \boldsymbol{r}. \tag{11}$$

The frequency $\hbar\omega_{\mathrm{L},1}$ is chosen such that it corresponds to the first dipole allowed excitation energy of the system. This models the pump excitation. We are using low enough intensities so that the plane-wave approximation of Eq. (6) is well justified [57]. After a waiting time, which we realize via a delayed ramp-up function $f_2(t)$ we turn on a second potential

$$v_{\mathrm{probe}}(\boldsymbol{r}, t) = e \sin(\omega_{\mathrm{L},2} t)\, f_2(t)\, \boldsymbol{E}_{0,2} \cdot \boldsymbol{r}. \tag{12}$$

We deliberately chose a frequency $\omega_{\mathrm{L},2}$ that only allows the ionization from the excited system, i.e., we chose $\hbar\omega_{\mathrm{L},2} < |\varepsilon_{\mathrm{HOMO}}|$, where $\varepsilon_{\mathrm{HOMO}}$ is the energy of the highest occupied ground state orbital φ_{HOMO}. Thus, the total time-dependent external field is given by (see Appendix B for details and a plot)

$$v_{\mathrm{dip}}(\boldsymbol{r}, t) = v_{\mathrm{pump}}(\boldsymbol{r}, t) + v_{\mathrm{probe}}(\boldsymbol{r}, t), \tag{13}$$

and we then record and evaluate the propagated Kohn-Sham orbitals with angular resolution as described above, cf. Eq. (10).

This is the general setup for the pump-probe TDDFT simulations. The approach can be realized with different numerical implementations of the real-time Kohn-Sham equations. For the calculations in this paper we used the real-space real-time technique of the BTDFT program package that has been detailed in Ref. [51]. It is numerically efficient and parallelizes well so that large grids can be used. Appendix B gives an overview of related numerical details.

Regarding the evaluation of the photoemission signals we note that on the one hand summing Eq. (10) over all detection points $\boldsymbol{R}_D$ yields the total kinetic energy spectrum (KES) of the photoemission process, as shown, e.g., in Fig. 1. In such

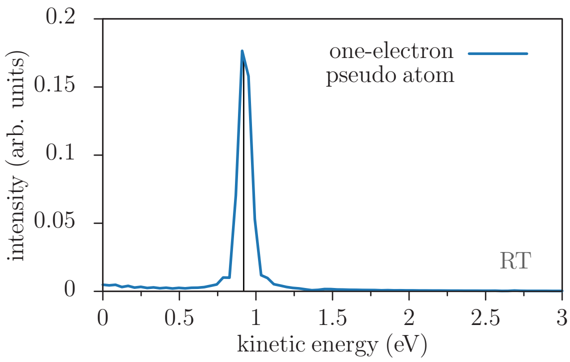

FIG. 1. KES of a one-electron Na atom in the pseudopotential approximation. The intensity weighted mean peak position $E_{\mathrm{kin}} = (0.93 \pm 0.03)\,\mathrm{eV}$ is indicated by the vertical black line. The theoretically expected peak position is $E_{\mathrm{kin}} = \hbar\omega_{\mathrm{L},2} - |\varepsilon_p| = 4.00\,\mathrm{eV} - 3.08\,\mathrm{eV} = 0.92\,\mathrm{eV}$. See main text for details.

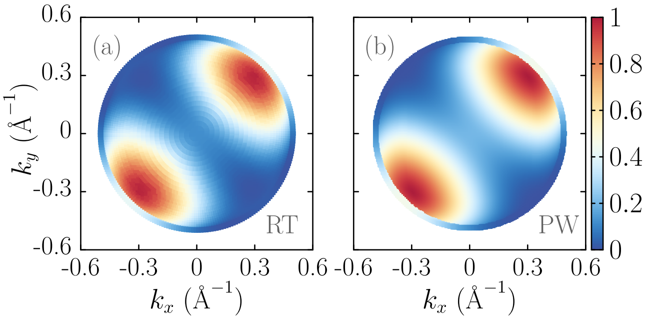

FIG. 2. Intensity momentum map for photoemission from the one-electron pseudoatom obtained from two different approaches. Left (a): Real-time simulation in the pump-probe setup with $\hbar\omega_{L,1} = 2.23$ eV and $\hbar\omega_{L,2} = 4.00$ eV as described in the main text. The map corresponds to the angle-resolved evaluation for the kinetic photoelectron energy interval of $E_{\text{kin}} \in [0.82, 1.04]$ eV centered around the main peak of the respective KES of Fig. 1. Right (b): Map for the p_1 orbital as obtained from Fermi's golden rule with a plane-wave final state and a photon energy of $\hbar\omega = 4.00$ eV and a kinetic energy $E_{\text{kin}} = 0.92$ eV. Intensities have been normalized to ease the comparison.

spectra we determine the mean peak position by weighting the energy with the intensity. The uncertainty in this mean value is estimated by choosing different energy intervals that all include the main peak, see Appendix B for a detailed explanation of this weighting procedure and for comments on further numerical details, e.g., regarding the background intensity.

On the other hand, we visualize ARPES spectra in the form of intensity maps for the photoelectron's momentum $\boldsymbol{p} = \hbar\boldsymbol{k}$, where $\boldsymbol{k}$ is the wave vector, as shown, e.g., in Fig. 2. In order to obtain these maps, we proceed in the following way. For evaluating the ARPES signal that corresponds to a certain single peak in the KES, one could in principle evaluate the spectrum at the kinetic energy that corresponds to the peak maximum. In practice, we evaluate Eq. (10) in an energy window around that peak, i.e., for a certain interval of frequencies, in order to increase the accuracy, cf. Appendix B. For a given frequency the magnitude of the momentum $|\boldsymbol{p}|$ can be calculated from Eq. (1) via $|\boldsymbol{p}| = \sqrt{2mE_{\text{kin}}}$. The vectorial components of $\boldsymbol{p}$ are directly determined by the photoelectron emission angle, which can be inferred from the detection point's position. This means that each position $\boldsymbol{R}_{\text{D}}$ relates to a specific emission direction $(\boldsymbol{p}/|\boldsymbol{p}|)$. Thus, the (relative) intensity of finding $\boldsymbol{p}(E_{\text{kin}})$ is revealed by the kinetic energy spectrum $I(\boldsymbol{R}_D, E_{\text{kin}})$ at the respective individual detection point $\boldsymbol{R}_D$. This evaluation is repeated for each kinetic energy in the aforesaid interval and the signals are then summed up over the interval. In Appendix B we elaborate on the more technical details of this real-time ARPES detection scheme and explain it in detail.

III. VERIFYING THE REAL-TIME PUMP-PROBE SCHEME: ONE-ELECTRON TEST CASE

We first demonstrate the general concept of the real-time pump probe scheme and its suitability for calculating photoemission from excited states in a proof-of-concept calculation for a transparent model system. In choosing the model, we are guided by two considerations. First, in order to eliminate uncertainties due to the exchange-correlation approximation, we chose a one-electron system. Second, for clarity of the analysis it is advantageous to look at a system in which transitions between well-specified states can be triggered. For the latter reason we chose the Na atom in the pseudopotential approximation. The latter also offers the third advantage that it can be conveniently represented on a real-space grid.

We would like to stress that the aim of this section is just a one-electron proof-of-principle calculation that the real-time, grid-based detection point scheme works for the pump-probe setup. Such a calculation could have been done with any one-electron potential. The Na pseudoatom is just a choice that can be conveniently realized in the grid-based code and that is numerically transparent. As we are looking at a one electron system, Eq. (2) can be turned into the time-dependent Schrödinger equation by setting the Hartree and XC potential to zero. The pseudopotential then just serves as the external potential of this one-electron system.

For this one-electron system we then follow the procedure described in Sec. II. First, we compute the ground state $\varphi_s(\boldsymbol{r})$ of the one-electron pseudoatom. It is of s type and the ground state eigenvalue is $\varepsilon_s = -5.31$ eV. Here and in all the following cases, bound states have negative eigenvalues. We also calculate the lowest unoccupied orbitals $\varphi_{p_k}(\boldsymbol{r})$. They are of p type, threefold ($k = 1, 2, 3$) degenerate orthonormal and with eigenvalues $\varepsilon_p = -3.08$ eV. Due to our numerical setup on a Cartesian grid with a finite spacing, the p-type orbitals preferentially align along specific spatial directions, as detailed below.

Next, we calculate the dipole-allowed excitation energies. The first excitation occurs at an energy of $E_{\text{exc}} = 2.23$ eV, which accurately relates to the eigenvalue difference $\Delta\varepsilon = \varepsilon_p - \varepsilon_s$, and thus, to the dipole-active transition $s \to p$.

We then solve the one-electron Schrödinger equation with the ground state as the initial state and the potential $v_{\text{dip}}(\boldsymbol{r}, t)$ of Eq. (13) with the parameters $\hbar\omega_{\text{L},1} = E_{\text{exc}}$ and $\hbar\omega_{\text{L},2} = 4.00$ eV. The latter choice ensures that the p states can be ionized, but that there is no direct ionization from the ground state, since $|\varepsilon_p| < \hbar\omega_{\text{L},2} < |\varepsilon_s|$. By judiciously choosing the polarization $\boldsymbol{E}_{0,l}$ of both the pump and probe lasers to match the orientation of one of the p orbitals, we can predominantly excite to and ionize from one specific p orbital. In the following discussion we focus on p_1, which is oriented in the (1,1,1) direction, i.e., the space diagonal of the Cartesian grid.

Figure 1 depicts the thus obtained KES, i.e., it results from the time evolution of what initially was the s orbital. The spectrum shows one clear peak at $E_{\text{kin}} = (0.93 \pm 0.03)$ eV (vertical black line in Fig. 1). The peak value matches Eq. (1), corresponding to a theoretical kinetic energy $E_{\text{kin}} = \hbar\omega_{\text{L},2} - |\varepsilon_p| = 0.92$ eV for the ionization from the excited p state. This is the first confirmation that our simulation captures the desired pump-probe process $s \to p \to$ continuum.

A second and more detailed confirmation that our simulation correctly describes the pump-probe photoemission is seen in Fig. 2. Figure 2(a) shows the ARPES intensity momentum map $I(k_x, k_y)$ corresponding to the kinetic energy interval of [0.82, 1.04] eV that encompasses the peak from Fig. 1. The map features two intensity spots, which are centered around

$(k_x, k_y) \approx \pm(0.3, 0.3)\,\text{Å}^{-1}$. In order to demonstrate that this intensity map correctly reflects photoemission from the p_1 orbital, we also compute $I(k_x, k_y)$ for photoemission from the p_1 orbital in an independent, second approach using perturbation theory and Fermi's golden rule. For an electromagnetic field in the dipole approximation and under the assumption that the emitted electron's final state is a plane wave, the ARPES intensity I is given [9,32] by the Fourier transform of the initial orbital $\tilde{\varphi}_{in}(\boldsymbol{k})$ from which the electron is emitted, evaluated at the value

$$|\boldsymbol{k}| = \sqrt{2m(\hbar\omega - |E_\mathrm{B}|)}/\hbar \tag{14}$$

determined by the energy conservation Eq. (1), i.e.,

$$I(k_x, k_y) \propto |\boldsymbol{A}\cdot\boldsymbol{k}|^2 |\tilde{\varphi}_{in}(\boldsymbol{k})|^2_{k=\mathrm{const}}\,. \tag{15}$$

The vector potential $\boldsymbol{A}$ describes the electromagnetic field corresponding to the photon energy $\hbar\omega$ and $\boldsymbol{k}$ is the wave vector of the plane-wave final state. This line of thinking leads to the famous "visualization of orbital densities in reciprocal space" interpretation of ARPES patterns [9].

The ARPES intensity momentum map from the golden rule Eq. (15) can be compared to the one obtained from the real-time simulation along the following lines: When one substitutes the Fourier transform $\tilde{\varphi}_{p_1}(\boldsymbol{k})$ and binding energy ε_p of the respective p_1 state into Eq. (14) and Eq. (15), and ensures that the vector potential $\boldsymbol{A}$ and photon energy $\hbar\omega$ correspond to the polarization ($\boldsymbol{E}_{0,2}$) and energy of the probe laser ($\hbar\omega_{\mathrm{L},2}$) of the real-time simulation (where $\boldsymbol{E} = -\partial\boldsymbol{A}/\partial t$), then the two momentum maps should show the same relative intensity pattern if the real-time simulation describes photoemission from the p_1 orbital.

The right panel, Fig. 2(b), shows the intensity map that one obtains by evaluating Eq. (15) for the p_1 orbital as just described. When comparing Figs. 2(a) and 2(b), one can see small differences, e.g., evaluating Eq. (15) leads to slightly higher intensity towards the $\boldsymbol{k}$-space origin. Small deviations are to be expected, e.g., because the real-time simulation goes beyond the plane-wave final state approximation [61]. However, it is very reassuring to see that overall the two intensity maps are very similar and feature the same characteristic bright spots at $(k_x, k_y) \approx \pm(0.3, 0.3)\,\text{Å}^{-1}$. For completeness we mention that we repeated this procedure for the other two p_k orbitals ($k = 2, 3$) in separate calculations. This leads to identical findings.

Finally, as a further test, we also calculated the direct ionization from the s ground state. To this end, we repeated the calculations using only one laser ($\hbar\omega_\mathrm{L} = 6.23\,\mathrm{eV} > |\epsilon_s|$). Figure 3 shows that the resulting ARPES intensity momentum map clearly differs from the one seen in Fig. 2, i.e., emission from the s and the p orbitals can clearly be distinguished from each other. Furthermore, comparing the left and the right panel in Fig. 3 shows that again the signal from the time-dependent calculation (evaluated around the main peak at 0.92 eV in the interval [0.82, 1.04] eV) on the one hand, and from Fermi's golden rule evaluated at the same energy on the other, are very similar and correspond to the emission that one expects from an s ground state. We also note that we verified explicitly that using LDA and ALDA in these calculations does not change the figures noticeably. This proof-of-principle study thus shows that our setup allows us to simulate the pump-probe process and to visualize the excited state.

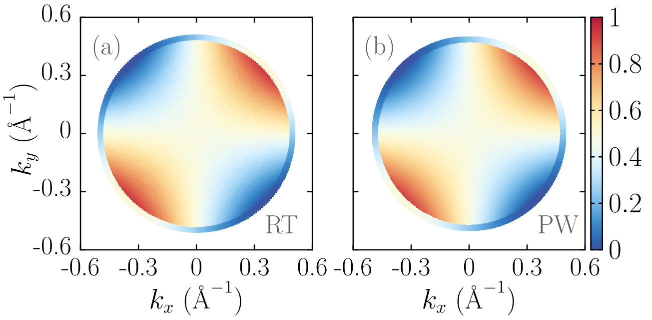

FIG. 3. Intensity momentum map for for direct photoemission from the s-orbital ground state of the one-electron pseudoatom. Left (a): Real-time simulation using a single probe laser with energy $\hbar\omega_\mathrm{L} = 6.23$ eV evaluated around the main peak at 0.92 eV. Right (b): Map for the s orbital as obtained from Fermi's golden rule with a photon energy of $\hbar\omega = 6.23$ eV at the kinetic energy $E_\mathrm{kin} = 0.92$ eV.

IV. MANY-PARTICLE SIGNATURES IN THE PHOTOEMISSION FROM PTCDA

We proceed by studying the PTCDA molecule, which is of interest because it is a model organic semiconductor that forms well-defined films on, e.g., silver surfaces, and photoemission signals can be obtained with high accuracy. It has frequently been studied both experimentally and theoretically [7,11–15,17–20,61,71–75].

Being a many-electron system, the question of which XC approximation to use now becomes relevant. For our study, we benefit from previous work in which the electronic structure of PTCDA and how its depends on the XC approximation has been analyzed in great detail [4,6,7,11,12,76]. The finding that is decisive in the present context is that the molecular orbitals of PTCDA can be divided into two groups: Ones that are delocalized over the entire molecule and others that are more localized on the side groups. An overall correct description of, e.g., the orbital ordering, can only be reached with advanced functionals such as, e.g., the optimized effective potential self-interaction correction. The delocalized orbitals, however, are reasonably well described even by inexpensive approximations such as the LDA. As we point out in the following and also discuss in Appendix A, the process that we study here involves predominantly delocalized orbitals, and we can therefore reach a qualitatively correct description with the LDA.

Our study proceeds in the same way as in the previous section, with the only difference that we are now investigating a molecule with 140 valence electrons instead of a one electron system. We first calculate the ground state with LDA. The corresponding frontier eigenvalues are listed in Table I. Next, we calculate the dipole-allowed excitation energies with the adiabatic LDA (ALDA) and find the first at $E_\mathrm{exc} = 2.14\,\mathrm{eV}$, with a transition dipole moment in the direction of the long molecular axis. Experimentally, the optical gap is $E_\mathrm{exc} = 2.6\,\mathrm{eV}$ [72]. Thus, ALDA quantitatively underestimates the first excitation energy. However, we calculated the first excitation also with

TABLE I. Eigenvalues for the two lowest-unoccupied (l) and eleven highest-occupied (h) KS eigenvalues from an LDA DFT ground state calculation, in eV.

$\varphi_{\mathrm{l+3}}$	$\varphi_{\mathrm{l+2}}$	$\varphi_{\mathrm{l+1}}$	φ_{l}	φ_{h}	$\varphi_{\mathrm{h-1}}$	$\varphi_{\mathrm{h-2}}$	$\varphi_{\mathrm{h-3}}$	$\varphi_{\mathrm{h-4}}$	$\varphi_{\mathrm{h-5}}$	$\varphi_{\mathrm{h-6}}$	$\varphi_{\mathrm{h-7}}$	$\varphi_{\mathrm{h-8}}$	$\varphi_{\mathrm{h-9}}$	$\varphi_{\mathrm{h-10}}$
−3.17	−3.66	−3.71	−5.08	−6.57	−7.16	−7.17	−7.70	−7.71	−7.83	−8.03	−8.04	−8.09	−8.64	−8.71

the hybrid functional B3LYP [77,78], which has been shown to yield an eigenvalue spectrum that compares well to the photoemission experiment [7]. We compared the character of the first excitation that we find with the ALDA to the one from the B3LYP functional, see Appendix A for details. This comparison shows that both functionals describe the structure of the first excitation very similarly. In both cases, the excitation is dominated by a transition from the highest-occupied molecular orbital (HOMO) to the lowest-unoccupied molecular orbital (LUMO), but also shows contributions from other orbitals. Also the difference between the density of the first excitation and the ground state density is extremely similar in the ALDA and the B3LYP calculation. Thus, although ALDA underestimates the first excitation energy, it correctly captures the main character of the first electronic excitation of PTCDA. Therefore, we can proceed with the ALDA, which can efficiently be evaluated on the large real-space grids that are needed for the real-time calculation of the photoemission.

Following our pump-probe photoemission protocol, we start a real-time propagation from the ground state and subject the molecule to a first excitation with a frequency that we chose to match the first excitation energy, i.e., $\hbar\omega_{\mathrm{L},1} = E_{\mathrm{exc}}$. After 10 fs we switch on the second pulse that triggers the photoemission and chose $\hbar\omega_{\mathrm{L},2} = 6.00\,\mathrm{eV}$. This choice prevents direct ionization from the ground state HOMO ($\varepsilon_{\mathrm{h}} = -6.57\,\mathrm{eV}$). The laser polarization direction $\boldsymbol{E}_{0,l}/|\boldsymbol{E}_{0,l}|$ is chosen along the long molecular axis, i.e., in the direction of the above-mentioned transition dipole moment.

Figure 4 depicts the KES that results from the detection of the 11 highest-occupied KS orbitals; with lower orbitals not contributing noticeably to the emission. We focus on the kinetic energies between approximately 1 eV and 3.5 eV, since our numerical setup is designed to represent this part of the spectrum. There is a dominant peak around $E_{\mathrm{kin}} = (1.54 \pm 0.04)\,\mathrm{eV}$, followed by some smaller intensity structures. An orbital-by-orbital analysis of the signal reveals that the main peak results not just from one orbital, but from the contributions of two orbitals, the time-dependent HOMO and the time-dependent HOMO-9. This is intriguing, because as discussed in Sec. I, in the standard interpretation of PES from organic semiconductor molecules, one peak is typically associated with one orbital. Furthermore, in previous TDDFT simulations of the direct photoemission from PTCDA, i.e., emission from the ground state, there was a one-to-one correspondence between peaks and orbitals [61]. We note that direct photoemission out of HOMO-9 to the continuum is energetically not possible even if the energy of both lasers was absorbed at once, since $E_{\mathrm{kin}} = \hbar\omega_{\mathrm{L},1} + \hbar\omega_{\mathrm{L},2} + \varepsilon_{\mathrm{h}-9} < 0$, cf. Appendix A.

In order to elucidate the situation further, we analyzed the emission in the form of an ARPES intensity momentum map $I(k_x, k_y)$ according to Eq. (10). Figure 5(a) shows the result. It depicts the total momentum distribution corresponding to the kinetic energy interval $[1.44, 1.64]\,\mathrm{eV}$, i.e., to the main peak seen in Fig. 4. Figure 4(b) shows the contribution from the time-dependent HOMO and Fig. 4(c) the one from the

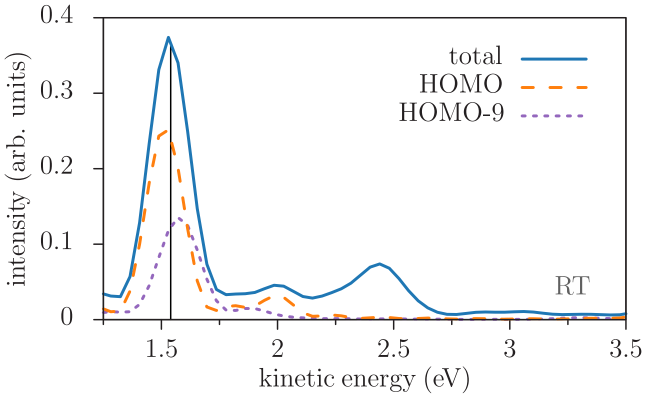

FIG. 4. KES of PTCDA obtained from the real-time pump-probe simulation. The spectrum corresponds to a pump and probe photon energy of $\hbar\omega_{\mathrm{L},1} = 2.14\,\mathrm{eV}$ and $\hbar\omega_{\mathrm{L},2} = 6.00\,\mathrm{eV}$, respectively. The total signal is computed from the detection of the eleven highest occupied time-dependent KS orbitals. The intensity weighted mean position of the main peak $E_{\mathrm{kin}} = (1.54 \pm 0.04)\,\mathrm{eV}$ is indicated by the vertical black line. The main peak predominantly results from the detection of the HOMO and HOMO-9 orbitals.

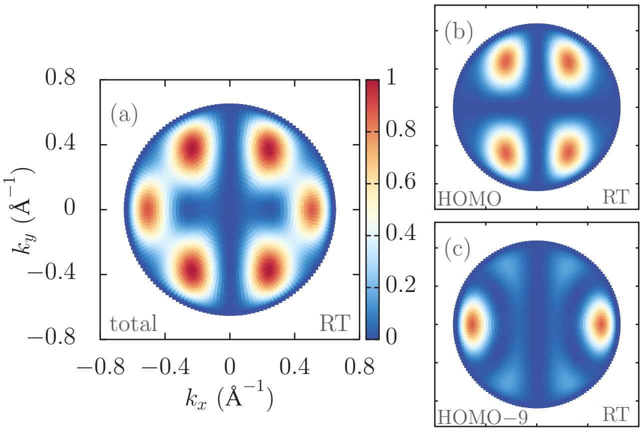

FIG. 5. Intensity momentum map of PTCDA calculated for a pump-probe scenario as explained in the main text. The long molecular axis of PTCDA coincides with the x axis. Left (a): Total signal from the real-time detection of the eleven highest occupied KS orbitals. Top right (b): Signal from the time-dependent HOMO. Bottom right (c): Signal from the time-dependent HOMO-9. Intensities are in arbitrary units and normalized to the intensity maximum 0.0021 of (a).

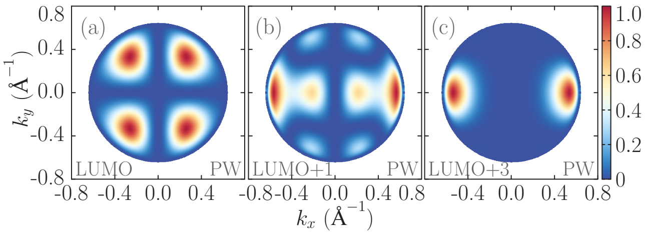

FIG. 6. (a) Fourier transform of the LUMO, (b) LUMO + 1, (c) and the LUMO + 3 evaluated at 1.54 eV. See main text for discussion.

time-dependent HOMO-9 according to Eq. (9). Comparing the left- and the right-hand sides shows that a superposition of the signatures from the two time-dependent orbitals on the right can explain the dominant features of the total signal seen on the left. Thus, the real-time simulation of the ARPES process after an initial excitation shows without doubt that more than one time-dependent orbital is involved.

It is highly instructive to look at these results also from another perspective. The first excitation of PTCDA out of which the photoemission takes place after the second pulse can also be analyzed using Casida's formulation of linear-response TDDFT based on perturbation theory [79,80]. From the point of view of the Casida formalism, a many-particle excitation is a superposition of one-electron excitations that go from occupied to unoccupied (virtual) single-particle orbitals that are the eigenstates of the time-independent, ground state Hamiltonian. The percentage with which each of the electron-hole pair excitations contributes to the true, many-particle system excitation can readily be computed. We found, cf. Appendix A, that in the ALDA the HOMO to LUMO transition contributes 96.4% to the first dipole-allowed excitation, but there are also contributions from other electron-hole pairs. The second and third highest contribution stem from the pair HOMO-8 to LUMO + 1 and HOMO-5 to LUMO + 3, respectively.

Thus, if one thinks about pump-probe ARPES in the perturbation theory picture, then the first pulse leads to an excitation that can predominantly be understood as a superposition of LUMO, LUMO + 1, and LUMO + 3, and the second pulse then leads to emission from this superposition. Figure 6 shows the Fourier transform of the LDA LUMO [Fig. 6(a)], LUMO + 1 [Fig. 6(b)], and LUMO + 3 [Fig. 6(c)] evaluated at 1.54 eV. In the straightforward interpretation of ARPES signals based on the single-particle picture and a plane-wave final state [9,32], one expects that the ARPES signal after the second pulse be dominated by these signatures. Since we do not know whether the different virtual orbitals will react differently to the second, ionizing pulse, we cannot predict how strongly each of these virtual orbitals contributes to the ARPES signal. Yet in any case, comparing Fig. 6 to Fig. 5(a) shows that, qualitatively, also this interpretation is in agreement with the ARPES signal that the real-time pump-probe simulation shows. We note, e.g., that the superposition of Fig. 6(b) and Fig. 6(c) reveals features that are seen in panel Fig. 5(c), e.g., the vertical intensity lines at $\approx k_x = \pm 0.3$ Å^{-1}.

V. CONCLUSION

In this paper we demonstrated that one can simulate photoemission from an excited system quantitatively with real-time TDDFT. Our approach unites the key elements of the process—excitation, ionization, and detection—in a single calculation.

We first studied a one electron system as a proof of concept. In our simulation, an electron is excited from the ground state by a first pulse and the system is then ionized with a second pulse. For this one-electron case, the ARPES pattern closely corresponds to the pattern that one expects for an electron emitted out of the first excited orbital, i.e., out of the orbital that is the LUMO or one of the LUMOs, respectively, in the ground state calculation.

Then we investigated the same situation for the PTCDA molecule, which is a paradigm test system for photoemission and a many-particle system with 140 valence electrons. Our calculations rely on the ALDA to ease the numerical burden, which is high due to the need for large real-space grids to numerically capture the emission process far away from the molecule's center. Using the ALDA somewhat limits the accuracy of our calculations, but we have carefully evaluated its trust range and confirmed its reliability for the observables that we report here.

We subjected the PTCDA molecule to a first pulse whose frequency was chosen to match the energy difference between the ground state and the first excitation. A second pulse then leads to the emission of electrons. The resulting ARPES signal clearly shows contributions from two time-dependent orbitals, the time-dependent HOMO and the time-dependent HOMO-9. This means that the total electronic process cannot be understood as a single electron being excited to an unoccupied orbital and then ionized by the second pulse. Instead, the process must be considered as a many-electron process. We have verified this by repeating the analysis from the complementary perspective of first-order perturbation theory in the Casida linear-response formalism. From this point of view, the first excitation is dominantly a superposition of three electron-hole pairs, one involving the LUMO and the others the LUMO + 1 and LUMO + 3, respectively. Correspondingly, the ARPES signal can also be interpreted as a superposition of the signals from the time-independent LUMO, LUMO + 1 and LUMO + 3 orbitals. Thus, our calculations have demonstrated that real-time propagation and linear-response theory offer complementary views of the same physical reality. In both cases, the photoemission from PTCDA after an initial excitation shows clear signatures of the many-particle character of the first excitation and cannot be interpreted in a simple one-orbital picture. Extending the simulations to surface situations, e.g., by including parts of the substrate in addition to the active molecule, is a worthwhile task for future work. Time-dependent simulations of the type that we presented here can help to understand time-dependent experiments, e.g., of the type that was recently presented in Ref. [81].

ACKNOWLEDGMENTS

We are grateful to M. Dauth for discussions about the real-time ARPES technique, and S.H. thankfully acknowledges being introduced to many technical aspects by M. Dauth. We are grateful to I. Schelter for discussions about the BTDFT code. S.K. further acknowledges discussions with M. Dinh and P. Wopperer about their calculations of photoemission with real-time TDDFT, and we acknowledge financial support from the SFB840, project B1, from the Bavarian State Ministry of Science, Research, and the Arts for the Collaborative Research Network "Solar Technologies go Hybrid", and from the Bavarian Polymer Institute in terms of computing resources.

APPENDIX A: DETAILED ANALYSIS OF THE ELECTRONIC EXCITATION OF PTCDA

In this Appendix we give additional information about the calculations for PTCDA. First, we report in Table I the LDA ground state eigenvalues from the real-space grid calculation. We have also checked the character of the orbitals. The orbitals that contribute decisively to the physics that we discuss in the main text, i.e., HOMO, HOMO-9, LUMO, LUMO + 1, and LUMO + 3, are all delocalized and, therefore [4], represented qualitatively correct in the LDA calculation.

Second, we report details about the explicitly linearized TDDFT calculations in the Casida formalism [79,80]. In the latter, excitations energies are computed by solving a matrix equation that is defined in the basis of KS electron-hole pairs. Hence, the contributions of the latter to the many-particle excitation are obtained straightforwardly. For these calculations we used the TURBOMOLE [82] code and the def2-TZVP basis set.

First, we employed the ALDA. It yields the first dipole-allowed excitation (optical gap) at $E_{\mathrm{exc}}^{\mathrm{LR}} = 2.16\,\mathrm{eV}$. This confirms the real-space excitation energy, and the small difference of $\pm 0.02\,\mathrm{eV}$ is within the range that one expects due to numerical differences such as basis set limitations. The Casida coefficients for the ALDA electron hole pairs are listed in the left half of Table II. From these coefficients we see that the LUMO, LUMO + 1, and the LUMO + 3 orbitals contribute the strongest to the first excitation energy. The next lower electron-hole contributions are 0.1 % or less, and are therefore neglected. We did a corresponding calculation with the B3LYP [77,78] functional, which was successfully used in previous studies of PTCDA [7]. Our result $E_{\mathrm{exc}}^{\mathrm{LR}} = 2.38\,\mathrm{eV}$ is close to the optical gap reported in Ref. [14], with a difference of only $\pm 0.03\,\mathrm{eV}$). The right-hand side of Table II reports the Casida coefficients for the B3LYP calculation.

We further confirm the many-particle nature of the first excitation energy by an analysis of the transition density. The transition density of an excitation of a many-particle system can directly be obtained accurately in a real-time calculation [51]. For an excitation that is purely of one-electron character going from one occupied to one unoccupied orbital, the transition density would be just the product of the occupied and the unoccupied orbital. We calculated the single-particle KS transition densities $\varrho_j^k(\mathbf{r}) = \langle \varphi_k | \hat{n} | \varphi_j \rangle$ for the 11 highest-occupied and 15 lowest-unoccupied stationary orbitals, where $\hat{n}$ denotes the density operator. The transition density of the single-particle transition HOMO → LUMO shows the largest similarity to the many particle transition density. However, Fig. 7 shows that there are differences between the full transition density $\rho(\boldsymbol{r}; E_{\mathrm{exc}})$ [Fig. 7(a), left] and the single-particle $\varrho_{\mathrm{HOMO}}^{\mathrm{LUMO}}(\boldsymbol{r})$ [Fig. 7(b), right]. These plots, as well as the ones shown in Fig. 8 and Fig. 9, used an isovalue of $0.0001\,a_0^{-3}$. Thus, the transition density analysis confirms the conclusion from the Casida coefficients, i.e., the first excitation of PTCDA, although dominated by the HOMO-LUMO transition, differs noticeably from a single-particle excitation.

This conclusion can be further confirmed also in other ways. One can compare the density that corresponds to the first excitation $n(\boldsymbol{r}; E_{\mathrm{exc}})$ (as output by TURBOMOLE) to the density that is associated with the single-particle transition HOMO → LUMO. The latter can be calculated straightforwardly as $n_{\mathrm{HOMO}}^{\mathrm{LUMO}} = n_0 - |\varphi_{\mathrm{HOMO}}|^2 + |\varphi_{\mathrm{LUMO}}|^2$, where $n_0(\boldsymbol{r})$ is the ground state density of PTCDA. The difference between

TABLE II. Casida linear response first excitation energy in eV (first column) and electron-hole pair contributions from HOMO-j → LUMO+k, notated as j,k., in percent, for the first three electron-hole pairs that contribute most, for two different XC approximations.

LDA	(0,0)	(8,1)	(5,3)	B3LYP	(0,0)	(6,1)	(1,3)
2.16	96.4	2.5	0.5	2.38	98.1	0.9	0.4

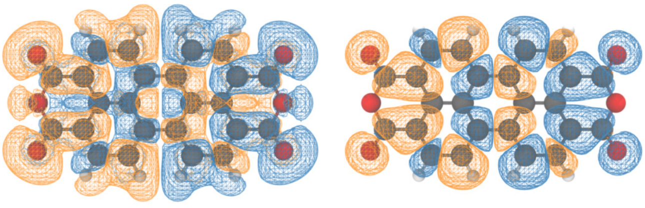
(a) full excitation (b) only HOMO→LUMO

FIG. 7. Left (a): Transition density of the first dipole-allowed excitation ($E_{\mathrm{exc}} = 2.14\,\mathrm{eV}$) of PTCDA obtained from a real-time TDDFT calculation with ALDA. Right (b): Transition density of the single-particle KS transition HOMO → LUMO calculated from the corresponding stationary orbitals via $\varrho_{\mathrm{HOMO}}^{\mathrm{LUMO}}(\mathbf{r}) = \langle \varphi_{\mathrm{LUMO}} | \hat{n} | \varphi_{\mathrm{HOMO}} \rangle$ with LDA. Blue and orange colors correspond to positive and negative values, respectively.

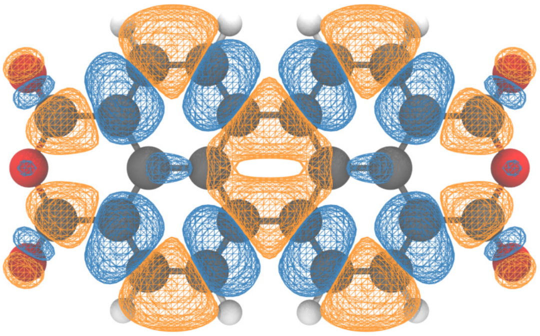

FIG. 8. Difference between the density of the first excitation (with ALDA) and the excited state density that corresponds to the single-particle transition from the ground state HOMO to the LUMO (LDA) of PTCDA. See text for details.

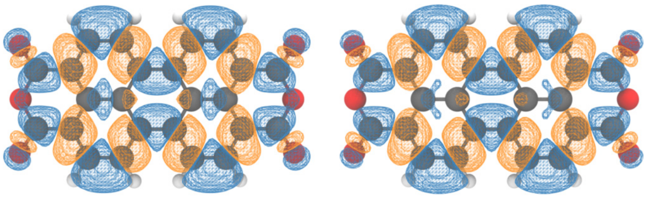
(a) ALDA (b) B3LYP

FIG. 9. Difference density of the first excitation and the ground state of PTCDA with (a) ALDA and (b) B3LYP. See main text for discussion.

$n(\boldsymbol{r}; E_{\text{exc}})$ (ALDA) and $n^{\text{LUMO}}_{\text{HOMO}}(\boldsymbol{r})$ (LDA) is shown in Fig. 8. The notable differences again confirm that the first excitation of PTCDA cannot be explained solely by the dominant single-particle transition of HOMO → LUMO.

In order to check whether the ALDA represents the decisive features of the density of the first excitation faithfully we have calculated the difference density of the first excitation and the ground state with both the ALDA and the B3LYP functional. The results are shown in Fig. 9. The difference density from the ALDA [Fig. 9(a), left] and from B3LYP [Fig. 9(b), right] are in very good qualitative agreement.

Finally, we computed the direct ARPES from the ground state of the PTCDA molecule in the gas phase with the ALDA as a crosscheck and reference for the pump-probe results discussed in the main text. We used a single ionizing pulse with $\hbar\omega_{\text{L}} = 8.14\,\text{eV} > |\epsilon_h| = 6.57\,\text{eV}$ and with the same polarization $\boldsymbol{E}_0$ along the long molecular axis as in the pump-probe scenario. Figure 10 shows the corresponding KES. Each peak results from the (real-time) detection of either one or several KS orbitals. In contrast to the pump-probe process in Sec. IV, however, the multiple contributions here are simply due to the (quasi)degeneracy of the corresponding orbitals in the initial state, cf. Table I. This can be seen from the peak positions of the individual orbital signals in Fig. 10, as they correspond to a direct ionization from the corresponding ground state orbitals, i.e., the peak positions

$$E_{\text{kin},j} = \hbar\omega_{\text{L}} - |\varepsilon_j| , \qquad \text{(A1)}$$

can be explained from the occupied KS eigenvalues, cf. Table I.

It is instructive to compare the ARPES pattern due to emission from the HOMO in the direct process here to the emission from the HOMO in the pump-probe process of Sec. IV. The peak at $E_{\text{kin}} \approx 1.57\,\text{eV}$ in Fig. 10(a) results from the detection of only the HOMO. Other lines and Fig. 10(b) depict other orbital contributions. Figure 11 shows the HOMO contribution to the ARPES intensity momentum map in the direct photoemission from the ground state of PTCDA. The map corresponds to a kinetic energy interval $E_{\text{kin}} \in [1.44, 1.64]$ that encompasses the peak in Fig. 10(a) that results from the HOMO detection. The comparison of Fig. 5 and Fig. 11 shows significant differences, and thus confirms that in the pump-probe process one does not just see the initial ground state.

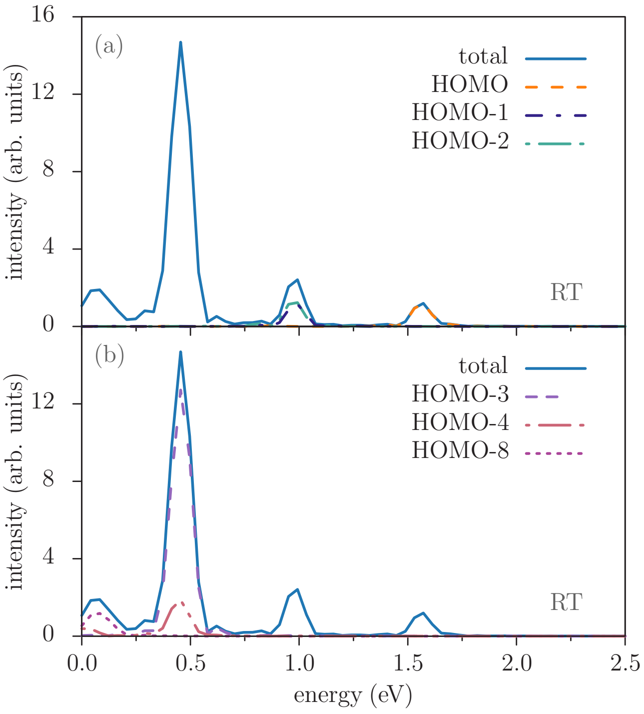

FIG. 10. KES of the direct ARPES of PTCDA. The spectrum results from the detection of the eleven highest occupied time-dependent KS orbitals. For better visualization, (a) shows the significantly contributing orbitals HOMO, HOMO-1, and HOMO-2 to the total spectrum and (b) separately shows the contributions of HOMO-3, HOMO-4, and HOMO-8. See main text for details.

APPENDIX B: NUMERICAL DETAILS

We used the real-space and real-time code BT-TDDFT [51], whose implementation of pseudopotentials originated in the PARESC code [83]. In the calculations for this paper we used an

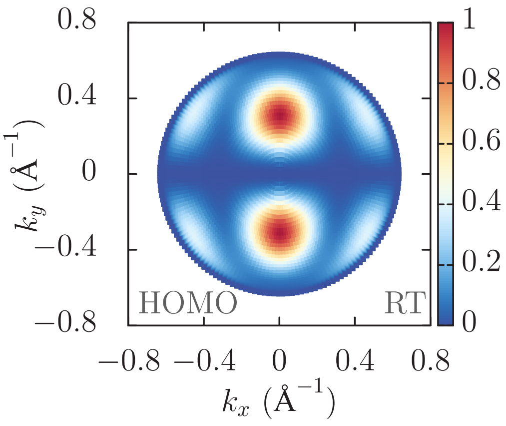

FIG. 11. Intensity momentum map of PTCDA obtained from a real-time TDDFT ARPES simulation using a single ionizing pulse with energy $\hbar\omega_{\text{L}} = 8.14\,\text{eV}$. The map results from the detection of the KS HOMO and corresponds to the angle-resolved evaluation for the kinetic photoelectron energy interval of $E_{\text{kin}} \in [1.44, 1.64]\,\text{eV}$ that encompasses the KES peak from the HOMO contribution at ≈1.57 eV shown in Fig. 10.

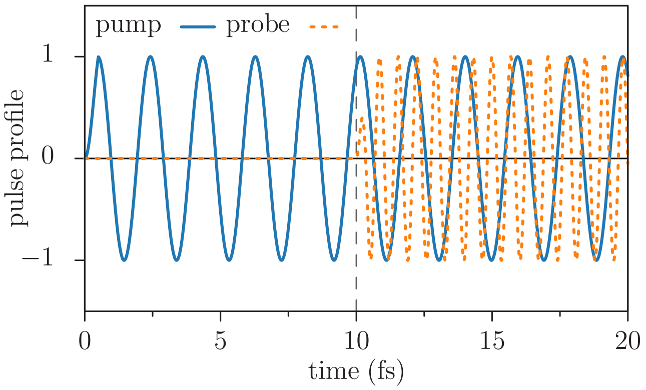

FIG. 12. The pulse profile $f_j(t)\sin[\omega_{\mathrm{L},j}(t-t_{0,j})]$ used for the PTCDA calculation (pump: $\hbar\omega_{\mathrm{L},1}=2.14\,\mathrm{eV}$, $t_{0,1}=0$, probe: $\hbar\omega_{\mathrm{L},2}=6.00\,\mathrm{eV}$, $t_{0,2}=10\,\mathrm{fs}$) for the first 20 fs. The delay of 10 fs between the pump and probe pulse is indicated by the vertical black line. After the ramp-up phase of 0.5 fs, both the pump and probe pulse keep oscillating with $\sin[\omega_{\mathrm{L},j}(t-t_{0,j})]$. See main text for details.

equidistant grid with a spherical boundary. The grid spacing was $\Delta r = 0.5\,a_0$ and $\Delta r = 0.38\,a_0$, and the boundary sphere radius was $R = 55\,a_0$ and $R = 60\,a_0$, for the calculations in Sec. III and Sec. IV, respectively. The atomic cores were described by norm-conserving Troullier-Martins [84] pseudopotentials with the following cutoff radii: H 1.39 a_0 (s), C 1.09 a_0 (s and p), O 1.10 a_0 (s and p), and Na 3.09 a_0 (s, p, and d). Considering only the valence electrons explicitly is well justified as the excitation energies in our simulations fall in the regime of VIS (pump laser) and UV-B up to UV-C (probe laser), respectively, and thus do not liberate core electrons.

The time evolution of the KS orbitals, cf. Eq. (2), was done with a Crank-Nicolson [51,85,86] propagator, a time step of $\Delta t = 0.002$ fs and a total propagation time of $T = 50$ fs. We used the following pulse shape $f_j(t)$ ($j = 1, 2$) in all ARPES simulations:

$$f_j(t)=\begin{cases}0, & t<t_{0,j}\\ (t-t_{0,j})/t_{\mathrm{r}}, & t_{0,j}\leqslant t<t_{0,j}+t_{\mathrm{r}},\\ 1, & t\geqslant t_{0,j}+t_{\mathrm{r}}\end{cases} \tag{B1}$$

where $t_{0,j}$ specifies the time at which the pulse is switched on and t_{r} is the duration of the linear ramp up. The functions $f_j(t)$ in the classical dipole fields of Eqs. (11) and (12) were chosen to ramp up within $t_{\mathrm{r}} = 0.5$ fs to a constant intensity I_0, cf. Eq. (B1). In the pump-probe simulations, we chose a delay of 10 fs between the pump and probe pulse, i.e., $t_{0,1} = 0$ and $t_{0,2} = 10$ fs. Figure 12 shows the pulse profile used in the pump-probe simulation of PTCDA.

The magnitude of the laser polarization $|\boldsymbol{E}_0|$ and intensity I_0 are related via $I_0 = \frac{\epsilon_0 c}{2}|\boldsymbol{E}_0|^2$; c is the speed of light in vacuum and ϵ_0 the vacuum permittivity. We use a laser intensity of 5×10^8 W/cm^2 for both the pump and the probe laser in Sec. III, and an intensity of 5×10^9 W/cm^2 for the calculations for PTCDA. If one wants to model a specific experiment, one can choose for the simulation the same intensity as in the experiment. In the absence of experiments, it is prudent to choose the intensity according to the following guidelines: On the one hand, low intensities are beneficial for the reasons mentioned in the context of Eq. (6) in Sec. II, for keeping higher-order effects small, and a low rate of density escape avoids overstraining the absorbing boundary. On the other hand, higher intensities lead to higher density emission and thus increase the numerical accuracy of the observation-point-based ARPES detection scheme. In practice, our experience is that the decisive ARPES features are rather robust. As an example we mention the small peak around 2.14 eV in Fig. 4, which is related to numerical noise at the frequency of the pump pulse (which was long in our simulation to get clear orbital signatures), and which does not interfere with accurately evaluating the main peak signal.

In Sec. III, we utilize the laser polarization $\hat{\boldsymbol{e}}_{0,j} = \boldsymbol{E}_{0,(j)}/|\boldsymbol{E}_{0,(j)}|$ to control which of the degenerate p_k ($k = 1, 2, 3$) orbitals is accessed in the process $s \to p_k \to$ continuum. We maximize the excitation and ionization to one of the p_k orbitals by choosing the laser polarization direction of both the pump and probe laser such that it coincides with the fictitious line that connects the centers of the dumbbells of that orbital. We calculate that direction $\hat{\boldsymbol{e}}_0(p_k)$ from $\boldsymbol{d}_{p_k} = \int \boldsymbol{r}\varphi_{p_k}(\boldsymbol{r})d^3r$, which reveals the centers of the dumbbells of the stationary orbital φ_{p_k}. In our Cartesian grid setup the directions are p_1: $\hat{\boldsymbol{e}}_{0,1}(p_1) = \hat{\boldsymbol{e}}_{0,2}(p_1) \approx (0.5904, 0.5746, 0.5668)$; p_2: $\hat{\boldsymbol{e}}_{0,1} = \hat{\boldsymbol{e}}_{0,2} \approx (-0.7894, 0.5575, 0.2571)$; p_3: $\hat{\boldsymbol{e}}_{0,1} = \hat{\boldsymbol{e}}_{0,2} \approx (0.1682, 0.5992, -0.7827)$. In the calculations for PTCDA, the polarization direction of the pulses always coincides with the long molecular axis of PTCDA, which is oriented along the x axis in our coordinate system.

In our angle-resolved real-time detection scheme we use a set of N_{D} equally distributed points $\{\boldsymbol{R}_D\}_{D=1,\ldots,N_{\mathrm{D}}}$ on a hemisphere with radius $R_{\mathrm{D}} = |\boldsymbol{R}_D|$. R_{D} must be sufficiently large so that the interaction between the emitted density and the remaining ionized system is negligible at $\boldsymbol{R}_D$. $R_{\mathrm{D}} = 40\,a_0$ and $N_d = 6400$ in all calculations shown in this paper, with the initial system being in the coordinate system's center. Recording photoemission signals on the upper hemisphere is sufficient in this study due to the symmetry of the one-electron system and the planar PTCDA molecule, respectively.

The vectorial components of the photoelectron's momentum $\boldsymbol{p} = \hbar\boldsymbol{k}$ can be written as ($E_{\mathrm{kin}} = \frac{\hbar^2k^2}{2m}$)

$$\hbar k_x = \sqrt{2mE_{\mathrm{kin}}}\cos\phi\sin\theta \tag{B2}$$

$$\hbar k_y = \sqrt{2mE_{\mathrm{kin}}}\sin\phi\sin\theta \tag{B3}$$

$$\hbar k_z = \sqrt{2mE_{\mathrm{kin}}}\cos\theta \tag{B4}$$

using spherical coordinates for the description of the photoelectron's emission angles (ϕ, θ). We derive the latter from the angular position of the detection point at which the wave packet is recorded. The resolution of the intensity momentum maps $I(\boldsymbol{p}(E_{\mathrm{kin}}))$ that we construct depends on the surface density of the detection points $\{\boldsymbol{R}_D\}$.

We determine the momentum intensity maps not only for a single kinetic energy, but for an energy interval via

$$I(\boldsymbol{p};[E_{\min},E_{\max}]) = \int_{E_{\min}}^{E_{\max}} I(\boldsymbol{p}(E_{\mathrm{kin}}))\,dE_{\mathrm{kin}}. \tag{B5}$$

In choosing the interval of frequencies that we associate with a single peak, we proceed in the following pragmatic way: In the case of nonoverlapping peaks, that interval extends until the intensity has significantly vanished, e.g., (approximately) at the first intensity minimum to the left and right of the single peak. For overlapping peaks or closely spaced signatures, the interval is chosen to be narrower, approximately between the full width at half-maximum and these latter minima, to reduce interfering signals. In the numerical implementation using a discrete-time fast Fourier transform $\mathcal{FT}$ for calculating $\mathcal{FT}\{\varphi_j(t;\boldsymbol{R}_D)\}$, the interval $[E_{\mathrm{min}}, E_{\mathrm{max}}]$ is a discontinuous sequence and consequently, the integral in Eq. (B5) becomes a sum. We express the ARPES intensity maps in terms of the components $\boldsymbol{k}$ as $I(k_x, k_y)$ of the wave vector evaluated in the above-mentioned energy interval ($[E_{\mathrm{min}}, E_{\mathrm{max}}]$). Specifying (k_x, k_y) also determines k_z, which is positive due to the detection of outgoing wave packets,

$$k_z = \sqrt{\frac{2mE_{\mathrm{kin}}}{\hbar^2} - k_x^2 - k_y^2}\,. \tag{B6}$$

The ARPES detection scheme is numerically demanding. Figure 1 nicely exemplifies some of the consequences. There are small kinetic energy signals before and after the main peak, e.g., around $E_{\mathrm{kin}} \approx 1.45\,\mathrm{eV}$, which we consider to be numerical noise. These can result from our ground state and real-time calculations being subject to finite convergence criteria, such as the discrete grid spacing and the finite numerical accuracy with which the ground state orbitals are computed. The latter limitation can be more noticeable in the propagation than in usual ground state calculations because we need to use large grids in order to be able to place the detection points far away from the ionized molecule's center. The exponential decay of the ground state orbitals leads to very small numerical values on far outlying grid points, which are difficult to represent numerically accurately. Under propagation with an ionizing pulse, numerical limitations can lead to noticeable numerical noise intensity at low kinetic energies.

After the angle-resolved detection, we absorb the outgoing density to prevent reflections at the numerical boundaries. This is achieved with a complex potential as described in Refs. [87–89] and in the form, which has been explicitly detailed in Eq. (1) in the Supplemental Material of Ref. [61]. For both the one electron and the PTCDA calculations the onset of that potential is at $R_{\mathrm{S}} = 40\,a_0$ and a shift of $\Delta = 3\,a_0$ relocates the singularity of the potential outside of the numerical sphere.

Finally, we list the details for the propagation calculations with which we determine the transition energies and densities of the initial, neutral systems. Following the procedure described in Ref. [51], we calculate the dipole-allowed electronic excitation energies and transition densities by fitting the data from the numerical propagation to the analytical form of the electronic dipole response to a dipolelike boost excitation applied to the system's ground state. All calculations are performed on a spherical grid with an equidistant grid spacing. For calculating the dipole spectrum in Sec. III we use a time step of $\Delta t = 0.01$ fs, a total propagation time of $T = 50$ fs and a boost strength of 0.0001 Ry. We choose a spherical grid radius of $R = 30\,a_0$ with a spacing of $\Delta r = 0.5\,a_0$. For PTCDA we used a time step of $\Delta t = 0.01$ fs, a total propagation time of $T = 50$ fs and a boost strength of 0.0001 Ry in combination with a grid radius $R = 40\,a_0$ and grid spacing $\Delta r = 0.38\,a_0$. After determining the energetic position of the first excitation in the dipole spectrum of PTCDA, we obtain the transition density of the former from a separate calculation employing the same numerical setup.

---

[1] T. Koopmans, Physica **1**, 104 (1933).

[2] D. P. Chong, O. V. Gritsenko, and E. J. Baerends, J. Chem. Phys. **116**, 1760 (2002).

[3] J. Akola, M. Manninen, H. Häkkinen, U. Landman, X. Li, and L.-S. Wang, Phys. Rev. B **60**, R11297 (1999).

[4] T. Körzdörfer, S. Kümmel, N. Marom, and L. Kronik, Phys. Rev. B **79**, 201205(R) (2009).

[5] U. Salzner and R. Baer, J. Chem. Phys. **131**, 231101 (2009).

[6] T. Körzdörfer and S. Kümmel, Phys. Rev. B **82**, 155206 (2010).

[7] N. Dori, M. Menon, L. Kilian, M. Sokolowski, L. Kronik, and E. Umbach, Phys. Rev. B **73**, 195208 (2006).

[8] S. Kera, S. Tanaka, H. Yamane, D. Yoshimura, K. K. Okudaira, K. Seki, and N. Ueno, Chem. Phys. **325**, 113 (2006).

[9] P. Puschnig, S. Berkebile, A. J. Fleming, G. Koller, K. Emtsev, T. Seyller, J. D. Riley, C. Ambrosch-Draxl, F. P. Netzer, and M. G. Ramsey, Science **326**, 702 (2009).

[10] A. Schöll, L. Kilian, Y. Zou, J. Ziroff, S. Hame, F. Reinert, E. Umbach, and R. Fink, Science **329**, 303 (2010).

[11] M. Dauth, T. Körzdörfer, S. Kümmel, J. Ziroff, M. Wiessner, A. Schöll, F. Reinert, M. Arita, and K. Shimada, Phys. Rev. Lett. **107**, 193002 (2011).

[12] P. Puschnig, E.-M. Reinisch, T. Ules, G. Koller, S. Soubatch, M. Ostler, L. Romaner, F. S. Tautz, C. Ambrosch-Draxl, and M. G. Ramsey, Phys. Rev. B **84**, 235427 (2011).

[13] M. Marks, N. L. Zaitsev, B. Schmidt, C. H. Schwalb, A. Schöll, I. A. Nechaev, P. M. Echenique, E. V. Chulkov, and U. Höfer, Phys. Rev. B **84**, 081301(R) (2011).

[14] L. Kronik, T. Stein, S. Refaely-Abramson, and R. Baer, J. Chem. Theory. Comput. **8**, 1515 (2012).

[15] S. Sharifzadeh, A. Biller, L. Kronik, and J. B. Neaton, Phys. Rev. B **85**, 125307 (2012).

[16] B. Stadtmüller, M. Willenbockel, E. M. Reinisch, T. Ules, F. C. Bocquet, S. Soubatc, P. Puschnig, G. Koller, M. G. Ramsey, F. S. Tautz, and C. Kumpf, Europhys. Lett. **100**, 26008 (2012).

[17] M. Wießner, D. Hauschild, C. Sauer, V. Feyer, A. Schöll, and F. Reinert, Nature Commun. **5**, 4156 (2014).

[18] D. Lüftner, T. Ules, E. M. Reinisch, G. Koller, S. Soubatch, F. S. Tautz, M. G. Ramsey, and P. Puschnig, Proc. Natl. Acad. Sci. **111**, 605 (2014).

[19] M. Marks, A. Schöll, and U. Höfer, J. Electron Spectrosc. **195**, 263 (2014).

[20] P. Puschnig, A. D. Boese, M. Willenbockel, M. Meyer, D. Lüftner, E. M. Reinisch, T. Ules, G. Koller, S. Soubatch, M. G. Ramsey, and F. S. Tautz, J. Phys. Chem. Lett. **8**, 208 (2017).

[21] N. Haag, D. Lüftner, F. Haag, J. Seidel, L. L. Kelly, G. Zamborlini, M. Jugovac, V. Feyer, M. Aeschlimann, P. Puschnig, M. Cinchetti, and B. Stadtmüller, Phys. Rev. B **101**, 165422 (2020).

[22] T. Kirchhuebel, S. Kera, T. Munakata, N. Ueno, R. Shiraishi, T. Yamaguchi, K. Yonezawa, T. Ueba, F. Bussolotti, J. Yang, T. Yamada, R. Mori, S. Kunieda, T. Huempfner, M. Gruenewald, R. Forker, and T. Fritz, J. Phys. Chem. C **124**, 19622 (2020).

[23] W. H. E. Schwarz, Angew. Chem. **45**, 1508 (2006).

[24] L. Kronik and S. Kümmel, First principle approaches to spectroscopic properties of complex materials, *Topics in Current Chemistry 347* (Springer, Berlin, 2014), pp. 137–192.

[25] G. Onida, L. Reining, and A. Rubio, Rev. Mod. Phys. **74**, 601 (2002).

[26] L. Hedin, Phys. Rev. **139**, A796 (1965).

[27] M. S. Hybertsen and S. G. Louie, Phys. Rev. B **34**, 5390 (1986).

[28] F. Caruso, P. Rinke, X. Ren, M. Scheffler, and A. Rubio, Phys. Rev. B **86**, 081102(R) (2012).

[29] L. Leppert, T. Rangel, and J. B. Neaton, Phys. Rev. Mater. **3**, 103803 (2019).

[30] S. V. Faleev, M. van Schilfgaarde, and T. Kotani, Phys. Rev. Lett. **93**, 126406 (2004).

[31] E. Perfetto, D. Sangalli, A. Marini, and G. Stefanucci, Phys. Rev. B **94**, 245303 (2016).

[32] M. Dauth, M. Wiessner, V. Feyer, A. Schöll, P. Puschnig, F. Reinert, and S. Kümmel, New. J. Phys. **16**, 103005 (2014).

[33] A. Scholl, L. Baumgarten, R. Jacquemin, and W. Eberhardt, Phys. Rev. Lett. **79**, 5146 (1997).

[34] Y. Beyazit, J. Beckord, P. Zhou, J. P. Meyburg, F. Kühne, D. Diesing, M. Ligges, and U. Bovensiepen, Phys. Rev. Lett. **125**, 076803 (2020).

[35] M. Wollenhaupt, V. Engel, and T. Baumert, Ann. Rev. Phys. Chem. **56**, 25 (2005).

[36] M. Seel and W. Domcke, J. Chem. Phys. **95**, 7806 (1991).

[37] J. K. Freericks, H. R. Krishnamurthy, and T. Pruschke, Phys. Rev. Lett. **102**, 136401 (2009).

[38] K. Yabana and G. F. Bertsch, Phys. Rev. B **54**, 4484 (1996).

[39] F. Calvayrac, P.-G. Reinhard, E. Suraud, and C. Ullrich, Phys. Rep. **337**, 493 (2000).

[40] M. A. L. Marques, A. Castro, G. F. Bertsch, and A. Rubio, Comput. Phys. Commun. **151**, 60 (2003).

[41] X. Chu and S.-I. Chu, Phys. Rev. A **70**, 061402(R) (2004).

[42] M. Mundt and S. Kümmel, Phys. Rev. B **76**, 035413 (2007).

[43] S. Meng and E. Kaxiras, J. Chem. Phys. **129**, 054110 (2008).

[44] D. A. Telnov, T. Heslar, and S.-I. Chu, Chem. Phys. **391**, 88 (2011).

[45] K. Lopata and N. Govind, J. Chem. Theory Comput. **7**, 1344 (2011).

[46] W. Liang, C. T. Chapman, and X. Li, J. Chem. Phys. **134**, 184102 (2011).

[47] X. Andrade, D. Strubbe, U. D. Giovannini, A. H. Larsen, M. J. T. Oliveira, J. Alberdi-Rodriguez, A. Varas, I. Theophilou, N. Helbig, M. J. Verstraete, L. Stella, F. Nogueira, A. Aspuru-Guzik, A. Castro, M. A. L. Marques, and A. Rubio, Phys. Chem. Chem. Phys. **17**, 31371 (2015).

[48] A. Bruner, D. Lamaster, and K. Lopata, J. Chem. Theory Comput. **12**, 3741 (2016).

[49] A. Wardlow and D. Dundas, Phys. Rev. A **93**, 023428 (2016).

[50] M. R. Provorse and C. M. Isborn, Int. J. Quantum Chem. **116**, 739 (2016).

[51] I. Schelter and S. Kümmel, J. Chem. Theory. Comput. **14**, 1910 (2018).

[52] J. J. Goings, P. J. Lestrange, and X. Li, WIREs Comput. Mol. Sci. **8**, e1341 (2018).

[53] E. Plésiat, M. Lara-Astiaso, P. Decleva, A. Palacios, and F. Martén, Chem. Eur. J. **24**, 12061 (2018).

[54] C. A. Ullrich, P.-G. Reinhard, and E. Suraud, J. Phys. B: At. Mol. Opt. Phys. **30**, 5043 (1997).

[55] A. Pohl, P.-G. Reinhard, and E. Suraud, Phys. Rev. Lett. **84**, 5090 (2000).

[56] U. De Giovannini, D. Varsano, M. A. L. Marques, H. Appel, E. K. U. Gross, and A. Rubio, Phys. Rev. A **85**, 062515 (2012).

[57] P. M. Dinh, P. Romaniello, P.-G. Reinhard, and E. Suraud, Phys. Rev. A **87**, 032514 (2013).

[58] M. Dauth and S. Kümmel, Phys. Rev. A **93**, 022502 (2016).

[59] P. Wopperer, U. D. Giovannini, and A. Rubio, Eur. Phys. J. B **90**, 51 (2017).

[60] S. A. Sato, H. Hübener, A. Rubio, and U. D. Giovannini, Eur. Phys. J. B **91**, 126 (2018).

[61] M. Dauth, M. Graus, I. Schelter, M. Wießner, A. Schöll, F. Reinert, and S. Kümmel, Phys. Rev. Lett. **117**, 183001 (2016).

[62] S. Beaulieu, J. Schusser, S. Dong, M. Schüler, T. Pincelli, M. Dendzik, J. Maklar, A. Neef, H. Ebert, K. Hricovini, M. Wolf, J. Braun, L. Rettig, J. Minár, and R. Ernstorfer, Phys. Rev. Lett. **125**, 216404 (2020).

[63] J. P. Perdew and A. Zunger, Phys. Rev. B **23**, 5048 (1981).

[64] M. E. Casida, Phys. Rev. A **51**, 2005 (1995).

[65] T. Körzdörfer and N. Marom, Phys. Rev. B **86**, 041110(R) (2012).

[66] V. Atalla, M. Yoon, F. Caruso, P. Rinke, and M. Scheffler, Phys. Rev. B **88**, 165122 (2013).

[67] M. Dauth, F. Caruso, S. Kümmel, and P. Rinke, Phys. Rev. B **93**, 121115(R) (2016).

[68] M. E. Casida, *Recent Developments and Applications in Density-Functional Theory* (Elsevier Science, Amsterdam, 1996), pp. 391–439.

[69] X. Andrade, S. Botti, M. A. L. Marques, and A. Rubio, J. Chem. Phys. **126**, 184106 (2007).

[70] F. Hofmann, I. Schelter, and S. Kümmel, J. Chem. Phys. **149**, 024105 (2018).

[71] E. Umbach and R. Fink, in *Proceedings of the International School of Physics Enrico Fermi, Course CXLIX* (IOS Press, Amsterdam, 2002).

[72] M. Wewer and F. Stienkemeier, Phys. Rev. B **67**, 125201 (2003).

[73] M. Wewer and F. Stienkemeier, J. Chem. Phys. **120**, 1239 (2004).

[74] S. Refaely-Abramson, R. Baer, and L. Kronik, Phys. Rev. B **84**, 075144 (2011).

[75] M. Marks, S. Sachs, C. H. Schwalb, A. Schöll, and U. Höfer, J. Chem. Phys. **139**, 124701 (2013).

[76] T. Schmidt and S. Kümmel, Phys. Rev. B **93**, 165120 (2016).

[77] A. D. Becke, J. Chem. Phys. **98**, 5648 (1993).

[78] P. J. Stephens, F. J. Devlin, C. F. Chabalowski, and M. J. Frisch, J. Phys. Chem. **98**, 11623 (1994).

[79] M. E. Casida, Time-dependent density functional response theory for molecules, *Recent Advances in Density Functional Methods* (World Scientific, Singapore, 1995), pp. 155–192.

[80] M. E. Casida, J. Chem. Phys. **122**, 054111 (2005).

[81] R. Wallauer, M. Raths, K. Stallberg, L. Münster, D. Brandstetter, X. Yang, J. Güdde, P. Puschnig, S. Soubatch, C. Kumpf, F. C. Bocquet, F. S. Tautz, and U. Höfer, Science **371**, 1056 (2021).

[82] TURBOMOLE V7.4, 2019, a development of University of Karlsruhe and Forschungszentrum Karlsruhe GmbH, 1989-2007, TURBOMOLE GmbH, since 2007; available from http://www.turbomole.com.

[83] L. Kronik, A. Makmal, M. L. Tiago, M. M. G. Alemany, M. Jain, X. Huang, Y. Saad, and J. R. Chelikowsky, Phys. Status Solidi B **243**, 1063 (2006).

[84] N. Troullier and J. L. Martins, Phys. Rev. B **43**, 8861 (1991).

[85] W. Press, S. Teukolsky, W. Vetterling, and B. Flannery, *Numerical Recipes in FORTRAN: The Art of Scientific Computing*, 2nd ed. (Cambridge University Press, 1992).

[86] A. Castro, M. A. L. Marques, and A. Rubio, J. Chem. Phys. **121**, 3425 (2004).

[87] D. E. Manolopoulos, J. Chem. Phys. **117**, 9552 (2002).

[88] L. Zhang, J. Chen, and J. Wang, Phys. Rev. B **87**, 205401 (2013).

[89] P. Schaffhauser and S. Kümmel, Phys. Rev. B **93**, 035115 (2016).

Acknowledgments

I am deeply grateful to numerous persons for their support in the process of creating this thesis. In particular, I wish to thank …

- **Stephan Kümmel**, for his guidance and genuine support over all these years, starting with the first day of my bachelor thesis. His wealth of ideas, inspiration, and the feeling of refreshed motivation after meetings were invaluable to this work. I am particularly impressed that with all the science, he never lost sight of the human aspect and what goes with it.

- **Thiago Branquinho de Queiroz**, for his great hospitality during my time in Brazil, which played a huge role in making my stay truly memorable. The many discussions we had and his comprehensive advice and ideas are reflected in our joint work. Obrigado por me receberem tão calorosamente e por me integrarem à vida no Brasil. Nossas reuniões no escritório em casa, no jardim, também foram bem legais.

- **All former and current members of the Theoretical Physics IV group** for the superb atmosphere and the unconditional mutual helpfulness. In particular, I would like to thank: **Linn Leppert**, for introducing me to many technical aspects of dealing with metal nanoparticles. **Matthias Dauth**, for introducing me to many technical aspects of ARPES. **Ingo Schelter**, for helpful discussions about the BTDFT code. **Alexander**, **Thomas**, **Ingo**, and **Rian**, for carefully proofreading large parts of this thesis. Moreover, it has been a pleasure to share an office with **Matthias**, **Fabian**, **Julian**, **Johannes**, and **Sabrina**.

- **Mara Klarner**, for her great engagement in our joint project in the SFB840 and for her patience in discussing all possible aspects of catalytic mechanisms with a theoretical physicist.

- **Monika Birkelbach**, **Markus Hilt**, and **Ingo Schelter** for their administrative and technical assistance.

- Among my best friends, **Rüdiger Kempf**, **Andreas Bereczuk** and **Johannes Landgraf**, for the good times we had on- and off-campus and will continue to have for many years to come.

- **Franziska Strube**, for accompanying me during my doctoral studies and, not least, making valuable comments on my defense presentation.

- My wonderful family. In particular: My parents, **Christa** and **Wolfgang**, and my sis **Marion**, who always have my back and were always understanding when I still had ”something [supposedly] important to do”. I especially also wish to thank my godfather **Erich Seeberger**, in this context, for sharing his joy in nature and technology with me.

This thesis was supported by the German Research Foundation (DFG SFB 840, B1 and DFG GRK 1640). I further acknowledge support from the Bavarian Polymer Institute in terms of computing resources (University of Bayreuth, KeyLab Theory and Simulation) and financial support from the Bavarian State Ministry of Science, Research, and the Arts for the initiative ”Solar Technologies go Hybrid”.

Eidesstattliche Versicherung

Hiermit versichere ich an Eides statt, dass ich die vorliegende Arbeit selbstständig verfasst und keine anderen als die von mir angegebenen Quellen und Hilfsmittel verwendet habe.

Weiterhin erkläre ich, dass ich die Hilfe von gewerblichen Promotionsberatern bzw. -vermittlern oder ähnlichen Dienstleistern weder bisher in Anspruch genommen habe, noch künftig in Anspruch nehmen werde.

Zusätzlich erkläre ich hiermit, dass ich keinerlei frühere Promotionsversuche unternommen habe.

Bayreuth, den 05. August 2022

Sebastian Hammon